



Forschungszentrum Karlsruhe
in der Helmholtz-Gemeinschaft

Wissenschaftliche Berichte
FZKA 6993

Transient Dynamic Finite Element Analysis of Hydrogen Distribution Test Chamber Structure for Hydrogen Combustion Loads

R.-K. Singh, R. Redlinger, W. Breitung
Institut für Kern- und Energietechnik
Programm Nukleare Sicherheitsforschung

September 2005

Forschungszentrum Karlsruhe

in der Helmholtz-Gemeinschaft

Wissenschaftliche Berichte

FZKA 6993

**Transient Dynamic Finite Element Analysis
of Hydrogen Distribution Test Chamber Structure
for Hydrogen Combustion Loads**

R.-K. Singh, R. Redlinger, W. Breitung

Institut für Kern- und Energietechnik

Programm Nukleare Sicherheitsforschung

Forschungszentrum Karlsruhe GmbH, Karlsruhe

2005

Impressum der Print-Ausgabe:

**Als Manuskript gedruckt
Für diesen Bericht behalten wir uns alle Rechte vor**

**Forschungszentrum Karlsruhe GmbH
Postfach 3640, 76021 Karlsruhe**

**Mitglied der Hermann von Helmholtz-Gemeinschaft
Deutscher Forschungszentren (HGF)**

ISSN 0947-8620

urn:nbn:de:0005-069935

Transient Dynamic Finite Element Analysis of Hydrogen Distribution Test Chamber Structure for Hydrogen Combustion Loads

Summary

Design and analysis of blast resistant structures is an important area of safety research in nuclear, aerospace, chemical process and vehicle industries. Institute for Nuclear and Energy Technologies (IKET) of Research Centre- Karlsruhe (Forschungszentrum Karlsruhe or FZK) in Germany is pursuing active research on the entire spectrum of safety evaluation for efficient hydrogen management in case of the postulated design basis and beyond the design basis severe accidents for nuclear and non-nuclear applications. This report concentrates on the consequence analysis of hydrogen combustion accidents with emphasis on the structural safety assessment. The transient finite element simulation results obtained for 2gm, 4gm, 8gm and 16gm hydrogen combustion experiments concluded recently on the test-cell structure are described. The frequencies and damping of the test-cell observed during the hammer tests and the combustion experiments are used for the present three dimensional finite element model qualification. For the numerical transient dynamic evaluation of the test-cell structure, the pressure time history data computed with CFD code COM-3D is used for the four combustion experiments. Detail comparisons of the present numerical results for the four combustion experiments with the observed time signals are carried out to evaluate the structural connection behavior. For all the combustion experiments excellent agreement is noted for the computed accelerations and displacements at the standard transducer locations, where the measurements were made during the different combustion tests. In addition inelastic analysis is also presented for the test-cell structure to evaluate the limiting impulsive and quasi-static pressure loads. These results are used to evaluate the response of the test cell structure for the postulated over pressurization of the test-cell due to the blast load generated in case of 64 gm hydrogen ignition for which additional sets of computations were performed. The computational results are also confirmed with the simplified analytical computations for the structural dynamic behavior and collapse load prediction for the quasi-static and impulsive loading of the test-cell structure.

Eine transiente, dynamische, finite-element Analyse der Wasserstoffverteilungs-Prüfzelle unter Wasserstoffverbrennungslasten

Zusammenfassung

Entwurf und Analyse von explosionsresistenten Strukturen ist ein wichtiges Gebiet in der Sicherheitsforschung der Nuklear-, Luftfahrt-, Fahrzeug- und Chemie-Industrie. Das Institut für Kern- und Energietechnik (IKET) des Forschungszentrums Karlsruhe (FZK) betreibt aktive Forschung über das ganze Spektrum der Sicherheitsmaßnahmen zum effizienten Management eines postulierten, schweren Wasserstoffunfalls in nuklearen und nicht-nuklearen Anlagen. Der vorliegende Bericht beinhaltet eine Folgeabschätzung von Wasserstoffverbrennungsunfällen mit Schwerpunkt auf der Strukturanalyse. Die Ergebnisse der transienten, finite-element Simulationen, die für Verbrennungsexperimente mit 2, 4, 8 und 16 Gramm Wasserstoff in einer Prüfzelle erhalten wurden, werden beschrieben. Die Frequenzen und Dämpfungsfaktoren der Prüfzelle, die während der Hammer- und Verbrennungs-Experimente beobachtet wurden, werden für die Kalibrierung eines 3-dimensionalen finite-element Modells verwendet. Für die numerische, transiente, dynamische Untersuchung des Verhaltens der Prüfzellenstruktur während der vier Verbrennungsexperimente werden die vom CFD-Code COM3D berechneten Druck-Zeit-Verläufe benutzt. Detaillierte Vergleiche der numerischen mit den experimentell erhaltenen Daten werden zur Validierung der modellierten Strukturverbindungen verwendet. Für alle vier Experimente zeigt sich an den Standard-Druckaufnehmerpositionen eine sehr gute Übereinstimmung der berechneten Beschleunigungen und Verschiebungen. Zusätzlich wird auch noch eine inelastische Analyse der Prüfzellenstruktur vorgestellt, mit der begrenzte dynamische und quasi-statische Drucklasten abgeschätzt werden können. Diese Ergebnisse werden dann dazu benutzt, um das Verhalten der Prüfzelle unter Explosionslasten, die durch (numerische Simulation einer) Zündung von 64 Gramm Wasserstoff erzeugt werden, vorherzusagen. Die so erhaltenen Resultate werden auch von einfachen analytischen Abschätzung bestätigt, mit denen das dynamische Verhalten und die Bruchlasten der Prüfzellen angenähert vorhergesagt werden können.

Contents

- 1. Introduction 1
- 2. Description of Test-Cell Structure 2
- 3. 3D Finite Element Model of the Test-Cell Structure 4
 - 3.1 Input Data for Transient Structural Dynamics Simulation 4
- 4. Qualification of 3D FEM Model for Test-Cell Structure 5
- 5. FEM Analysis and Results 6
 - 5.1 Phase-I Computations 8
 - 5.2 Phase-II Computations 9
 - 5.2.1 Computational Results for 2 gm Hydrogen Combustion Experiment 11
 - 5.2.2 Computational Results for 4 gm Hydrogen Combustion Experiment 12
 - 5.2.3 Computational Results for 8 gm Hydrogen Combustion Experiment 12
 - 5.2.4 Computational Results for 16 gm Hydrogen Combustion Experiment 13
 - 5.3 Evaluation of Dynamic Response for the Combustion Experiments 14
 - 5.4 Phase-III Computations (Inelastic Analysis) 16
- 6. Conclusions 18
- 7. References 20
- ANNEX I: Figures 23
- ANNEX II: Tables 115

1. Introduction

Design and analysis of blast resistant structures is an important area of safety research in nuclear, aerospace, chemical process and vehicle industries. Institute for Nuclear and Energy Technologies (IKET) of Research Centre- Karlsruhe (Forschungszentrum- Karlsruhe or FZK) in Germany is pursuing active research on the entire spectrum of safety evaluation for efficient hydrogen management in case of the postulated design basis and beyond the design basis severe accidents for nuclear and non-nuclear applications. The important steps for the overall safety evaluation involves (i) estimation of explosive mixture generation such as with accidental release of hydrogen within air and or air-steam mixture environment, (ii) investigation of the potential hazards and its evaluation with focus on the initiating events (iii) computational fluid mechanics (CFD) simulation of the combustion process for deflagration and detonation phenomena and finally (iv) the consequence analysis with structural safety evaluation. A few representative publications for the first three steps of the safety evaluation are due to Breitung et al. [2002], Baumann et al. [2002], Krieg et al. [2003], Royl et al. [2002] and Redlinger et al. [1999]. This report concentrates on the fourth step of consequence analysis with emphasis on the structural safety assessment. The objective of this report is to show that the transient response of the blast resistant structures can be simulated with confidence if the fluid transient loads and the structural model details such as the boundary conditions and the material constitutive properties are defined with desired accuracy. As in the earlier papers on the subject the emphasis is on the evaluation of the numerical analysis procedure and validation of the computational predictions with the experimental results. This is demonstrated with the transient structural dynamics finite element simulation of hydrogen distribution test chamber structure where in confined hydrogen combustion experiments were carried out. The responses such as overpressure, acceleration and displacement time histories were recorded for 1 gm, 2 gm, 4 gm, 8 gm and 16 gm hydrogen combustion experiments. The details of the experiments and the preliminary analytical structural dynamic evaluations with help of the experimental data of the test-cell structure for these transient loads are available in Singh et. al. [2004a, 2005a, 2005b].

For the prediction of the transient dynamic response of the structures due to blast load a variety of simplified methods with closed form solutions, semi-empirical maps and curves are available such as those presented by Clough and Penzin [1993], Baker et al. [1988] and Bangash [1993]. However numerical method such as finite element method is more suitable to predict the response of complex structures such as nuclear containments, blast resistant barriers and confinement vessels as these structures cannot be over simplified as a single degree of freedom structure. In the numerical analysis the linear modal analysis method is suitable for linear dynamic problems, where the structure behaviour is linear elastic and the overall response is obtained by superposition of sufficient number of modes. Method of direct time integration is often required for short duration blast loads as the structure behaviour is normally in the non linear regime either due to geometrical nonlinearity resulting in to instability and or material non linearity with large inelastic deformations or sometimes both the nonlinearities together could be significant for a problem. The finite element method with detail modeling of geometrical discontinuities and openings can be successfully used to study the limit load and predict the ultimate collapse mode of the blast resistant structures. The non linear behaviour is often important as these structures are designed with very little or marginal safety factors for the extreme loads due to the postulated initiating events such as hydrogen deflagration or detonation induced transient loads.

The present report describes the finite element simulation results obtained for 2gm, 4gm, 8gm and 16gm hydrogen combustion experiments concluded recently on the test-cell structure. Simplified analytical computations for the structural dynamic behavior and collapse load evaluations for the quasi-static and impulsive loading of the test-cell are presented in Singh et al. [2005a]. The frequencies and damping of the test-cell observed during the hammer test and the combustion experiments along with the transient pressure, acceleration and displacement time histories have been presented in Singh [2005b]. However for the present detail numerical transient dynamic evaluation of the test-cell structure, the pressure time history data computed with CFD code COM-3D by Warzecha [2004] and Kotchourko [2004] is used for the four combustion experiments. This is important as the structural behavior of the test-cell structure cannot be oversimplified for the determination of the realistic response as observed during the combustion experiments. Detail comparisons of the present numerical results for the four combustion experiments with the observed time signals are included in report by Singh et. al. [2005b]. Here details of numerical scheme such as finite model qualification with observed experimental frequencies during the hammer test and results obtained for the four combustion experiments are described. In addition inelastic analysis is also presented for the test-cell structure to evaluate the limiting impulsive and quasi-static pressure loads. These results are used to evaluate the response of the test cell structure blast load due to 64 gm hydrogen ignition postulated within the test-cell enclosure.

In the present work finite element numerical simulations are carried out with code ABAQUS version 6.3 [2002] to compare the available experimental test results. This finite element code and the analysis procedure have been qualified by Singh et. al. [2003a] with the experimental and numerical results of air blast tests reported by Jacinto et. al. [2001]. Further the influence of geometrical non-linear effects on the blast induced dynamic response of the test-cell structure and its stability problems are also investigated in the present study. This is important as the test-cell structure has an additional mass of 10 tons due to the air house above it and the influence of initial compressive stresses in the walls due to the self weight and air house weight must be investigated for the present problem. Geometrical nonlinear effects can lead to dynamic instability problems for the blast loaded structures. Hence the realistic simulation of in-plane stiffness and in-situ initial stresses is important for this class of problems. Some of the observations made with the analytical and experimental analyses reported by Singh et. al. [2003b, 2005b] for the test-cell structure are also examined. The motivation of this work is to evolve and benchmark the finite element analysis procedure for the prediction of structural transient dynamic response of the test-cell structure experimental facility with desired confidence. The present numerical study would also help in simulating postulated accident scenarios for important safety related nuclear and non nuclear structures with desired confidence for the hydrogen economy program being actively pursued at the Institute for Nuclear and Energy Technologies (IKET) of Research Centre (Forschungszentrum) Karlsruhe.

2. Description of Test-Cell Structure

The test-cell structure is housed within the experimental facility 608 of FZK (Fig 1a-1d) where all the hydrogen combustion experiments were performed. It consists of four levels; the structures under the floor, the test-cell structure, the intermediate ceiling and the ventilation structure. The main test-cell structure has an underground support structure (Fig 1e) with concrete foundation on which the floor slab of the test-cell is supported with the help of massive HEM-600 beams. In addition vibration dampers are placed below this floor for absorbing shock induced loads. Above the test-cell structure there is an intermediate ceiling

structure which separates the test-cell from the air house for the ventilation system. The weight of the air house is ~ 10 tons and the total weight of the test-cell structure is ~ 70 tons. Near the central platform (Fig 1e and 1f) combustion units in form of cubes were hung from the ceiling within which stoichiometric mixtures of hydrogen and air were ignited. In the hydrogen combustion experiments, the combustion unit cubes were placed in front of an angular drive. The objective was to simulate a leak in the supply line through which hydrogen escapes and which is subsequently ignited. During the experiments the overpressure, displacement and acceleration responses were measured. The details of the experiment and the data analysis are reported by Singh et al. [2005b]. The test-cell structure has an entry door for accessing the enclosure for locating various instruments and equipments. The door of the test-cell structure has a special design feature as it is mounted independent of the engine test-cell and has no firm connection with it. As a consequence of the blast load and the high stresses which may be generated in an accident, the door needs additional support on the outside. To prevent vibrations generated during an engine test run from being transmitted, the door is mounted to a frame which has no connection with the test-cell structure. Should there be an explosion within the engine test-cell in an accident, the door locking system would yield under these loads and open the doors to the outside. For this reason, door catchers are mounted to the frame in which the doors can engage to prevent them from returning. A pair of dampers is located in the rear wall, which serve as pressure relief device. These are designed to open at an overpressure in the test-cell of approximately 25 mbar (2.533 kPa) and thus reduce the blast induced loads acting on the test-cell structure. Although the design pressure for the test-cell structure is specified as 7.5 kPa but this arrangement is necessary due to uncertainties of the structural behavior during the combustion experiments.

The inner wall of the test-cell is lined with sheet metal sections formed into a corrugated shape with 0.8 mm thickness. It is mounted to the basic frame structure of the test-cell consisting of I-beams of various sizes. This structure is backed by an insulating layer (Egobon) ~2 mm thick attached to an outer steel plate of 3 mm thickness. At the outside again 1 mm of galvanized sheet metal forms the test-cell enclosure. For thermal and acoustic insulation of the engine test-cell, all spaces are filled with insulating material (Armaflex). The above information about the structure of the walls of the test-cell is important especially in combustion experiments, as acceleration and pressure sensors are to be installed at different points along the wall. Moreover, the loads and stresses acting on the wall of the test-cell during combustion experiments are to be simulated by computer codes, thus enabling the data obtained in this way to be compared with readings obtained in the combustion experiments.

The details of the frame structure are shown in Fig 2a-2f. The left wall (wall-A) and right wall (wall-B) are identical in construction and are made of I beams of IPB-80 and HEB-100 within the frame work of IPE-200 beams on the periphery. These frames have connections at two points with the floor frame (Fig2f) and are connected to IPE-200 beams at the ceiling level. The front wall (wall-1) has opening for the door and the door frame is connected subsequently to another frame structure as described above. The front frame is connected to the floor frame and the ceiling frame. Similarly on the rear wall (wall-2) the frame is connected to the floor and the ceiling. The floor of the test-cell has a central plate and peripheral plate with stiffeners. The inside of the test-cell has corrugated wall with bolt connections to the frame structure and the outer 3 mm steel plate is also joined to the frame structure with bolts.

3. 3D Finite Element Model of the Test-Cell Structure

Fig 3a shows the three dimensional finite element model for the full test-cell structure. It consists of the 3D frame structure (Fig 3b), the outer steel plate enclosure model (Fig 3c) and the inner corrugated wall model (Fig 3d). For the sake of computational ease the corrugated walls have been converted into equivalent orthotropic plates without any loss of accuracy and this approach has been validated with observed experimental response. This simplification resulted into a practical moderate size of finite element model where all the combustion experiments could be simulated efficiently. Fig 3e-3g show the details of the composite wall model for the typical left wall formed with the frame structure and the two plate structures namely the inner corrugated wall and the outer steel plate connected on the inside and outside of the frame structure with bolt elements. Below the test-cell the floor is supported with support structure made of massive HEM-600 beams which were included in the model and were assumed to be fixed to the ground.

Four node thick shell elements and two node beam elements have been used for the present finite element model along with connector bolt elements for simulating the bolts. There are total 4571 elements with 4702 nodes in the model along with 1987 bolt elements to provide the connections between the frame grid and the two plates for the test-cell enclosure. All the transducer locations were included in the finite element model for predicting the acceleration and displacement transient histories. It was observed during the combustion experiments that the inner corrugated walls and the corresponding location on the outer steel plate have slightly different responses even if the two plate structures are connected to the supporting frame grid structure. In view of this observation for each transducer location a pair of standard output location was identified in the finite element model one on the corrugated wall and the other on the corresponding location on the outer plate.

3.1 Input Data for Transient Structural Dynamics Simulation

The detail of input data used in the transient dynamic finite element simulation is described here that was used with the 3D FEM model of the test-cell structure. Table 1 lists all the mechanical properties of steel grade St 37-2 and St 52-3 as provided in a private communication by Henke [2003]. In addition the equivalent orthotropic properties for the corrugated walls, stiffened floor plate and stiffened central floor plate are also listed in the table, which were obtained with the calculation scheme reported by Singh et al. [2005a]. In this report preliminary simplified computations were made to judge the capability of the test-cell structure for combustion tests during the experimental phase with computer code COLLAPSE. Some of the previous results that were obtained with simplified energy theorems including finite deformations were found to be very useful for finite element model qualification presented in the next section. As shown in table 1 the steel grades St 37-2 and St 52-3 have Young's modulus of elasticity of $2.1E05$ MPa, Poisson's ratio of 0.3, density of 7800 Kg/m^3 . The yield stresses for these two grades of steel are 235 MPa and 355 MPa along with the ultimate tensile strengths of 340 MPa and 510 MPa and percentage elongations of 26 % and 22 % respectively. The stiffened plates and corrugated wall have higher rigidities along the stiffener / corrugation directions as shown in this table. The damping value of 7 % was used for the computations, which was obtained from the hammer tests and was also confirmed with the acceleration time signal data analysis of combustion experiments as reported by Singh et al. [2005b].

4. Qualification of 3D FEM Model for Test-Cell Structure

The Eigen value free vibration analysis was carried out for the test-cell 3D finite element model and the typical first ten vibration modes and natural frequencies are shown in Fig 4a - Fig 4j. The first mode with frequency 8.973 Hz results due to sway of the frame structure below the main cell. Other modes typically show excitations of various walls where local modes appear predominantly. For example the mode 2 with 16.556 Hz frequency is a local mode near the vent opening on the ceiling wall (Fig 4b). Similarly mode 3 to mode 7 with respective frequencies in the range of 16.806 to 18.561 Hz (Figs 4c-4g) show predominant local vibration modes for the front and rear walls, while mode 8 is typically the global vibration mode of the ceiling wall (Fig 4h) with frequency of 18.975 Hz. All together 500 vibration modes were extracted to study the dynamic behavior of the test-cell structure and the first ten modes have been shown here for illustration.

Subsequently the frequencies obtained with the finite element model were confirmed with the frequency evaluation reported for the simplified composite left wall analytical model (including the frame, inner corrugated sheet and the outer steel plate) using the orthotropic properties reported by Singh et. al. [2003-b]. In this evaluation the plates with the orthotropic properties are assumed to have simple support condition provided with IPE-200 beams on the boundary. As shown in Fig 5a-5h all the frequencies are in very good agreement with the simplified close form solution obtained earlier for the left wall with orthotropic properties. In all of the cases the agreement is within ~ 3 % difference, except for the first frequency of 8.973 Hz which includes the sway mode of the frame structure below the floor plate which was not simulated for the analytical model and the frequency predicted was higher (10.71 Hz) due to the shorter vertical span and simplified boundary condition of the plate at the floor level. It may be noted that this comparison is possible only for the global vibration modes of the left wall with the simplified analytical model as in the equivalent orthotropic plate model the details of local vibration mode due to frame grid stiffeners cannot be obtained. However it shows that the structural model with finite element simulation is qualified for the present problem of transient analysis for combustion induced transient loads.

Further the local modes of vibration for the different walls were confirmed with the experimental data obtained during the hammer tests. Due to repeated periodic structure with slightly different spans formed by the two plates with the frame grid structure all the walls of the test-cell structure have a range of closely spaced frequencies. This was observed during the hammer test also. With the independent observations of the vibration modes for the inner corrugated wall and the composite wall; the computed frequencies for the test-cell could be confirmed with the observed experimental hammer test data. For example the left wall showed the measured average frequency of 83.4 Hz where the inner corrugated wall along with the composite frame structure were excited. It is confirmed with the present finite element model for the computed frequency of 80.88 Hz as shown in Fig 6a. Similarly for the right wall the measured frequency with centrally located accelerometer is 76.2 Hz while the present computed value is 76.5 Hz (fig 6b). For the front wall the measured average frequency is 86.6 Hz and the computed value is 83.7 Hz as shown with the vibration modes for the corrugated wall and the composite wall in Fig 6c. Fig 6d shows the inner corrugated wall and the gcomposite wall (with outer plate and the frame structure) vibration modes for the ceiling of the test-cell structure and again the computed value of 116.11 Hz shows very good comparison with the measured frequency of 116.8 Hz.

Thus the finite element model for the test-cell structure could be qualified with the simplified analytical calculation and the experimental frequency data obtained during the hammer test. The present finite element model was evolved for the analysis of combustion loads, where significant number of modes is required to be included. This was verified during the initial phase with modal analysis. Fig 7a shows the frequency spectrum for 500 modes with a maximum frequency of 178.3 Hz which is well beyond the predominant frequencies observed during the hammer test and the present finite element numerical model represents the accurate dynamic behavior of the test-cell structure. Some of these natural modes were also confirmed during the combustion test as reported by Singh et. al. [2005b] with Fourier transforms of the acceleration time signals sampled at the later time after the impulse decays significantly and the walls vibrate in the natural mode. Figures 7b-7d show the distribution of the effective masses over the frequency spectrum up to 178.3 Hz for the three global directions; namely the longitudinal, vertical and the transverse directions of the model. It is clear that the frequencies observed for the test cell are well below the significant modes and are thus accurately included in the finite element model. Fig 7e shows the generalized mass for the test-cell structure over the frequency spectrum of 178.3 Hz and again the adequacy of the present model is illustrated.

In the course of the combustion tests the predominant pressure acoustic modes were observed below 500 Hz as shown in Singh et. al. [2005b]. So a time step of 0.1 m-sec was selected for the implicit transient finite element analysis, which would filter all the higher pressure modes not significant for the present problem and the higher insignificant structural modes with their poor representation could also be excluded. In all the transient computations the damping value of 7 % was used which was confirmed with hammer test and data analysis for the acceleration signals obtained during the combustion test as reported by Singh et. al. [2005b]. Thus the present finite element model is qualified to predict the dynamic response for combustion induced blast load, where high frequency significant modes need to be included and higher spurious modes need to be filtered out for an accurate analysis.

5. FEM Analysis and Results

The finite element analyses were carried out to compute the transient structural dynamic response of the test-cell structure for the combustion experiments with 2gm, 4gm, 8gm and 16gm of hydrogen ignition in the test-cell. The transient pressure time history data available from CFD code COM-3D by Warzecha [2004] and Kotchourko [2004] for all the experiments were adapted as input to the individual shell element surfaces of the corrugated wall through an interface program which could map the COM-3D transient pressure data in the present finite element grid. Direct implicit time integration was performed for all the cases, which is required for including the geometrical and material nonlinear effects for this class of problems.

As described earlier, with the experimental observation on the different dynamic responses of the inner corrugated wall and the outer steel plate in spite of its connections at the identical location of the relatively stiff frame grid structure, it was necessary to evaluate the structural response with different structural joint stiffness assumptions. The structural joint behavior depends on the bolt stiffness, amount of bolt tightening and the friction coefficient which decide whether the joint is slip critical or bearing type as described by Brockenbrough and Merritt [1994]. The slip critical joints carry the loads with the amount of pre-tension developed by bolt tightening and are influenced by the available bolt area and the friction which decides the slip load. These joints carry load almost like welds up to a certain limit.

The bearing type joints form structural connections by constraint offered by the bolt shanks and the stiffness is governed by the shear and bearing resistances. In most of the cases the joint behavior needs to be determined by the experimental tests and the extensive test data available in ASTM standards as mentioned in the handbook by Brockenbrough and Merritt [1994]. For the present problem of the test cell the number of joints is very large and the scatter in the in-situ joint behavior is also expected. Hence parametric analyses were made to study the response of the test-cell structure for the combustion experiments as the detail information on the structural connection behavior was unavailable.

The computational analyses for the test-cell structure were carried in three phases. The phase-I analysis was carried out to study the influence of the structural bolted joints for with and without rotation constraint conditions for the bolt elements. In addition, the case of the fully constraint joints; where in the corrugated wall and the outer plate are kinematically constrained to deform in an identical manner was also analyzed. The influence of additional damping provided by the Armaflex rubber sheets was also investigated with increased damping simulation of 10 % for the inner corrugated wall to study its significance on the dynamic response. This was based on the observations of higher damping as noticed during the data analysis for combustion experiments at a few locations. In case of controlled hammer test with small amplitude vibration, the damping values were closed to 7 % and were repeatable in different experiments. However in case of the combustion experiments with relatively larger amplitudes of vibration observed for the walls, higher damping ~ 10 % was also observed at a few locations. The time signals showed rapid decay in these cases. The finite element transient analysis showed that the structural damping does not influence the test-cell structural response significantly as the response is primarily impulsive in nature. The decay in response noticed for the time signals could be due to the partial contact developed between the corrugated wall and the rubber sheets for high amplitude vibrations. In this Phase-I analysis the corrugated wall model had slightly lower orthotropic compliances as the lateral stiffness normal to the corrugated channel direction was neglected with simplified strength of material approach; but it was improved in the subsequent phase-II computations. This preliminary phase of analysis was only useful to understand the influence of bolt element boundary constraint conditions and the structural damping on the overall dynamic response of the test-cell structure.

In phase-II analysis the bolt joints behavior was studied in more detail for the four combustion experiments. The equivalent orthotropic plate properties for the corrugated wall were evaluated more accurately as shown in Table 1 and the earlier report by Singh et. al. [2005a]. The bolt element stiffness values were evaluated for the model and comparative studies were made for the four analyses cases; (i) with stiff link element for bolt simulation, (ii) with true bolt stiffness for the corrugated wall and stiff link elements for the plate connectors, (iii) with true bolt stiffness for both the corrugated wall and the outer steel plate and finally a fourth model (iv) with bolted connections for the corrugated wall and the outer plate along with kinematic constraint conditions between the two plates for the locations that are joined with the frame structure. With the evaluation of these four models it was possible to obtain the transient structural dynamic response of the test-cell structure in good agreement with the experimental results. The variations in the computational results could also be explained with the experimental data.

The phase-III analysis concentrates on the inelastic behavior of the test-cell structure. In this case the test-cell structure was analyzed for its ultimate load carrying capacity with the qualified bolted wall model obtained from Phase-II analysis. With the background

information on the observed peak pressure in different combustion experiments and its transient duration of ~ 0.15 sec, uniform rectangular impulses were applied on all the walls of the test-cell structure. The inelastic responses of the corrugated wall, the outer plate and the frame structure were obtained for these impulses. In all the cases the analysis included pre-load effect due to the self weight and 10 ton additional gravity load due to the air house. This study helped to arrive at the limiting impulse that the test-cell would be capable to sustain in case of accidental over pressurization. In addition the limiting quasi-static pressure for the test-cell is also evaluated in this study. For all these cases the criteria of global failure is decided by the limiting strain of $\sim 5\%$, which is normally used for steel structures subjected to blast load as has been reported by Loucca and Friis [2000] and Boh et. al. [2004]. In their study they have described the energy based failure criteria to overcome the limitations of the mesh sensitivity, which needs a separate study with detail modeling of welds and structural connections. However, in the present case also the analysis describes the observed energy dissipated in the different members which could be used to arrive at the failure criteria if additional experimental data on material constitutive behavior is available. Finally a case study of 64 gm hydrogen ignition within the test-cell is also analyzed in this phase, which is based on the pressure time history generated with COM-3D code by Kotchourko [2004]. This analysis shows that the test-cell goes in to the plastic regime for 64 gm combustion event in the test cell.

The results for the three phases of computations are further described in detail in the following sections.

5.1 Phase-I Computations

In this phase the following four models were used for simulating the structural bolted joints between the corrugated wall and the outer plate with the frame structure. These models are also listed in table 2, where the predicted maximum displacements obtained with these models are compared with the experimental results. But for the sake of completeness the model description is repeated below again.

LINK Model - This finite element model simulates stiff link connections between the inner corrugated wall and the frame structure and between the outer plate and the frame structure. It provides constraints to displacement and rotation degrees of freedom with uniform damping of 7 percent for the test cell structure.

FREE Model - This finite element model simulates stiff link connections between the inner corrugated wall and the frame structure and between the outer plate and the frame structure. It provides constraints to only displacement degrees of freedom with uniform damping of 7 percent for the test cell structure.

LINK-DAMPED Model – This finite element model is same as the LINK model with higher damping value of 10 percent for the inner corrugated walls and 7 percent damping for the other members of the test cell structure.

CONSTRAINED Model – This finite element model simulates ideal constraint between the inner corrugated wall and the outer plate structure with link connections to the frame structure. A uniform damping of 7 percent is used in this case.

The maximum displacements for the different combustion experiments predicted with the above four numerical models are shown in table 2. The computational results are included for each transducer location for both the outer plate and the inner corrugated wall although the measurement data was available for one of the two locations only for most of the cases. This study was made with a view to understand the structural joint behavior of the test-cell structure for blast loads and hence computational results for both the inner corrugated wall and the outer steel plates are included. As shown in the comparative statement of table 2, the maximum displacement responses for the different combustion experiments could be predicted with good accuracy for the transducers located on the outer plate with LINK model. However the behavior on the inner corrugated wall was not satisfactory in some cases with this model; as for example for transducers Laser L2 on the left wall, Needle N7 on the right wall and Laser L1 on the front wall. The response for Needle N4-N5 located on the rear corrugated wall was consistent with the test results. With the FREE model with no rotation constraints; the behavior was close to the LINK model in most of the cases and response was not sensitive to the rotation constraint. The influence of increased damping of 10 % for the inner corrugated sheet with LINK-DAMPED model was also not significant as the response is predominantly impulse governed. The corrugated walls still show relatively larger maximum displacement compared to the recorded values even with higher damping. The CONSTRAINED model show some improvement at a few locations like for Laser L2, Needle N3 transducers on the left wall and Laser L1 transducer at the front wall but again the performance further deteriorated at the other locations such as for Needle N4-N5 at the rear plate and the wall and for Needle N6 and N7 located on the right wall of the test-cell structure.

The acceleration values computed for the different experiments are shown in table 3. In this case also the predictions with finite element analysis were shown to have large difference with the test results. Although there were a few transducers where the experimental data had less reliability due to instrumentation problems still for most of the healthy accelerometers also the structural behavior could not be definitely explained during phase-I analysis.

Phase-I analysis could help to establish the fact that the test-cell structural dynamic response is predominantly impulsive in nature as was observed during the preliminary analysis with code COLLAPSE and the experimental data analysis reported by Singh et. al. [2003b, 2005b]. The damping did not influence the structural response significantly. Since the corrugated wall orthotropic properties were estimated more accurately later during Phase-II analysis; this phase of analysis was concluded with the above remarks observed on the test-cell structural dynamic response.

5.2 Phase-II Computations

During this phase of the computation the improved orthotropic properties of the corrugated wall as shown in table 1 were included in the finite element model. In addition with the insight gained during the phase-I analysis, the following four models were evolved for the computation and to study the influence of the structural bolt connections.

LINK Model - This finite element model simulates stiff link connections between the inner corrugated wall and the frame structure and between the outer plate and the frame structure. It simulates the most rigid connection between the structural members.

BOLTED-WALL Model - This finite element model simulates the true bolt stiffness between the inner corrugated plate and the frame structure and stiff link is simulated between the outer plate and the frame structure.

BOLTED-WALL-PLATE Model – This finite element model uses identical bolt stiffness values between the outer plate and the frame structure and between the inner corrugated wall and the frame structure. This model simulates most flexible connection.

BOLTED-WALL CONSTRAINED-PLATE Model– This finite element model simulates ideal constraint between the inner corrugated wall and the outer plate structure with bolt connections between the corrugated wall and the frame structure. Thus at the frame grid locations the inner corrugated wall and the outer plate are kinematically constrained to have identical displacements.

Table 4 gives the summary of the maximum displacement values obtained with the above four models along with the experimental test data. As mentioned before for phase-I analysis the computed responses for both the inner corrugated wall and the outer steel plate are included for each transducer location to study the structural joint behavior. It may be noted from this table that the agreement between the measured displacements and the computation in general is very good for the BOLTED-WALL model which predicts the response bounded by the LINK model and the BOLTED-WALL-PLATE model. This behavior is expected as the simulation is carried out with accurate stiffness of the bolt members. The influence of ideally large bolt pre-stress is included in the LINK model, which simulates the stiffest structural joint behavior and the BOLTED-WALL-PLATE model predicts the response with most flexible structural joint behavior. In case of transducers on the left wall as for example, Laser L2 and Needle N2 and on the right wall such as Needle N6 and N7 the BOLTED-WALL CONSTRAINED-PLATE model predicted improved response in better agreement with the experimental results compared to the BOLTED-WALL model. For rear wall transducer Needle N4-N5 and for Needle N3 which is although on the left wall but close to the ceiling the response prediction with the LINK model is found to be in the closest agreement with the test results; which may be due to high pre-load on various bolt elements. In case of front wall the displacement responses with transducers N8-N9 and Laser L1, the prediction was accurately obtained for the outer plate and the inner corrugated wall showed large difference with the test results. This may also be due to the significant differences in the transient pressure data predicted with code COM-3D compared to the recorded pressure values near the door of the test-cell structure, where the transducers are located.

Based on the above comparative study for the displacement data, the acceleration data recorded during the experiments were also compared with the present four computational models results. The comparative statement is shown in table 5. Again it is noted that the BOLTED-WALL model predicts the acceleration response for transducers 7B on the front wall and 3B on the ceiling in agreement with the test data compared to the other models. In case of the transducer 15B located on the ceiling wall a very high acceleration value $\sim 10.1E6 \text{ mm/sec}^2$ (1029 g) for example in case of 16 gm experiment has been recorded during the experiment. This is an order of magnitude higher as compared to the accelerations recorded with the other transducers approximately located at the symmetrical positions with respect to the blast source on the different walls including the ceiling. The responses of this transducer for the other cases namely the 8 gm, 4 gm and 2 gm hydrogen ignition experiments were consistently found to be very high. So the acceleration data at this location seems to have some instrumentation error. As noted previously with the comparative statement for the

displacement data for the left wall and the right wall, the structural behavior was found to be more accurately represented by the BOLTED-WALL CONSTRAINED-PLATE model. This could be again verified for the acceleration data also for transducer 1B on the right wall and 3A on the left wall for all the combustion experiments.

Thus the limitations observed during phase-I analysis for the numerical prediction of the acceleration response could be overcome in the phase-II analysis with improved corrugated wall orthotropic properties and the simulation of the reliable structural joint behavior despite the inherent scatter in the individual joint stiffness values. The detail comparison with plots for the acceleration and displacement time histories for all the transducers with the experimental data has been reported in the report by Singh et. al. [2005b] for all the combustion experiments and very good agreement has been noted between the measured response and predictions made during phase-II analysis.

The details of the finite element results are presented in the following four sub sections for 2 gm, 4 gm, 8 gm and 16 gm experiments. Here for illustration BOLTED-WALL model results have been selected as this model represents the structural behavior which was observed closest to the experimental results. The results are presented to show the maximum stresses, strains, plastic and viscous energy responses in the three structure groups formed by the outer plate structure, the inner corrugated wall structure and the frame structure. This approach is useful to study the relative load carrying capacity of three structural member groups.

5.2.1 Computational Results for 2 gm Hydrogen Combustion Experiment

Fig 8a and 8b show the maximum von Mises stresses and the maximum effective plastic strain in the outer plate group. Only small localized yielding is observed for the floor plate with almost negligible effective plastic strain of $1.876E-4$ %. Fig 8c and 8d show the maximum plastic and viscous energy distribution for the outer plate group. At this stage the plastic energy dissipation is insignificant ~ 8 mJ for the outer plate group. The maximum stress in the ceiling plate is 86.57 MPa with corresponding strain of 0.0362 %, which is well within the elastic limit as shown in Fig 8e and 8f respectively. For the corrugated wall the maximum strains of ~ 0.0228 % and stresses of ~ 255 MPa are developed as is shown in Fig 8g and 8h respectively. This indicates that the inner corrugated wall started yielding during the 2 gm hydrogen ignition experiment. It is also apparent with the observation of the maximum von Mises stress of ~ 235 MPa (Fig 8i) in the corrugated wall with effective plastic strain of 0.0335 % (Fig 8j). The plastic energy and the viscous energy distribution in the corrugated wall group are shown in Fig 8k and 8l respectively. Significant plastic energy dissipation of 2.46 J is shown by the corrugated wall as compared to the 8 mJ of plastic energy dissipated by the outer plate group (Fig 8c). So the first barrier of the corrugated wall shares the maximum blast energy. For the frame structure the maximum displacement of 2.1 mm is noticed for left wall frame, the right wall frame and front wall frame close to the door (Fig 8m). In this case the maximum stress of 60.64 MPa is noticed (Fig 8n) with corresponding maximum strain of 0.0288 % (Fig 8o) and the frame structure is well within the elastic limit. The viscous energy distribution for the frame group is shown in Fig 8p. The time variation of the external work due to the pressure impulse on the test cell structure along with the internal energy, the kinetic energy, plastic dissipation energy, the strain energy and viscous dissipation energy are shown in Fig 9a-9f. The detail discussion on the energy dissipation is described for all the combustion experiments in section 5.3. The analysis results show that for 2 gm experiment the initiation of yielding is noted for the inner corrugated walls and a much localized region on the floor plate near the door. These structures share the

maximum blast energy. The frame and the outer plates remain in purely elastic condition at this stage.

5.2.2 Computational Results for 4 gm Hydrogen Combustion Experiment

Fig 10a and 10b respectively show the maximum von Mises stresses and the maximum effective plastic strain in the outer plate group. Again localized yielding is observed for the floor plate near the door with very small effective plastic strain of $2.488\text{E-}3$ %. Fig 10c and 10d show the maximum plastic and viscous energy distribution for the outer plate group. In this case the plastic energy dissipation is 145.7 mJ. The maximum stress in the right plate is 147.2 MPa (Fig 10e) while for the ceiling plate the maximum stress is 144.8 MPa (Fig 10f). The corresponding strains in the right plate and the ceiling plate are 0.0618 % (Fig 10g) and 0.0586 % (Fig 10h) respectively; and these are within the elastic limit. In the corrugated wall ceiling the maximum strain of ~ 0.0307 % and the maximum stress of ~ 260.6 MPa are developed as shown in Fig 10i and 10j respectively. The front wall also goes into the plastic regime for 4 gm experiment with von Mises stress of 235 MPa (Fig 10k) and the effective plastic strain of 0.0419 % (Fig 10l). Hence further progressive yielding is noticed in the inner corrugated wall for the 4 gm hydrogen ignition experiment. The plastic energy and the viscous energy distribution in the corrugated wall group for 4 gm experiment are shown in Fig 10m and 10n respectively. Plastic energy dissipation of 3.087 J, higher than the 2 gm case, is shown for the corrugated walls in this case (Fig 10m). As observed for 2 gm experiment the first barrier of the corrugated wall shares the higher blast energy compared to the outer plate group. The maximum displacement of 4.11 mm is noticed for left wall frame, the right wall frame and front wall frame close to the door (Fig 10-o) with the maximum stress of 129.8 MPa (Fig 10p) and corresponding maximum strain of 0.0618 % (Fig 10q). So the frame structure is again within the elastic limit as observed for 2 gm hydrogen combustion experiment. The viscous energy distribution for the frame group is shown in Fig 10r. The time variation of the external work due to the pressure impulse on the test cell structure along with the internal energy, the kinetic energy, plastic dissipation energy, the strain energy and viscous dissipation energy are shown in Fig 11a-11f. The analysis results show that for 4 gm experiment the yielding is noted for the inner corrugated walls and a very localized region on the floor plate near the door. These structures, which are closest to the blast source, dissipate the maximum blast energy. The frame and the outer plates remain in purely elastic condition at this stage also. It may be concluded that the behavior of the test-cell structure is similar to the 2 gm experiment with slightly higher plastic strains noticed for the corrugated wall.

5.2.3 Computational Results for 8 gm Hydrogen Combustion Experiment

Fig 12a and 12b show the maximum von Mises stresses and the maximum effective plastic strain in the outer plate group. The yielding still remains localized for the floor plate near the door with effective plastic strain of 0.0126 %, as observed for the earlier two experiments. The plastic energy and viscous energy dissipation distribution for the outer plate group are shown in Fig 12c and 12 d respectively. At this stage the plastic energy dissipation in the outer plate group is ~ 894.1 mJ. The maximum stress in the left plate is 141.9 MPa (Fig 10e) and for the right plate it is ~ 195.3 MPa (fig 12f). In the ceiling plate the maximum stress is 171.6 MPa (Fig 12g) with the corresponding strain of 0.0806 % (Fig 12h) and these are within the elastic limit. The maximum strains for 8 gm experiment are 0.0945 % for the right outer plate (Fig 12i) and 0.0703 % for the left outer plate (Fig 12j). In the corrugated wall ceiling the maximum strain of ~ 0.0501 % and the maximum stress of ~ 268.9 MPa are developed as shown in Fig 12k and 12l respectively. In this stage both the rear and front walls go into the

plastic regime. The maximum stress of 259.6 MPa (Fig 12m) is noticed in the rear wall. The effective plastic strain of 0.0817 % (Fig 12n) is noticed in the front wall. The plastic energy and the viscous energy distribution in the corrugated wall group for 8 gm experiment are shown in Fig 12o and 12p respectively. At this stage increased plastic energy dissipation of 6.051 J higher than the previous two experiments is observed (Fig 12o). As noticed for the earlier two experiments the first barrier of the corrugated wall shares higher blast energy compared to the outer plate group. The maximum displacement of 6.87 mm is noticed for left wall frame, the right wall frame and the front wall frame close to the door (Fig 12q) with the maximum stress of 209.4 MPa (Fig 12r) with corresponding maximum strain of 0.0997 % (Fig 12s). So the frame structure is again within the elastic limit as observed for the previous two combustion experiments. The viscous energy distribution for the frame group is shown in Fig 12t. At this stage although the overall behavior of the frame was in the elastic regime but some plastic energy dissipation was noticed for the braces in the left frame near the door (Fig 12u) as these are the weakest members and are normally designed as sacrificial members for blast resistant structures. The advantage of the brace members is with their high plastic energy carrying capacity. Since yielding is first initiated in these members it results in to the stress relaxation for the welds. This behavior has been demonstrated by the braces in this analysis. The time variation of the external work due to the pressure impulse on the test cell structure along with the internal energy, the kinetic energy, plastic dissipation energy, the strain energy and viscous dissipation energy are shown in Fig 13a-13f. The analysis results show that for 8 gm experiment the yielding is still grossly confined for the inner corrugated walls and a very localized region on the floor plate near the door. The frames remain within the elastic regime but the braces start yielding at this stage thus relaxing the high stress in the weld joints. It may be concluded that the behavior of the test-cell structure at this stage also is similar to the 2 gm and 4 gm experiments with slightly higher plastic strains noticed for the corrugated wall and yielding of the braces.

5.2.4 Computational Results for 16 gm Hydrogen Combustion Experiment

The maximum von Mises stresses and effective plastic strain in the outer plate group are shown in Fig 14a and 14b respectively for 16gm combustion experiment. The localized yielding for the floor plate near the door with effective plastic strain of 0.034 % (Fig 14b) is noted, as has been observed for the earlier experiments. The plastic energy and viscous energy dissipation distribution for the outer plate group are shown in Fig 14c and 14d respectively. In this case plastic energy dissipation of 4.365 J is observed, which is higher than the earlier experiments since a few other locations also start yielding. This is shown in Fig 14e and 14f with stress levels of 355 MPa on the right wall outer plate and 250.3 MPa for the ceiling plate. Further the strain levels were examined and the maximum strain of 0.169 % is observed in the right wall outer plate (Fig 14g). Similarly the maximum strain of similar order ~ 0.143 % (Fig 14h) is observed in the left outer plate at the identical central position as observed for the outer right plate. This shows initiation of localized yielding at the central positions of the outer plate left and right walls of the test-cell. It may be recalled that the maximum strains for 8 gm experiment are 0.0945 % for the right outer plate (Fig 12i) and 0.0703 % for the left outer plate (Fig 12j), which are within the elastic limit but close to the yield initiation. In the ceiling plate the peak strain level of 0.099 % near the door (Fig 14i) is noticed. This location is close to the vent opening but is again within the elastic limit.

In the corrugated wall ceiling the maximum strain of 0.0754 % (Fig 14j) is noticed near the rear vent opening. The maximum stress of ~ 271.3 MPa is developed in the ceiling of the corrugated wall as shown in Fig 14k. For the rear wall the maximum stress of 265.1 MPa

(Fig 14l) is noticed. In this experiment the maximum effective plastic strain of 0.0964 % (Fig 14m) is observed for the front wall. As noticed for the 8gm experiment, both the rear and front walls go into the plastic regime. The plastic energy and the viscous energy distribution in the corrugated wall group for 16 gm experiment are shown in Fig 14n and 14o respectively. At this stage increased plastic energy dissipation of 9.125 J; higher than the earlier experiments is observed. So the first barrier of the corrugated wall shares higher blast energy compared to the outer plate group consistently as noticed in earlier experiments also. The maximum displacement of 10.27 mm is noticed for the left wall frame, the right wall frame and the front wall frame close to the door (Fig 14p) with the maximum stress of 334.8 MPa (Fig 14q) in the brace member of the left wall frame. The corresponding von Mises stress in this member is 345 MPa (Fig 14r). The maximum strain of 0.159 % (Fig 14s) with the equivalent plastic strain of ~ 0.0339 % (Fig 14t) is noticed in the brace member of the left wall frame near the door. Another brace member on the right wall frame near the front wall junction also shows plastic strain of ~ 0.026 % (fig 14t). Although the frame structure is still grossly within the elastic limit as observed for the previous combustion experiments, the braces start yielding as is intended in the design. The viscous energy distribution for the frame group is shown in Fig 14u. The maximum plastic energy dissipation in the frame at this stage is 10.33 J (fig 14v) due to the yielding of the brace members. The temporal variation of the external work due to the pressure impulse on the test cell structure along with the internal energy, the kinetic energy, plastic dissipation energy, the strain energy and viscous dissipation energy are shown in Fig 15a-15f. The analysis results show that the yielding; that has been grossly confined for the inner corrugated walls and a very localized region on the floor plate near the door in the earlier experiments, further were initiated in to the outer left and right plates and brace members of the left and right wall frame structures for 16 gm experiment. However, the frames remain grossly still within the elastic regime and the braces start yielding to relax the high stress in the weld joints as is intended in the design. It may be concluded that the behavior of the test-cell structure is still grossly elastic for 16 gm experiment except for a few locations as identified here and these show local yielding. Additional case study for 16gm combustion case was made by imposing the effect of the initial pre-stress due to self weight and an additional weight of 10 T for the air house weight and no significant difference in response was observed for 16gm experiment. Moreover for the case of assumed 20 ton top cell weight also the results were not different by more than 5 %; this case study was carried out as there were some uncertainties in the top cell weight due to additional equipments.

5.3 Evaluation of Dynamic Response for the Combustion Experiments

Now the comparative studies are presented for the energy absorbing capacity of the test-cell structure as this is an important aspect of design for blast resistant structures. First the different models evolved during phase-II analysis are compared for the typical 16 gm experiment in table 6. The maximum energies absorbed by the whole 3D models namely, the LINK model, the BOLTED-WALL model, the BOLTED-WALL-PLATE model and the BOLTED-WALL CONSTRAINED-PLATE model are included in this table. The input energy due to the blast with total work and the internal energy which is sum of kinetic energy and the strain energy are also included in addition to the energy dissipated due to plastic deformation and the viscous damping due to non conservative forces. This comparison is made to check the energy balance and to know the structural behavior for its energy absorbing capacity. In all the cases the maximum energy values are recorded in the table from their temporal variations as shown in previous sections for different combustion experiments typically for the BOLTED-WALL model. The stiffest behavior is represented by the

BOLTED-WALL CONSTRAINED-PLATE model with total external work of 25.86 kJ followed by the LINK model with 30.85 kJ of external work and then by the BOLTED-WALL model with 42.94 kJ of external work and finally for the most flexible structural joint with the BOLTED-WALL-PLATE model the external work is 50.20 kJ. In terms of relative energy dissipating capacity with plastic deformation the BOLTED-WALL-PLATE model and the BOLTED-WALL CONSTRAINED-PLATE model show the maximum relative energy dissipation capacity of 5.7 % compared to the other models. So for blast resistant structures with flexible structural connections a significant portion of the blast energy could be dissipated in the plastic deformation if it is ensured that hinge mechanisms do not lead to structural collapse. This is just an illustration and good fire walls can be designed with this concept with proper detailing of the structural joints so that the overall structural response remains grossly in the elastic regime with provision of plastic energy allowed to be dissipated in case of accidental over pressurization.

Table 7 shows the energy distribution in the inner corrugated wall, the outer plate group and the frame members, which was obtained with the four different numerical models for the structural joint simulation in the case of 16gm combustion experiment. It is noted that in all the models the corrugated walls absorb the maximum fraction of the plastic energy compared to other structural members in the range of 4.16 % (for the BOLTED-WALL-PLATE model) to 5.38 % (for the BOLTED-WALL CONSTRAINED-PLATE model). Hence all the models show the maximum energy dissipation capacity with the inner corrugated wall, which is closest to the blast source. This is followed by the outer plate group, which shows energy absorption in the range of 0.21 % (for the BOLTED-WALL model) to 1.51 % (for the BOLTED-WALL-PLATE model). Due to flexible connection the outer plate shares significant plastic energy for the BOLTED-WALL-PLATE model compared to the other models. Similarly the viscous energy dissipation in the corrugated wall is significant (43.7 % to 50.9 %) compared to the outer plate and frame structures for all the structural joint models. Further details of energy distribution are listed in table 8 for 16gm experiment with LINK model to illustrate the energy distribution due to the blast. In this table all the structural members are shown separately for the four walls, the ceiling and the floor for the three structural groups of the corrugated wall, the outer plate and the frame structure. It is observed that for the inner corrugated wall group left wall (Wall-A) absorbs 0.4057 kJ (1.32 %) of total energy in the plastic deformation compared to 0.2847 kJ (0.92 %) of total energy that is absorbed by the right corrugated wall (Wall-B). The front wall (Wall-1), the rear wall (Wall-2) and the ceiling wall (Wall-ceiling) absorb 0.1609 kJ (0.52 %), 0.2729 kJ (0.88 %) and 0.2774 kJ (0.90 %) of the total energy respectively. As discussed earlier the 16 gm experiment was grossly in the elastic regime so only the floor plate shares 0.2774 kJ (0.90 %) of the total energy and other outer plate members and the entire frame structures do not absorb any energy in plastic deformation.

Further energy distribution comparisons with the BOLTED-WALL structural joint model are made in table 9 for the whole finite element model and separately for different structural member groups of inner corrugated wall, the outer plate and the frame structure in table 10 for 2 gm, 4 gm, 8 gm and 16 gm hydrogen combustion experiments. Here only BOLTED-WALL model is used for illustration as the response predicted by this model has been found closest to the experimental measurements. It is noticed from table 9 that at higher energy levels of hydrogen (mass of hydrogen), the plastic energy dissipation increases as for example in case of 2gm experiment the plastic energy dissipation is 0.466 kJ which gradually increases to 0.698 kJ for 4gm experiment, to 1.416 kJ for 8gm experiment and 2.134 kJ for 16 gm experiment. This was noticed in earlier section and is due to higher plastic deformation in

corrugated wall which subsequently also spreads in outer plate members and the sacrificial brace members of the frame structure of the test-cell for 8gm and 16gm experiments. Similar observation is made for the damping energy dissipation which increases from 2.635 kJ for 2gm experiment, to 7.01 kJ for 4gm experiment, to 19.69 kJ for 8gm experiment and finally 39.51 kJ for the 16gm experiment. However, the relative energy dissipation as compared to the total input energy; listed in the table as total work, due to plastic deformation shows a decreasing pattern, such as 14.5 % for 2gm experiment, to 8.43 % for 4gm experiment, to 6.49 % for 8 gm experiment and 4.97 % for 16gm experiment. This is due to higher fractional energy dissipation in damping with high amplitude vibration, which shows an increasing trend from 82.1 % for 2gm experiment, to 84.7 % for 4gm experiment, to 90.2 % for 8gm experiment and finally to 92.0 % for 16 gm experiment. This can be also observed with more clarity in table 10 in which energy dissipation in the individual structural components are included. As it was mentioned in the earlier sections, the corrugated walls absorb the maximum amount of blast energy in the plastic deformation hence the relative energy dissipation in this member due to the plastic deformation is 14.52 % for 2 gm experiment, 8.42 % for 4gm experiment, 6.43 % for 8gm experiment and 4.71 % for 16gm experiment which continuously reduces with the energy (mass) of hydrogen. Similarly the damping energy in the corrugated wall increases from 45.5 % for 2 gm experiment, to 48.88 % for 4gm experiment, to 51.42 % for 8gm and almost saturates at the similar level of 50.91 % for 16gm experiment. Similarly in the outer plate group there is almost insignificant plastic deformation for 2gm and 4 gm experiments and hence no plastic energy dissipation is noted and for 8gm and 16gm experiments, the relative plastic energy dissipations are observed as 0.07 % and 0.21 % due to spread of plastic zone in the left and right outer plate members as has been described in the earlier sections. Due to small fraction of plastic energy dissipation for the outer plate group, the relative damping energy dissipation remains almost constant for the different experiments in the narrow band of 13.8 % to 16.8 %. Similarly since the frame members also do not absorb any significant plastic energy the damping energy dissipation remains in the narrow band of 22 % to 24.31 % for different combustion experiments.

5.4 Phase-III Computations (Inelastic Analysis)

In this study the BOLTED-WALL model is selected for the inelastic analysis. This was found to represent the test-cell structural behavior in close agreement with the experiment and it also represents the structural joint behavior, which is bounded by the LINK model and the BOLTED-WALL-PLATE model. First the transient structural dynamic analysis for 64 gm combustion case based on the pressure time history up to 0.05 sec computed by COM-3D code obtained from Kotchourko [2004] is presented. Fig 16a to Fig 16d show the deformed view of the test-cell at the end of the transient and the maximum displacement of 35.78 mm is observed at the rear outer pate. In the corrugated wall group, the maximum effective plastic strain of 1.396 % is observed at the rear wall (Fig 16b), for the outer plate group; the maximum effective plastic strain of 0.497 % is noted for the left plate (Fig 16c) and for the frame members the maximum effective plastic strain of 1.988 % is observed for the left wall frame near the door. The structure is in the plastic regime and even the massive frame members also show significant yielding ~ 2 %. After yielding of the corrugated wall the blast load is largely shared by the frame members.

Subsequently analysis of the test-cell structure for impulsive load was carried out. It was observed from the earlier results of COM-3D code and the test results that the significant pressure transient duration is for 0.15 sec and the first impulse duration for 16 gm combustion case has been observed as 0.015 sec. Hence, two cases were identified for the present studies

to obtain the limiting impulse for 0.015 sec duration and another case with limiting impulse for 0.15 sec duration. It may be noted that due to confined blast without venting there is possibility of the blast waves to undergo multiple reflections so these two cases are necessary to include in the study for identifying the limiting impulses. This range of impulse duration between 0.015 sec and 0.15 sec also includes all the predominant frequencies of excitation, 8.973 Hz (period 0.111 sec) to 116.8 Hz (period 8.56E-3 sec) as observed in the Eigen value analysis presented in Fig 4 to Fig 6 for the test-cell structure. The blast wave could possibly damage the walls due to impulsive load and hence these two limiting cases of impulsive load are identified. In addition the case of quasi-static uniform pressure load was also considered for the analysis in which the transient analysis was carried for 0.5 sec to get the quasi-static response of the test cell for a white signal of constant magnitude up to the limiting condition. As described earlier the limiting strain of 5 % is used as a criterion for steel structures as has been used by Loucca and Friis [2000] and Boh et. al. [2004] in their studies for fire-walls.

Figs 17a to Fig 17d show the results for limiting impulse of 0.012 MPa-sec. In this case the peak uniform pressure of 0.08 MPa for duration of 0.15 sec is found to cause the limiting strain in the test cell structure. The maximum displacement of 114.2 mm is noted for the front corrugated wall near the middle of the door (Fig 17a). The maximum effective plastic strain in the corrugated wall is 4.32 % on front wall (fig 17b), in the plate group the maximum effective plastic strain of 1.21 % is developed in the plate ceiling near the junction of the front door. For the frame structure the maximum effective plastic strain of 4.85 % is noted for the right wall vertical members near the ceiling junction. Thus both the frame and the inner corrugated wall have reached close to the limiting strain and this determines the limiting impulse of 0.012 MPa-sec with peak pressure of 0.08 MPa.

Subsequently the second limiting impulse of 1.575E-3 MPa-sec was determined for pulse duration of 0.015 sec with a higher peak pressure of 0.105 MPa, uniformly applied on the test-cell walls. Figs 18a to Fig 18d show the results for this limiting impulse of shorter duration but with higher peak pressure. The maximum displacement of 197.1 mm is noted for the front corrugated wall near the middle of the door (Fig 18a), at the same location that was observed for the long duration impulse of 0.15 sec. The maximum effective plastic strain in the corrugated wall is 4.78 % on front wall (fig 18b), in the plate group the maximum effective plastic strain of 1.04 % is developed in the plate ceiling near the junction of the front door and for the frame structure the maximum effective plastic strain of 4.49 % is noted for the right wall vertical members near the ceiling junction. Thus both the frame and the inner corrugated wall again are close to the limiting strain at the identical location as observed for the long duration impulse. This determines the limiting impulse of 1.575E-3 MPa-sec with peak pressure of 0.105 MPa for the test-cell structure.

Finally the response of the test-cell structure for the quasi-static response is determined. The transient analysis is carried out for a long duration up to 0.5 sec and it is ensured that the steady state response is reached. In this case with the peak pressure of 0.09 MPa is uniformly applied on the test-cell walls. Figs 19a to Fig 19d show the response of the test-cell structure for this limiting quasi-static pressure. The maximum displacement of 190.4 mm is noted for the ceiling wall (Fig 19a). The maximum effective plastic strain in the corrugated wall is 4.75 % on the front wall (fig 19b), in the plate group the maximum effective plastic strain of 1.30 % is developed in the plate ceiling near the junction of the front door (Fig 19c) and for the frame structure the maximum effective plastic strain of 4.09 % is noted for the right wall vertical members near the ceiling junction (Fig 19d). Thus both the frame and the inner corrugated wall again are close to the limiting strain at the identical location as observed for

the long and short duration impulsive loads. So a limiting quasi-static pressure of 0.09 MPa is determined for the test-cell structure. It may be noted that with the design pressure of 0.0075 MPa for the test-cell structure, as specified by the designer, it has a factor of safety of 12 for static load. However the local failure of joints, welds and other discontinuities need to be considered separately in a local analysis to determine the true margin against over pressurization of the test-cell structure, which would be considerably lower. The displacement time histories for the quasi-static response of the test-cell structure are presented in Fig 20a to Fig 20l at the different transducer locations. The response shows that steady state has been reached and the predicted displacements describe the response of the test-cell structure at the ultimate state for a sustained pressure of 0.09 MPa, which would result in to the limiting strain of ~5 %.

Table 11 presents the comparative statement of displacements at all the transducer locations for 64 gm combustion case with the short and long duration limiting impulsive loads and the ultimate quasi-static pressure load. The comparison with the short duration limiting impulsive load of 1.575E-3 MPa-sec shows that for 64 gm combustion case; the minimum displacement ratio is ~ 3.36 for the location of needle N3 on the left wall of the test cell, which reduces to 2.7 for impulse of 0.012 MPa for 0.15 sec duration. However as noted above, the consideration of discontinuities in the joints, inclusions in the welds and inherent presence of flaws (due to the uncertainties in the construction quality) would preclude the combustion test for the 64 gm case.

Table 12 shows the energy dissipation for 64 gm combustion case and for the two limiting impulsive loadings and the quasi-static pressure loading of the test-cell structure. In the case of 64 gm combustion the plastic energy dissipation for the whole structure is 8.86 %, out of which the inner corrugated wall contributes to the maximum energy dissipation of 6.44 %. The energy dissipation in the damping is 78.56 % out of which the corrugated wall shares the maximum energy of 40.44 % and the balance is nearly equally shared by the outer plate and frame structural members. But for the short duration limiting impulse of 1.575E-3 MPa-sec, the plastic energy of ~ 39.13 % is relatively higher than the previous combustion experiments and the 64 gm combustion case. In this case the frame structure dissipates the maximum plastic energy of 24.7 % followed by the inner corrugated wall of ~ 10.3 % and the outer plate structure which contributes about ~4.19 %. In this case the energy dissipation in damping is significantly lower ~ 30.84 %, out of which the wall and the frame contribute equally ~ 11 % each and the balance is shared by the outer plate member group. This study illustrates the importance of dissipating the limiting blast induced energy with the maximum plastic deformation. For the other limiting impulse of 0.012 MPa-sec for a longer duration of 0.15 sec similar behavior of the test-cell structure is noted. In case of quasi-static limiting pressure also the behavior of the test-cell structure shows that the maximum energy is dissipated in the plastic dissipation as the damping contribution is very small and would be almost zero after the steady state is reached.

6. Conclusions

The transient dynamic analyses for all the combustion experiments were obtained with good accuracy as observed with comparative statements presented in this report. This was possible with the detail evaluation and qualification of the finite element model with simple analytical computation and the available experimental data as reported by Singh et al. [2003b, 2005b]. The hammer tests and experimental data analysis further helped in correlating the present computational response with the combustion experiments.

The displacements and the peak stresses are shown to be grossly in the linear elastic range for all the combustion experiments up to 16gm experiment except for the plastic deformation noticed for the inner corrugated wall and outer plate structure. For 16 gm experiment initiation of yielding is observed in the frame structure brace members. The influence of geometrically nonlinearity was shown to be insignificant for combustion induced blast load up to 16 gm of hydrogen ignition experiments and the effect of uncertainties in the top cell air house weight is also negligible. In Phase-I analysis it was noticed that the damping does not influence the test-cell response significantly, as the response is predominantly impulsive. This was also concluded in the earlier analytical studies by Singh et al. [2005a and 2005b].

The Phase-II computations illustrate the following.

- For 2 gm hydrogen combustion experiment the behavior of the test-cell is within the elastic regime with small plastic deformation observed for the inner corrugated wall and the localized yielding around the door of the floor plate. The outer plate and the frame structure remain in the elastic state.
- In the 4 gm hydrogen combustion experiment also the test cell behavior was similar to 2 gm experiment with slightly increased plastic deformation in the inner corrugated wall and the floor plate.
- In the case of 8 gm hydrogen combustion experiment, high stresses developed on the right and left outer plates but the outer plate behavior was still within the elastic regime. The corrugated wall undergoes relatively larger plastic deformation. The frame structure is also within the elastic regime but the braces on the left wall frame near the door show yielding and share the blast load such that the stresses in the welds would be relaxed.
- In case of 16 gm experiment, further higher stresses are observed at the central locations of the left and right plate; which are at the identical locations as noted for 8 gm experiment and cause yielding due to high impulsive loading. Relatively larger strains are noted for this case, which are 0.169 % for the right outer plate and 0.143 % for the left outer plate. In the brace members the plastic strains of 0.0339 % on the left frame wall and 0.026 % on the right wall frame are noted.

In Phase-III computations, the inelastic limiting conditions, namely the short and long duration impulsive and quasi-static pressure loading were evaluated for the test-cell structure along with its response for such conditions. For the short duration impulse of 0.015 sec the limiting impulse of 1.575E-3 MPa-sec (peak pressure 0.105 MPa) is obtained, while for the long duration impulse of 0.15 sec the limiting impulse of 0.012 MPa-sec (peak pressure 0.08 MPa) has been predicted. In case of quasi-static pressure loading the limit pressure load of 0.09 MPa was obtained. The limiting condition is identified with the maximum strain of 5 % for the steel structure. The test cell response evaluation for 64 gm combustion test shows that all the structural members namely the inner corrugated wall, the frame and the outer plate would undergo plastic deformation and this test cannot be conducted on the test-cell. The limiting quasi-static pressure of 0.09 MPa computed with the present 3D finite element model of the test-cell structure overlaps the limiting quasi-static pressure of 0.075 MPa predicted with the analytical model due to Jones [1989], which was implemented in code COLLAPSE reported earlier by Singh et al. [2005a]. In addition the limiting impulse of 4.7355E-4 predicted with analytical model of Baker et al. [1987] for short duration impulse predicted by code COLLAPSE during the test-cell experiment phase is overlapped by the present limiting impulse of 1.575E-3 MPa-sec, and hence it meets the safety evaluation requirements as reported earlier by Singh et al. [2005a].

From fatigue considerations the test-cell should be limited to 8 gm tests, which meets the hydrogen detection threshold requirements. For repeated 16 gm tests, detail structural evaluation with help of measured strain and deformations of the test-cell walls would be required due to the plastic strains, which are observed during 16 gm test. The present study and the data generated in this report could be used for such evaluations in future.

7. References

1. "ABAQUS, A General Purpose Linear and Nonlinear Finite Element Code: Users Manual version 6.3", Hibbit, Karlsson and Sorensen, Inc., Rhode Island, [2002].
2. Baker W E, Cox P A, Westine P S, Kulesz J J, Strehlow J J, "Explosion Hazards and Evaluation", Elsevier Scientific Publishing Co., Amsterdam, [1988].
3. Bangash M Y H, "Impact and Explosion": Analysis and Design, Blackwell Scientific Publications, Oxford, UK [1993].
4. Baumann W, Breitung W, Kaup B, Necker G, Royl P, Travis J R, "A three-dimensional multi-volume analysis of combustible mixture generation due to in-vessel LOCA of ITER using GASFLOW code", Fusion Engg. and Des. vol. 63-64, p 173-180 [2002].
5. Blevins R D, "Formulas for natural frequencies and mode shapes", Krieger publishing co., Florida, [1995].
6. Boh J W, Louca L A, Choo Y S, "Strain Rate Effects on the Response of Stainless Steel Corrugated Firewall Subjected to Hydrocarbon Explosions", Journal of Constructional Steel Research, 60, p 1-29 [2004].
7. Breitung W, Royl P, "Procedures and tools for deterministic analysis and control of hydrogen behavior in severe accidents", Nuclear Engg. and Des. 202, p 249-268 [2002].
8. Brockenbrough Roger L, Merritt F S (eds.), "Structural Steel Designer's Handbook", Second Edition, McGraw Hill, New York [1994].
9. Clough R W, Penzien J, "Dynamics of Structures, McGraw Hill, New York [1993].
10. Henke Peter, Prüfenieur für Baustatik, München, Private Communication July-Aug [2003].
11. Harris Cyril M (ed), "Shock and Vibration Handbook", Fourth Edition, McGraw Hill, New York [1996].
12. Jacinto AC, Ricardo DA, Rodolfo FD, "Experimental and computational analysis of plates under air blast loading", Int. Jr. Impact Engg., vol 25, p 927-947, [2001].

13. Kotchourko A, "Private Communication on COM3D Code", [2004]
14. Krieg R, Dolensky B, Goller B, Breitung W, Redlinger R, Royl P, "Assessment of the load-carrying capacities of a spherical pressurized water reactor steel containment under a postulated hydrogen detonation", Nuclear Technology, vol. 141, p 109-121, Feb. [2003].
15. Jawad M H, "Theory and Design of Plate and Shell Structures", Chapman & Hall, New York, [1994].
16. Jones Norman, "Structural Impact", Cambridge University Press, Cambridge, UK [1989].
17. Louca L A and Friis J, "Modeling Failure of Welded Connections to Corrugated Panel Structures Under Blast Loading", Offshore Technology Report 2000/088, Health and Safety Executive, UK [2001].
18. NRC Report, "Protecting Buildings from Bomb Damage: Transfer of Blast-Effects Mitigation Technologies from Military to Civilian Applications", Commission on Engineering and Technical Systems, National Research Council, National Academy Press, Washington, USA [1995].
19. Palmer A C, "Breakup of the Firewall Between the B and C Modules of the Piper Alpha Platform- I Analysis by Hand Calculation", Engineering Failure Analysis, Vol. 5 No. 1, pp 57-67, [1998].
20. Palmer A C, "Breakup of the Firewall Between the B and C Modules of the Piper Alpha Platform- II Analysis by Finite Elements and Comparison with Hand Calculation", Engineering Failure Analysis 7, pp 311-322, [2000].
21. Redlinger R, "DET3D: A Code for Calculating Detonations in Reactor Containments", Annual Meeting on Nuclear Technology '99, ISSN 0720-9207, p-191, Karlsruhe, 18-20 May 1999, Bonn : INFORUM GmbH, S. 191-94 [1999].
22. Royl P, Travis J R, Baumann W, Breitung W, Krautschick V, Necker G, Starflinger J, "Status of Development, and Application of the 3D CFD Code GASFLOW at FZK", IAEA-OECD Technical Meeting on Use of Computational Fluid Dynamics (CFD) Codes for Safety Analysis of Reactor Systems, Including Containment, Pisa, I, November 11-14, 2002, [2002].
23. Singh R K, Redlinger R, Breitung W, unpublished report, Forschungszentrum Karlsruhe [2003a].

24. Singh R K, Redlinger R, Breitung W, “ Safety Assessment of Composite Structural Barriers for Hydrogen Combustion Transient Loads” 15th Annual US Hydrogen Conference, Los Angeles, April 26-30, 2004 [2004a].
25. Singh R K, “Simplified Computations for a Hydrogen Distribution Test Chamber Structure with Limiting Pressure Impulse and Response Evaluations for Hydrogen Combustion Experiments”, Forschungszentrum Karlsruhe, FZKA 6991, to be published [2005a]
26. Singh R K, Redlinger R, Breitung W, Vesper A, Andreas F, “Studies on Structural Dynamic Characteristics of a Hydrogen Distribution Test Chamber during Hydrogen Combustion Experiments”, Forschungszentrum Karlsruhe, FZKA 6991, to be published [2005b].
27. Troitsky M S, “Stiffened Plates Bending, Stability and Vibrations”, Elsevier Scientific Publishing Co., Amsterdam, [1976].
28. Warzecha E, "Numerische Simulation der Wasserstoff-Luft-Verbrennung in einer Prüfzelle mit dem COM3D Programm“ Graduate Thesis Karlsruhe University [2004].
29. Young C Warren, “Roark’s Formulas for Stress and Strain”, Sixth Edition, McGraw Hill, New York [1989].

ANNEX I: Figures

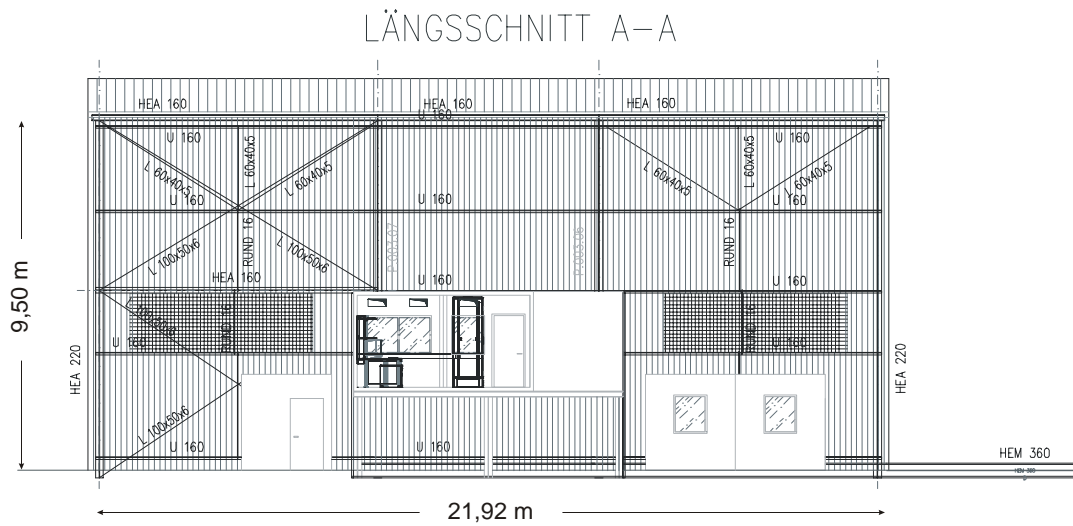
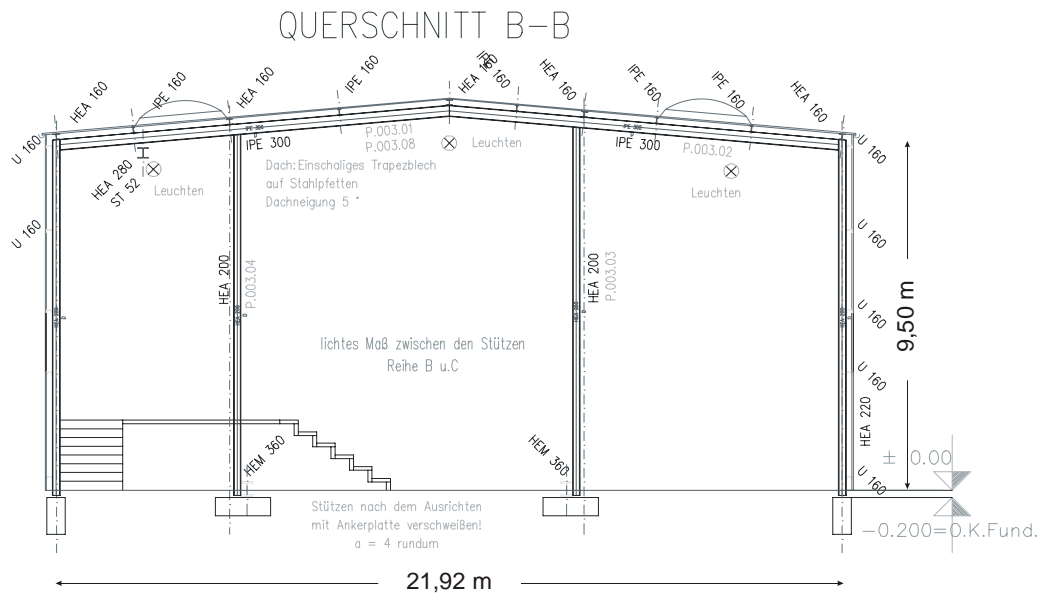


Fig. 1a: Test Cell Structure Experimental Facility for Hydrogen Combustion Experiments



Fig. 1b: Test cell Installation within the Experimental Facility



Fig. 1c: View of the Test cell Structure from Outside



Fig. 1d: Inside View of the Test-Cell with Internal Equipment Details

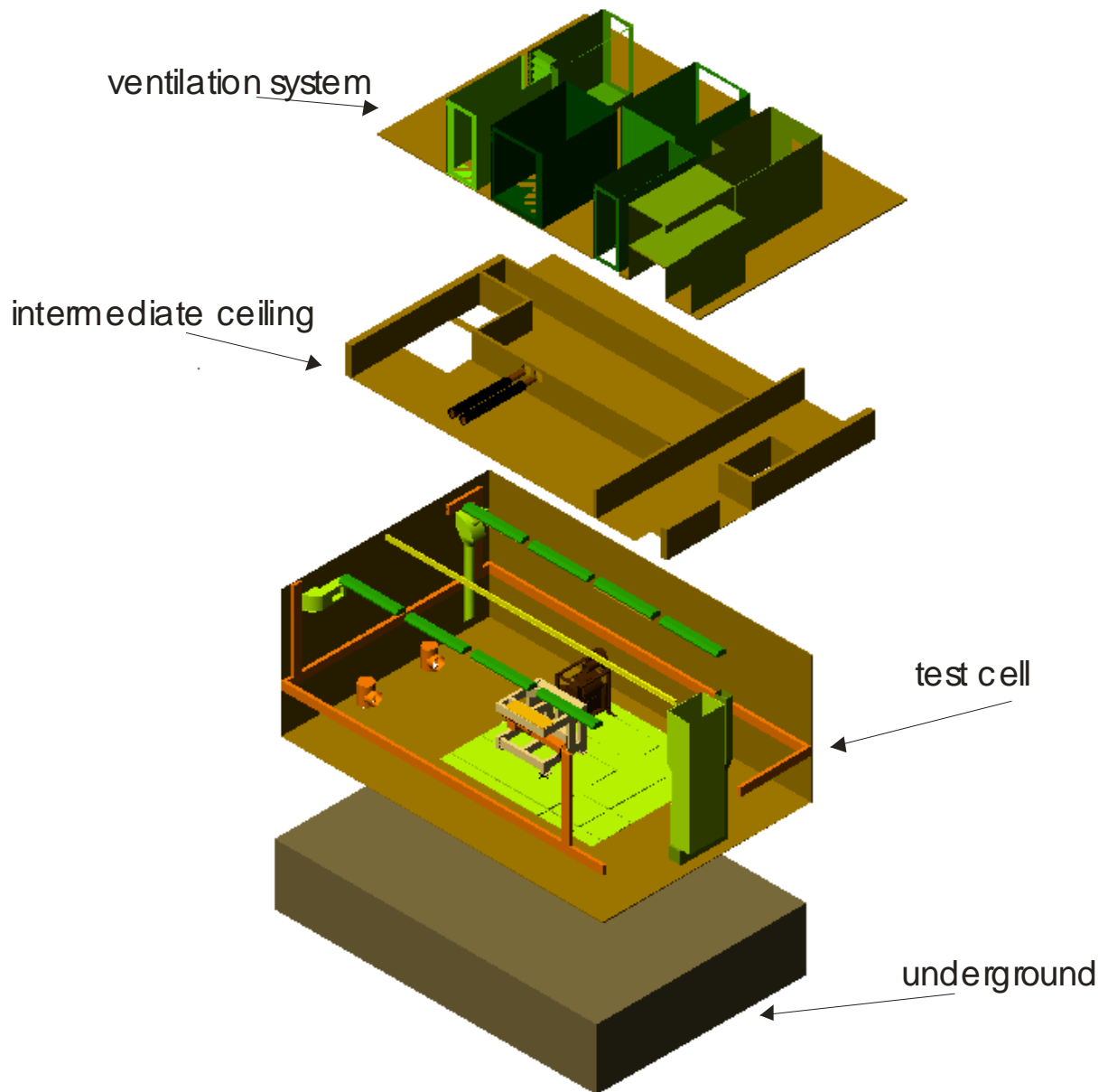


Fig. 1e: Detailed View of Test Cell, Support Structures, the Intermediate Ceiling and Ventilation System for Hydrogen Combustion Experiments.

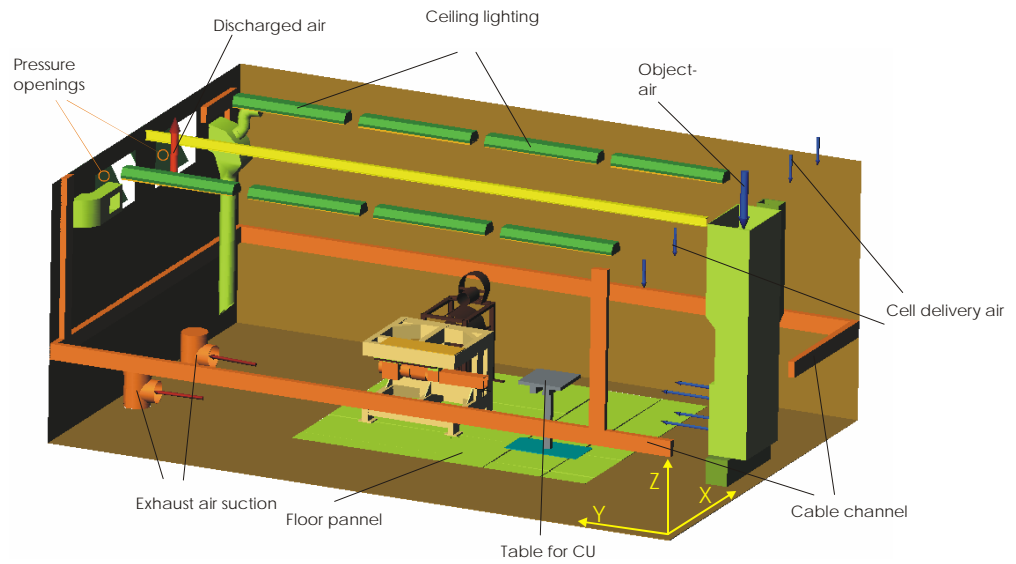
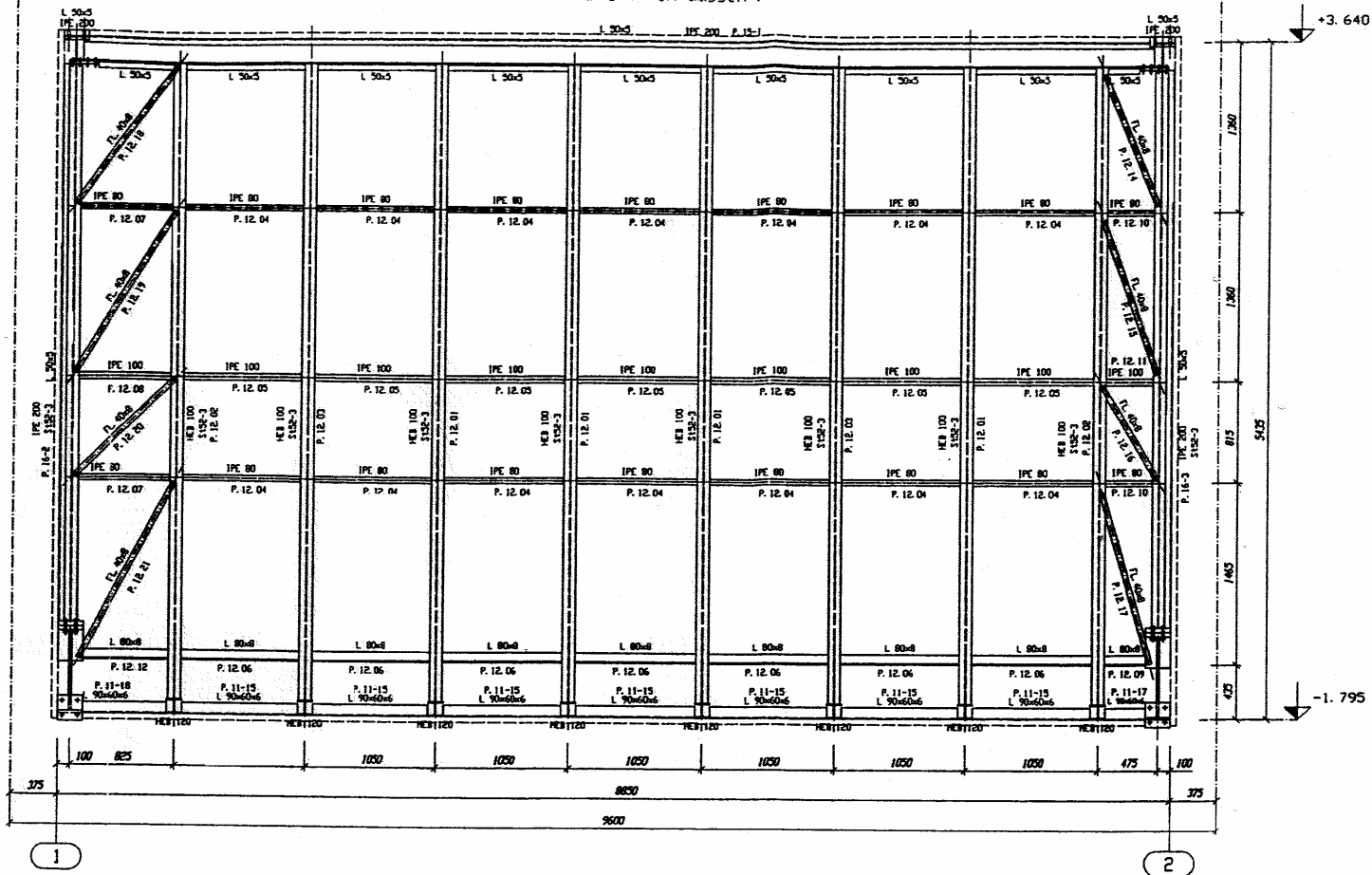


Fig. 1f: Detailed View of Test Cell with Central Platform, the Intermediate Ceiling and Ventilation System for Hydrogen Combustion Experiments.

Wand Reihe B
(Ansicht von aussen)



Wand Reihe 2
(Ansicht von aussen)

Fig. 2b: Right Wall (Wall-B) of Test-Cell.

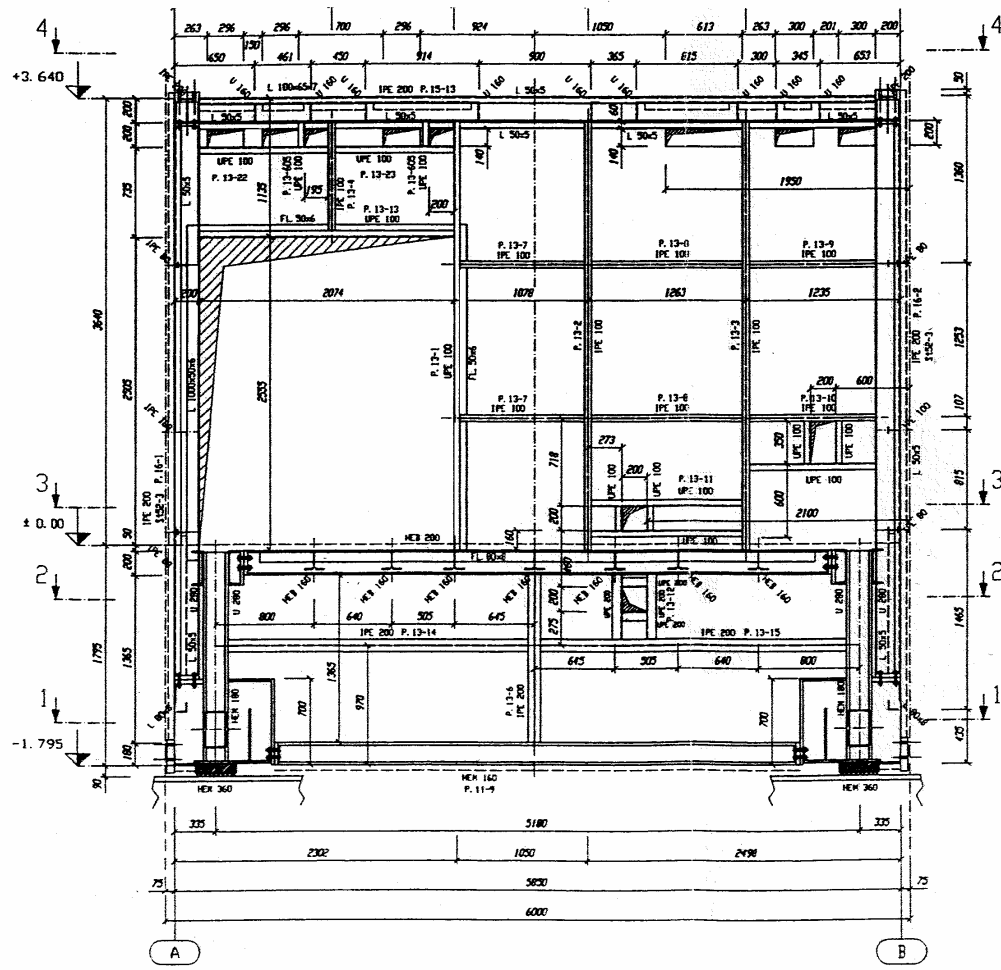


Fig. 2c: Front Wall (Wall-1) of Test-Cell

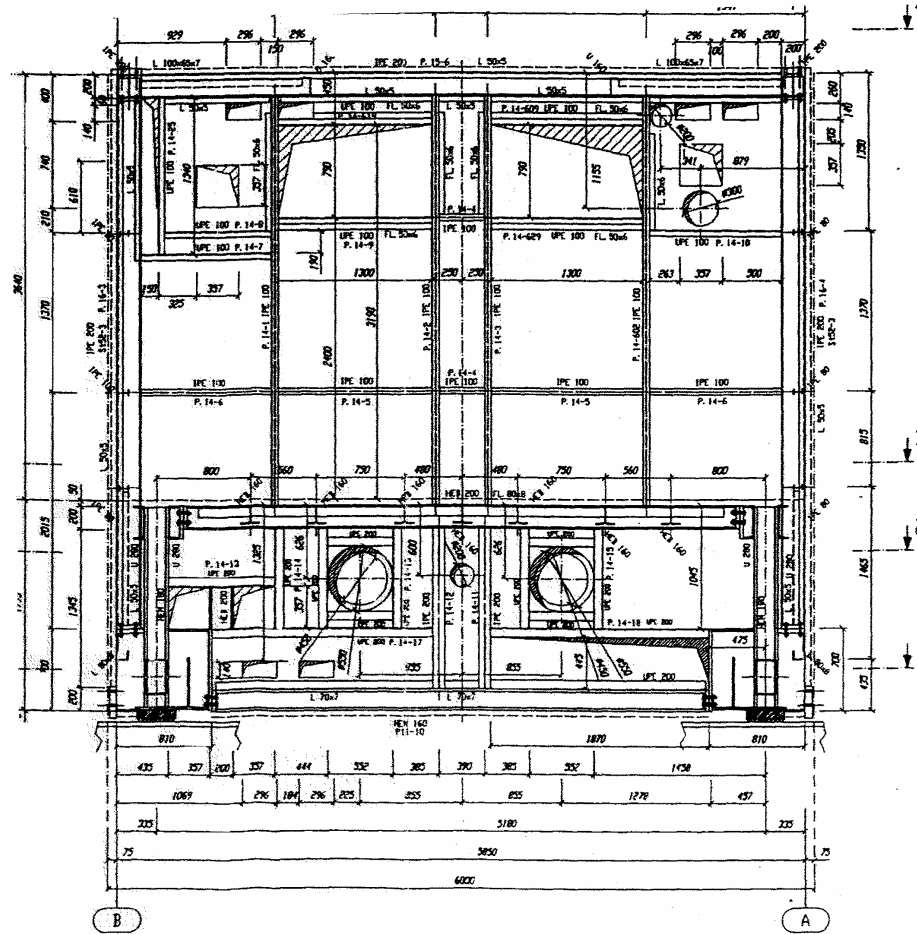


Fig. 2d: Rear Wall (Wall-2) of Test-Cell.

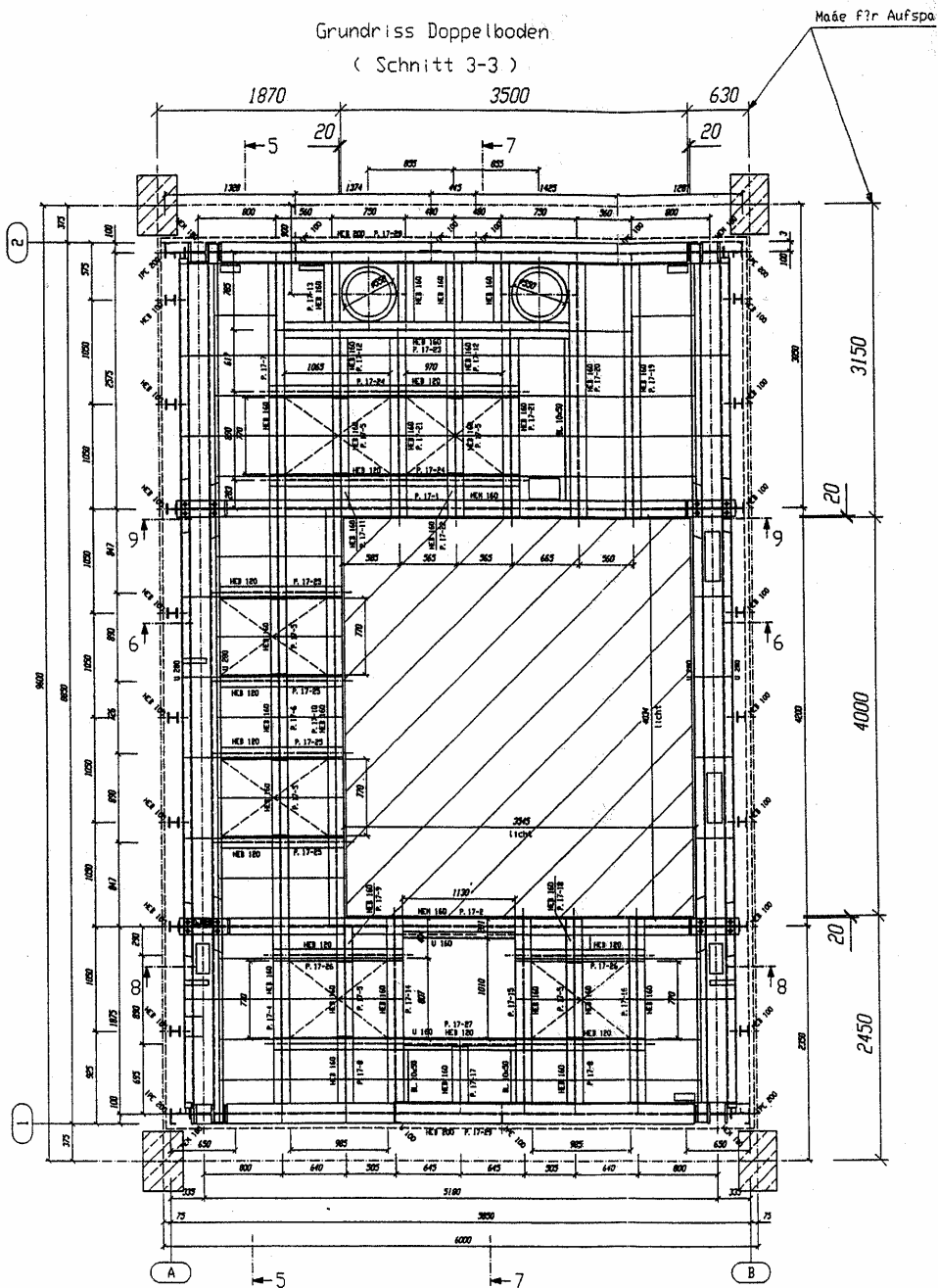


Fig. 2e: Floor of Test-Cell

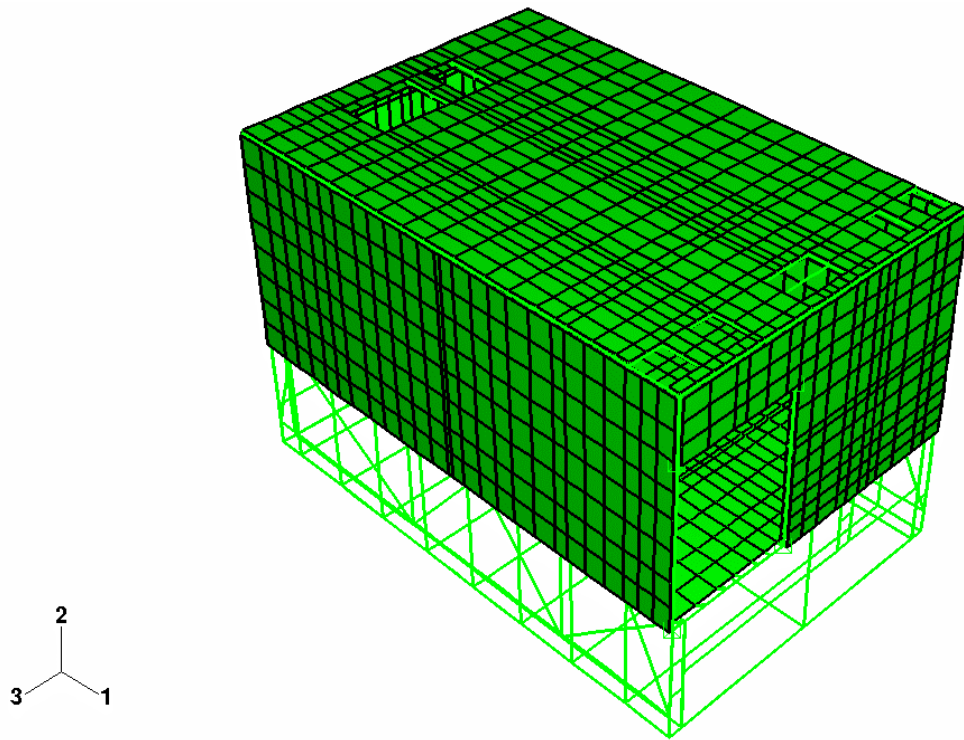


Fig. 3a: Three Dimensional Finite Element Model of Test-Cell Structure

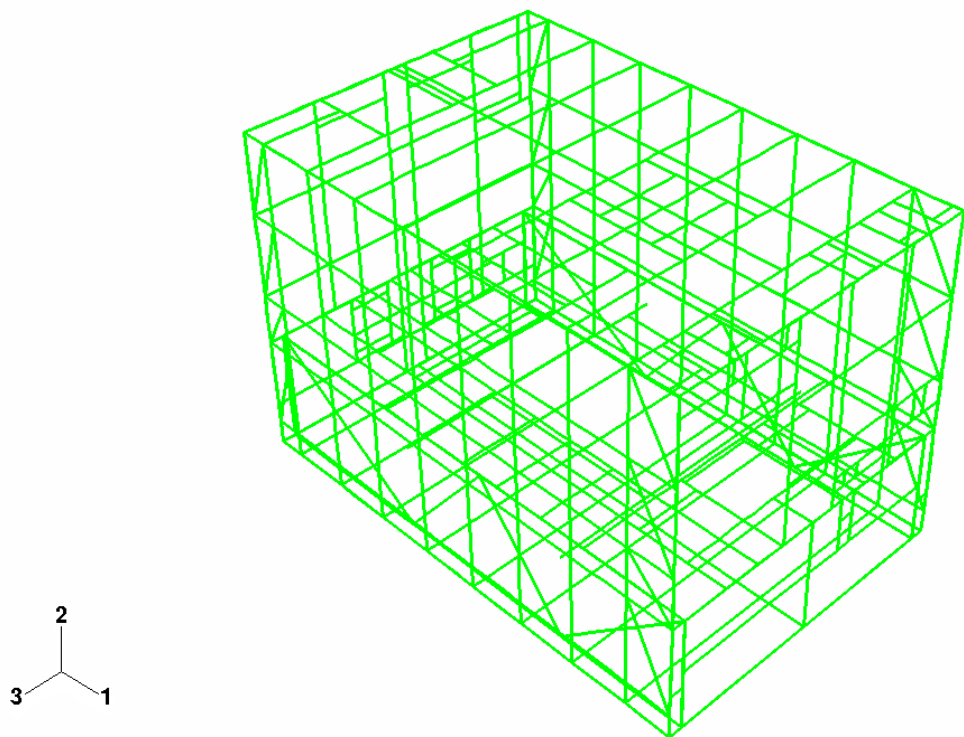


Fig. 3b: Three Dimensional Frame Model of Test-Cell Structure

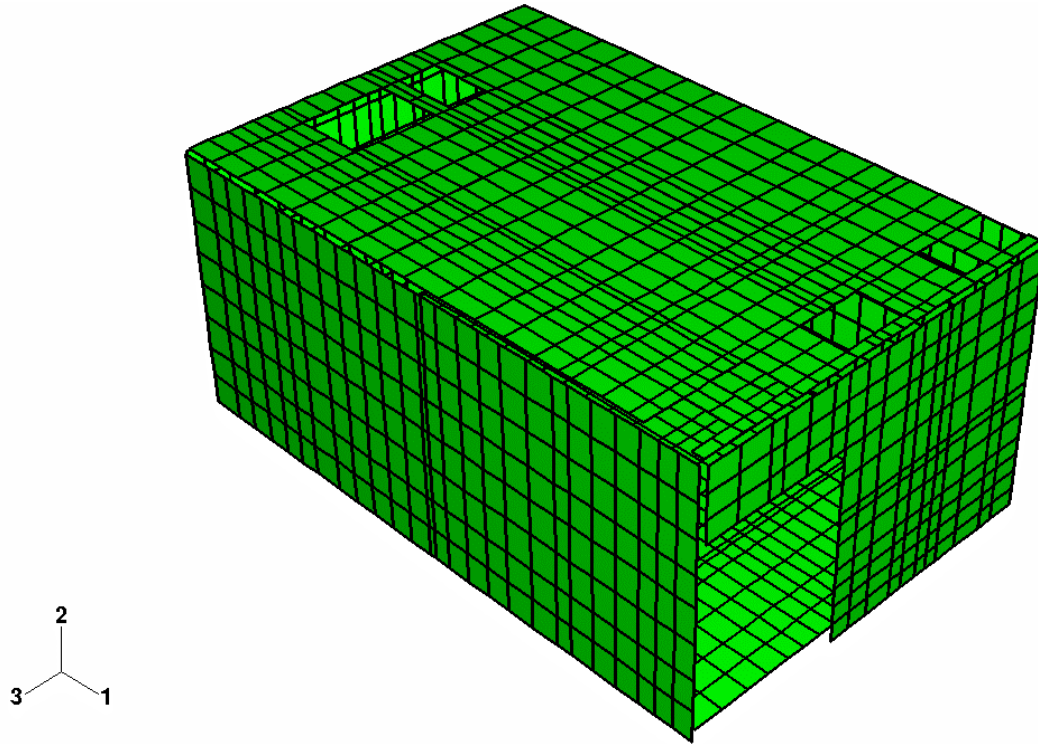


Fig. 3c: Three Dimensional Outer Plate Model of Test-Cell Structure

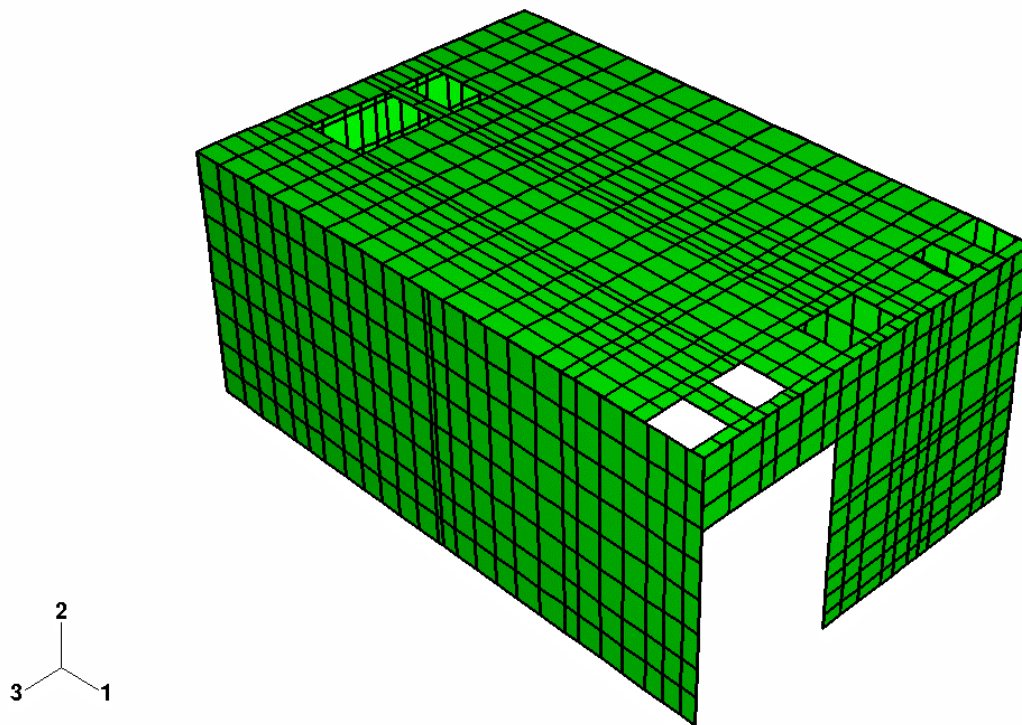


Fig. 3d: Three Dimensional Inner Corrugated Wall (Equivalent Orthotropic) Model of Test-Cell Structure

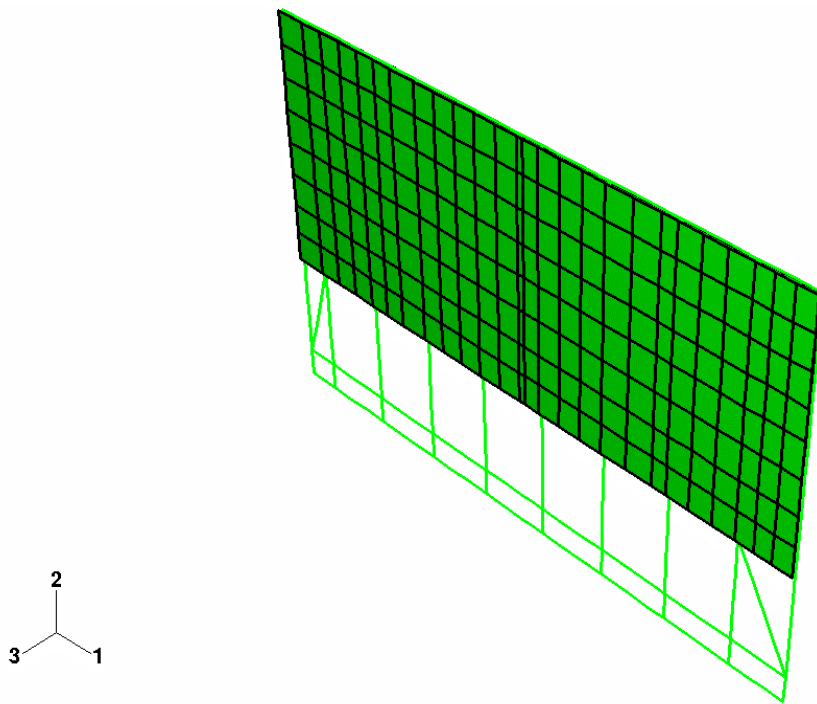


Fig. 3e: Composite Wall Model for Left Wall of Test-Cell Structure

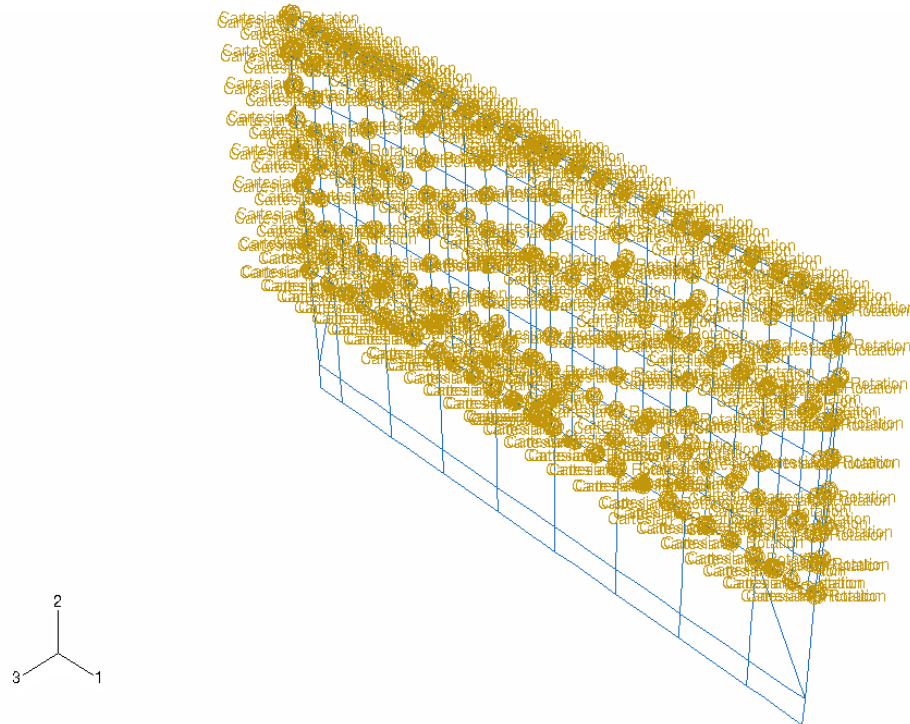


Fig. 3f: Bolt Elements on the Outer Plate and Inner Corrugated Wall for Connection to the Frame Structure for Left Wall of Test-Cell Structure FEM Model

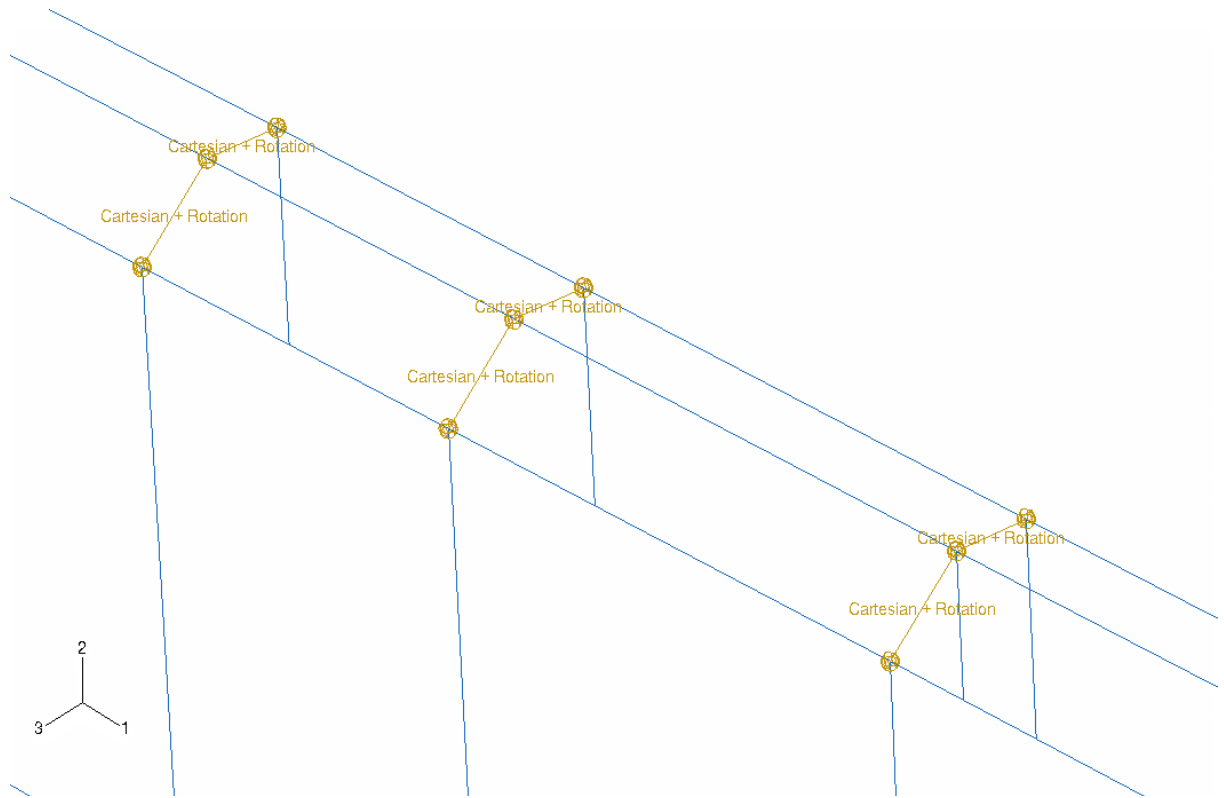


Fig. 3g: Local View of Bolt-Connectors Used between the Outer Plate and Inner Corrugated Wall in the Test-Cell Structure FEM Model

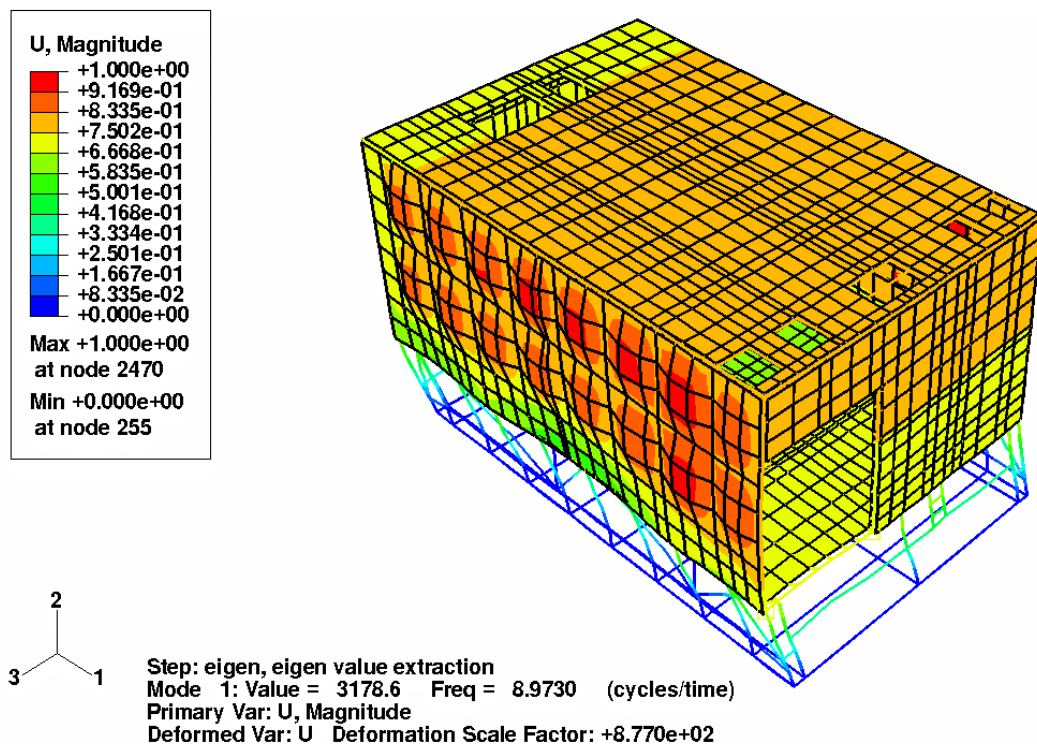


Fig. 4a: Test-Cell Structural Vibration Mode-1 at 8.973 Hz Frequency

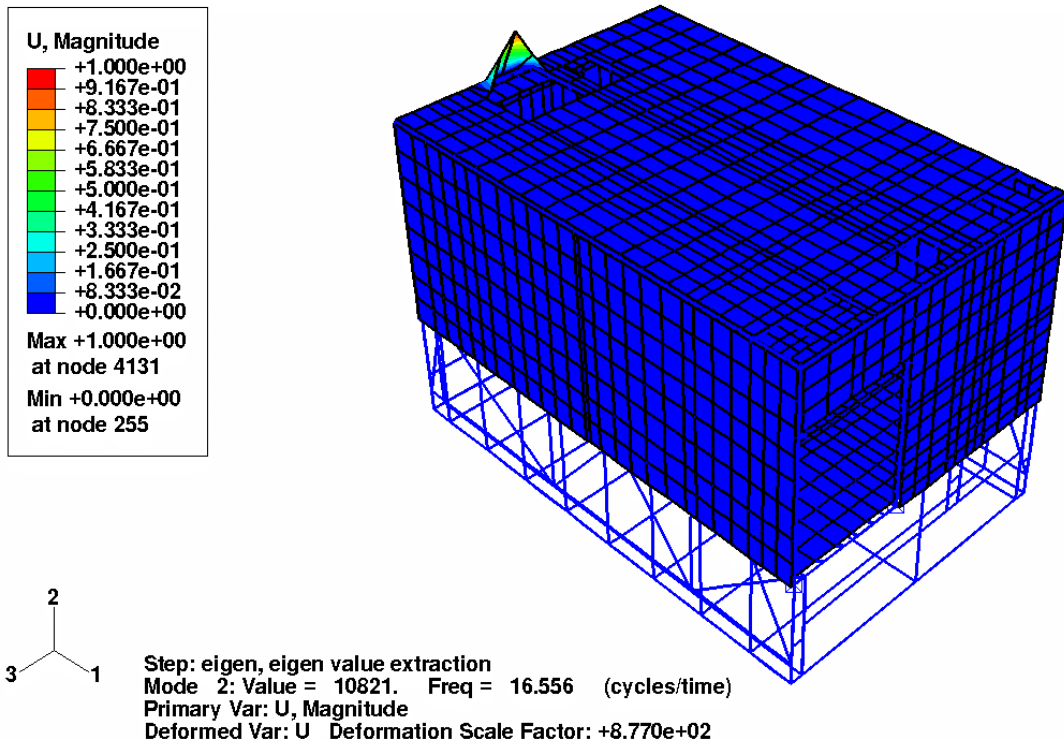


Fig. 4b: Test-Cell Structural Vibration Mode-2 at 16.556 Hz Frequency

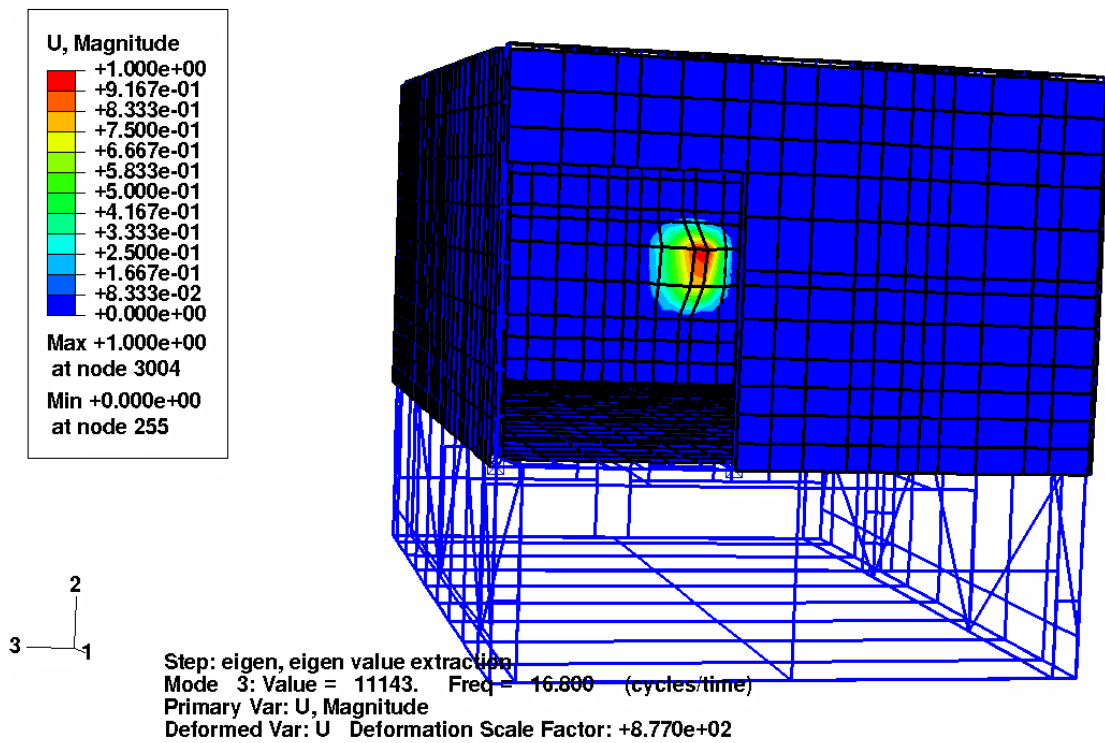


Fig. 4c: Test-Cell Structural Vibration Mode-3 at 16.806 Hz Frequency

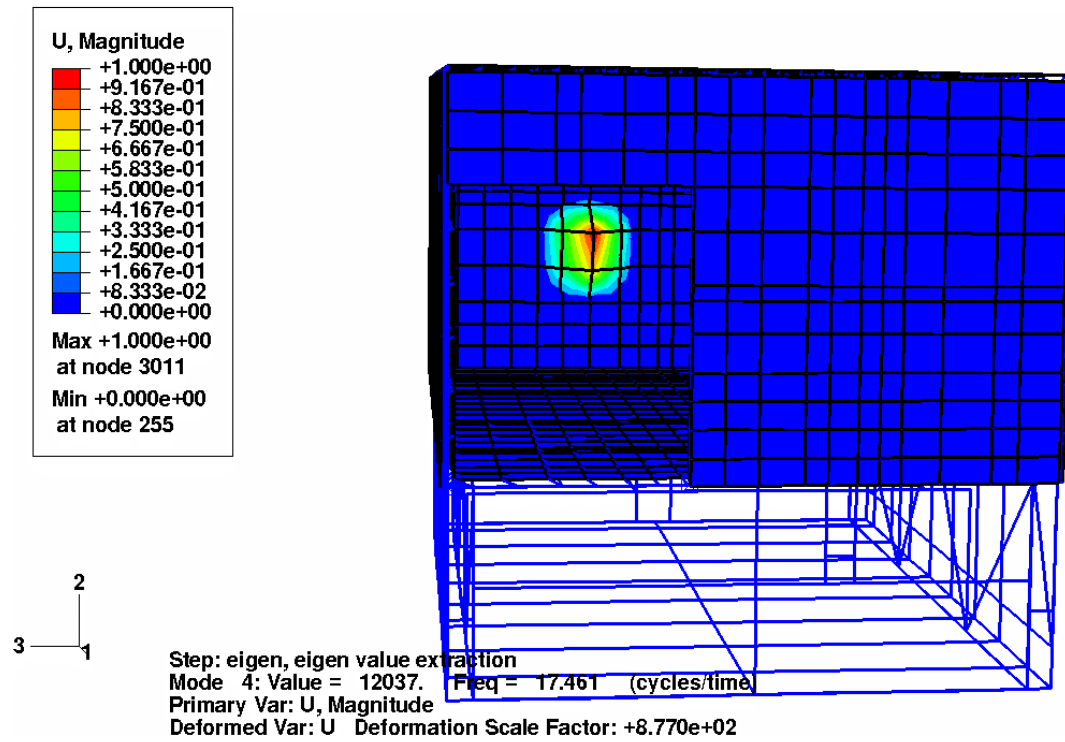


Fig. 4d: Test-Cell Structural Vibration Mode-4 at 17.461 Hz Frequency

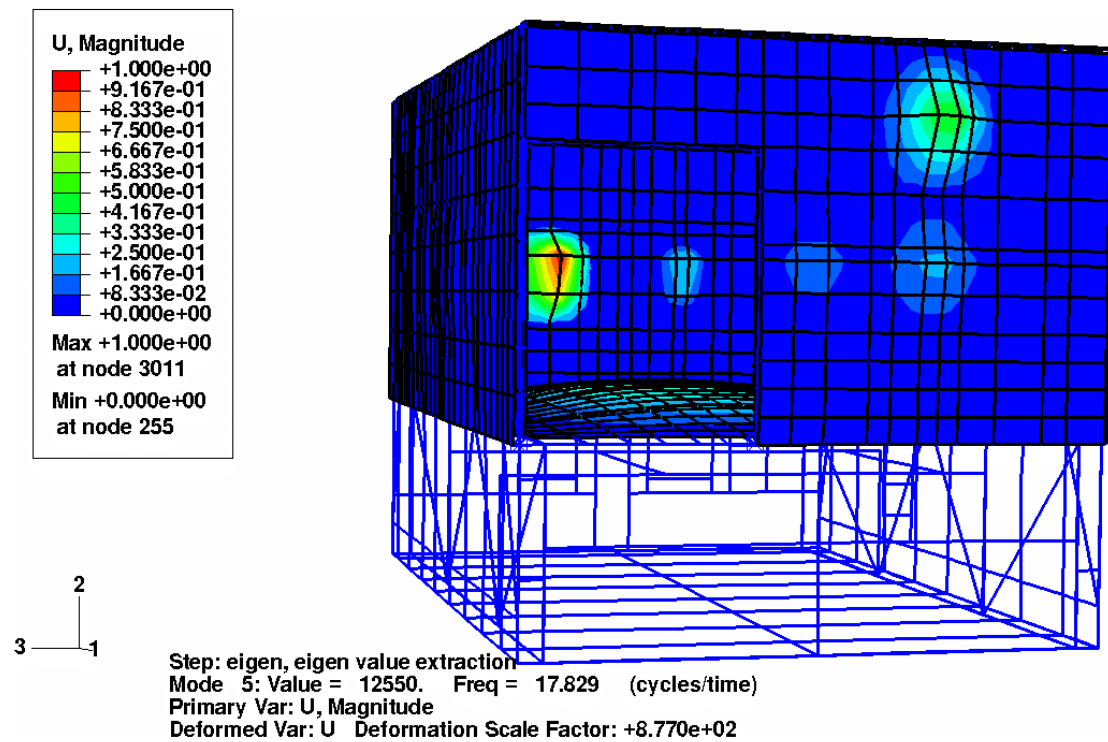


Fig. 4e: Test-Cell Structural Vibration Mode-5 at 17.829 Hz Frequency

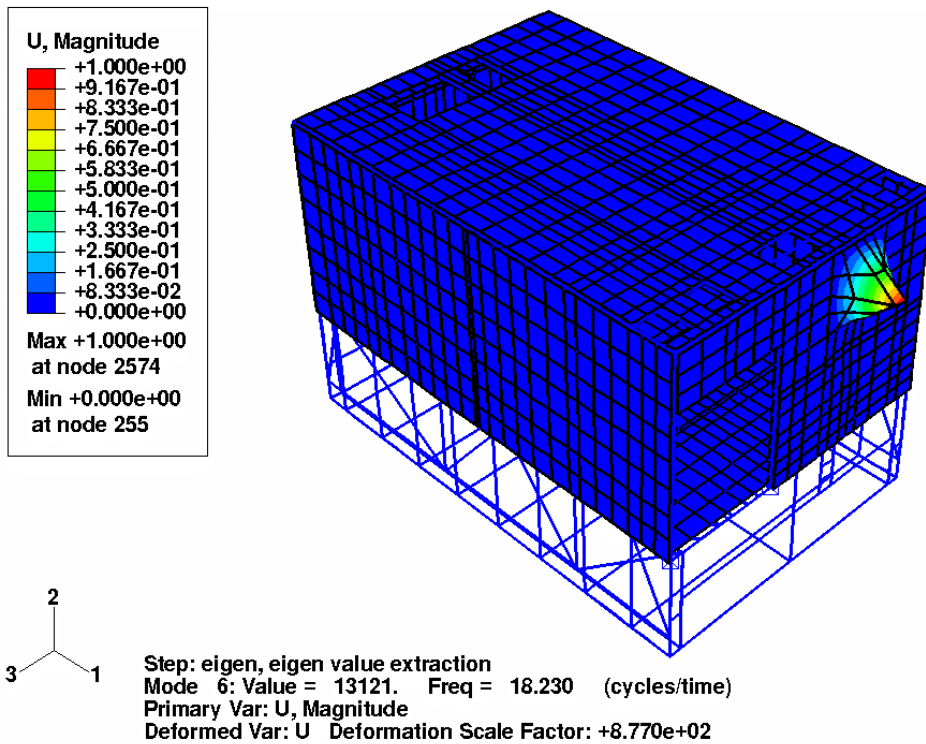


Fig. 4f: Test-Cell Structural Vibration Mode-6 at 18.230 Hz Frequency

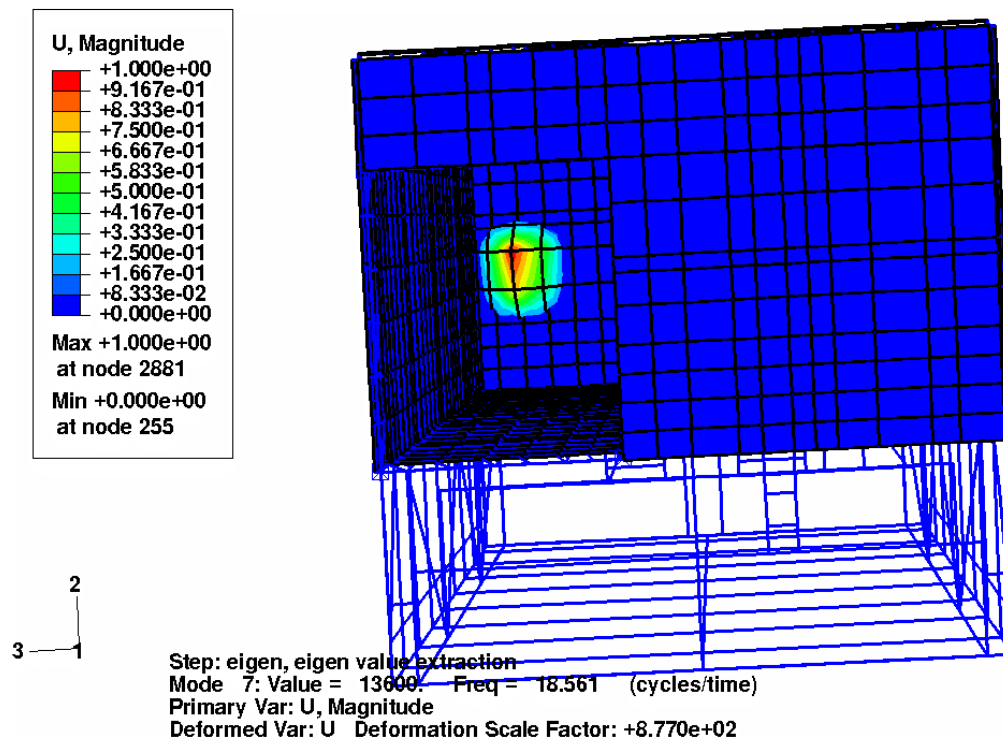


Fig. 4g: Test-Cell Structural Vibration Mode-7 at 18.561 Hz Frequency

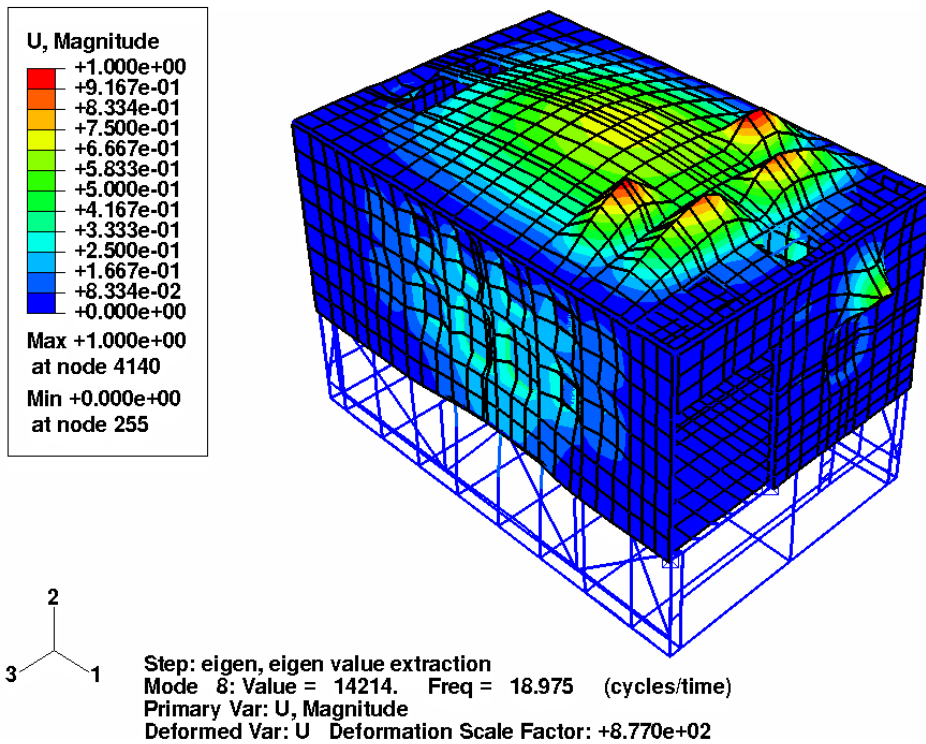


Fig. 4h: Test-Cell Structural Vibration Mode-8 at 18.975 Hz Frequency

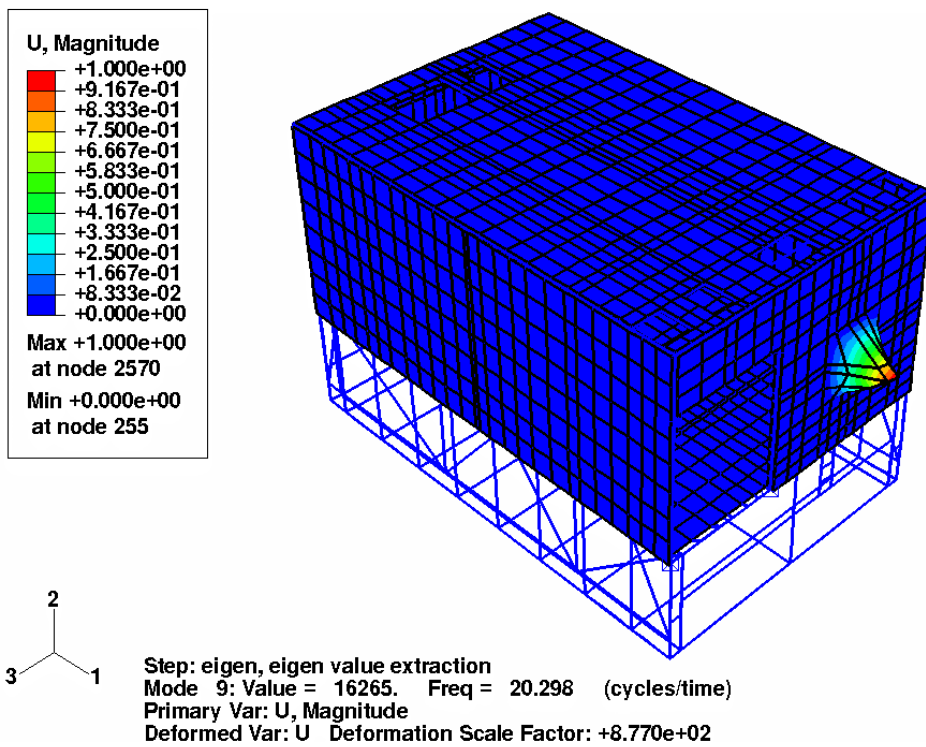


Fig. 4i: Test-Cell Structural Vibration Mode-9 at 20.298 Hz Frequency

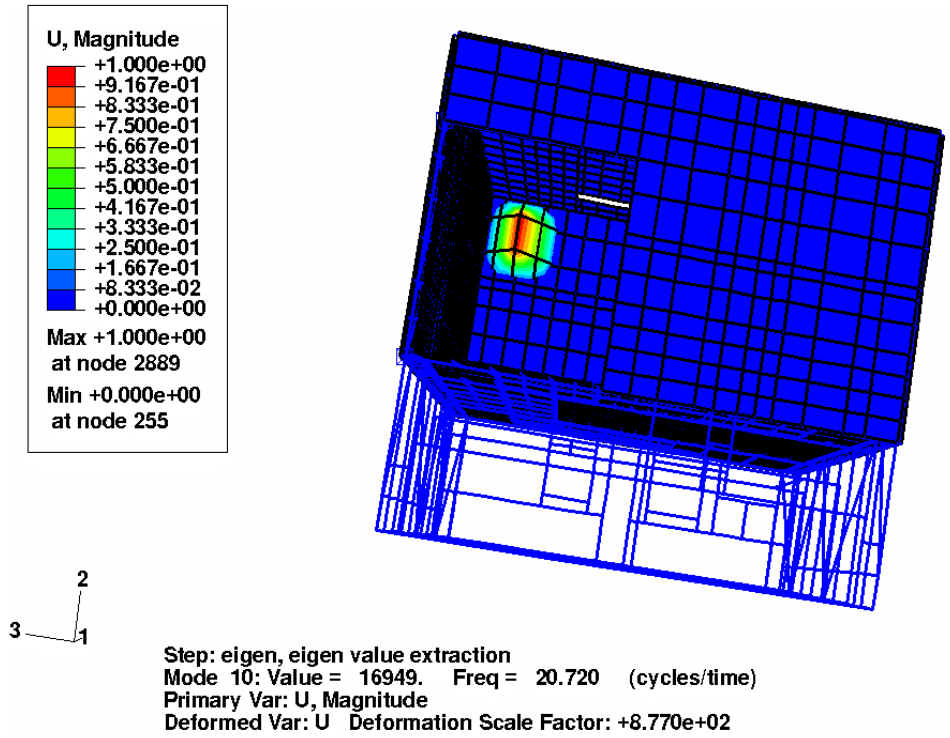


Fig. 4j: Test-Cell Structural Vibration Mode-10 at 20.720 Hz Frequency

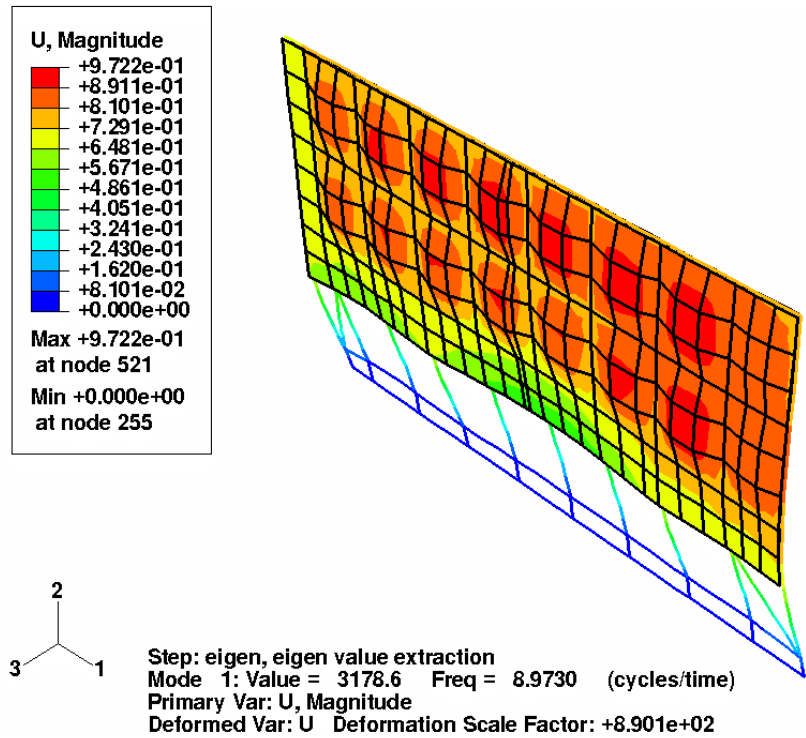


Fig. 5a: Left Composite Wall Mode at 8.973 Hz (Outer Plate-With Local Panel Mode) (Analytical Model Value 10.71 Hz)

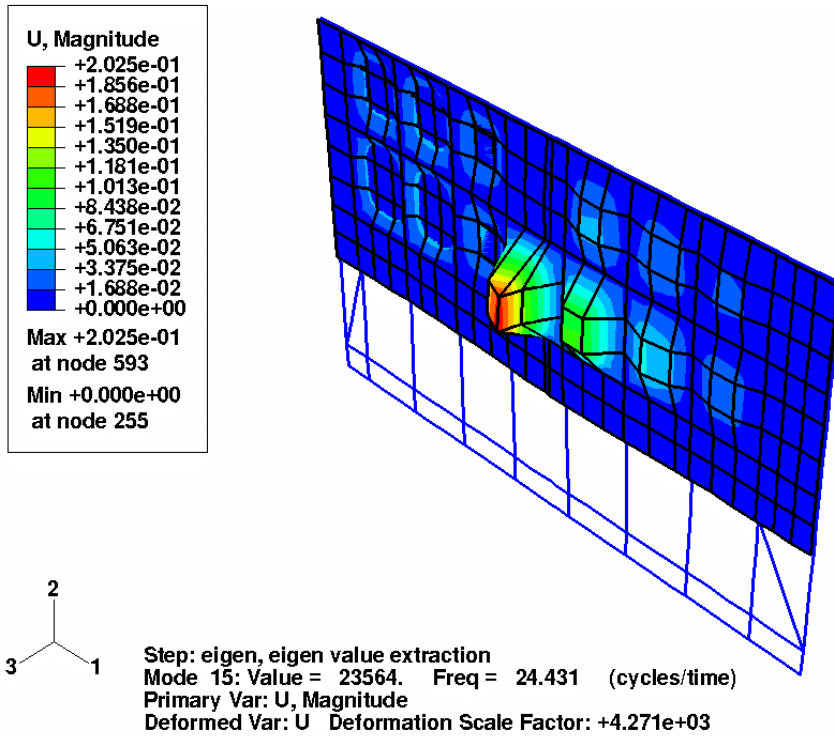


Fig. 5b: Left Composite Wall Mode at 24.43 Hz (Outer Plate-With Local Panel Mode) (Analytical Model Value 24.05 Hz)

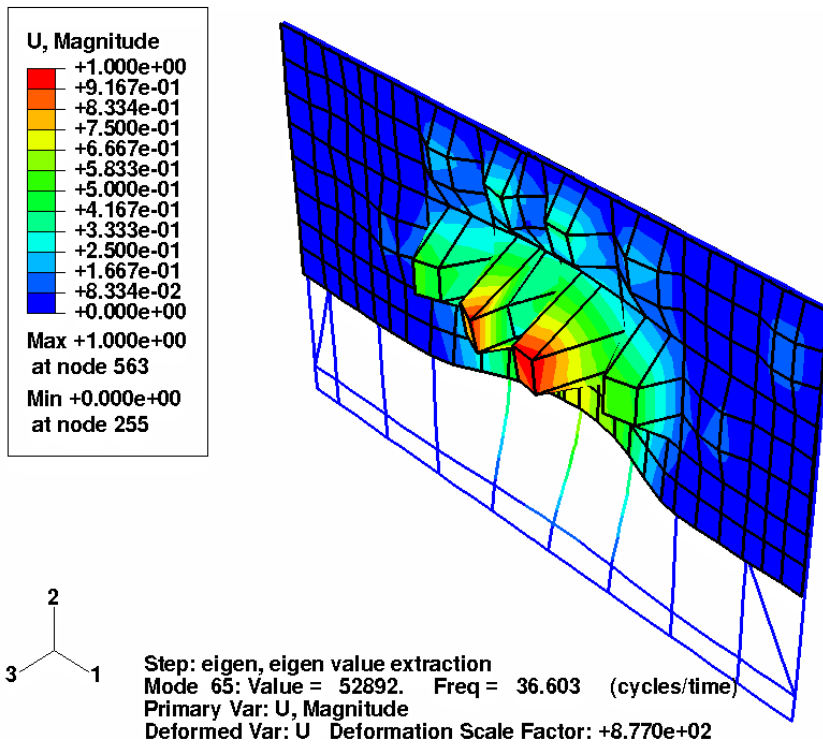
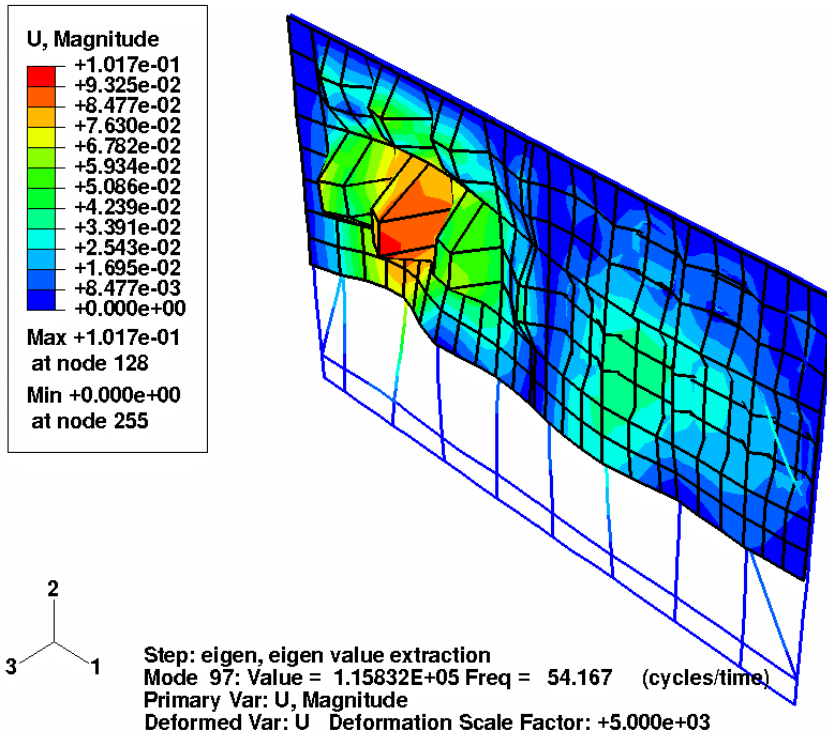
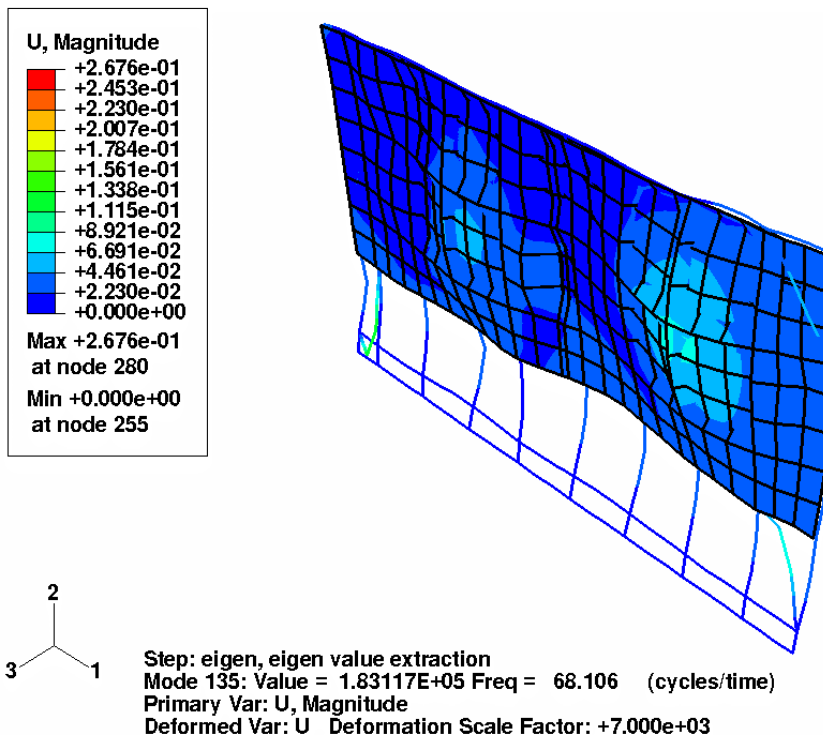


Fig. 5c: Left Composite Wall Mode at 36.60 Hz (Global Plate Mode-1,1) (Analytical Model Value 35.42 Hz)



**Fig. 5d: Left Composite Wall Mode at 54.17 Hz (Global Plate Mode-1,2)
(Analytical Model Value 53.19 Hz)**



**Fig. 5e: Left Composite Wall Mode at 68.11 Hz (Global Plate Mode-1,3)
(Analytical Model Value 68.85 Hz)**

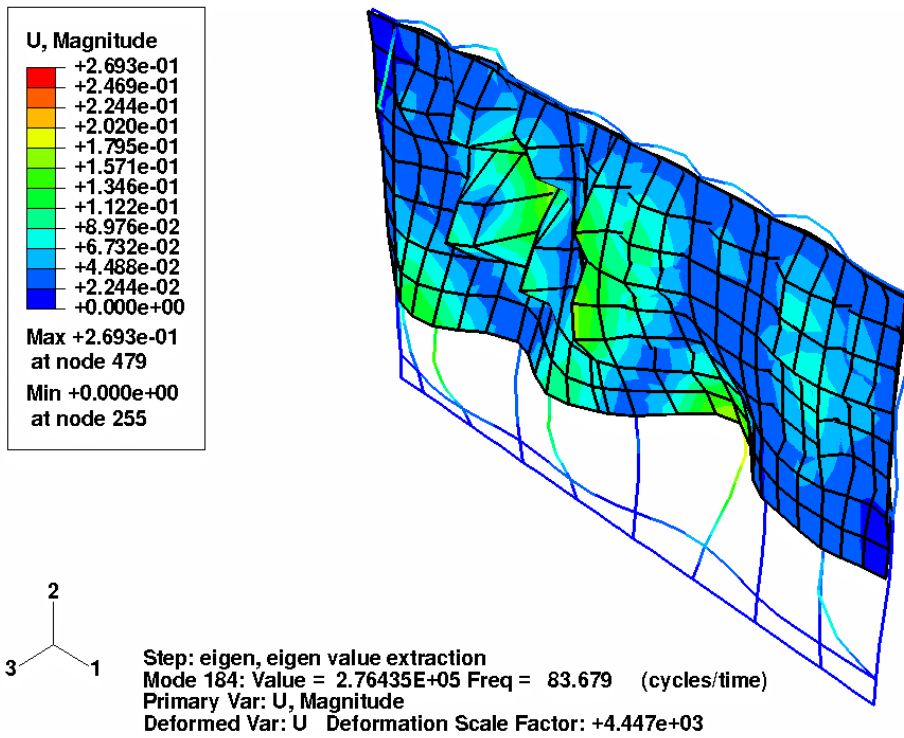


**Fig. 5f: Left Composite Wall Mode at 83.68 Hz (Global Plate Mode-1,4)
(Analytical Model Value 83.59 Hz)**

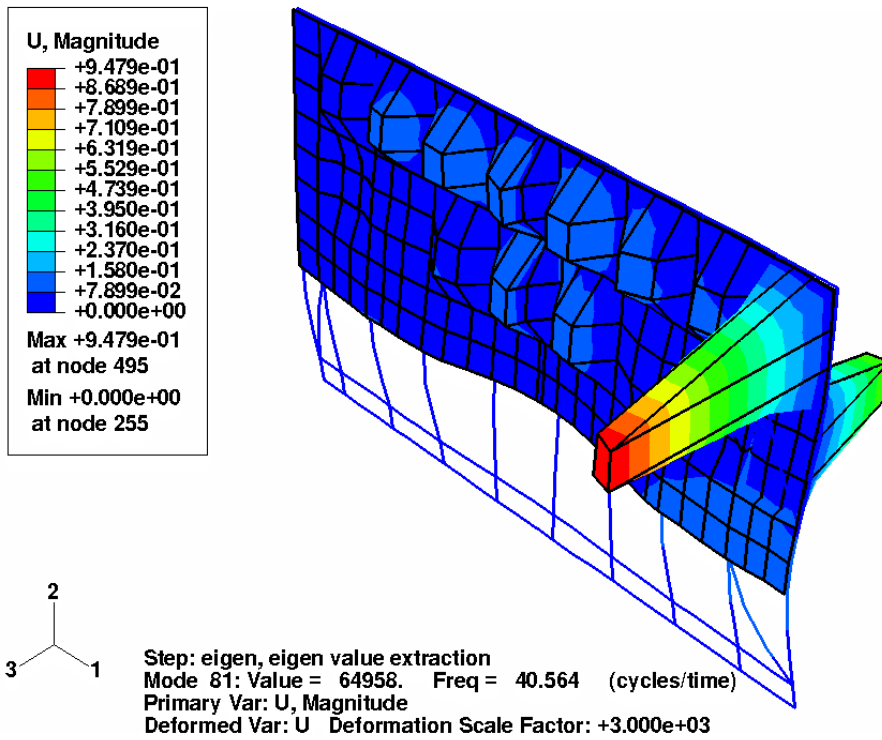


**Fig. 5g: Left Composite Wall Mode at 40.56 Hz (Global Plate Mode-2,1)
(Analytical Model Value 42.10 Hz)**

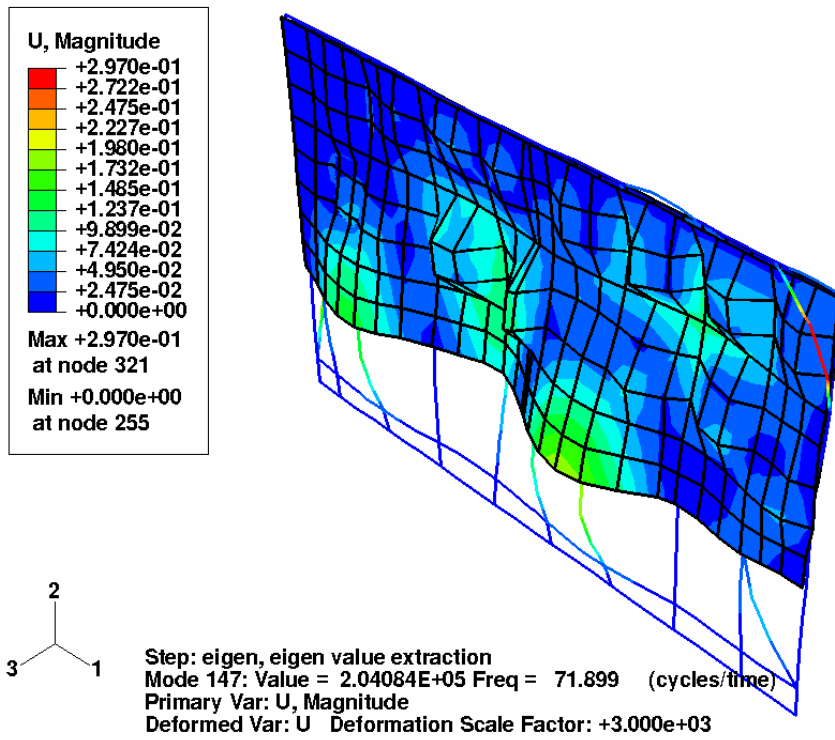


**Fig. 5h: Left Composite Wall Mode at 71.90 Hz (Global Plate Mode-2,2)
(Analytical Model Value 69.70 Hz)**

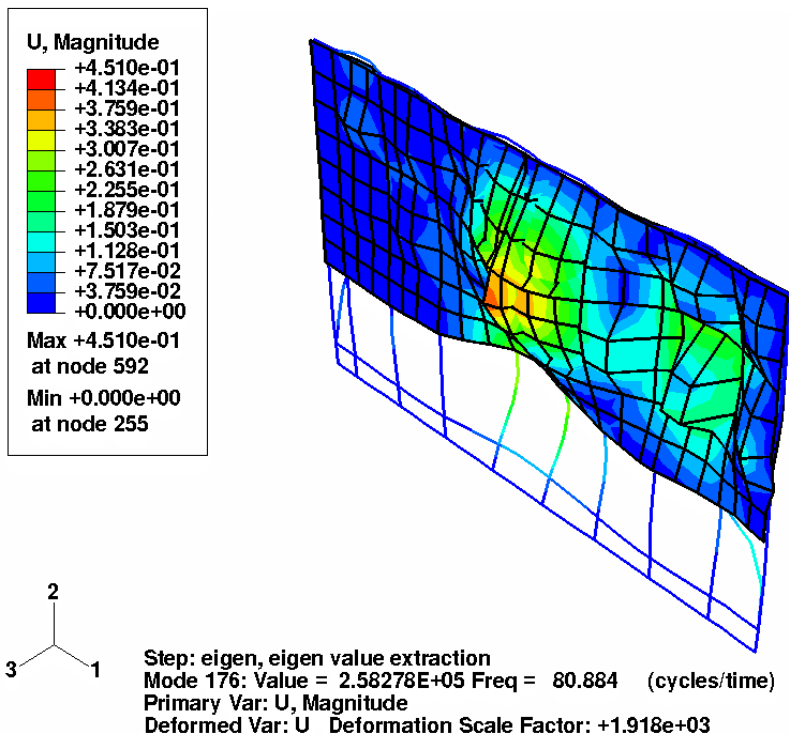
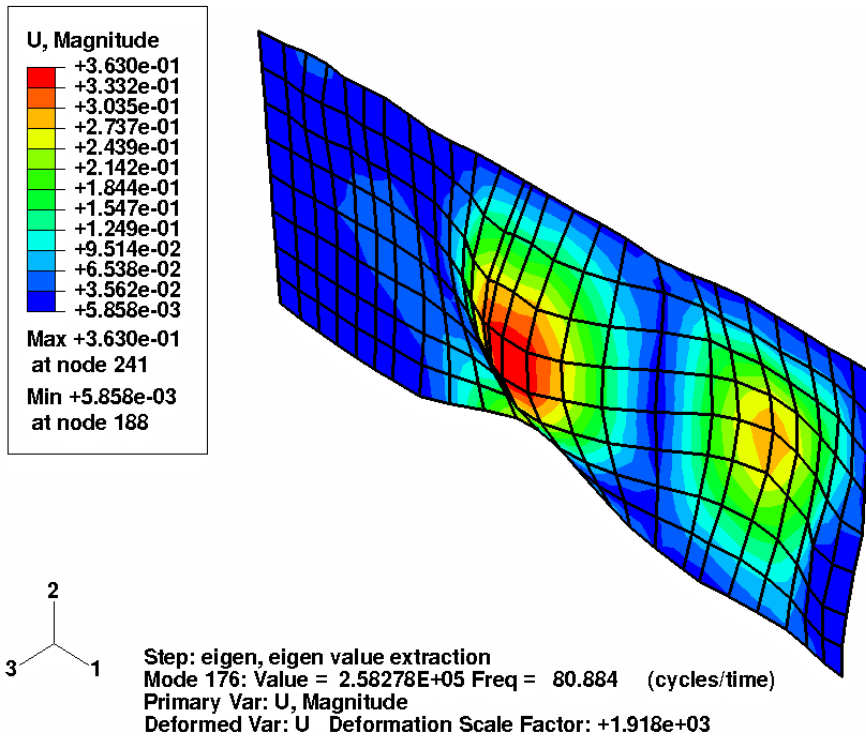


**Fig. 6a: Left Corrugated Inner Wall and Composite Wall Modes at 80.88 Hz
(Measured Value ~ 83.4 Hz)**

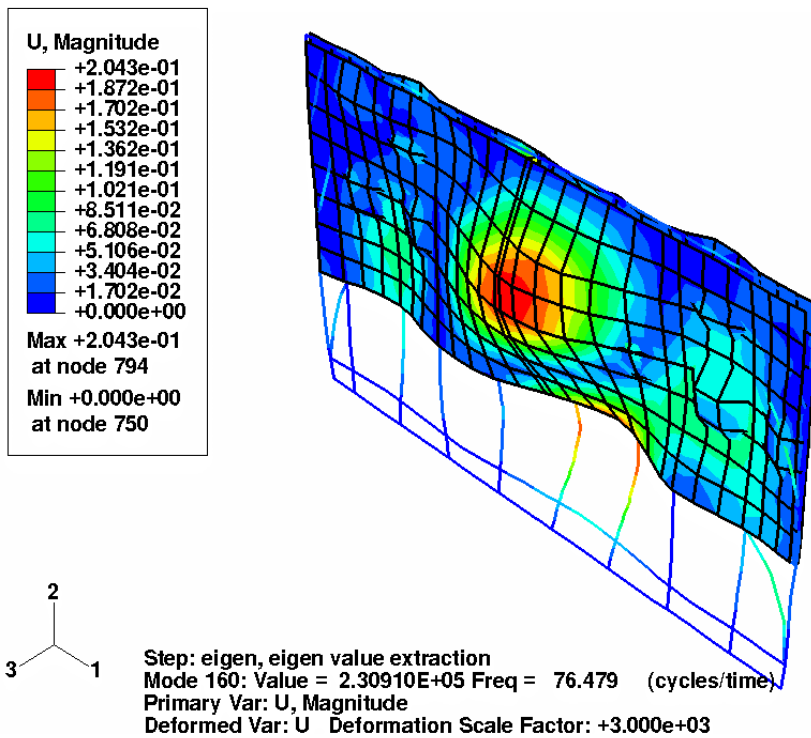
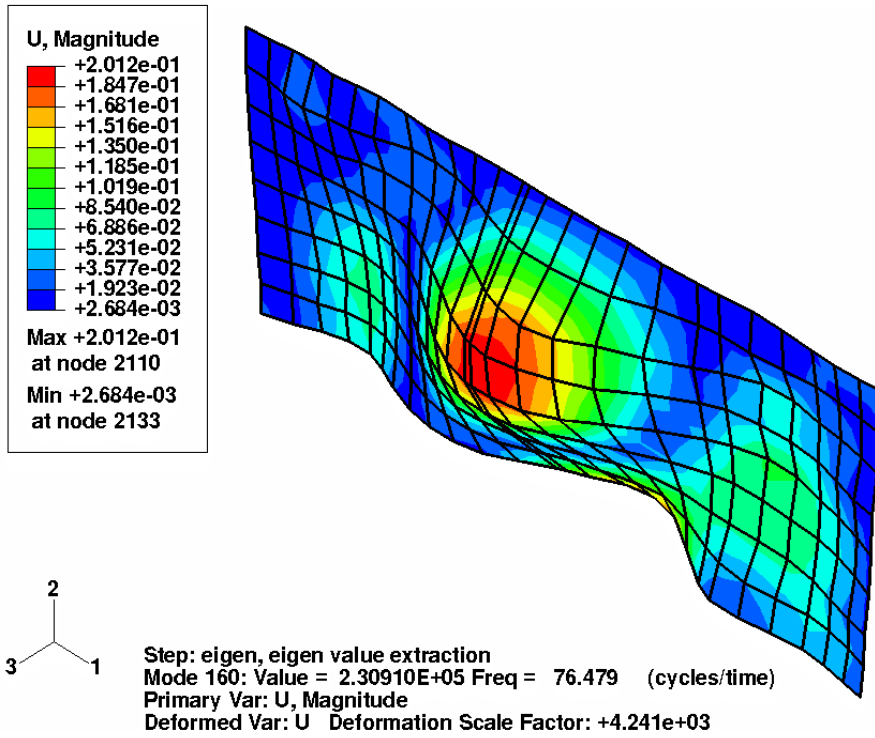


**Fig. 6b: Right Corrugated Inner Wall and Composite Wall Modes at 76.5 Hz
(Measured Value ~ 76.2 Hz)**

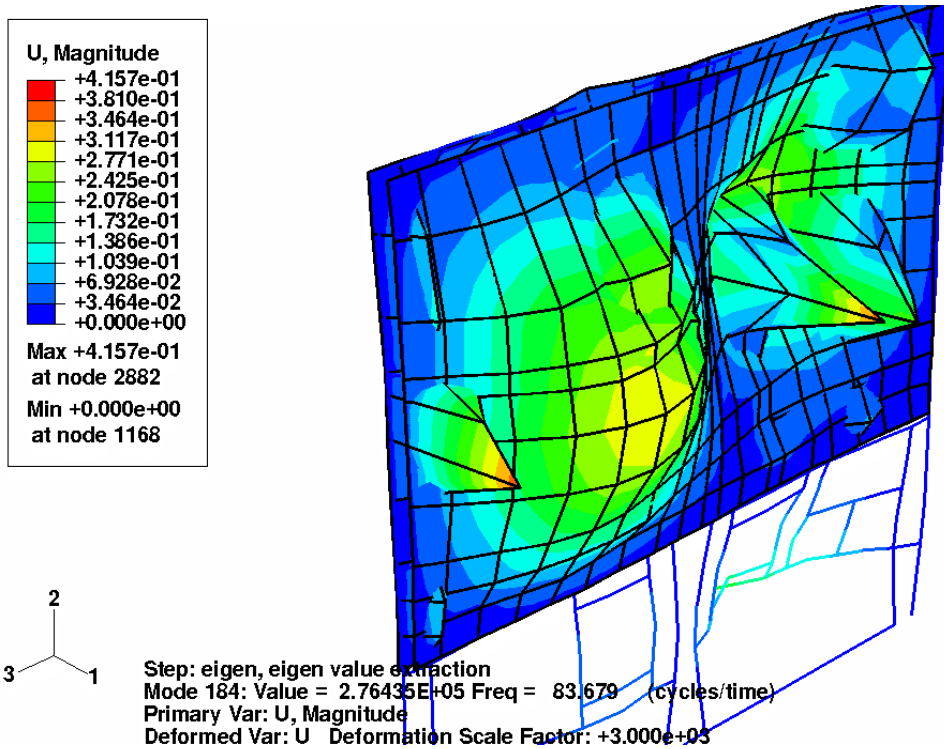
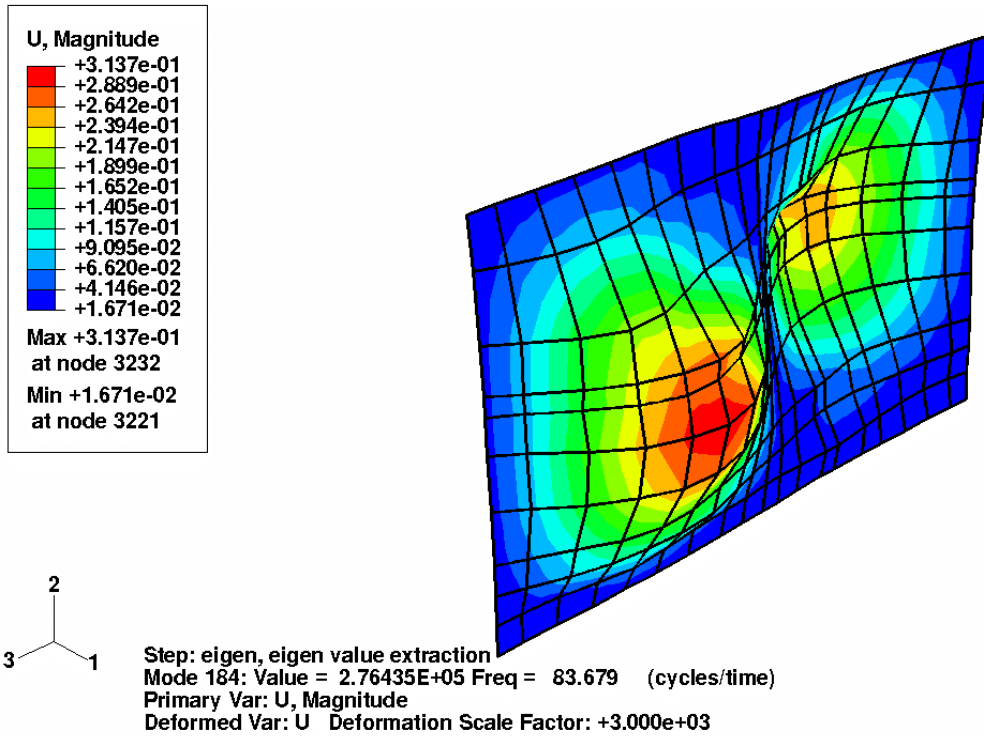


**Fig. 6c: Rear Corrugated Inner Wall and Composite Wall Modes at 83.7 Hz
(Measured Value ~ 86.6 Hz)**

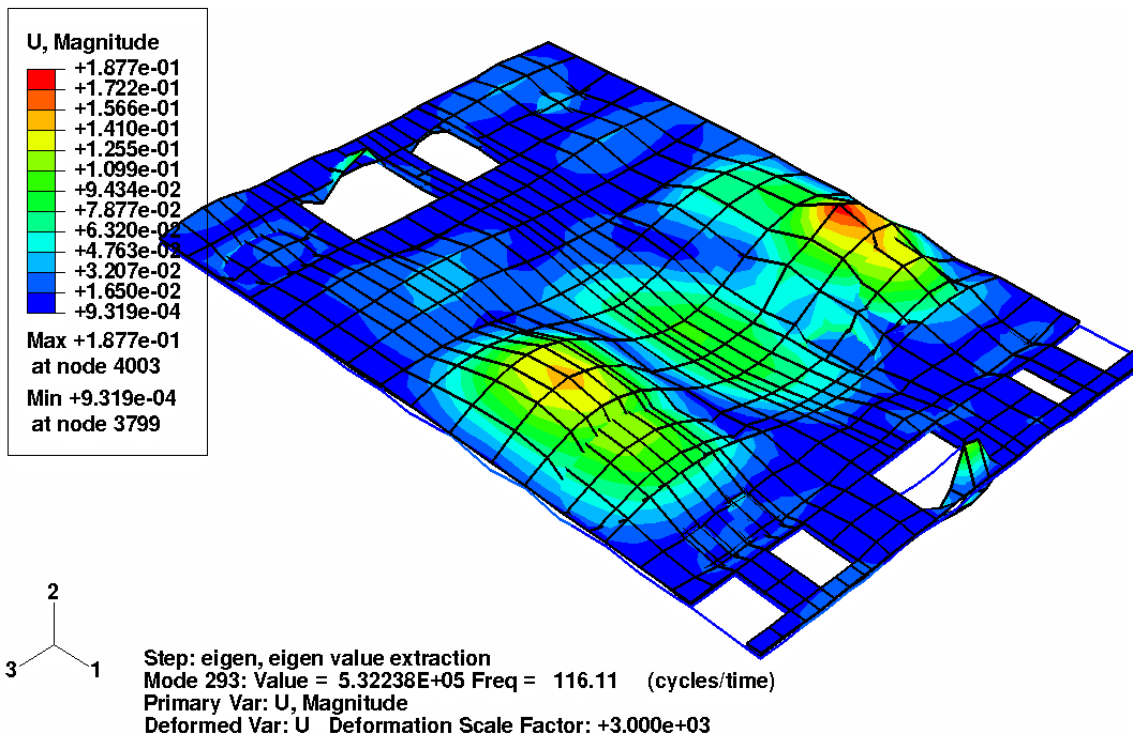
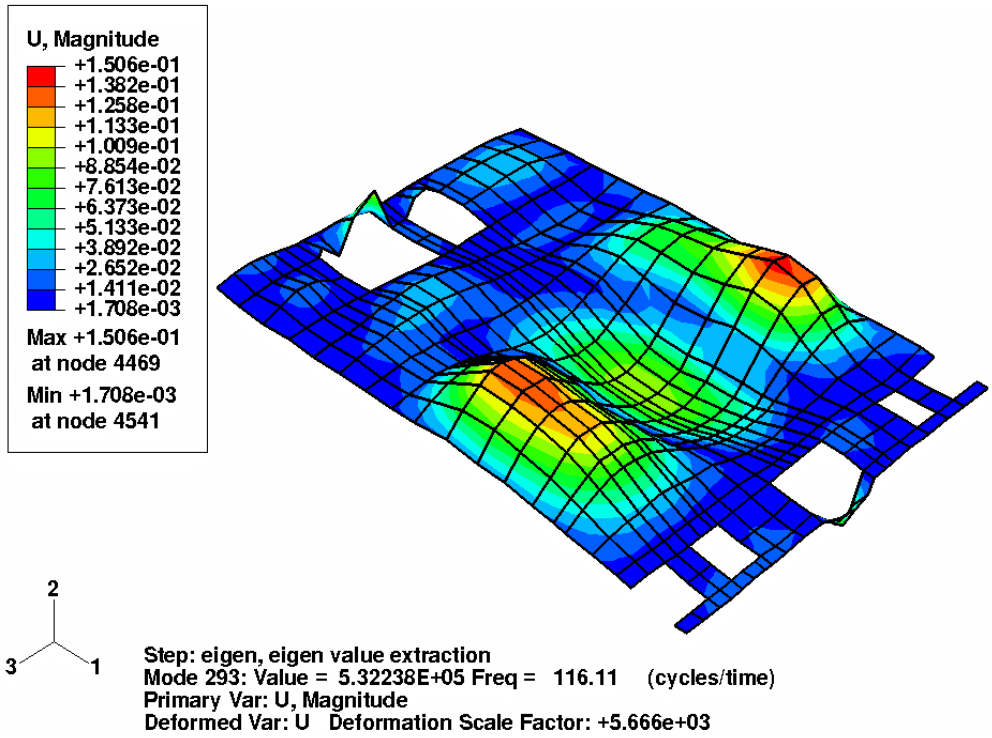


**Fig. 6d: Ceiling Corrugated Inner Wall and Composite Wall Modes at 116.11 Hz
(Measured Value ~ 116.8 Hz)**

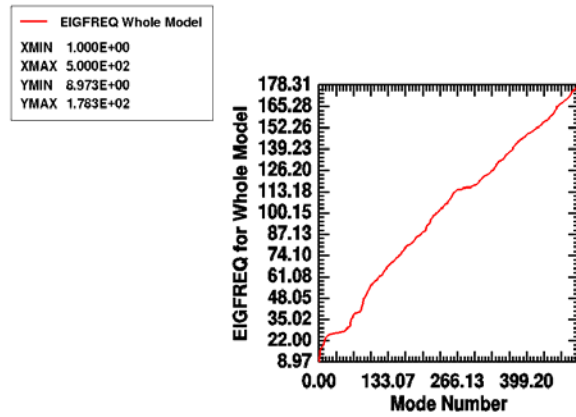


Fig. 7a: Frequency Spectrum for the Whole Model up to 500 Modes (178.3 Hz)

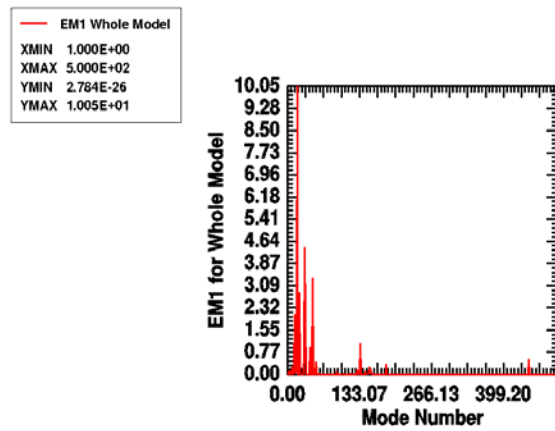


Fig. 7b: X Direction (Longitudinal) Effective Mass distribution Over the Frequency Spectrum of 500 Modes (178.3 Hz)

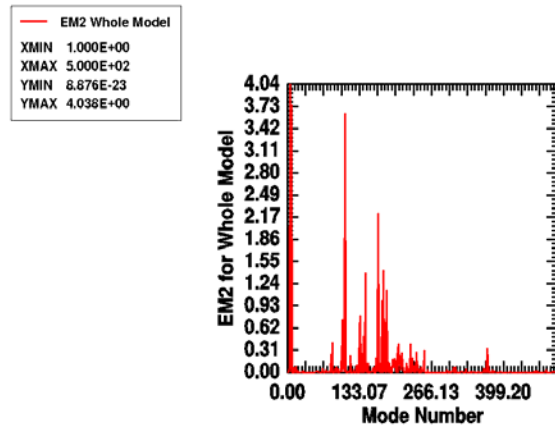


Fig. 7c: Y Direction (Vertical) Effective Mass distribution Over the Frequency Spectrum of 500 Modes (178.3 Hz)

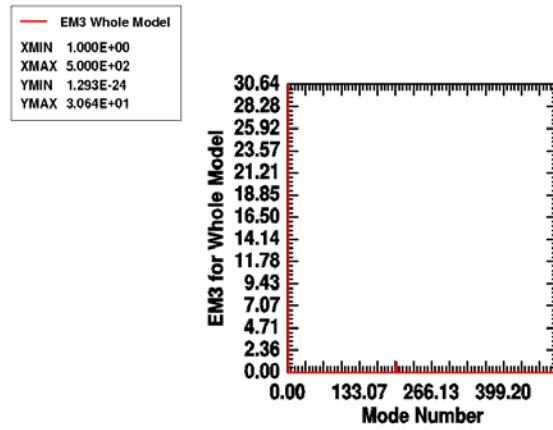


Fig. 7d: Z Direction (Transverse) Effective Mass distribution Over the Frequency Spectrum of 500 Modes (178.3 Hz)

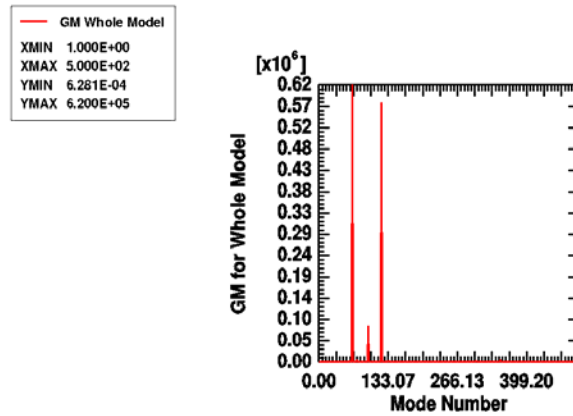


Fig. 7e: Generalized Mass distribution Over the Frequency Spectrum of 500 Modes (178.3 Hz)

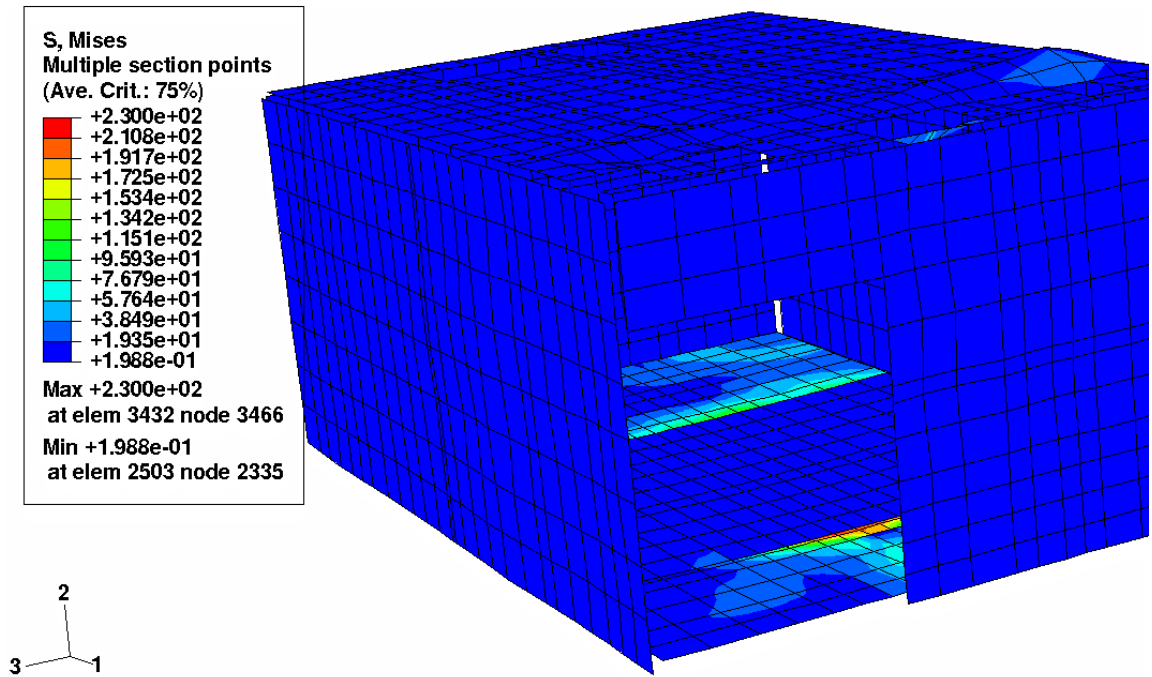


Fig. 8a: Maximum von Mises Stresses (MPa) in Outer Plate Group at Floor for 2 gm Hydrogen Combustion Experiment (at 89.15 m Sec)

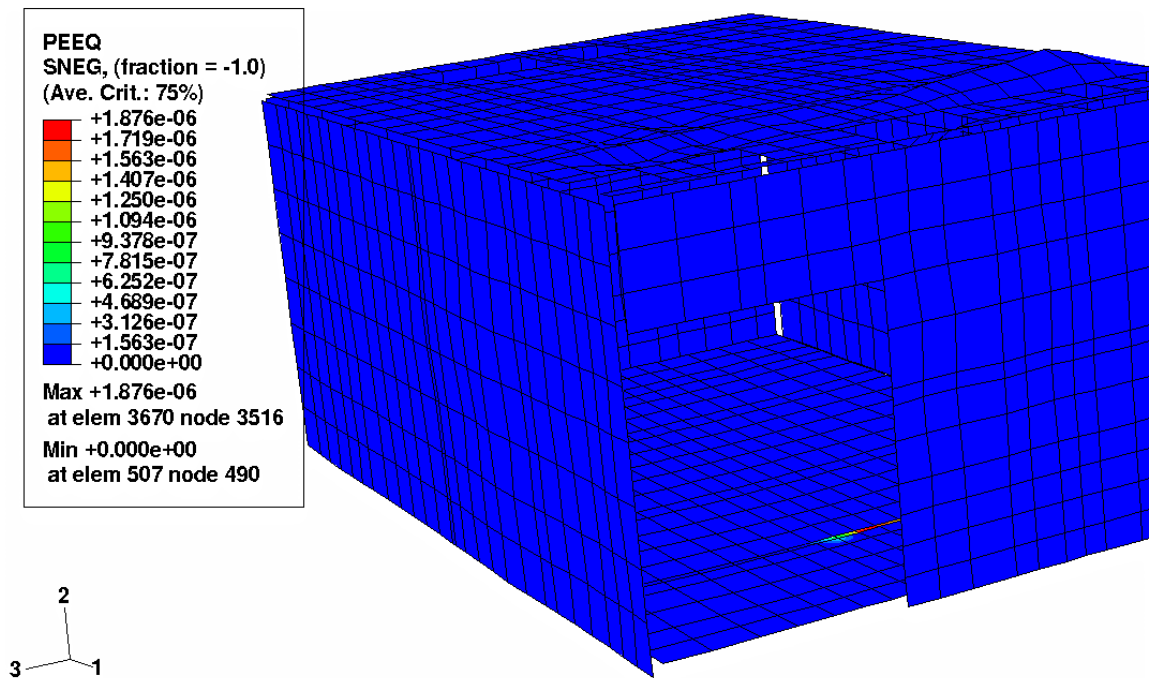


Fig. 8b: Maximum Effective Plastic Strain in Outer Plate Group at Floor for 2 gm Hydrogen Combustion Experiment (at 89.15 m Sec)

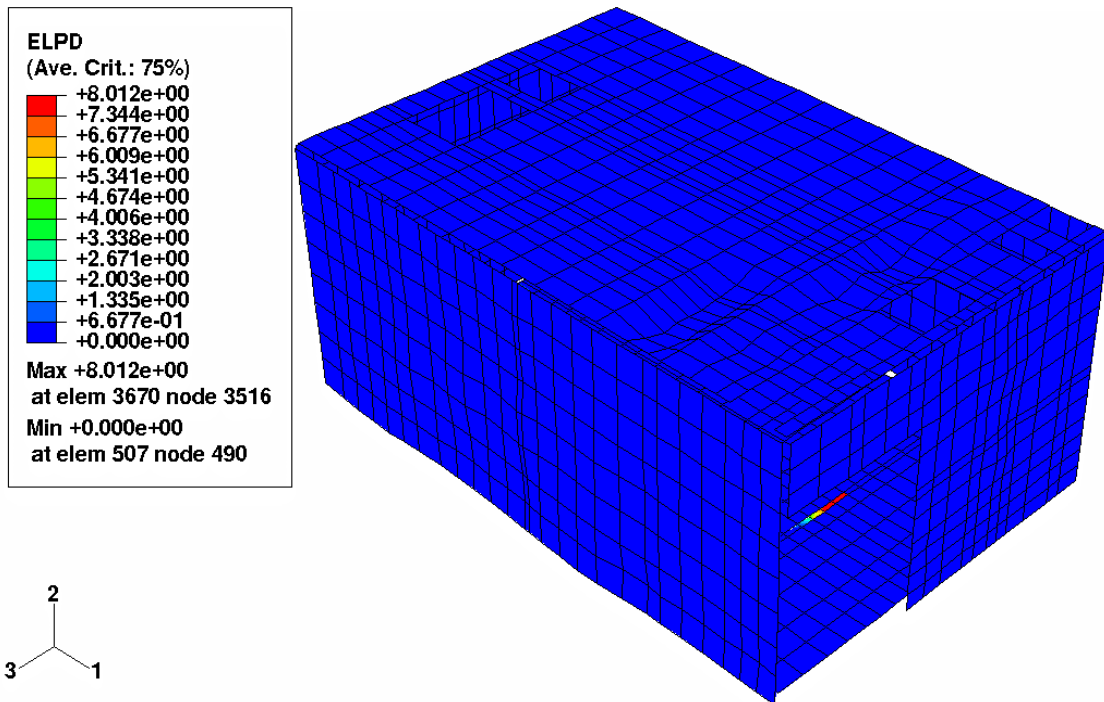


Fig. 8c: Maximum Plastic Energy (mJ) in Outer Plate Group at Floor for 2 gm Hydrogen Combustion Experiment (at 140 m Sec)

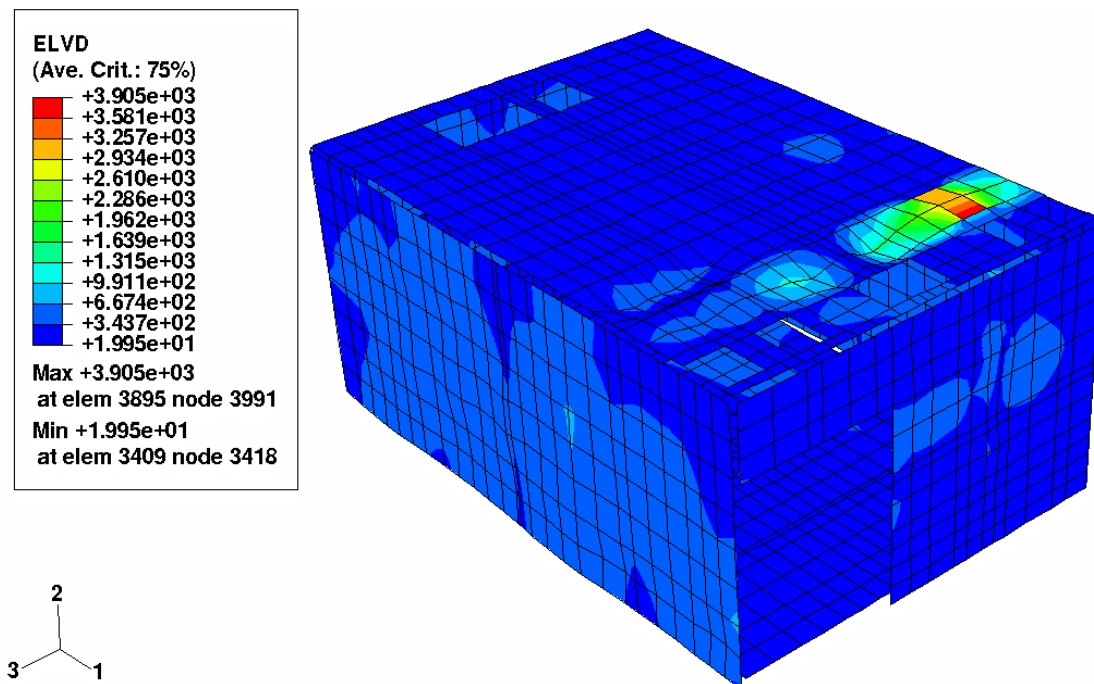


Fig. 8d: Maximum Viscous Energy (mJ) in Outer Plate Group at Ceiling Plate for 2 gm Hydrogen Combustion Experiment (at 140 m Sec)

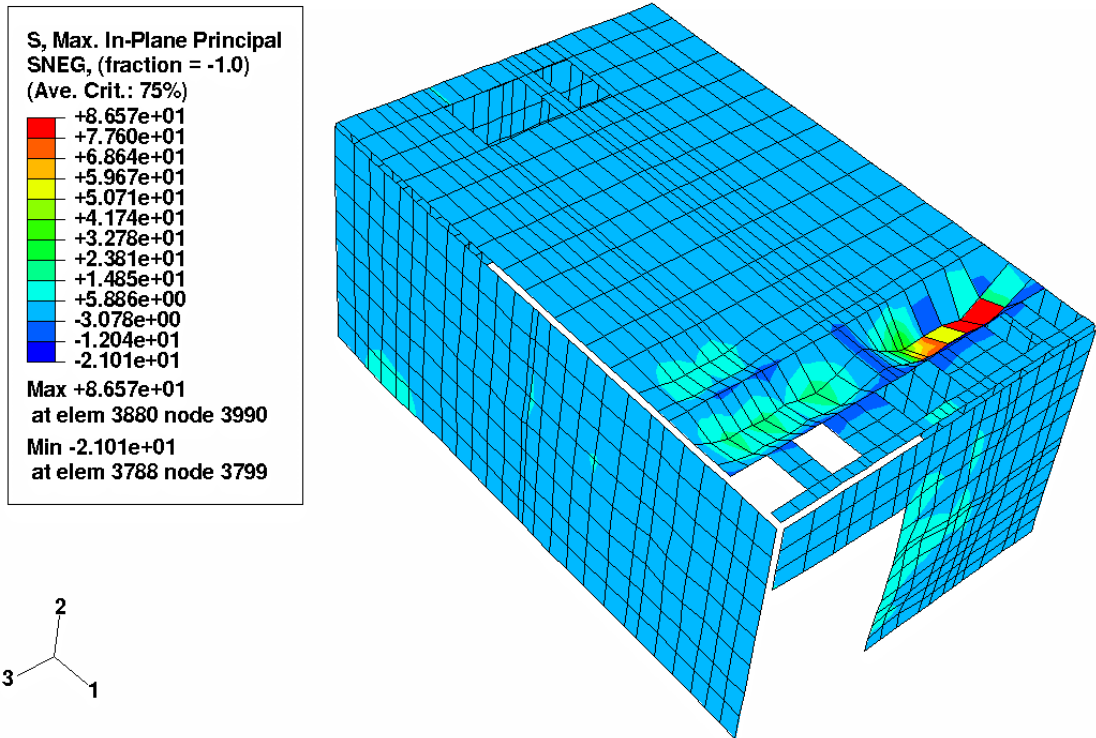


Fig. 8e: Maximum In-Plane Stress (MPa) in Outer Plate Group at Ceiling for 2 gm Hydrogen Combustion Experiment (at 67.15 m Sec)

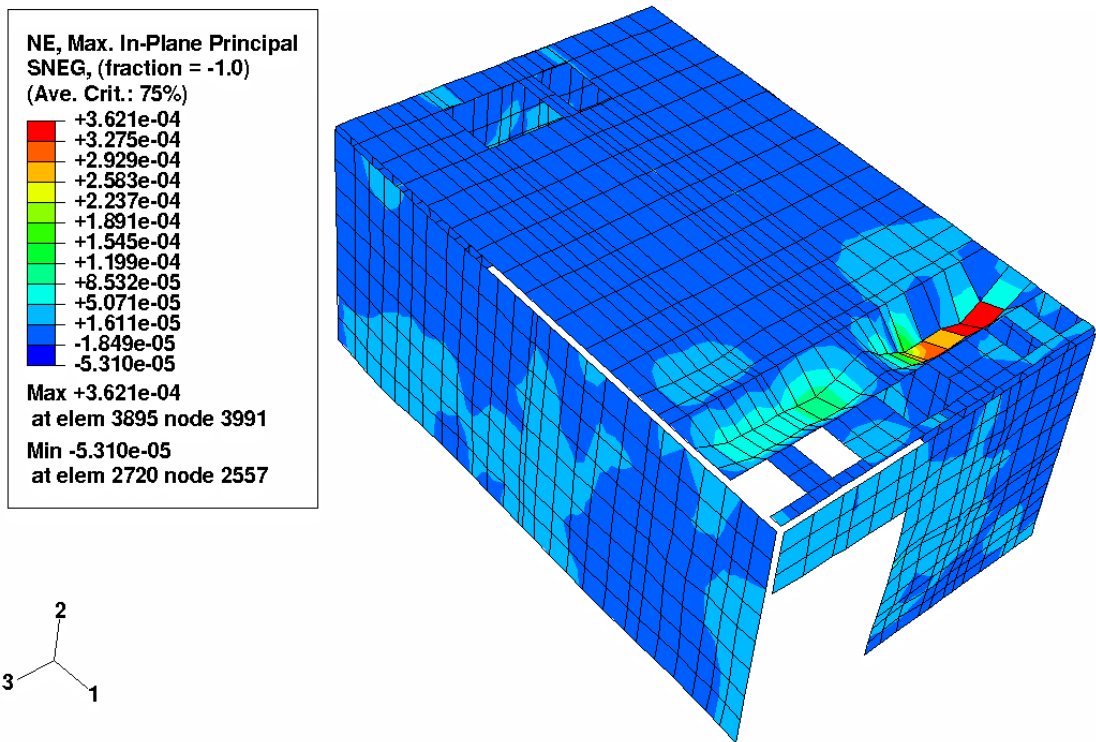


Fig. 8f: Maximum In-Plane Strain in Outer Plate Group at Ceiling for 2 gm Hydrogen Combustion Experiment (at 69.15 m Sec)

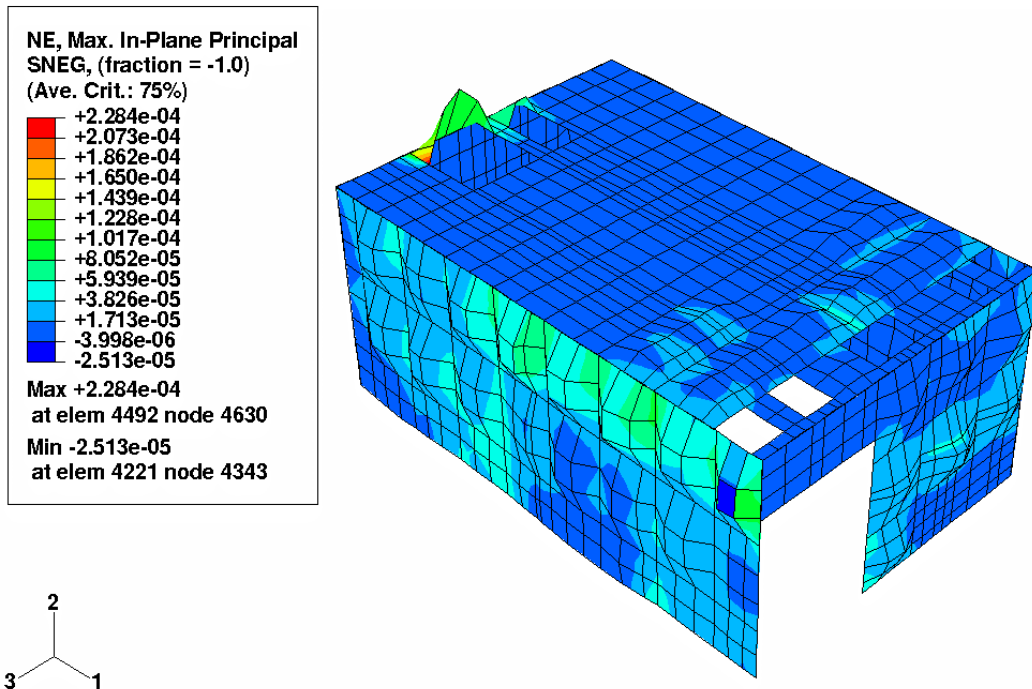


Fig. 8g: Maximum In-Plane Strain in Inner Corrugated Wall Group at Ceiling for 2 gm Hydrogen Combustion Experiment (at 140 m Sec)

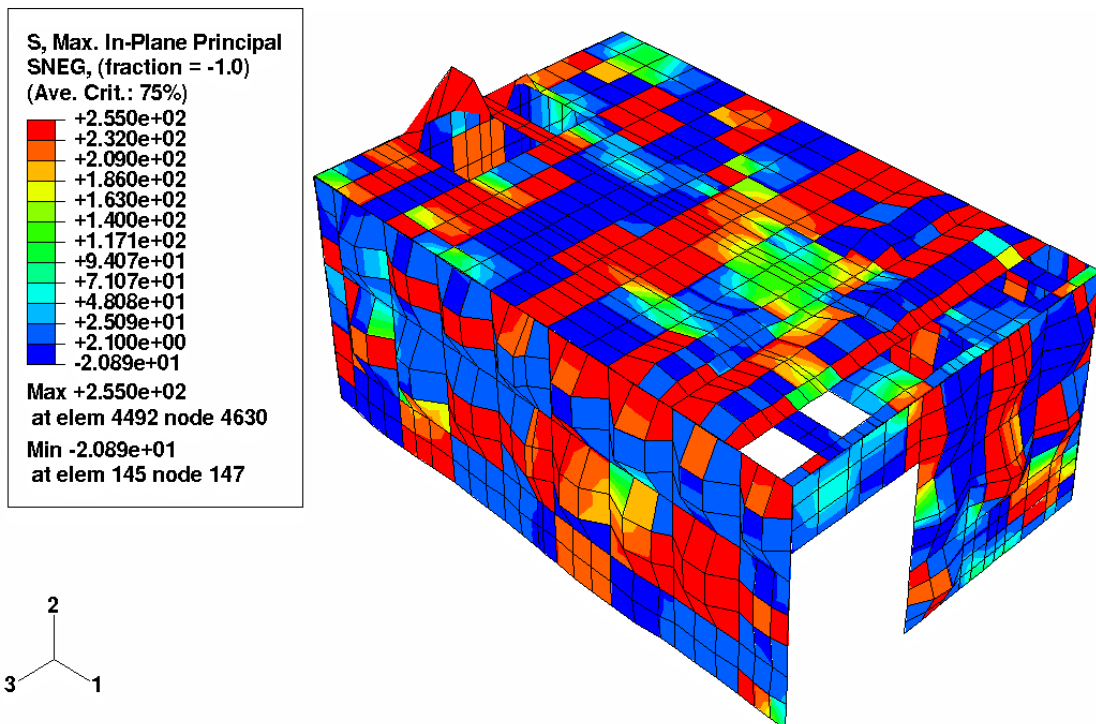


Fig. 8h: Maximum In-Plane Stress (MPa) in Inner Corrugated Wall Group at Ceiling Wall for 2 gm Hydrogen Combustion Experiment (at 139.1 m Sec)

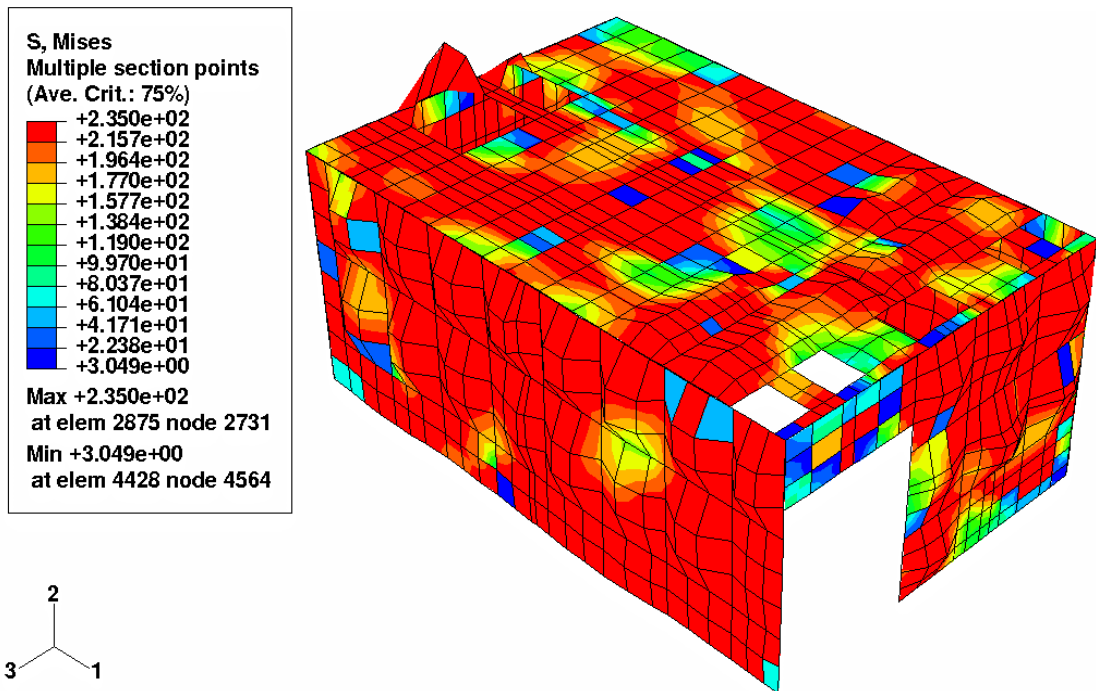


Fig. 8i: Maximum In-Plane von Mises Stress (MPa) in Inner Corrugated Wall Group at Front Wall for 2 gm Hydrogen Combustion Experiment (at 139.1 m Sec)

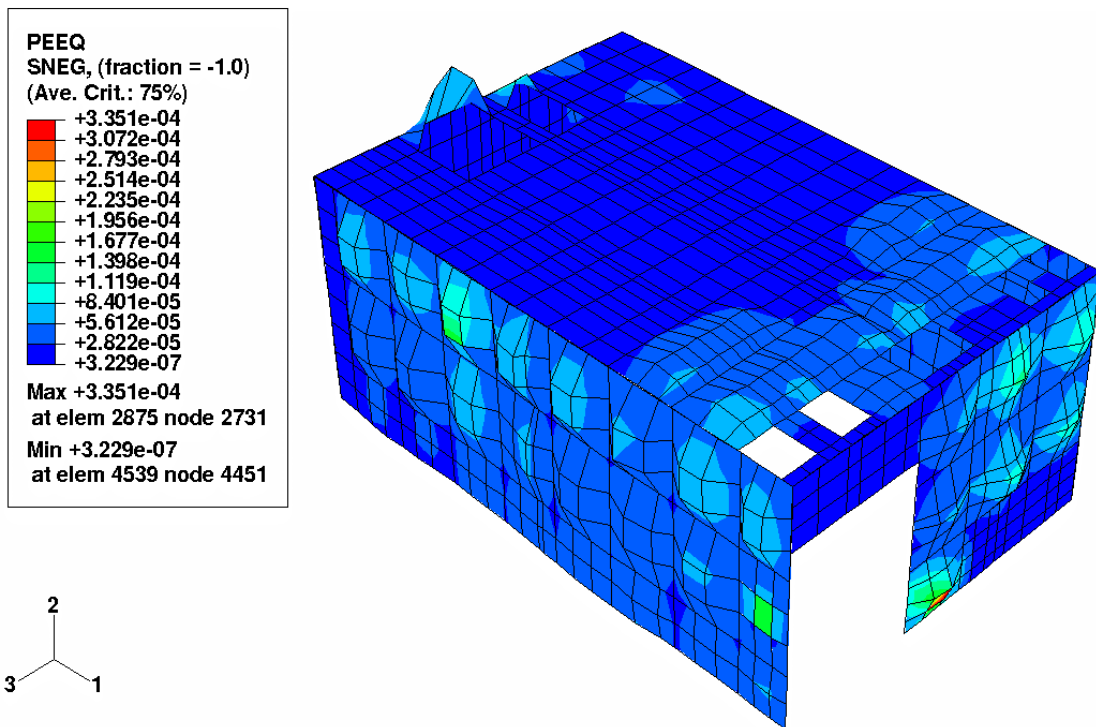


Fig. 8j: Maximum In-Plane Effective Plastic Strain in Inner Corrugated Wall Group at Front Wall for 2 gm Hydrogen Combustion Experiment (at 140 m Sec)

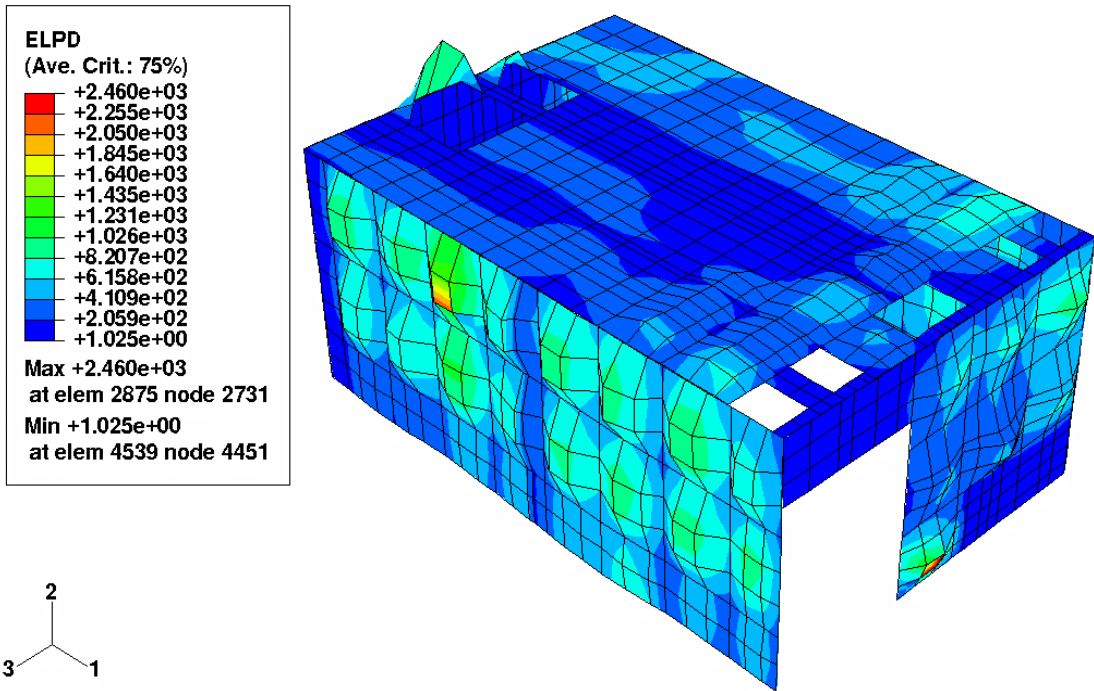


Fig. 8k: Maximum Plastic Energy (mJ) in Inner Corrugated Wall Group at Front Wall for 2 gm Hydrogen Combustion Experiment (at 140 m Sec)

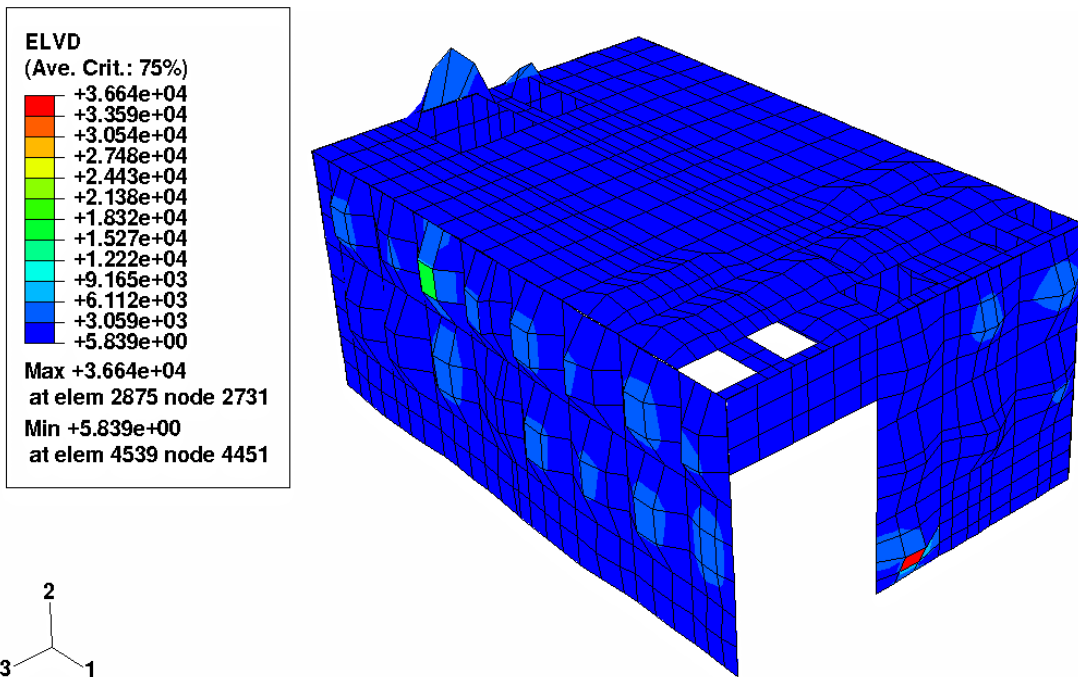


Fig. 8l: Maximum Viscous Energy (mJ) in Inner Corrugated Wall Group at Front Wall for 2 gm Hydrogen Combustion Experiment (at 140 m Sec)

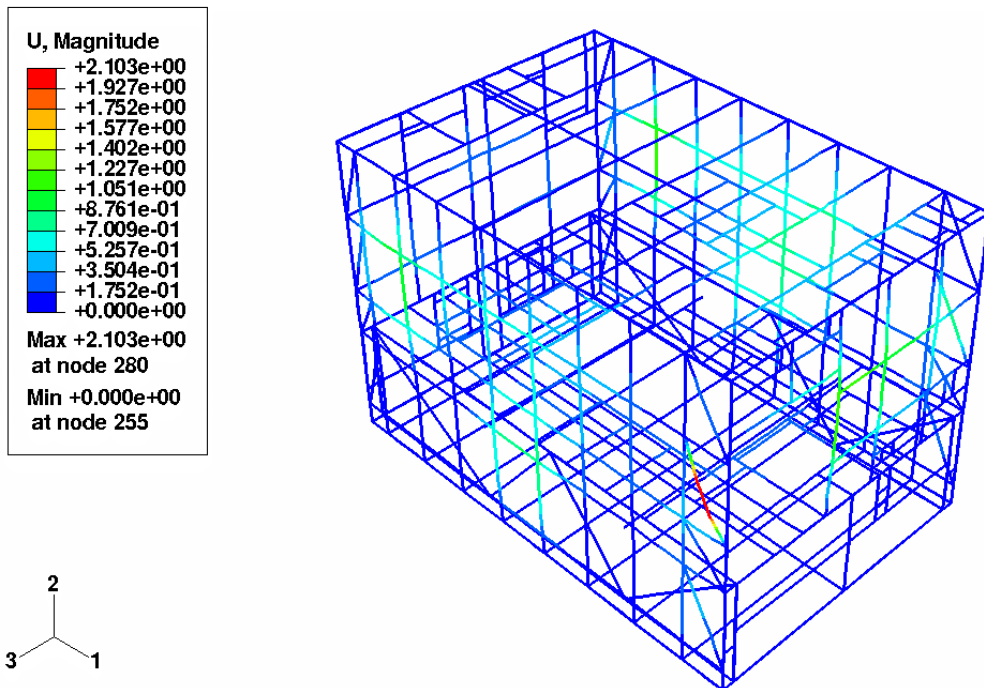


Fig. 8m: Maximum Displacement in Frame Group at Left Frame (Frame-A) for 2 gm Hydrogen Combustion Experiment (at 65.15 m Sec)

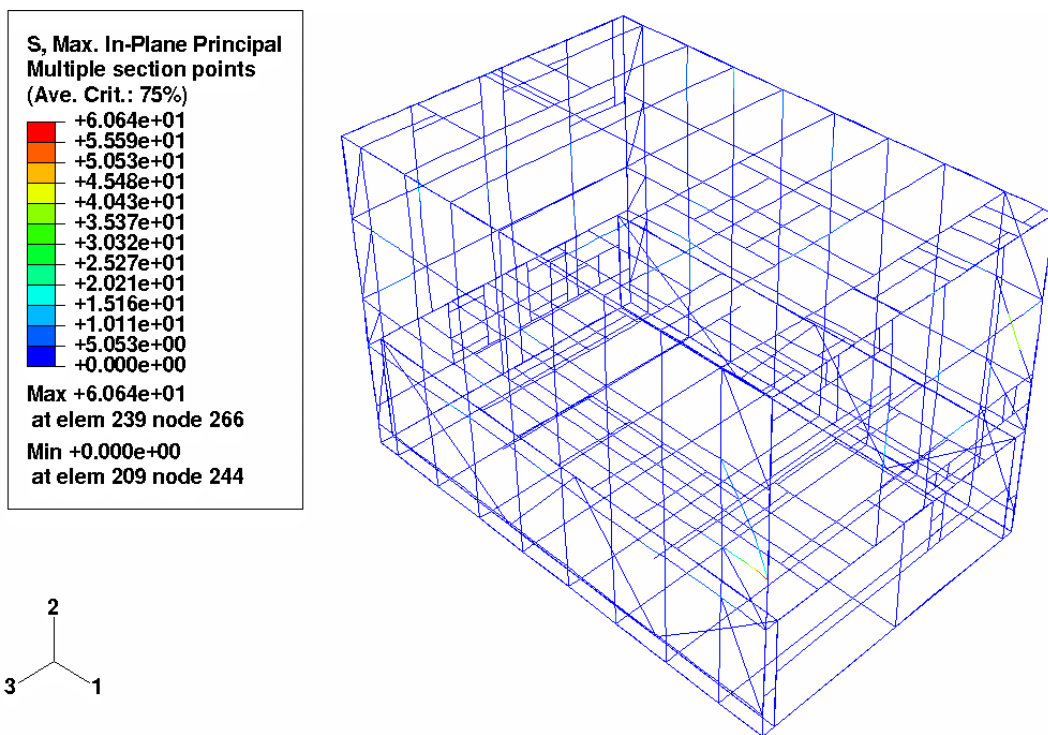


Fig. 8n: Maximum In-Plane Stress in Frame Group at Left Frame (Frame-A) for 2 gm Hydrogen Combustion Experiment (at 71.15 m Sec)

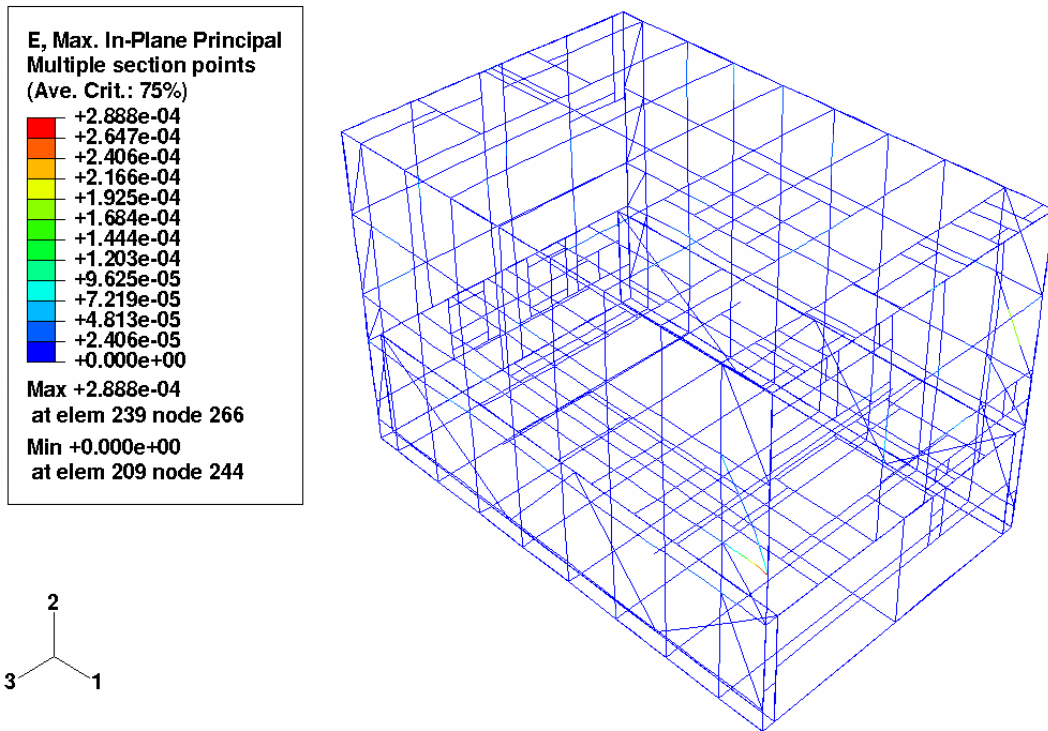


Fig. 8-o: Maximum In-Plane Strain in Frame Group at Left Frame (Frame-A) for 2 gm Hydrogen Combustion Experiment (at 71.15 m Sec)

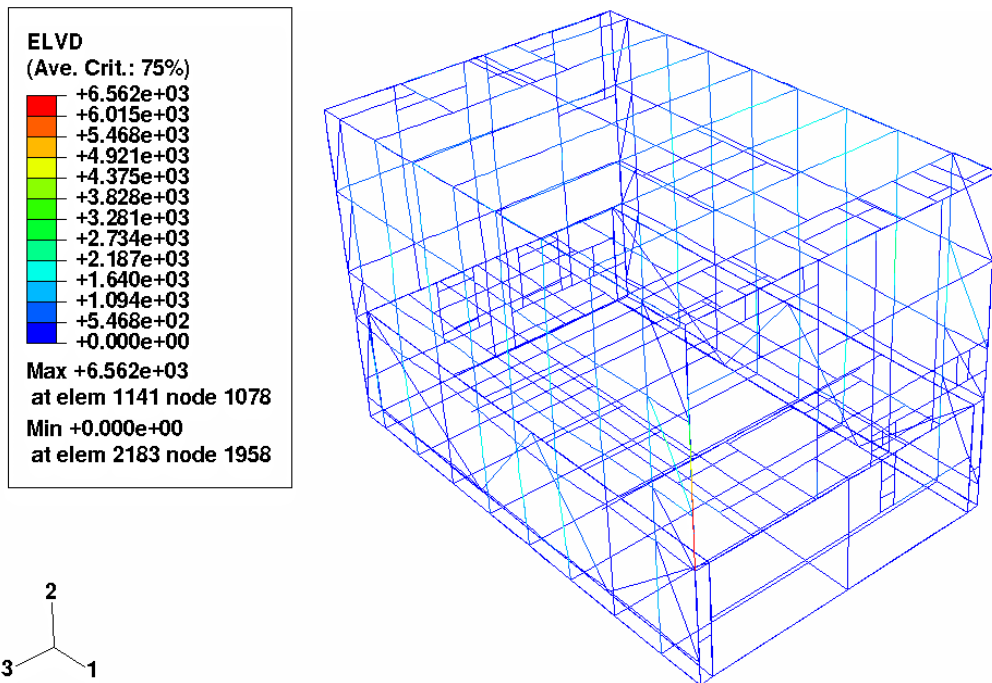


Fig. 8p: Maximum Viscous Energy (mJ) in Frame Group at Front Frame for 2 gm Hydrogen Combustion Experiment (at 140 m Sec)

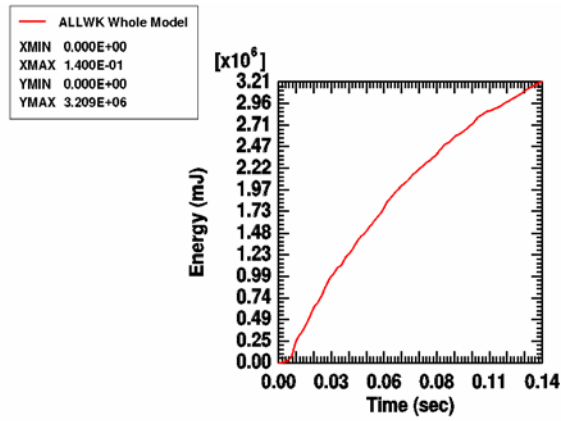


Fig. 9a: Total External Work (mJ) for 2gm Hydrogen Combustion Experiment

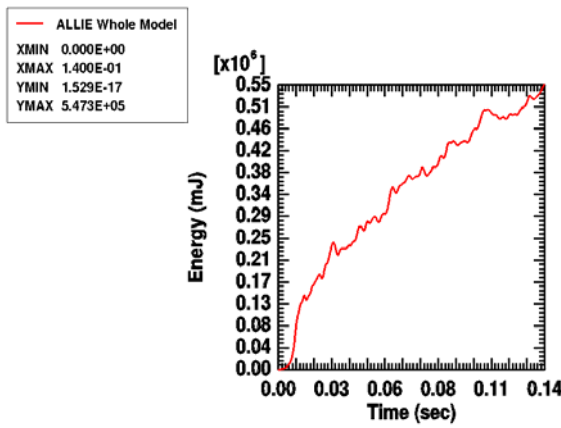


Fig. 9b: Total Internal Energy (mJ) for 2gm Hydrogen Combustion Experiment

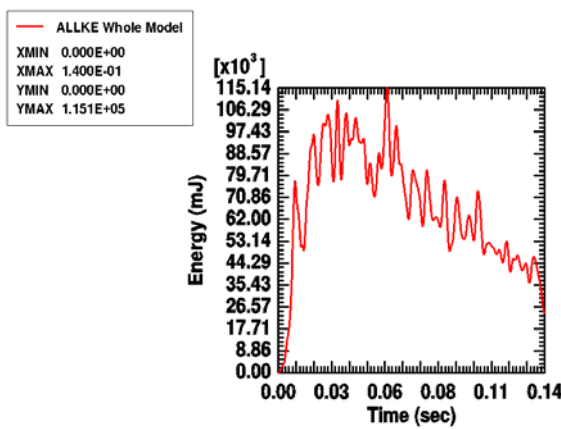


Fig. 9c: Total Kinetic Energy (mJ) for 2gm Hydrogen Combustion Experiment

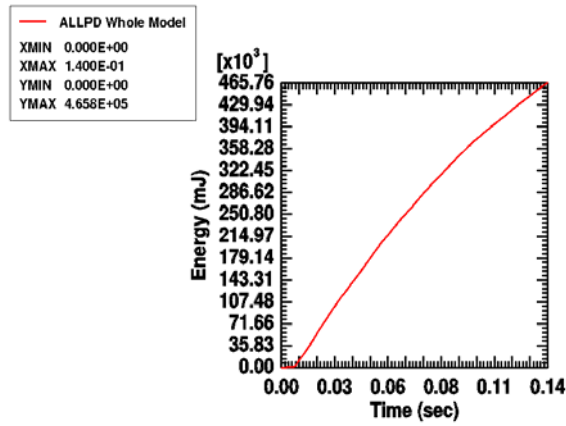


Fig. 9d: Total Plastic Energy (mJ) Dissipation for 2gm Hydrogen Combustion Experiment

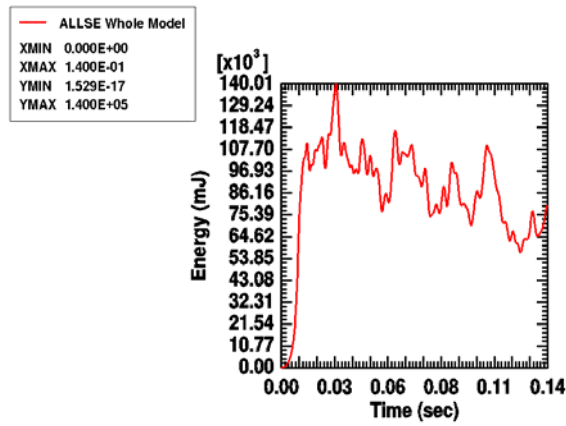


Fig. 9e: Total Strain Energy (mJ) for 2gm Hydrogen Combustion Experiment

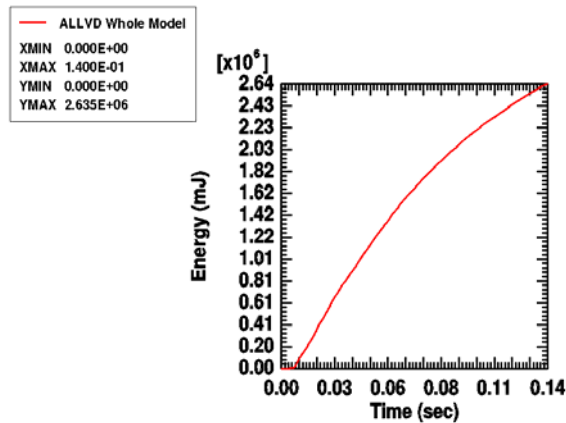


Fig. 9f: Total Viscous Energy (mJ) Dissipation for 2gm Hydrogen Combustion Experiment

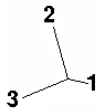
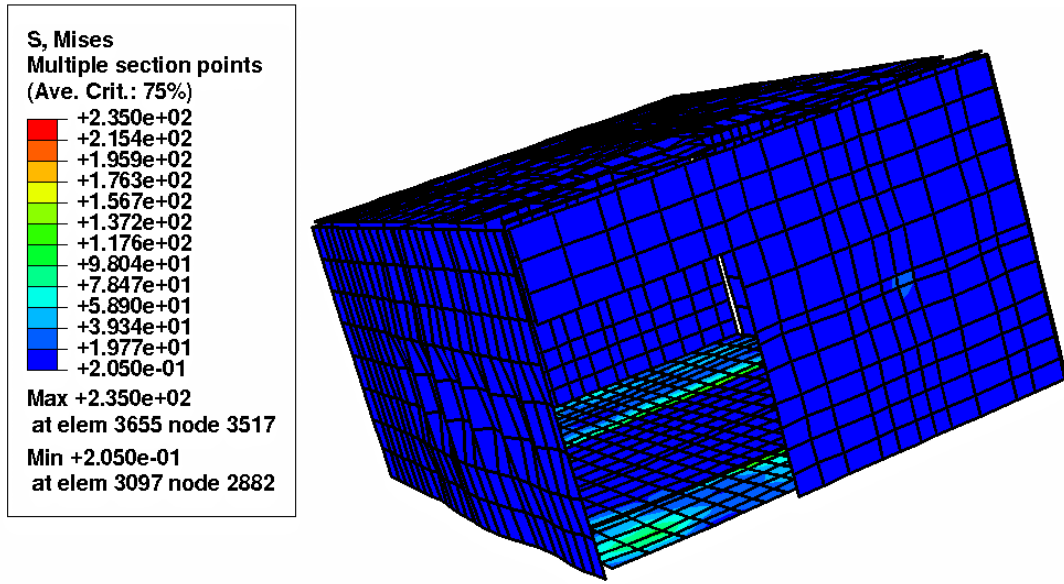


Fig. 10a: Maximum von Mises Stresses (MPa) in Outer Plate Group at Floor for 4 gm Hydrogen Combustion Experiment (at 11.15 m Sec)

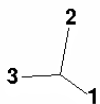
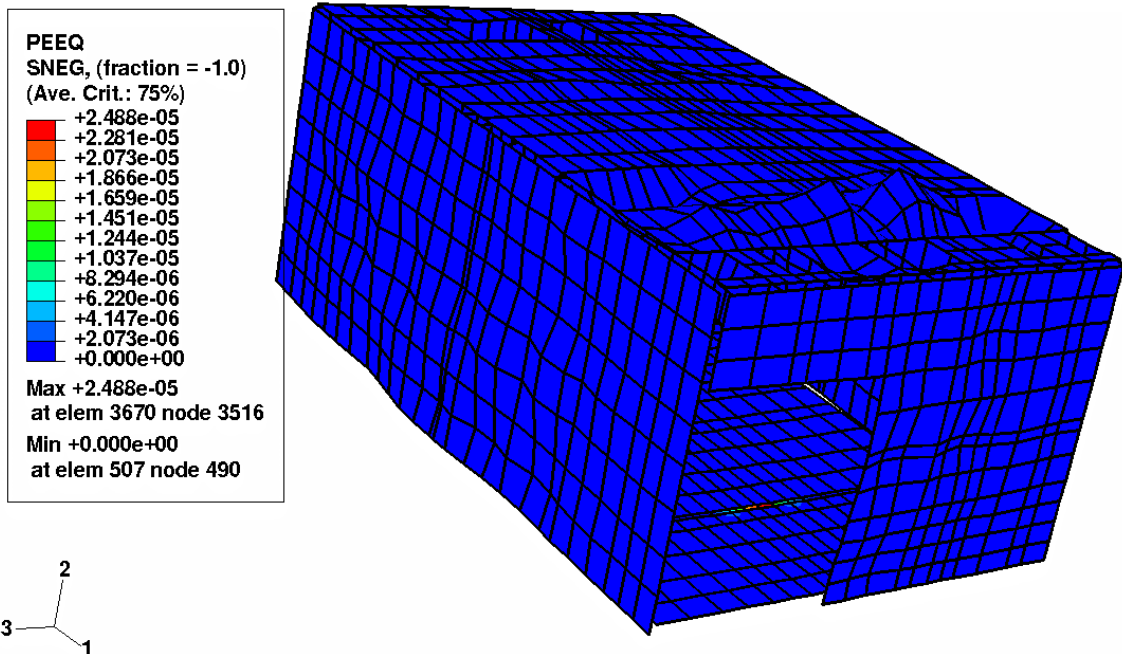


Fig. 10b: Maximum Effective Plastic Strain in Outer Plate Group at Floor for 4 gm Hydrogen Combustion Experiment (at 100 m Sec)

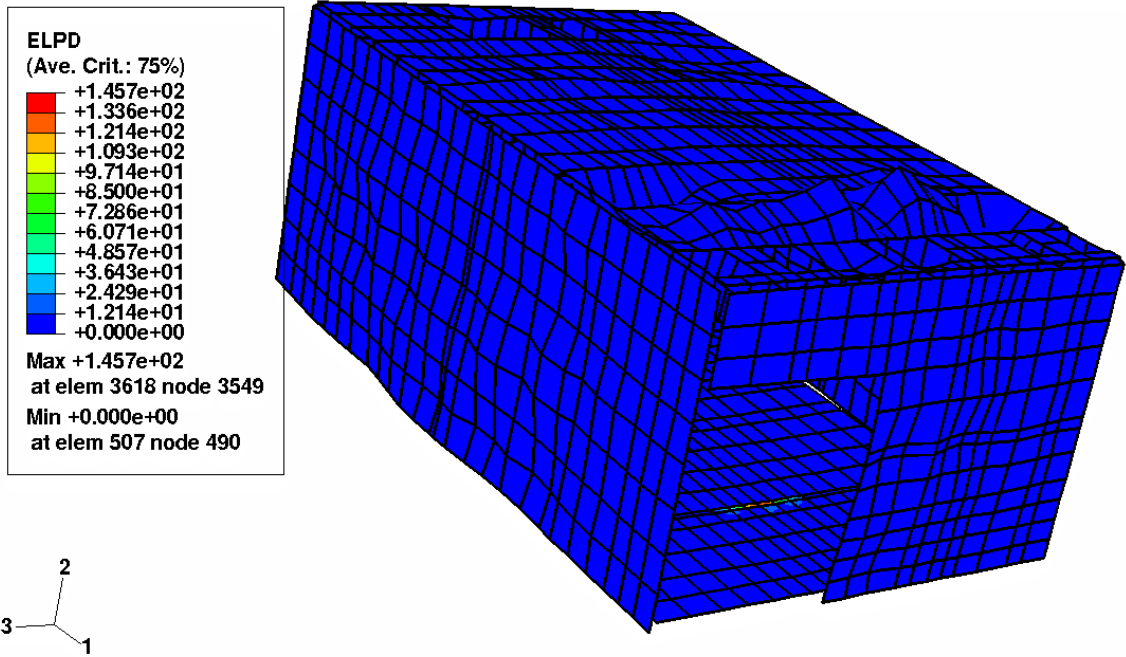


Fig. 10c: Maximum Plastic Energy (mJ) in Outer Plate Group at Floor for 4 gm Hydrogen Combustion Experiment (at 100 m Sec)

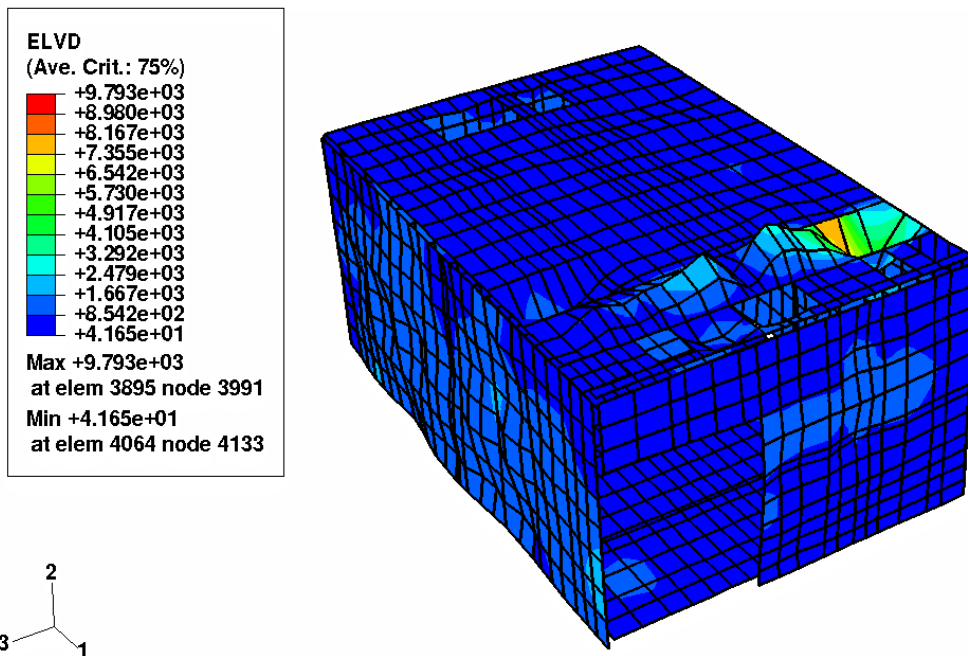


Fig. 10d: Maximum Viscous Energy (mJ) in Outer Plate Group at Ceiling Plate for 4 gm Hydrogen Combustion Experiment (at 100 m Sec)

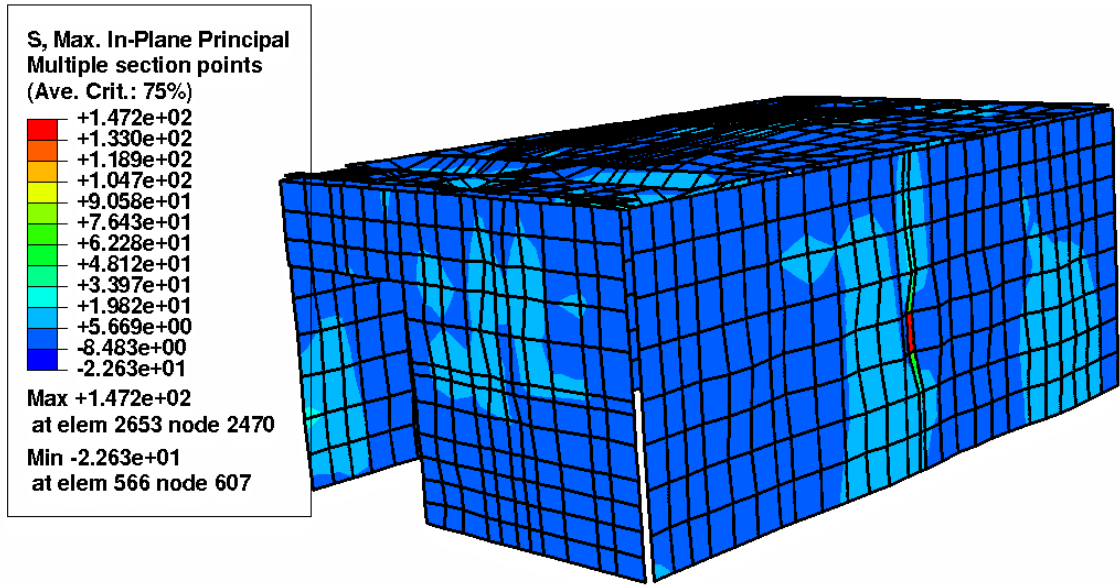


Fig. 10e: Maximum In-Plane Stress (MPa) in Outer Plate Group at Right Wall for 4 gm Hydrogen Combustion Experiment (at 33.15 m Sec)

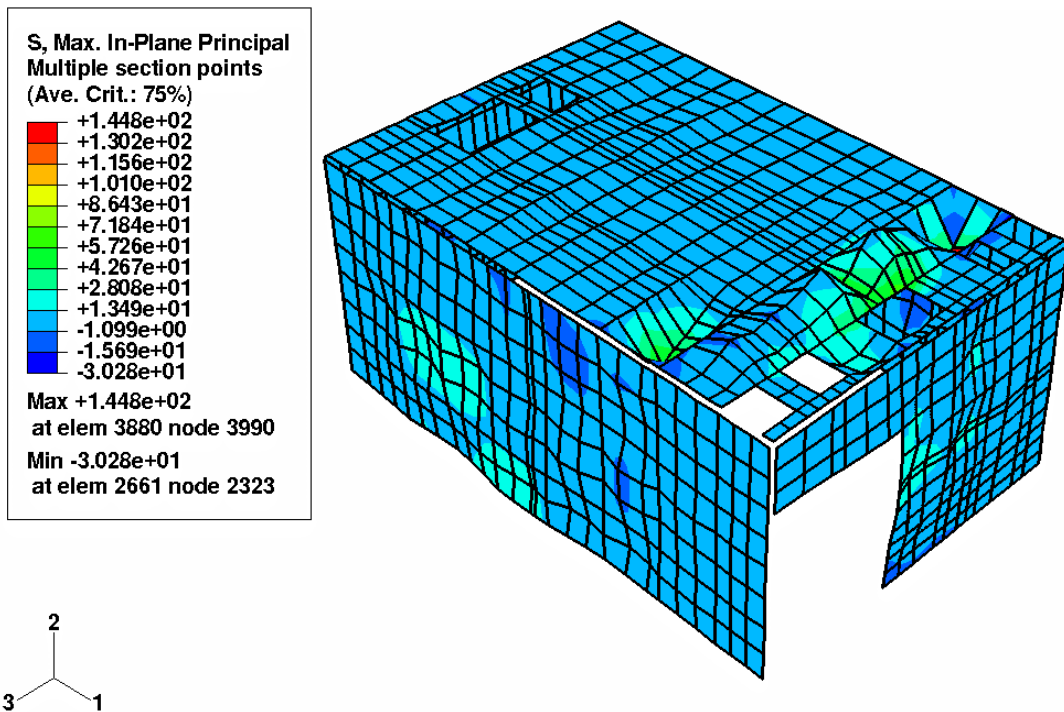


Fig. 10f: Maximum In-Plane Stress (MPa) in Outer Plate Group at Ceiling Wall for 4 gm Hydrogen Combustion Experiment (at 100 m Sec)

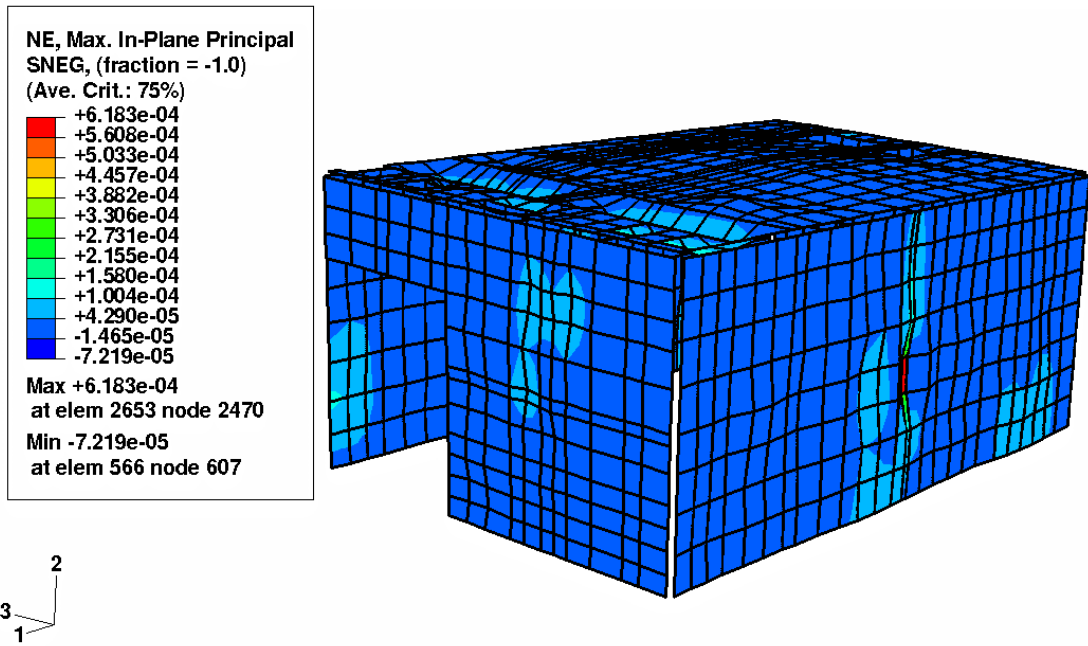


Fig. 10g: Maximum In-Plane Strain in Outer Plate Group at Right Plate for 4 gm Hydrogen Combustion Experiment (at 33.15 m Sec)

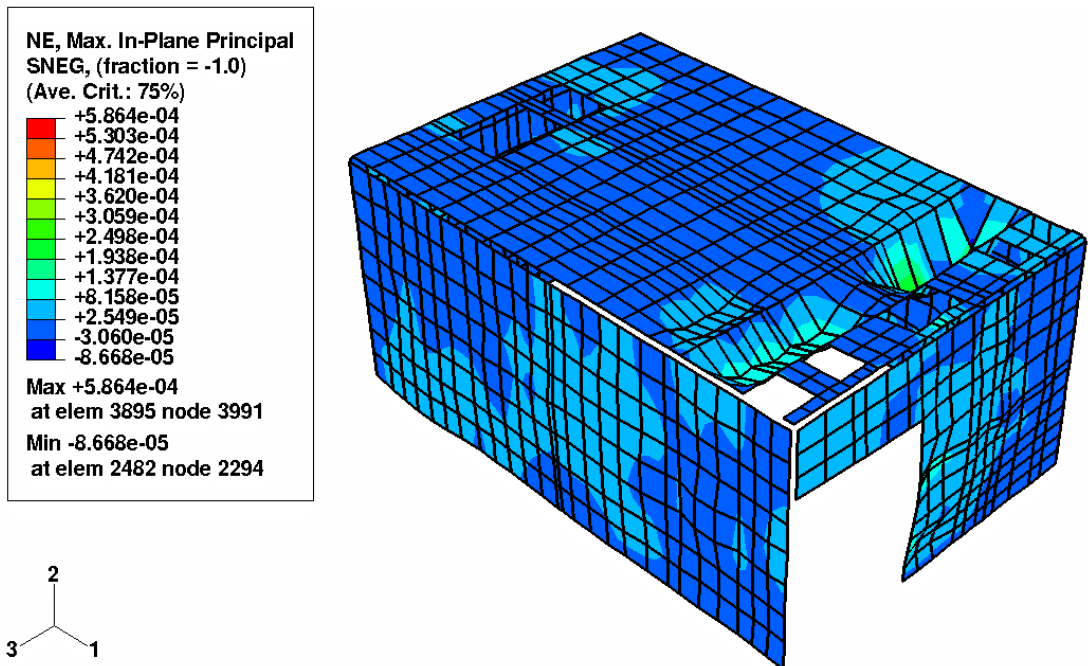


Fig. 10h: Maximum In-Plane Strain in Outer Plate Group at Ceiling for 4 gm Hydrogen Combustion Experiment (at 67.15 m Sec)

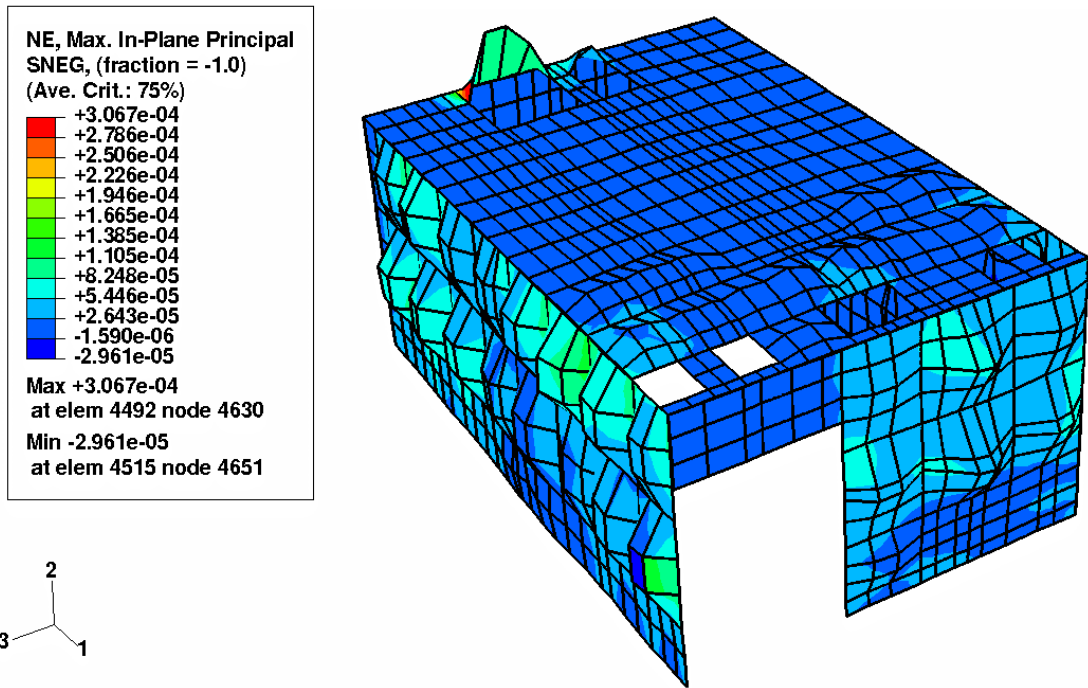


Fig. 10i: Maximum In-Plane Strain in Inner Corrugated Wall Group at Ceiling for 4 gm Hydrogen Combustion Experiment (at 93.15 m Sec)

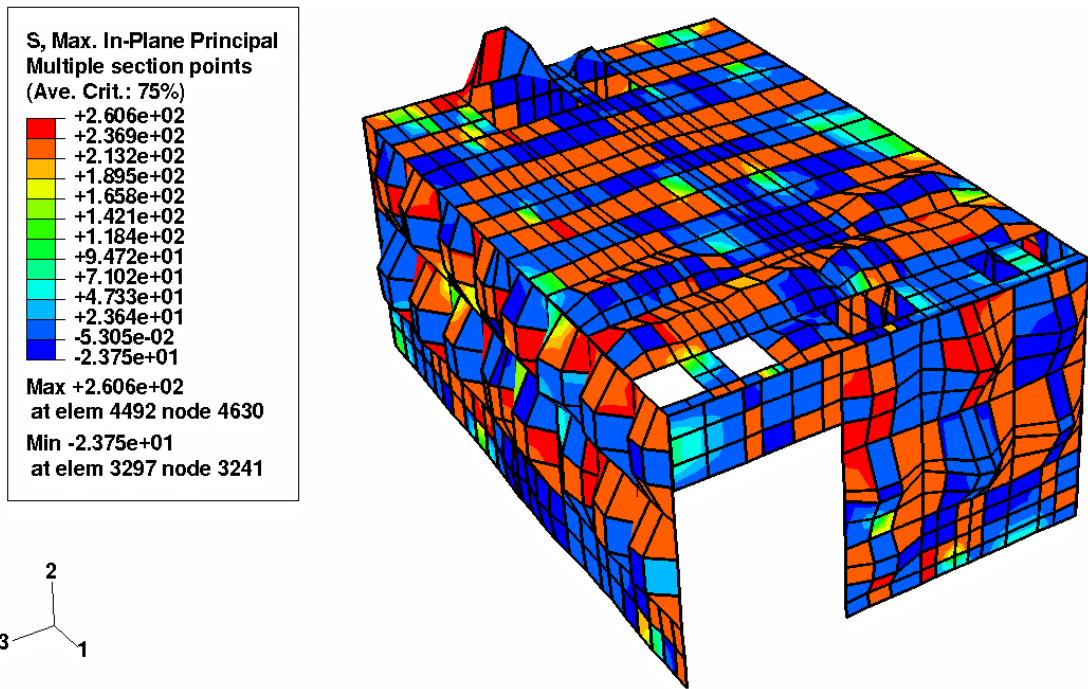


Fig. 10j: Maximum In-Plane Stress (MPa) in Inner Corrugated Wall Group at Ceiling Wall for 4 gm Hydrogen Combustion Experiment (at 93.15 m Sec)

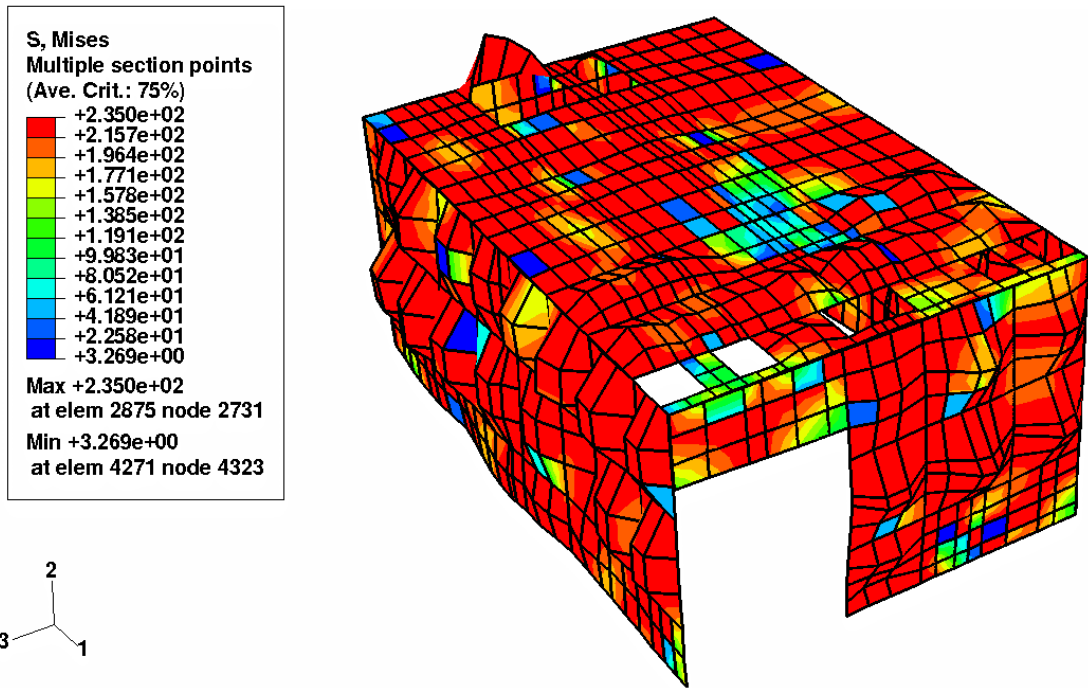


Fig. 10k: Maximum In-Plane von Mises Stress (MPa) in Inner Corrugated Wall Group at Front Wall for 4 gm Hydrogen Combustion Experiment (at 100 m Sec)

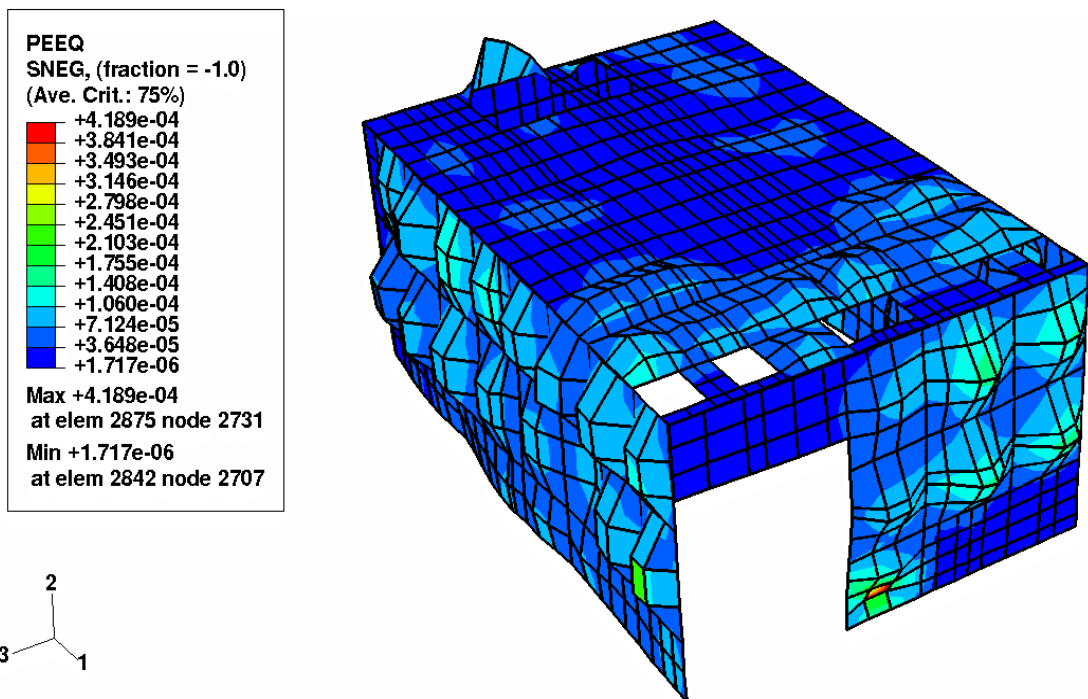


Fig. 10l: Maximum In-Plane Effective Plastic Strain in Inner Corrugated Wall Group at Front Wall for 4 gm Hydrogen Combustion Experiment (at 93.15 m Sec)

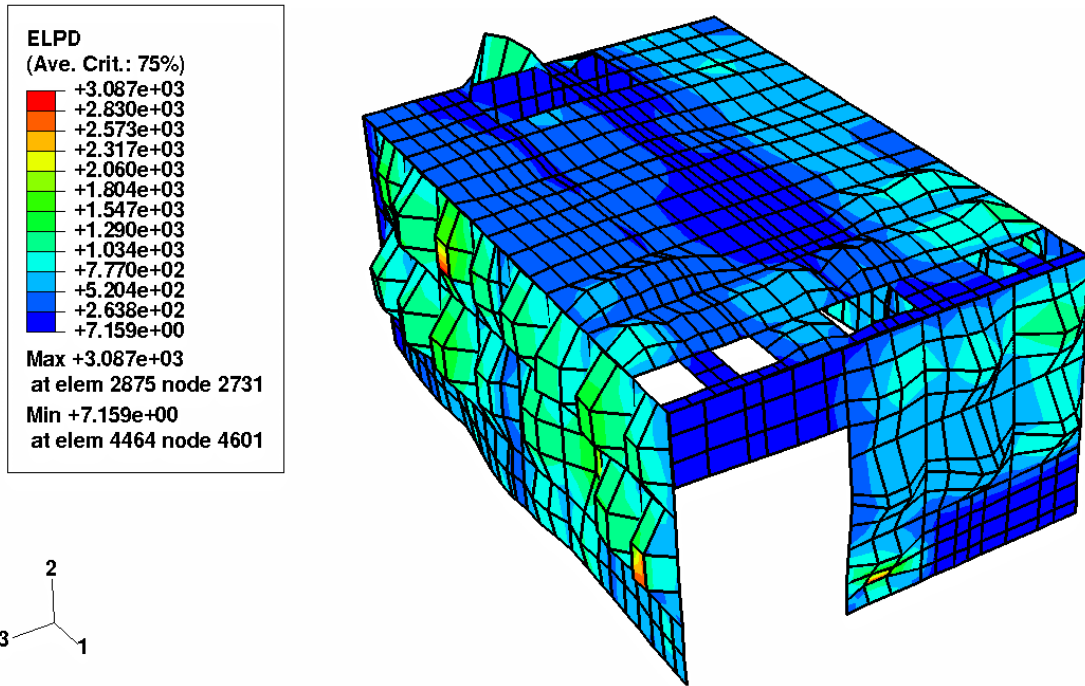


Fig. 10m: Maximum Plastic Energy (mJ) in Inner Corrugated Wall Group at Front Wall for 4 gm Hydrogen Combustion Experiment (at 100 m Sec)

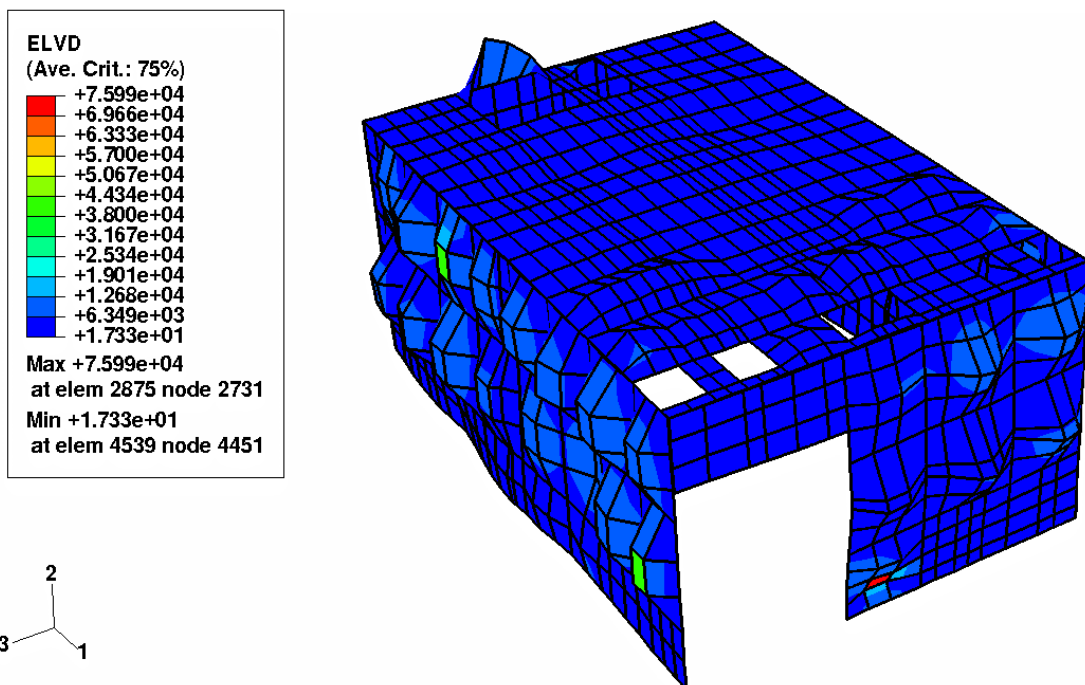


Fig. 10n: Maximum Viscous Energy (mJ) in Inner Corrugated Wall Group at Front Wall for 4 gm Hydrogen Combustion Experiment (at 100 m Sec)

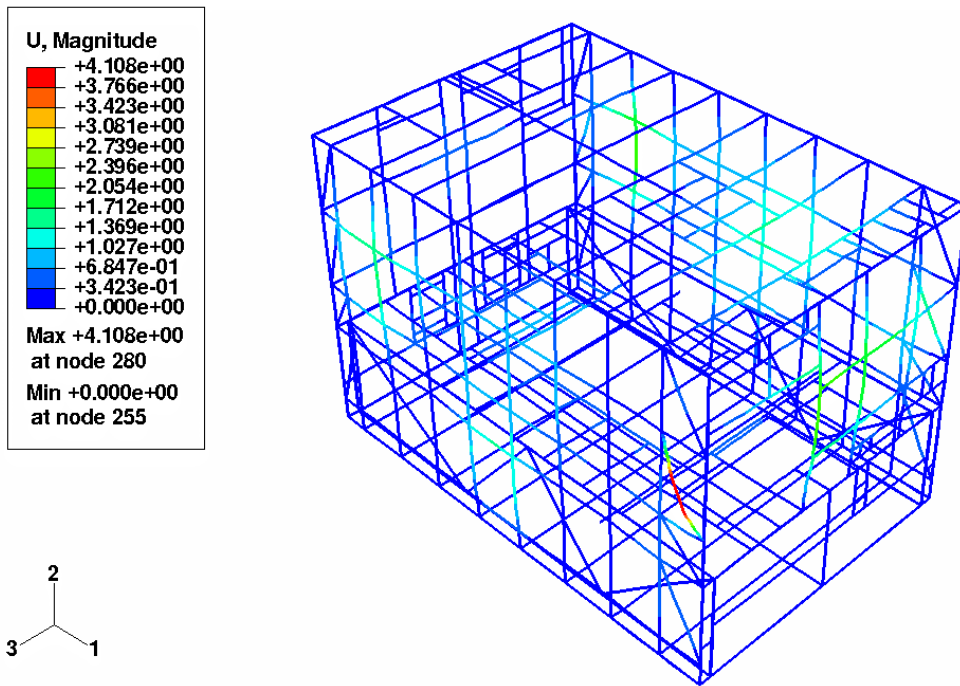


Fig. 10-o: Maximum Displacement in Frame Group at Left Frame (Frame-A) for 4 gm Hydrogen Combustion Experiment (at 65.15 m Sec)

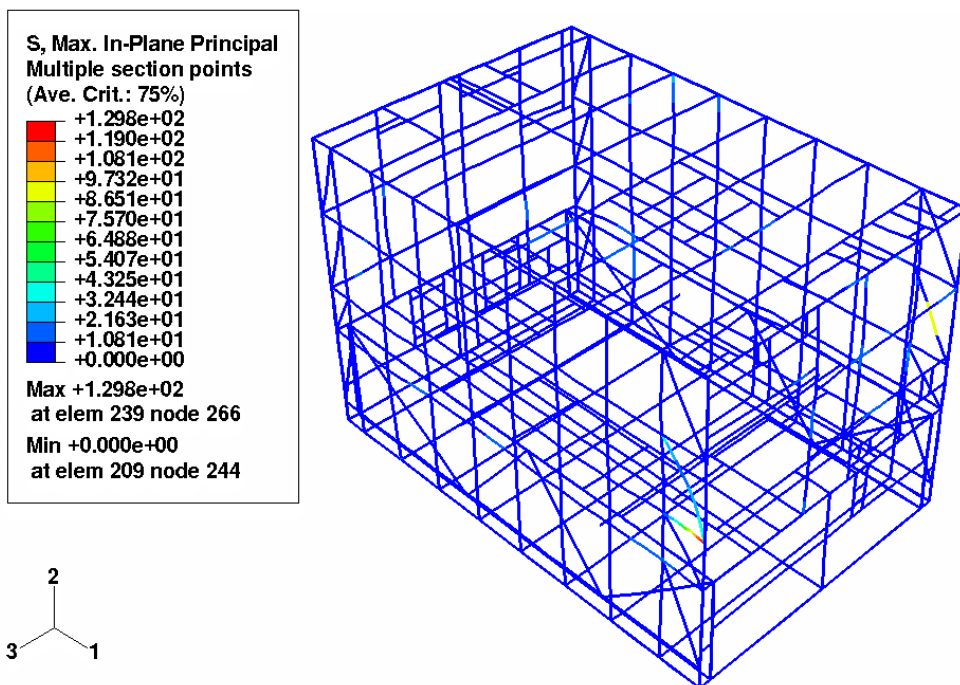


Fig. 10p: Maximum In-Plane Stress in Frame Group at Left Frame (Frame-A) for 4 gm Hydrogen Combustion Experiment (at 71.15 m Sec)

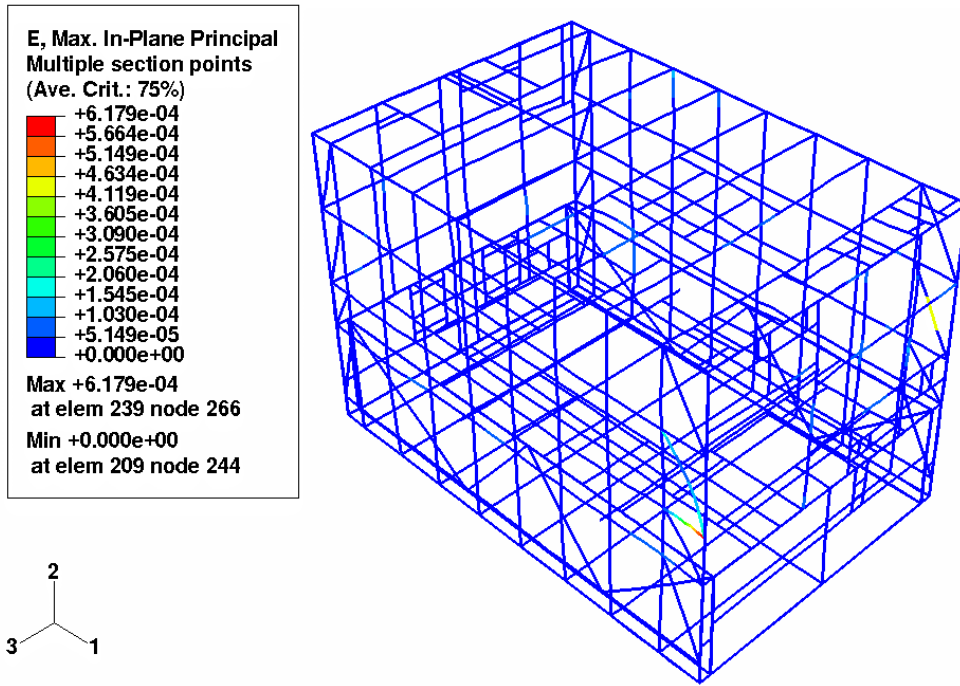


Fig. 10q: Maximum In-Plane Strain in Frame Group at Left Frame (Frame-A) for 4 gm Hydrogen Combustion Experiment (at 71.15 m Sec)

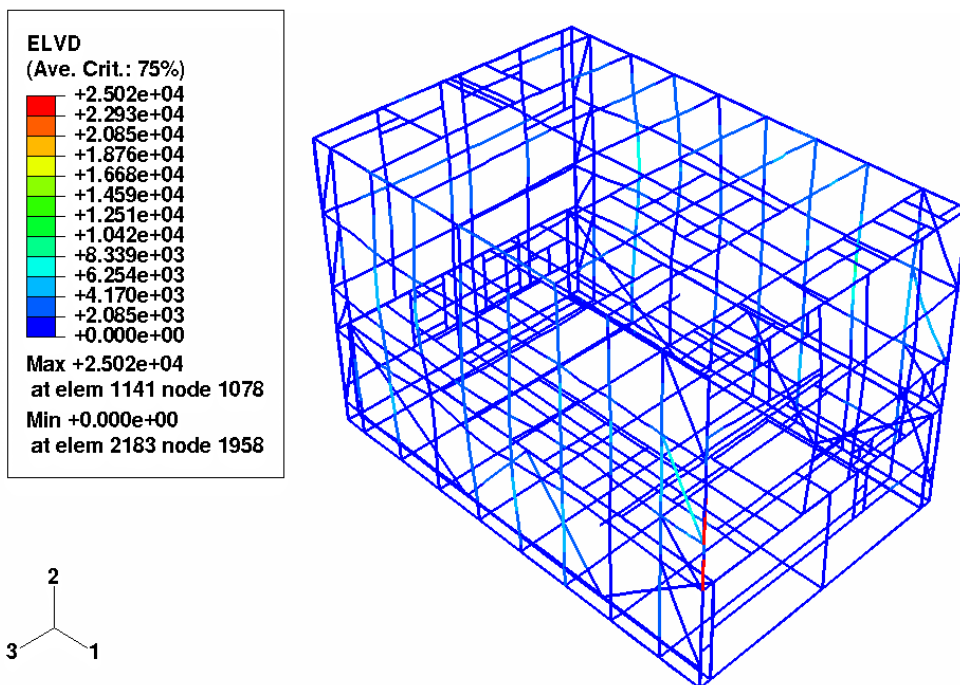


Fig. 10r: Maximum Viscous Energy (mJ) in Frame Group at Front Frame for 4 gm Hydrogen Combustion Experiment (at 100 m Sec)

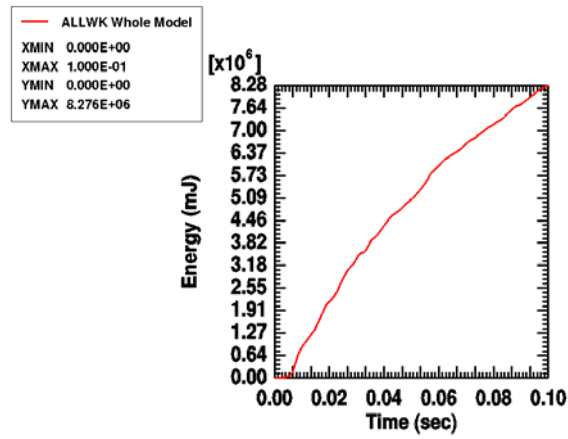


Fig. 11a: Total External Work (mJ) for 4 gm Hydrogen Combustion Experiment

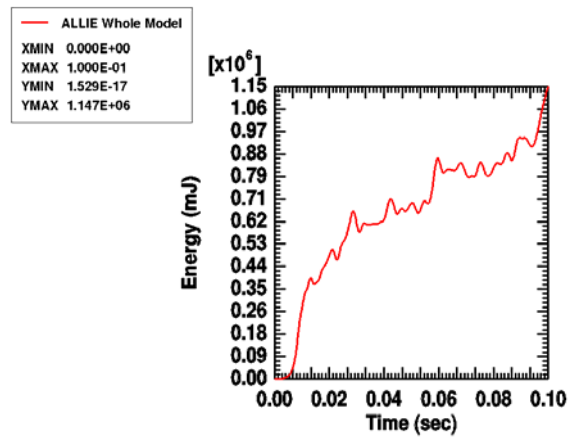


Fig. 11b: Total Internal Energy (mJ) for 4 gm Hydrogen Combustion Experiment

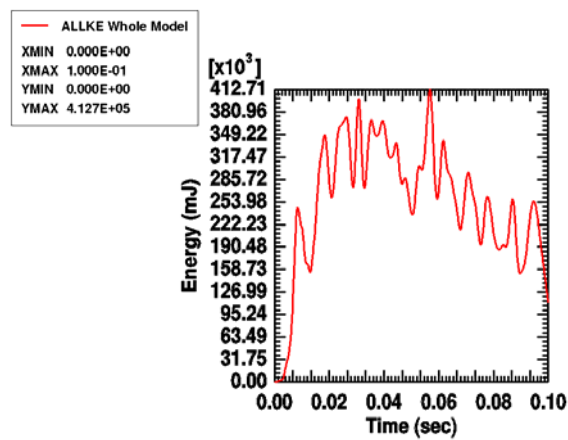


Fig. 11c: Total Kinetic Energy (mJ) for 4 gm Hydrogen Combustion Experiment

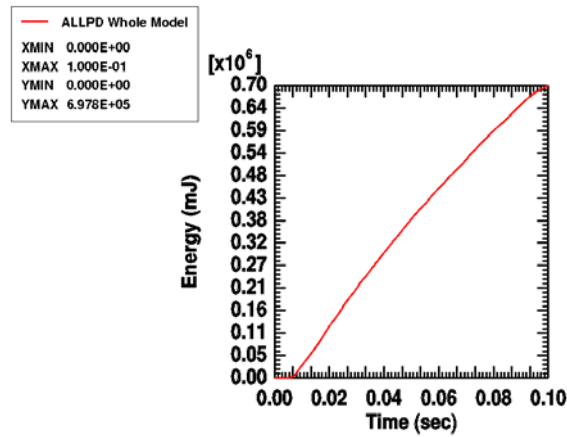


Fig. 11d: Total Plastic Energy (mJ) Dissipation for 4 gm Hydrogen Combustion Experiment

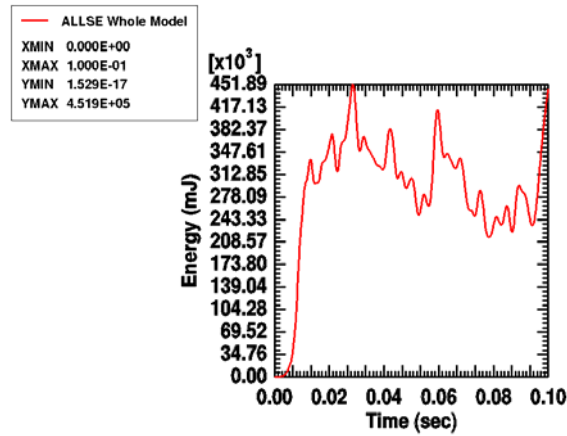


Fig. 11e: Total Strain Energy (mJ) for 4 gm Hydrogen Combustion Experiment

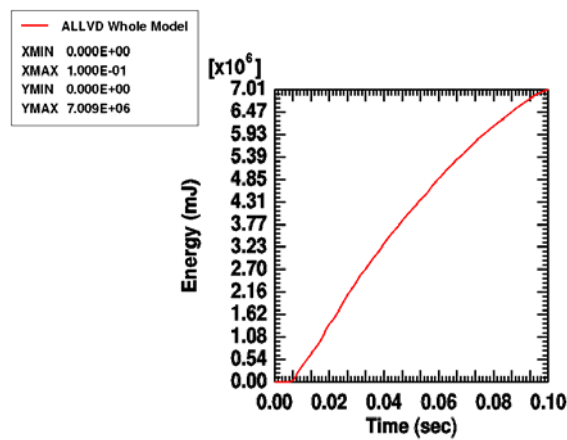


Fig. 11f: Total Viscous Energy (mJ) Dissipation for 4 gm Hydrogen Combustion Experiment

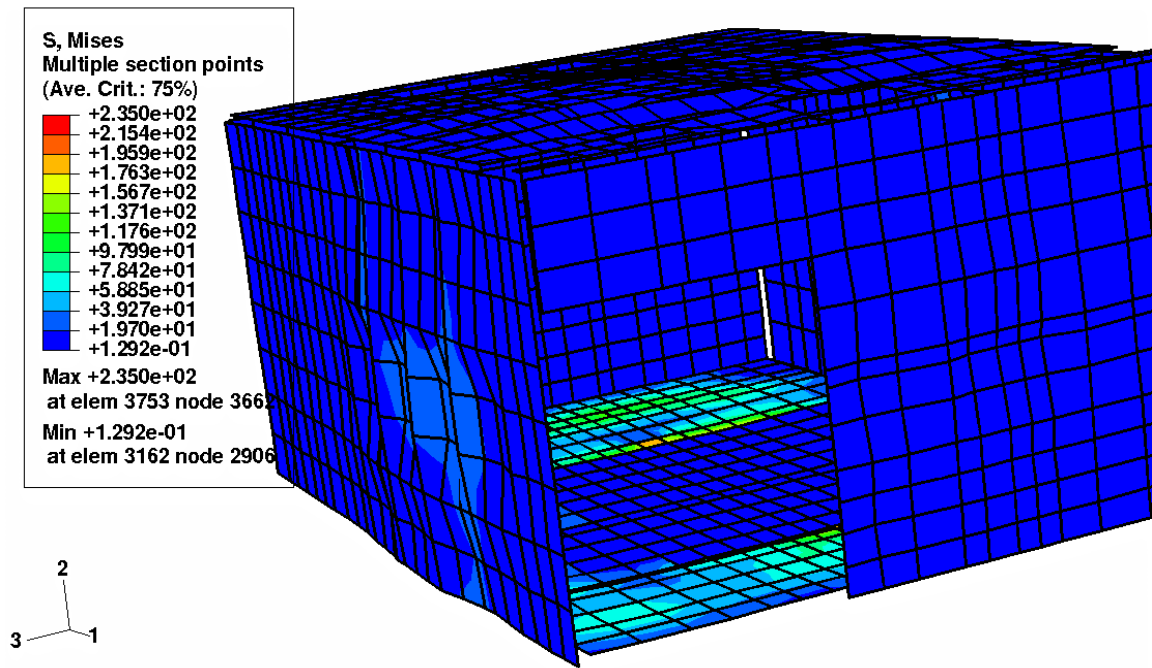


Fig. 12a: Maximum von Mises Stresses (MPa) in Outer Plate Group at Floor for 8 gm Hydrogen Combustion Experiment (at 9.15 m Sec)

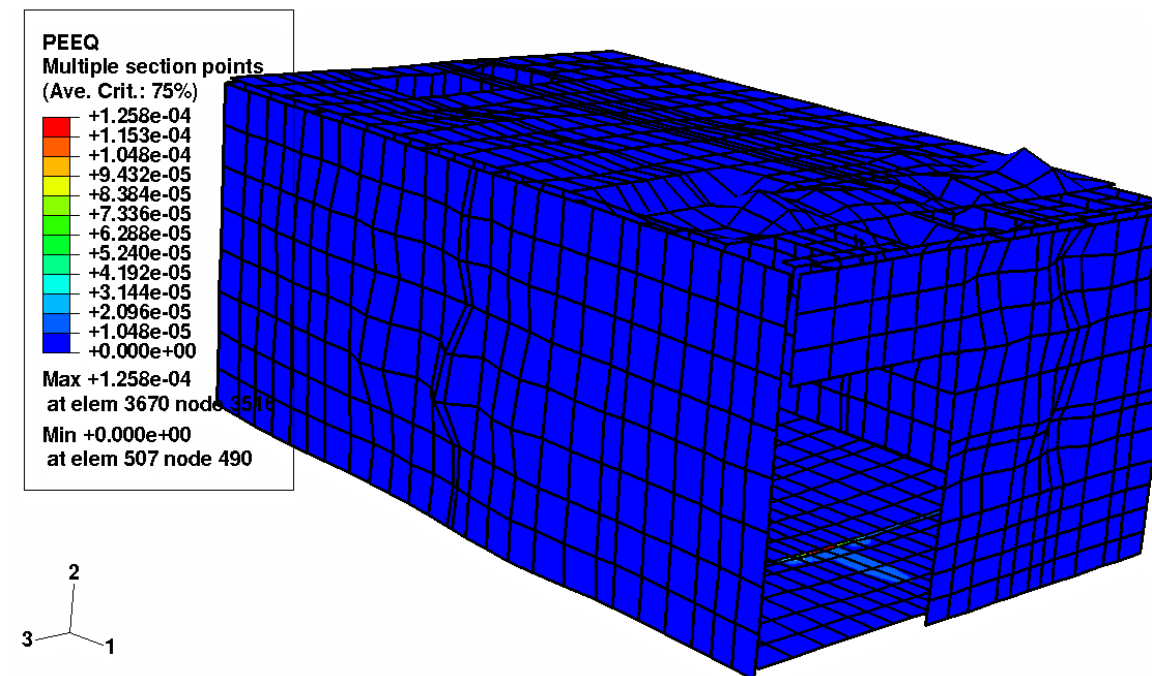


Fig. 12b: Maximum Effective Plastic Strain in Outer Plate Group at Floor for 8 gm Hydrogen Combustion Experiment (at 140 m Sec)

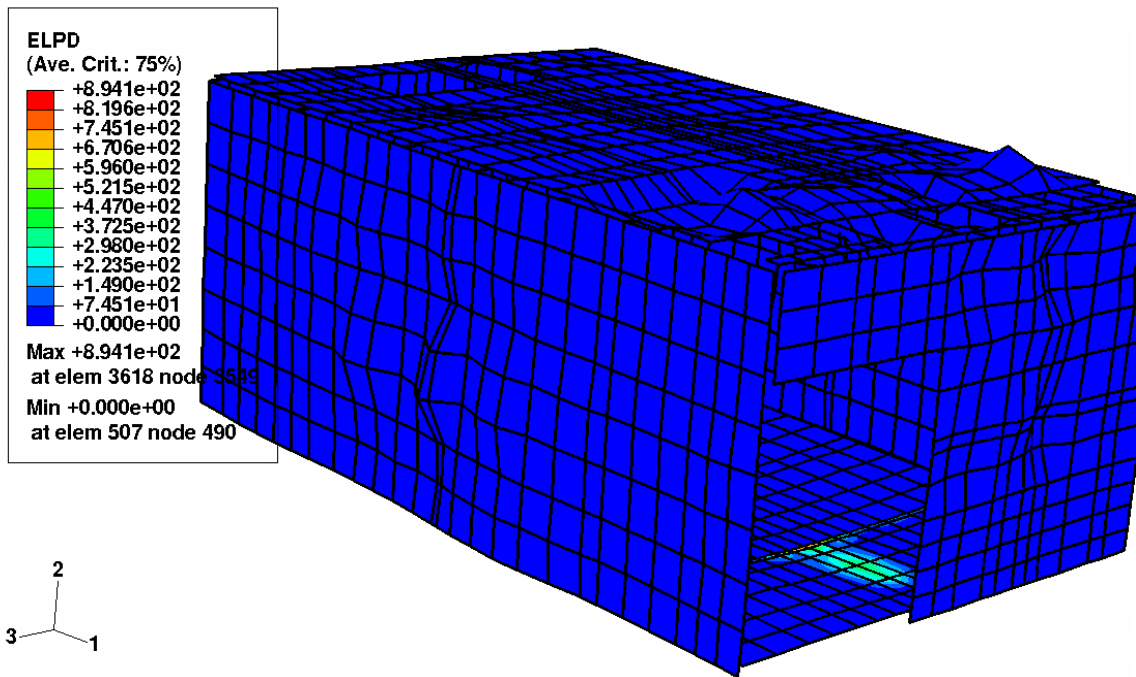


Fig. 12c: Maximum Plastic Energy (mJ) in Outer Plate Group at Floor for 8 gm Hydrogen Combustion Experiment (at 140 m Sec)

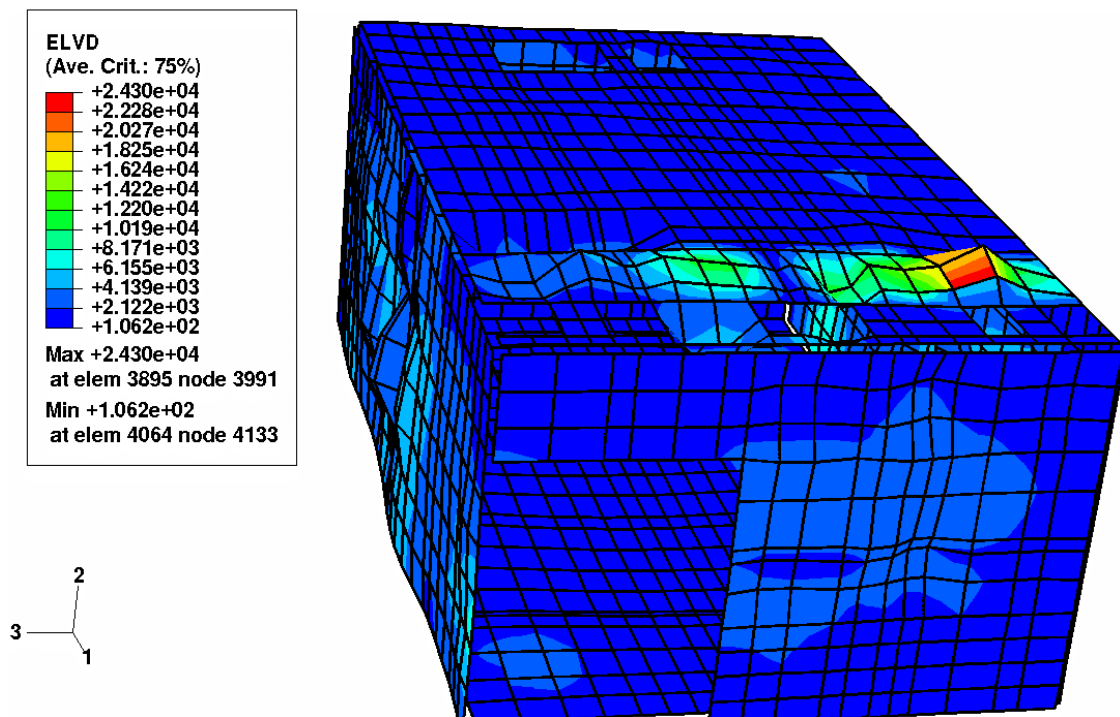


Fig. 12d: Maximum Viscous Energy (mJ) in Outer Plate Group at Ceiling Plate for 8 gm Hydrogen Combustion Experiment (at 140 m Sec)

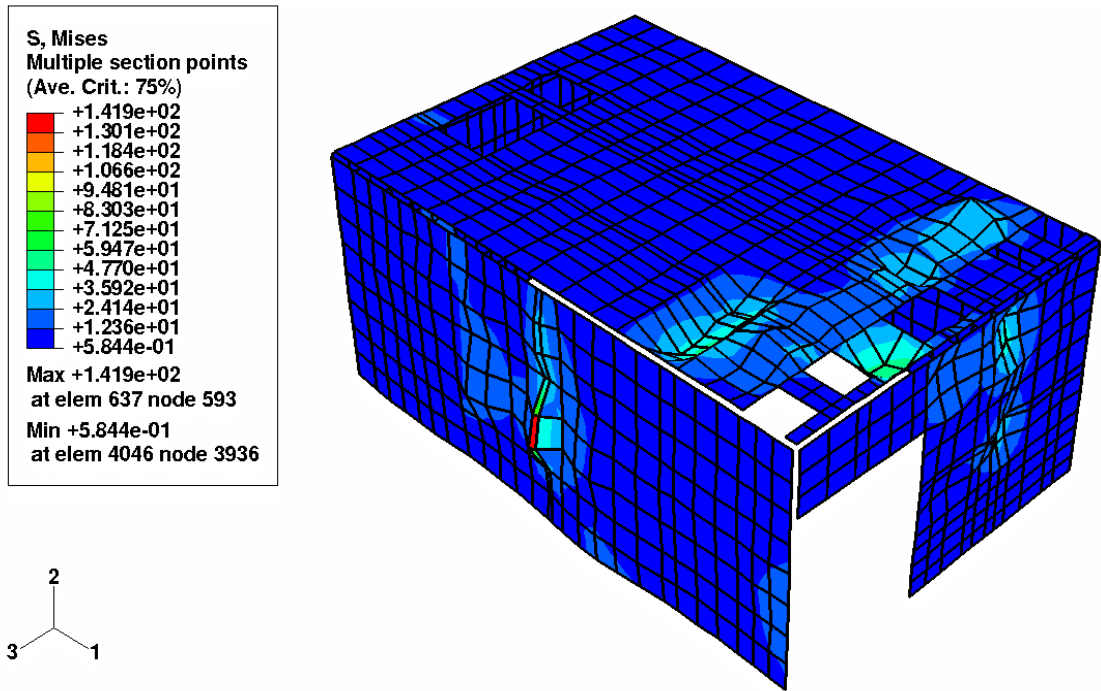


Fig. 12e: Maximum von Mises Stress (MPa) in Outer Plate Group at Left Wall for 8 gm Hydrogen Combustion Experiment (at 140 m Sec)

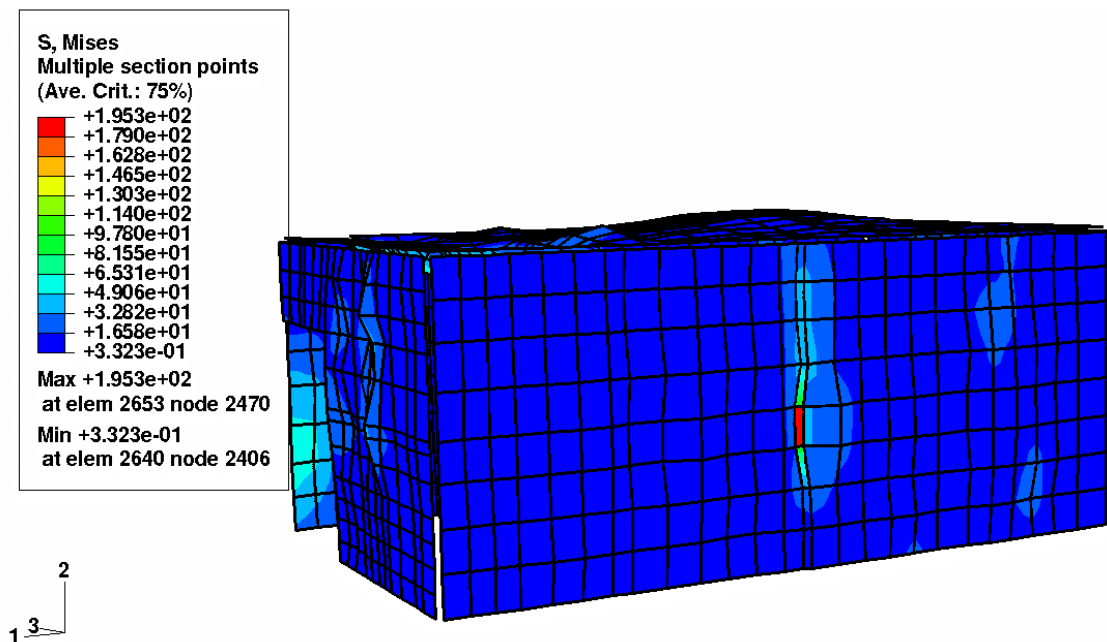


Fig. 12f: Maximum von Mises Stress (MPa) in Outer Plate Group at Right Wall for 8 gm Hydrogen Combustion Experiment (at 31.15 m Sec)

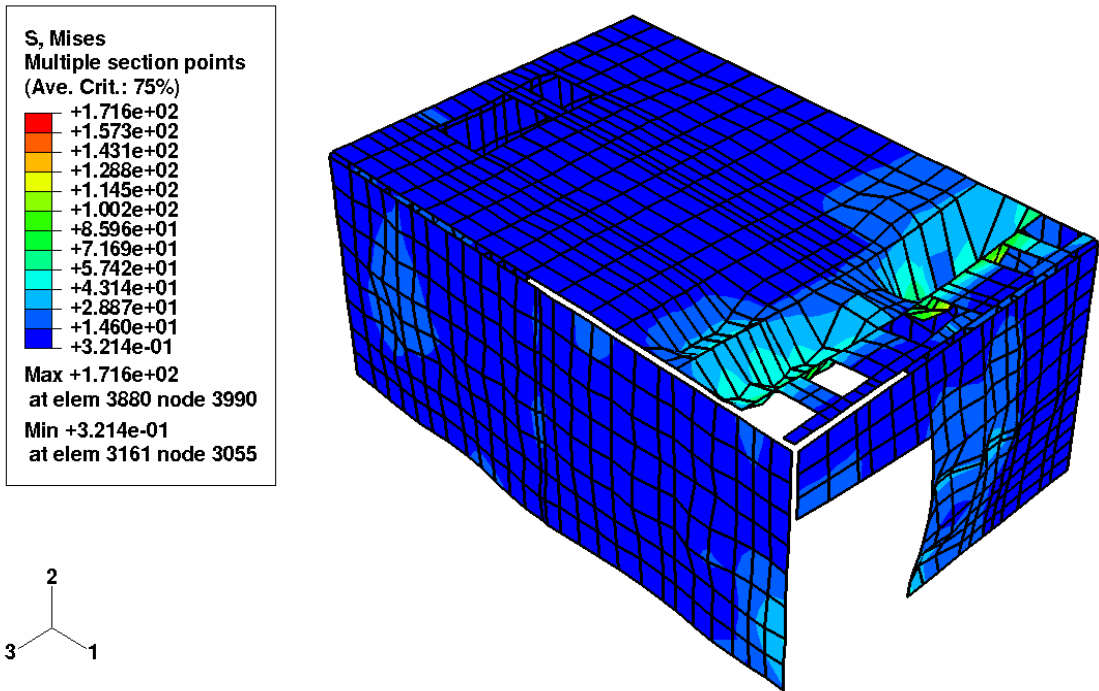


Fig. 12g: Maximum In-Plane Stress (MPa) in Outer Plate Group at Ceiling Wall for 8 gm Hydrogen Combustion Experiment (at 65.15 m Sec)

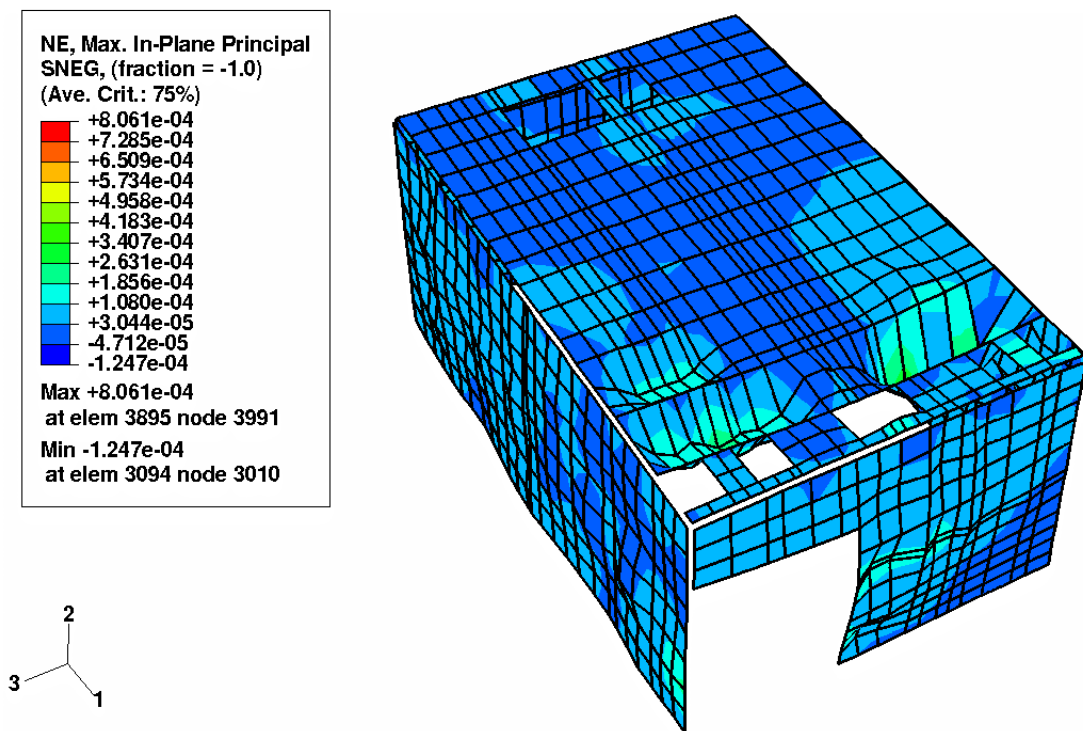


Fig. 12h: Maximum In-Plane Strain in Outer Plate Group at Ceiling for 8 gm Hydrogen Combustion Experiment (at 65.15 m Sec)

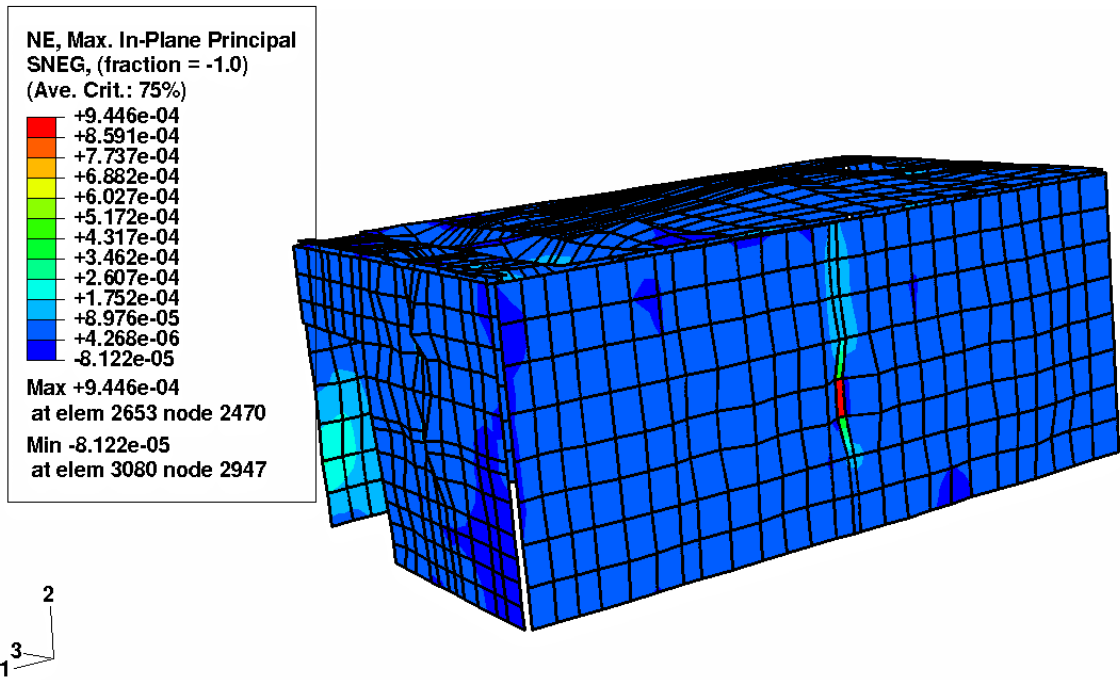


Fig. 12i: Maximum In-Plane Strain in Outer Plate Group at Right Plate for 8 gm Hydrogen Combustion Experiment (at 31.15 m Sec)

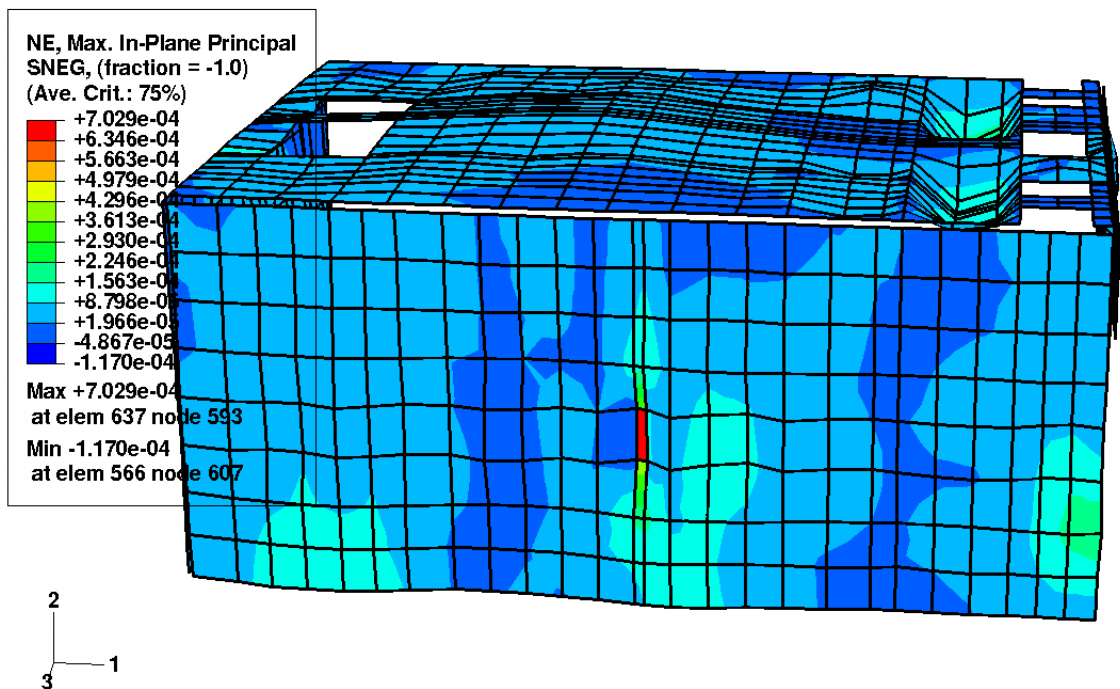


Fig. 12j: Maximum In-Plane Strain in Outer Plate Group at Left Plate for 8 gm Hydrogen Combustion Experiment (at 31.15 m Sec)

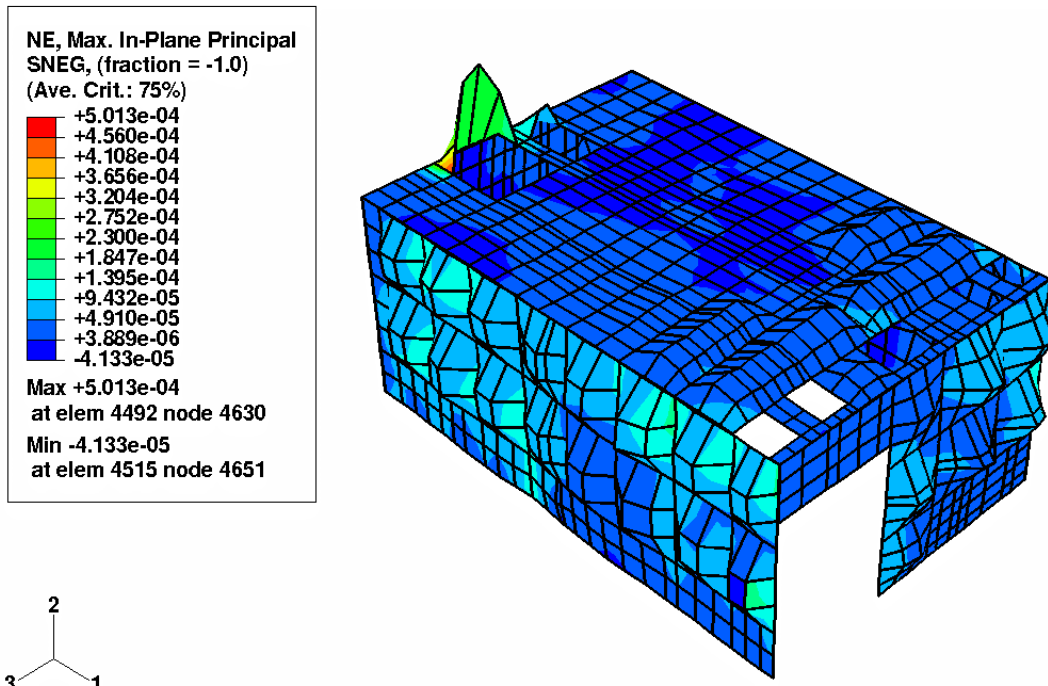


Fig. 12k: Maximum In-Plane Strain in Inner Corrugated Wall Group at Ceiling for 8 gm Hydrogen Combustion Experiment (at 91.15 m Sec)

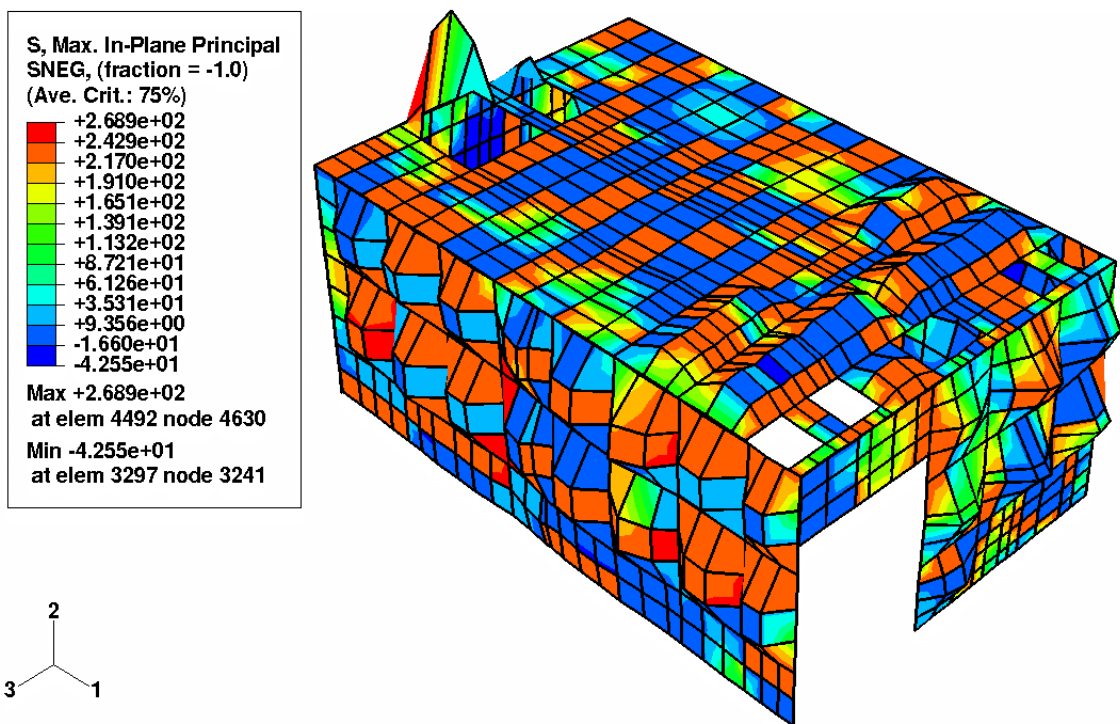


Fig. 12l: Maximum In-Plane Stress (MPa) in Inner Corrugated Wall Group at Ceiling Wall for 8 gm Hydrogen Combustion Experiment (at 91.15 m Sec)

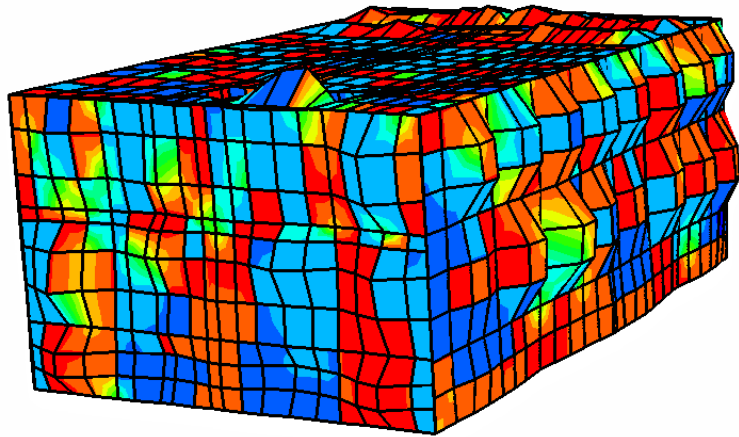
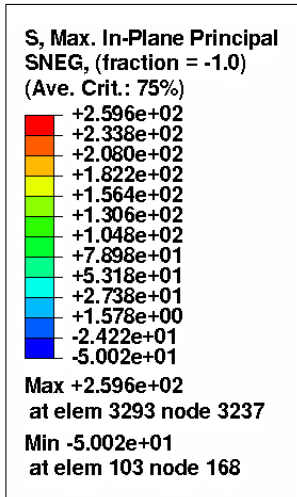


Fig. 12m: Maximum In-Plane Stresses (MPa) in Inner Corrugated Wall Group at Rear Wall for 8 gm Hydrogen Combustion Experiment (at 47.15 m Sec)

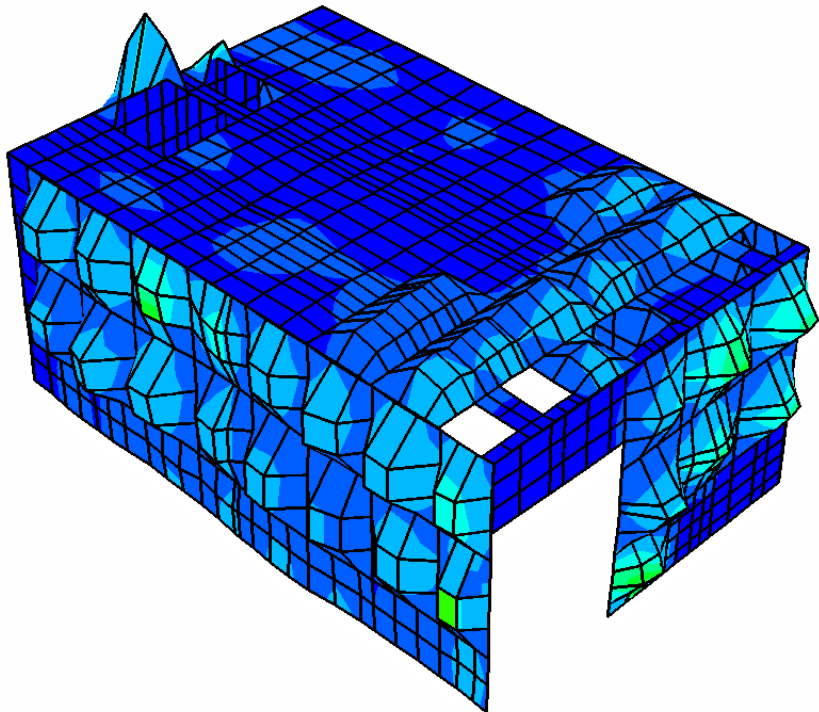
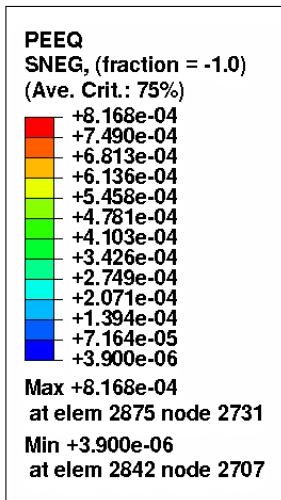


Fig. 12n: Maximum In-Plane Effective Plastic Strain in Inner Corrugated Wall Group at Front Wall for 8 gm Hydrogen Combustion Experiment (at 140 m Sec)

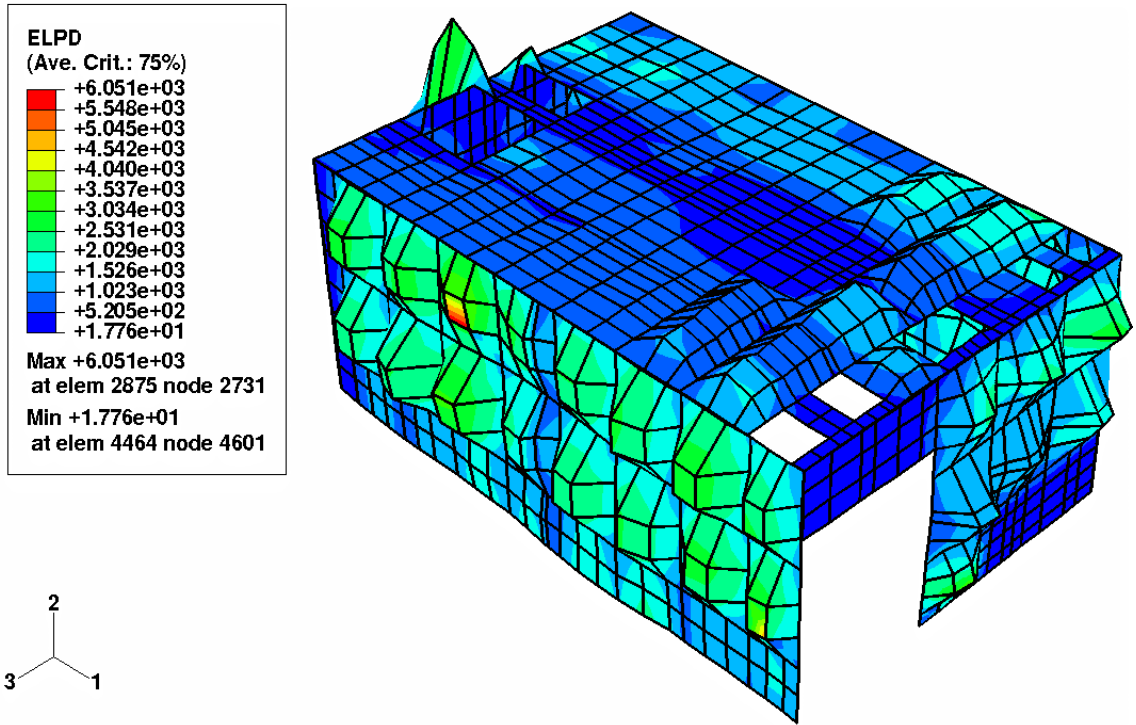


Fig. 12-o: Maximum Plastic Energy (mJ) in Inner Corrugated Wall Group at Front Wall for 8 gm Hydrogen Combustion Experiment (at 140 m Sec)

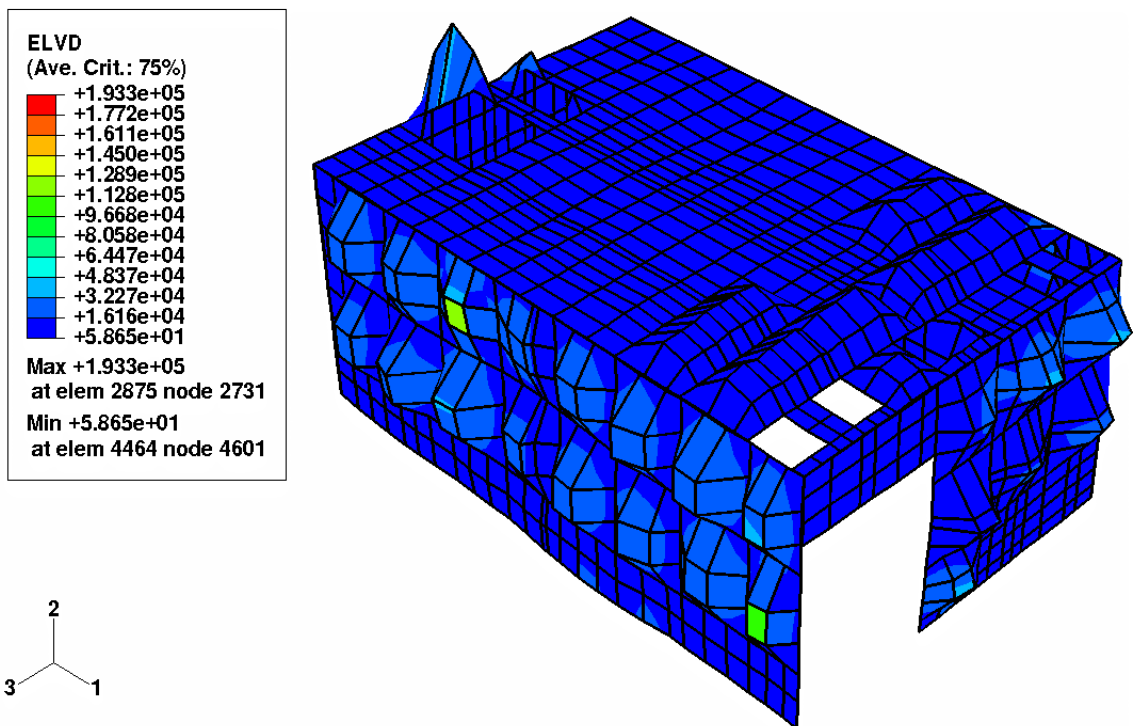


Fig. 12p: Maximum Viscous Energy (mJ) in Inner Wall Group at Front Wall for 8 gm Hydrogen Combustion Experiment (at 140 m Sec)

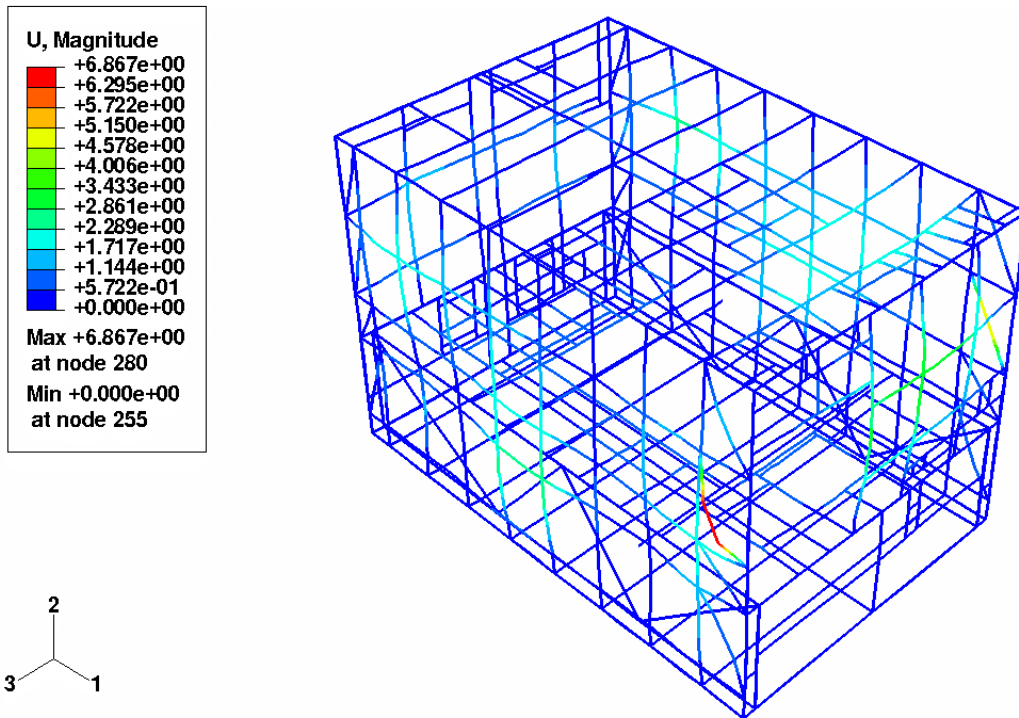


Fig. 12q: Maximum Displacement in Frame Group at Left Frame (Frame-A) for 8 gm Hydrogen Combustion Experiment (at 63.15 m Sec)

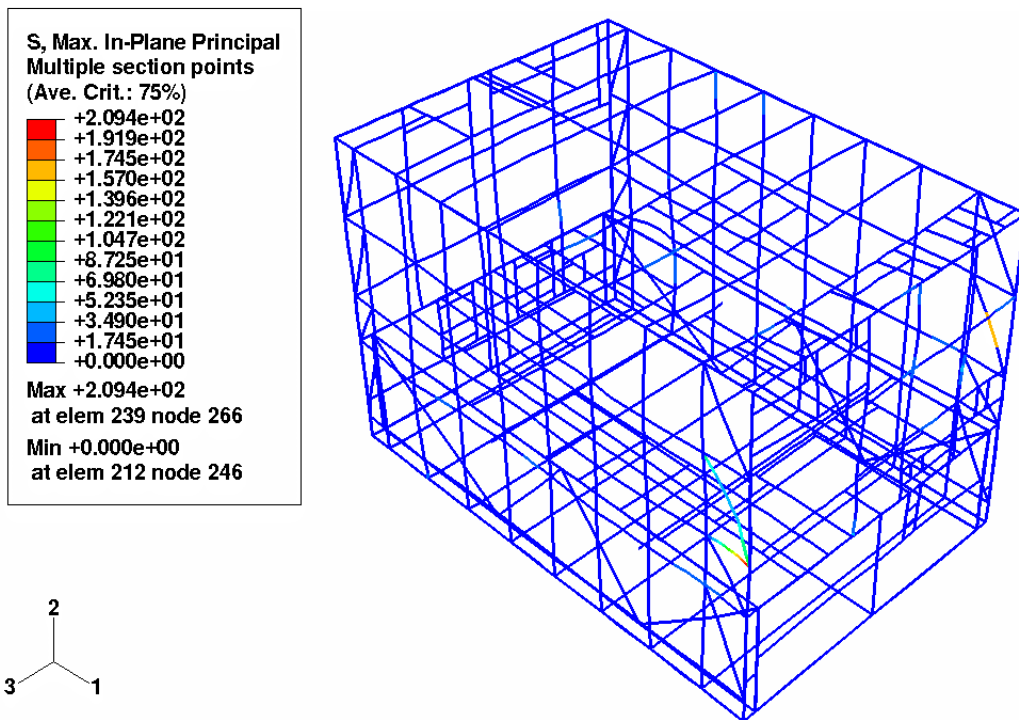


Fig. 12r: Maximum In-Plane Stress in Frame Group at Left Frame (Frame-A) for 8 gm Hydrogen Combustion Experiment (at 71.15 m Sec)

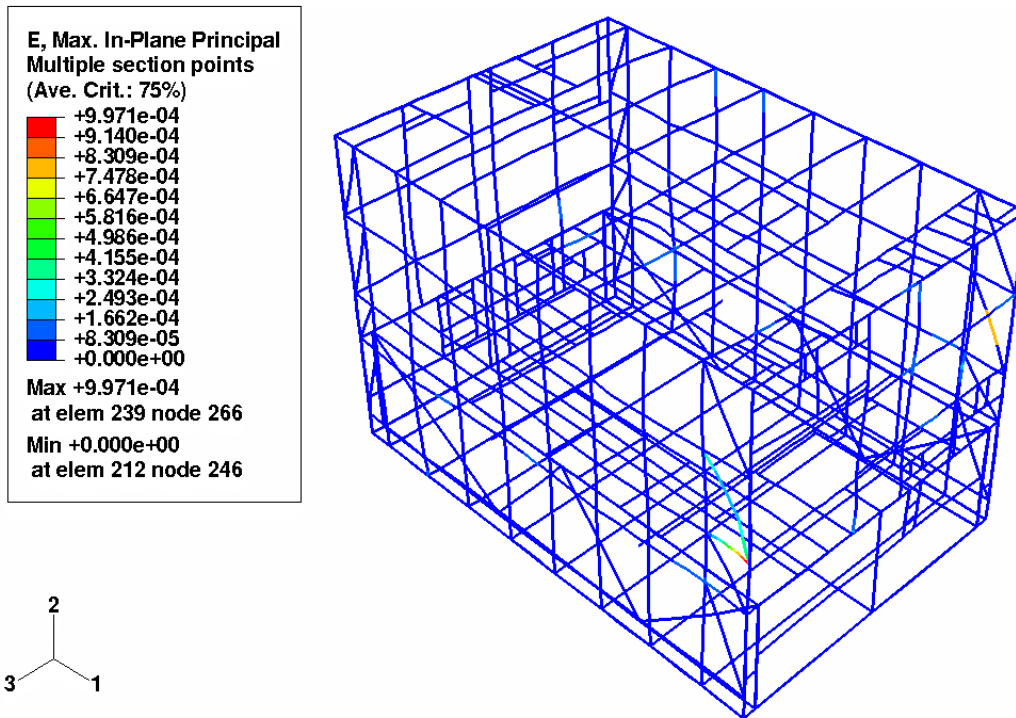


Fig. 12s: Maximum In-Plane Strain in Frame Group at Left Frame (Frame-A) for 8 gm Hydrogen Combustion Experiment (at 71.15 m Sec)

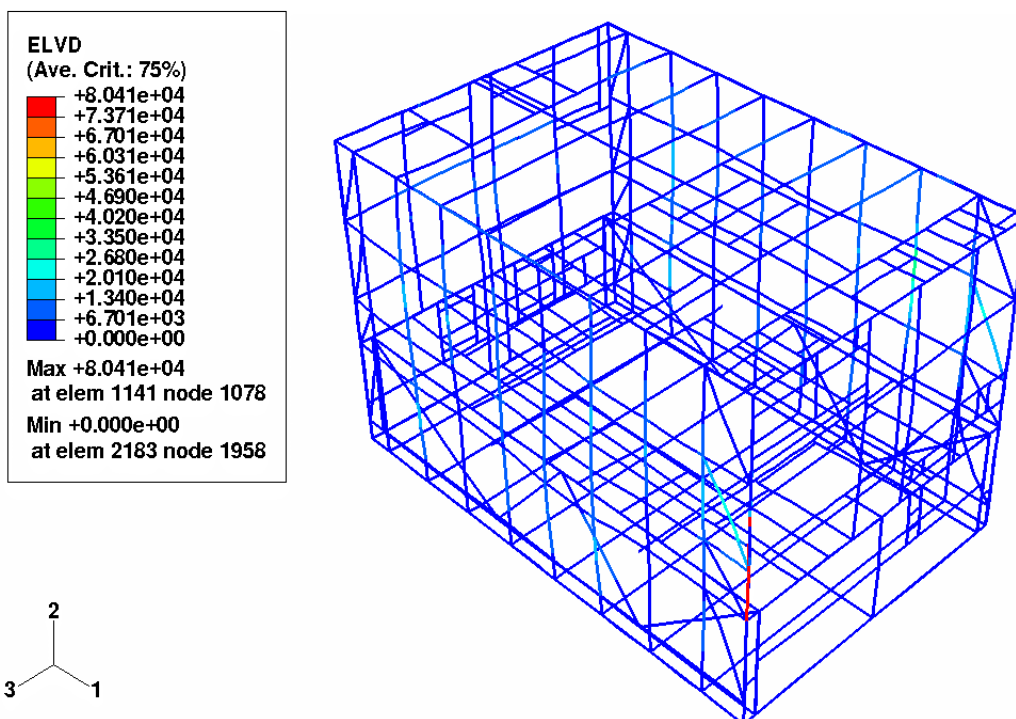


Fig. 12t: Maximum Viscous Energy (mJ) in Frame Group at Front Frame for 8 gm Hydrogen Combustion Experiment (at 140 m Sec)

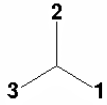
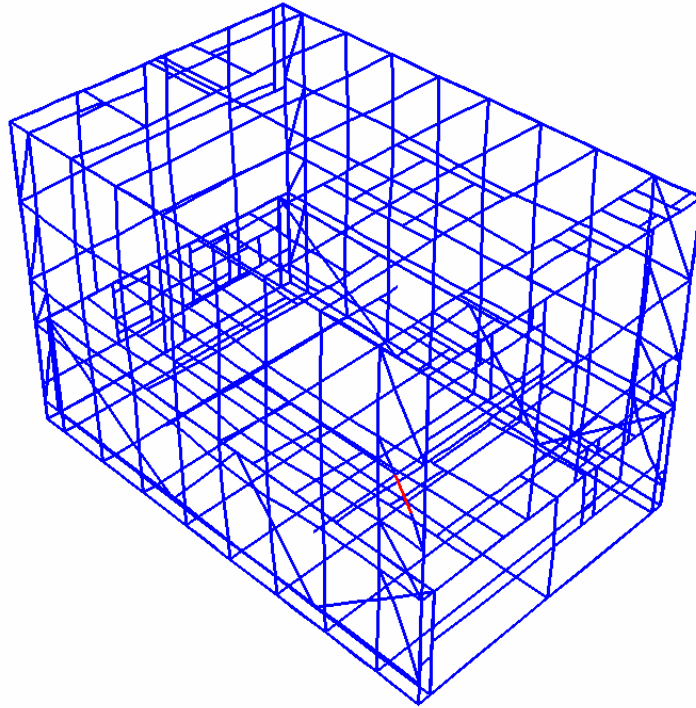
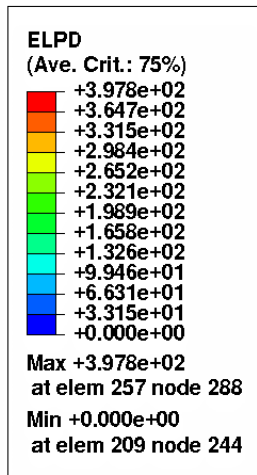


Fig. 12u: Maximum Plastic Energy (mJ) in Frame Group at Left Frame for 8 gm Hydrogen Combustion Experiment (at 140 m Sec)

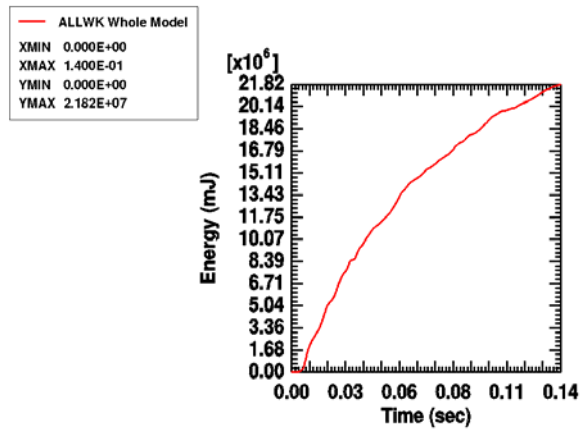


Fig. 13a: Total External Work (mJ) for 8 gm Hydrogen Combustion Experiment

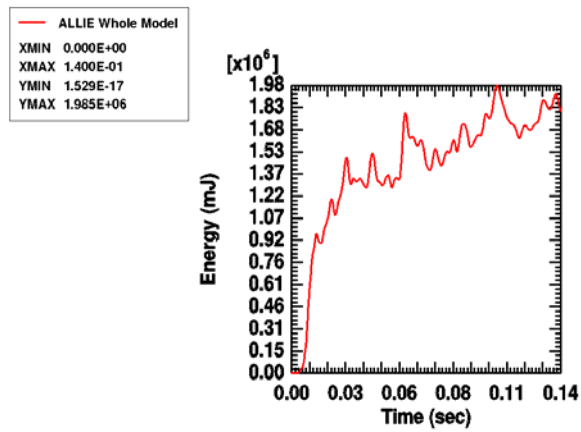


Fig. 13b: Total Internal Energy (mJ) for 8 gm Hydrogen Combustion Experiment

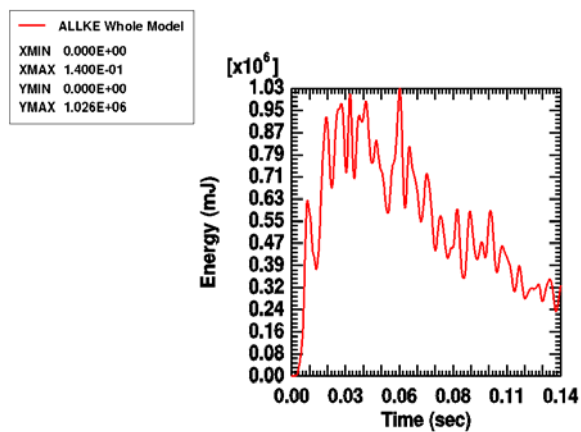


Fig. 13c: Total Kinetic Energy (mJ) for 8 gm Hydrogen Combustion Experiment

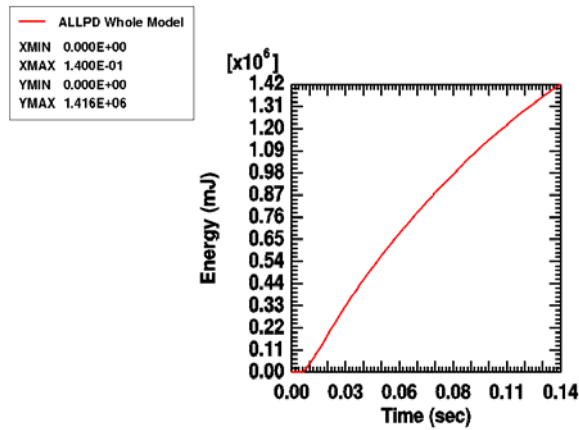


Fig. 13d: Total Plastic Energy (mJ) Dissipation for 8 gm Hydrogen Combustion Experiment

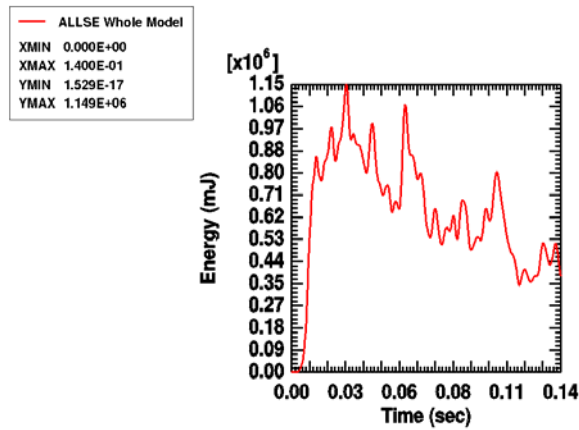


Fig. 13e: Total Strain Energy (mJ) for 8 gm Hydrogen Combustion Experiment

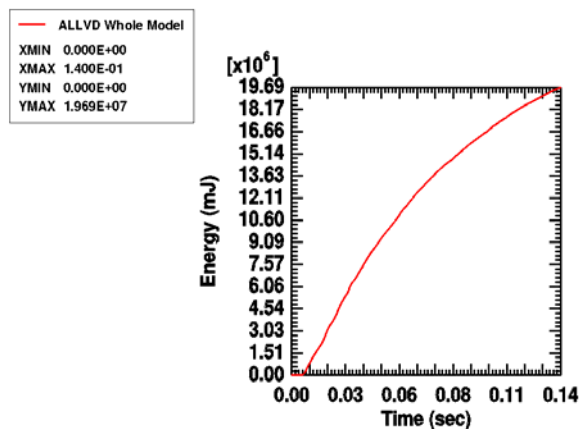


Fig. 13f: Total Viscous Energy (mJ) Dissipation for 8 gm Hydrogen Combustion Experiment

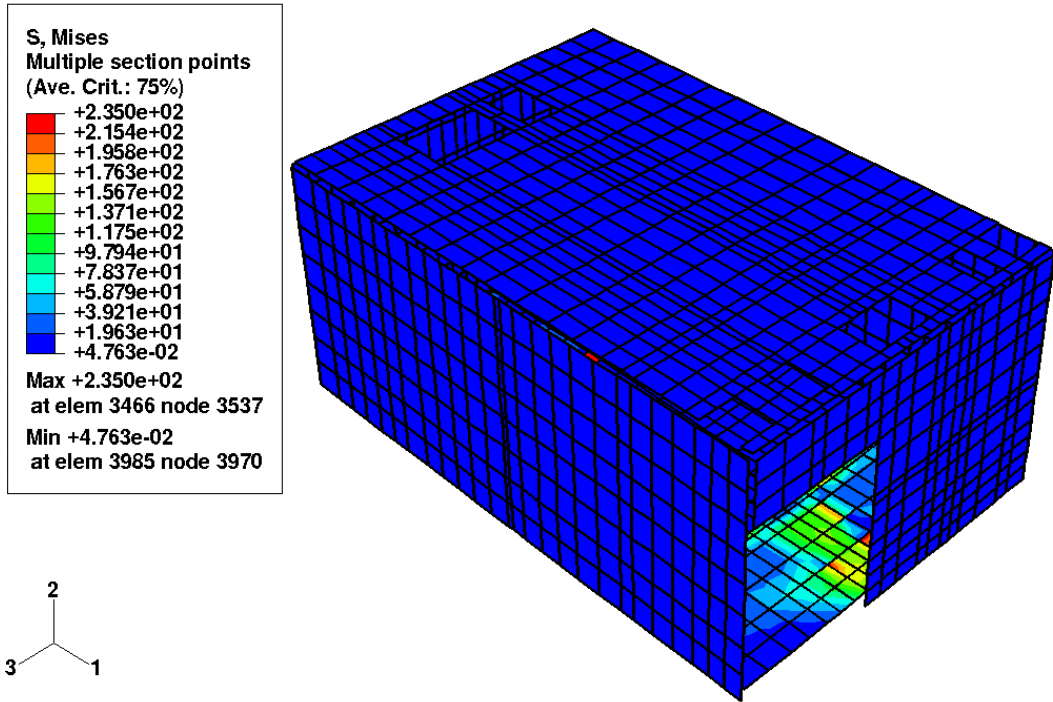


Fig. 14a: Maximum von Mises Stresses (MPa) in Outer Plate Group at Floor for 16 gm Hydrogen Combustion Experiment (at 5.15 m Sec)

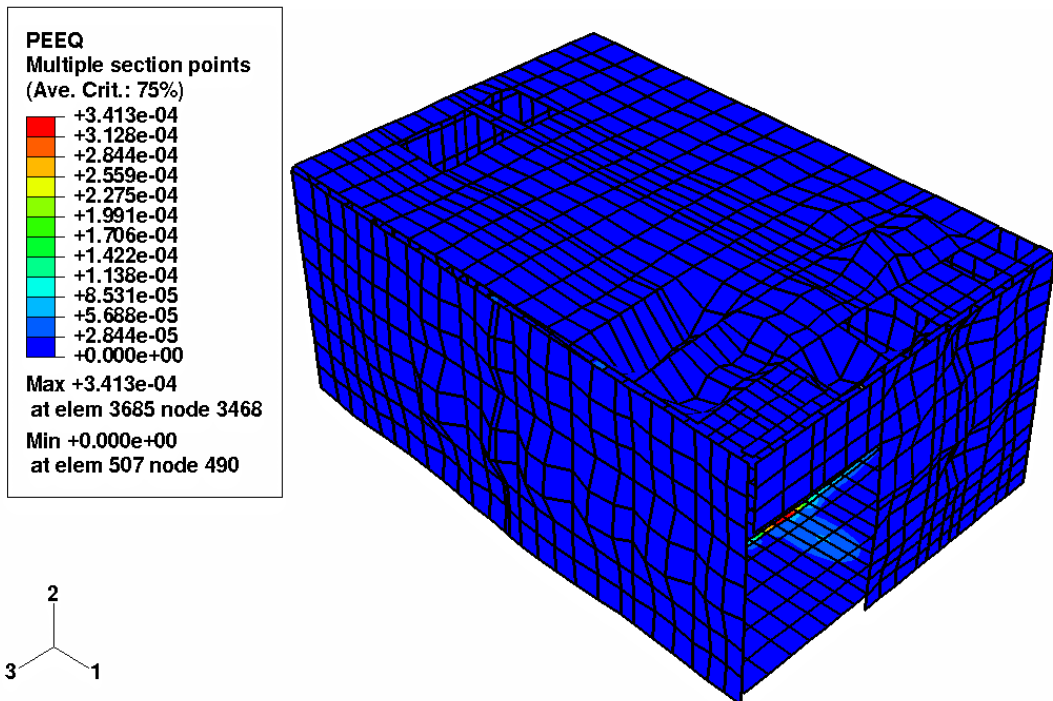


Fig. 14b: Maximum Effective Plastic Strain in Outer Plate Group at Floor for 16 gm Hydrogen Combustion Experiment (at 140 m Sec)

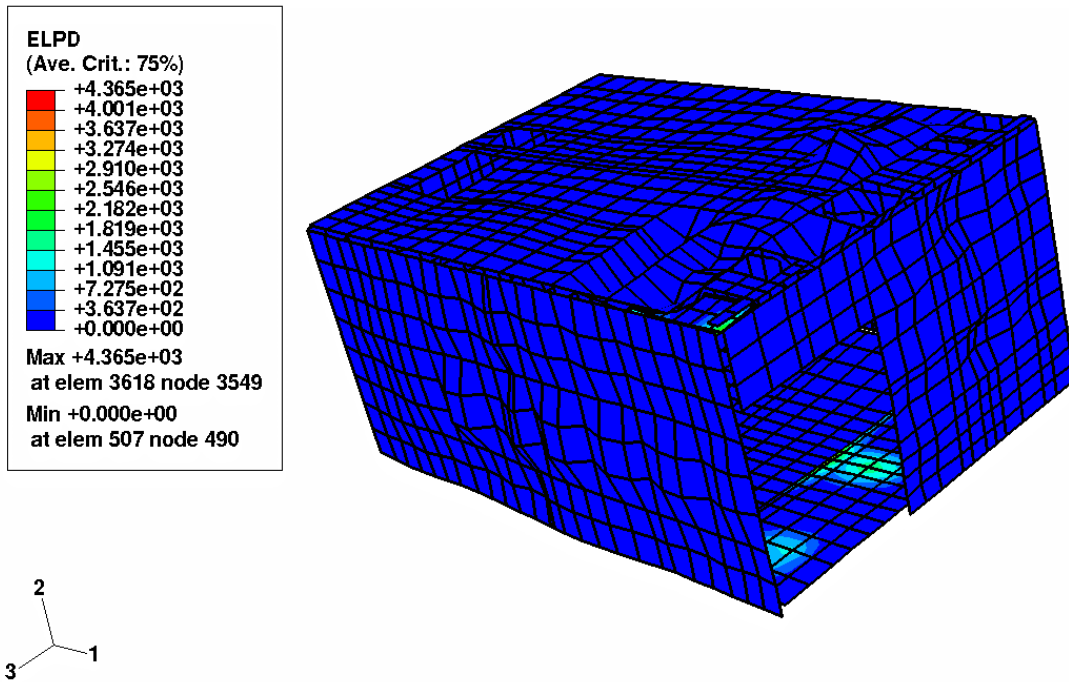


Fig. 14c: Maximum Plastic Energy (mJ) in Outer Plate Group at Floor for 16 gm Hydrogen Combustion Experiment (at 140 m Sec)

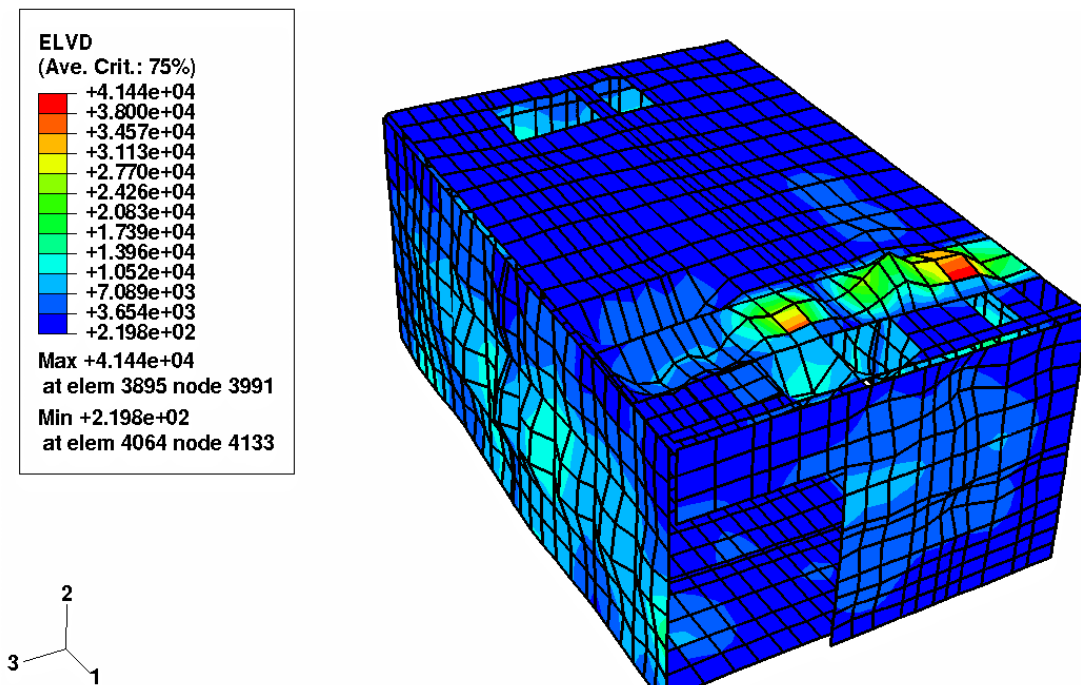


Fig. 14d: Maximum Viscous Energy (mJ) in Outer Plate Group at Ceiling Plate for 16 gm Hydrogen Combustion Experiment (at 140 m Sec)

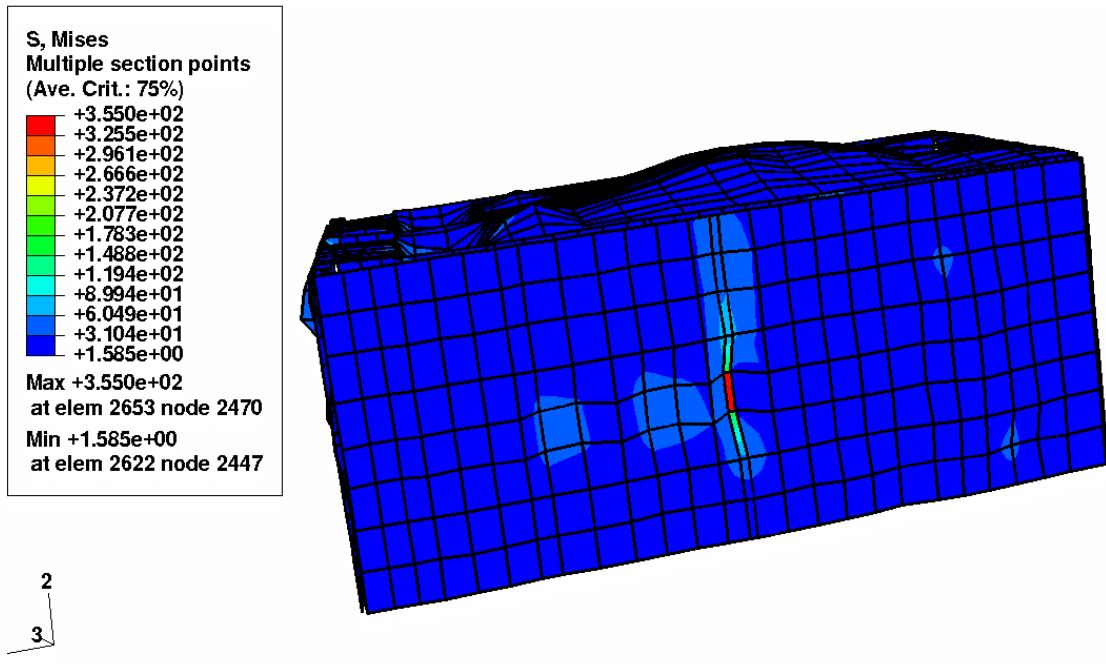


Fig. 14e: Maximum von Mises (MPa) in Outer Plate Group at Right Wall for 16 gm Hydrogen Combustion Experiment (at 33.15 m Sec)

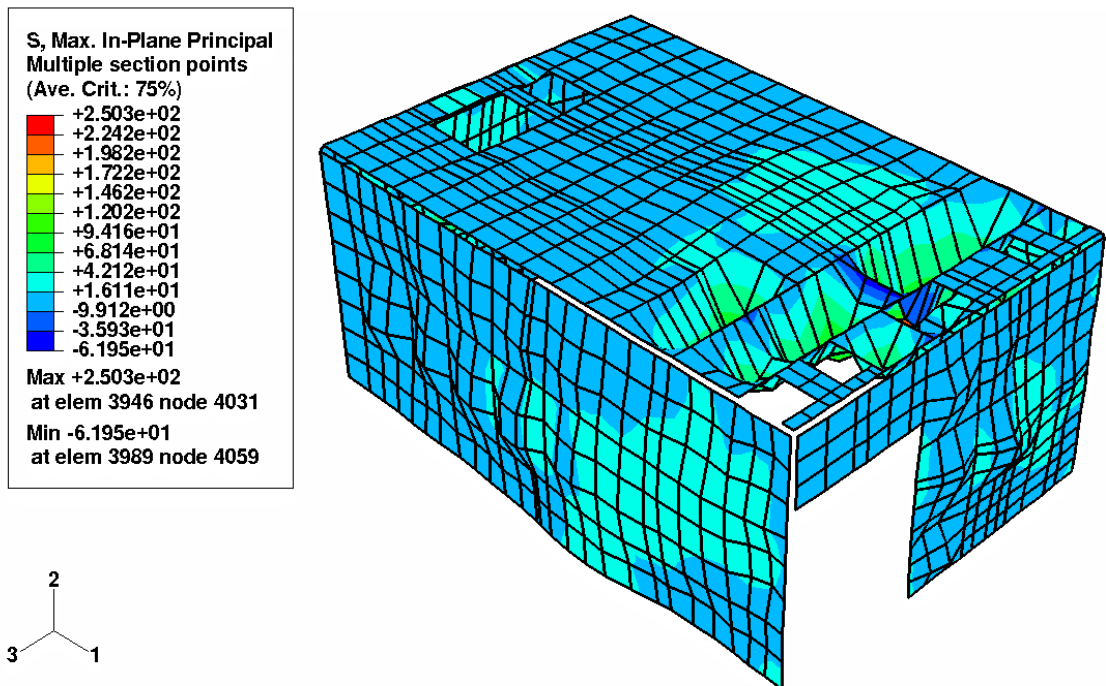


Fig. 14f: Maximum In-Plane Stress (MPa) in Outer Plate Group at Ceiling Wall for 16 gm Hydrogen Combustion Experiment (at 57.15 m Sec)

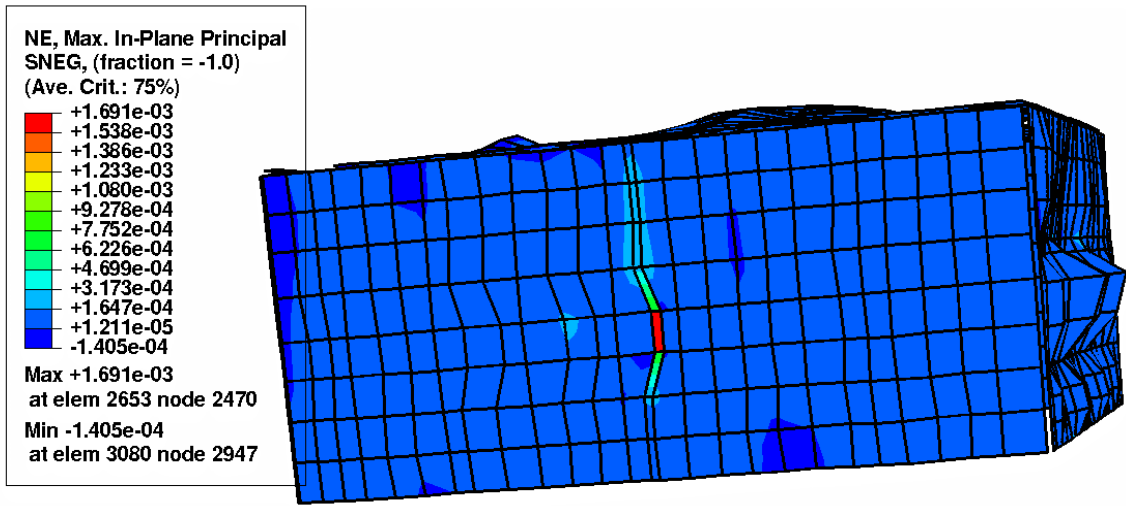


Fig. 14g: Maximum In-Plane Strain in Outer Plate Group at Right Plate for 16 gm Hydrogen Combustion Experiment (at 31.15 m Sec)

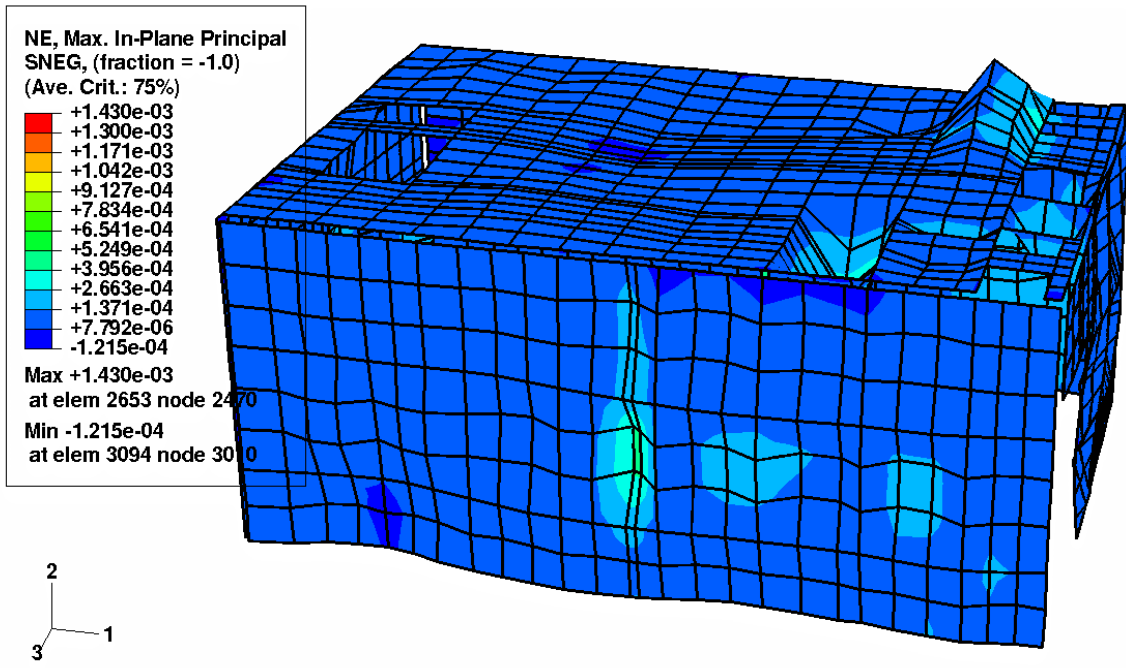


Fig. 14h: Maximum In-Plane Strain in Outer Plate Group at Left Plate for 16 gm Hydrogen Combustion Experiment (at 43.15 m Sec)

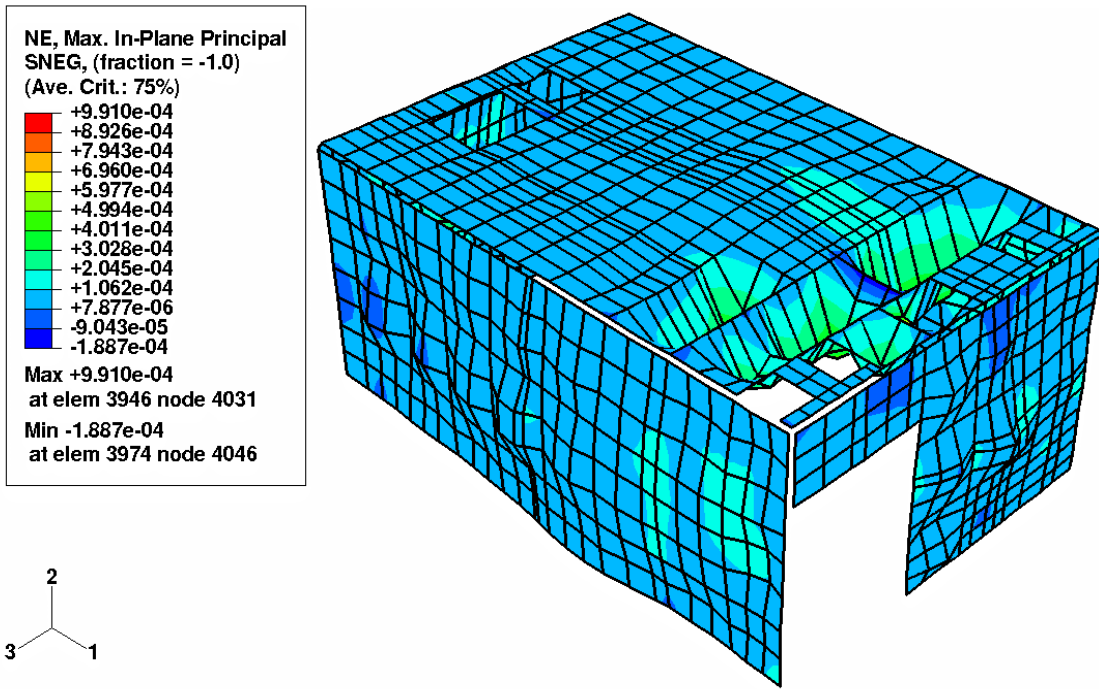


Fig. 14i: Maximum In-Plane Strain in Outer Plate Group at Ceiling for 16 gm Hydrogen Combustion Experiment (at 57.15 m Sec)

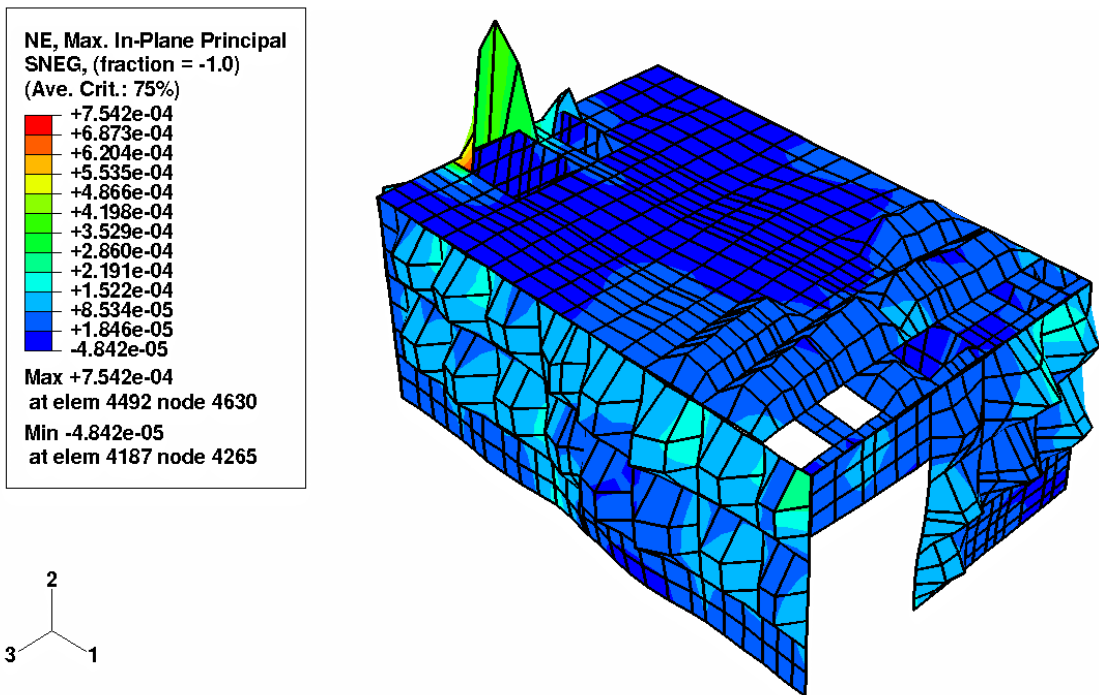


Fig. 14j: Maximum In-Plane Strain in Inner Corrugated Wall Group at Ceiling for 16 gm Hydrogen Combustion Experiment (at 89.15 m Sec)

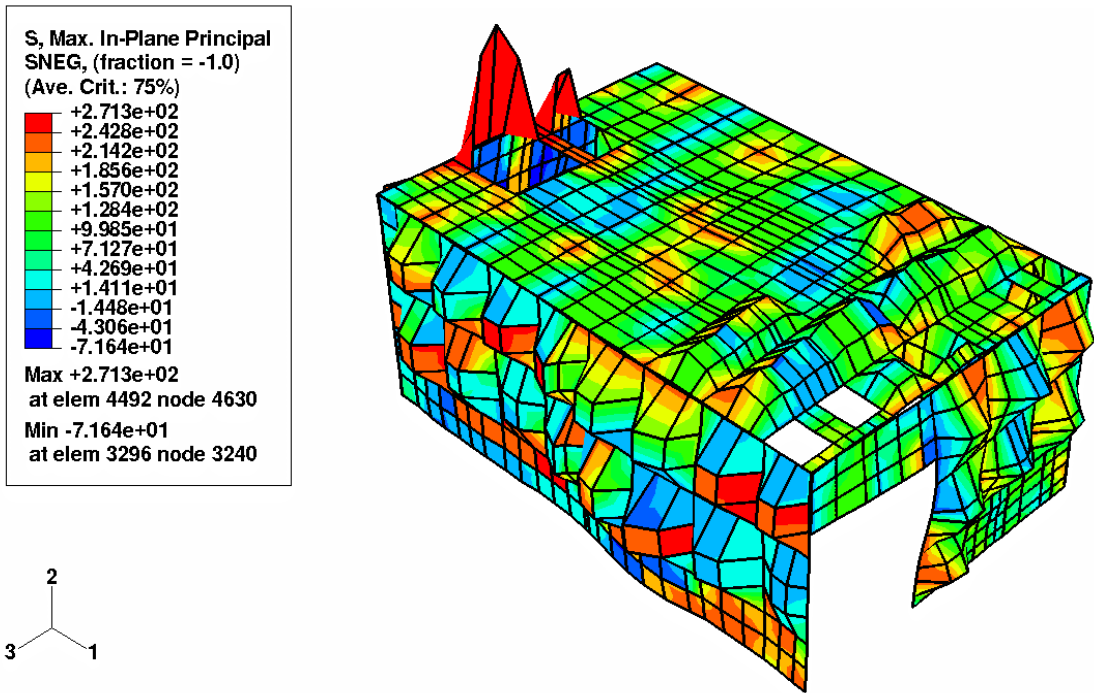


Fig. 14k: Maximum In-Plane Stress (MPa) in Inner Corrugated Wall Group at Ceiling Wall for 16 gm Hydrogen Combustion Experiment (at 87.15 m Sec)

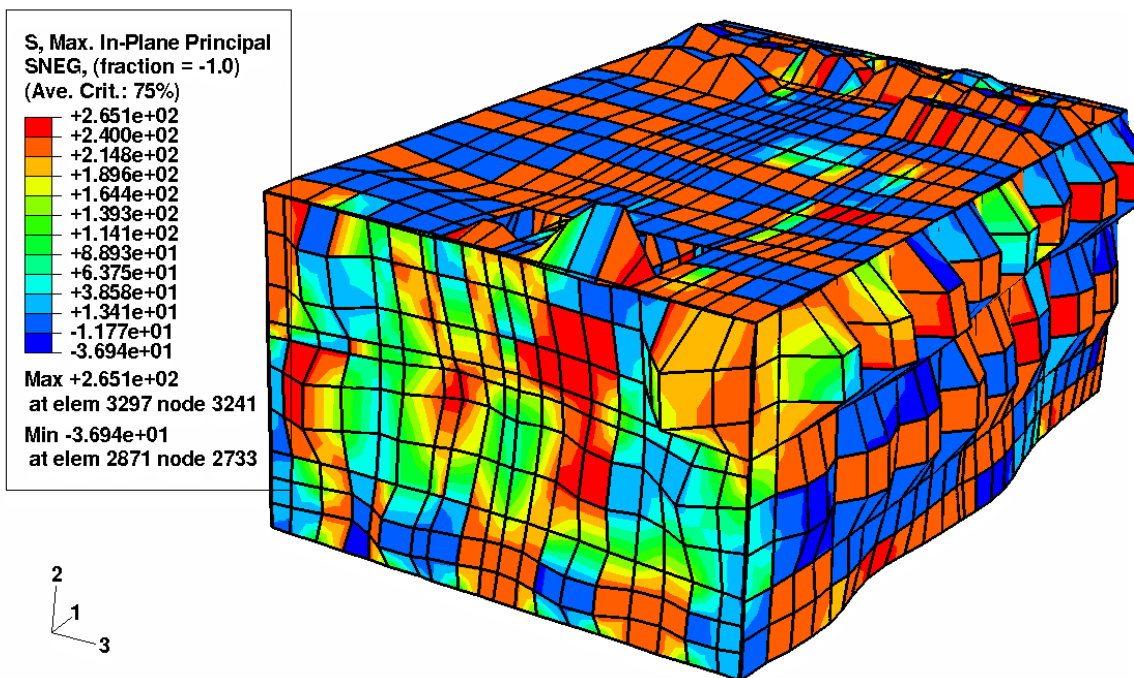


Fig. 14l: Maximum In-Plane Stresses (MPa) in Inner Corrugated Wall Group at Rear Wall for 16 gm Hydrogen Combustion Experiment (at 49.15 m Sec)

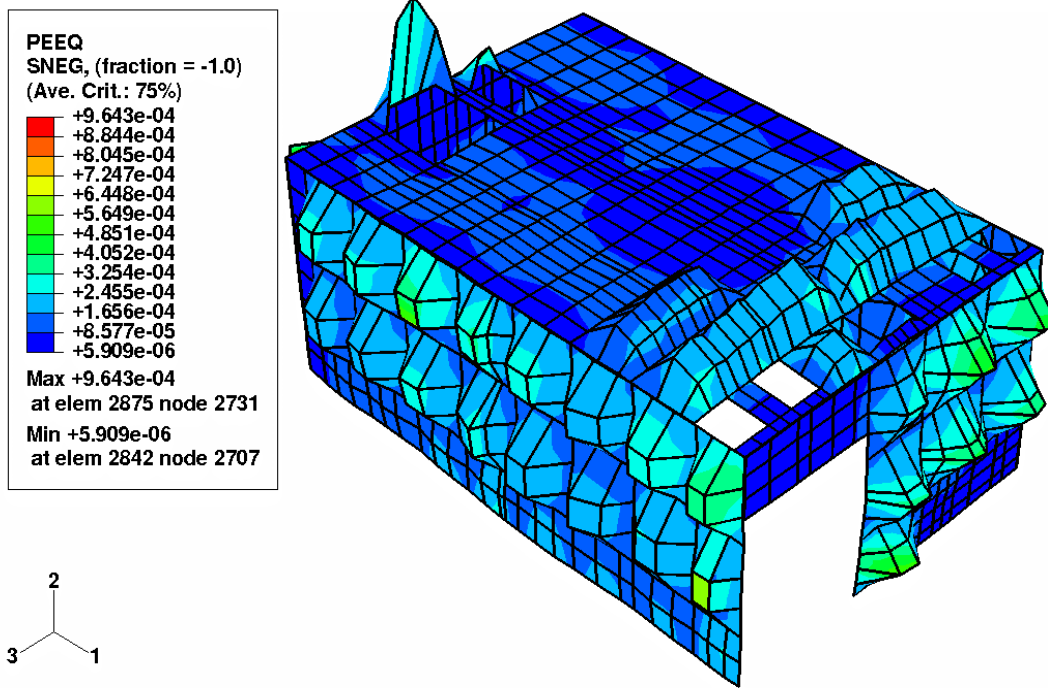


Fig. 14m: Maximum In-Plane Effective Plastic Strain in Inner Corrugated Wall Group at Front Wall for 16 gm Hydrogen Combustion Experiment (at 140 m Sec)

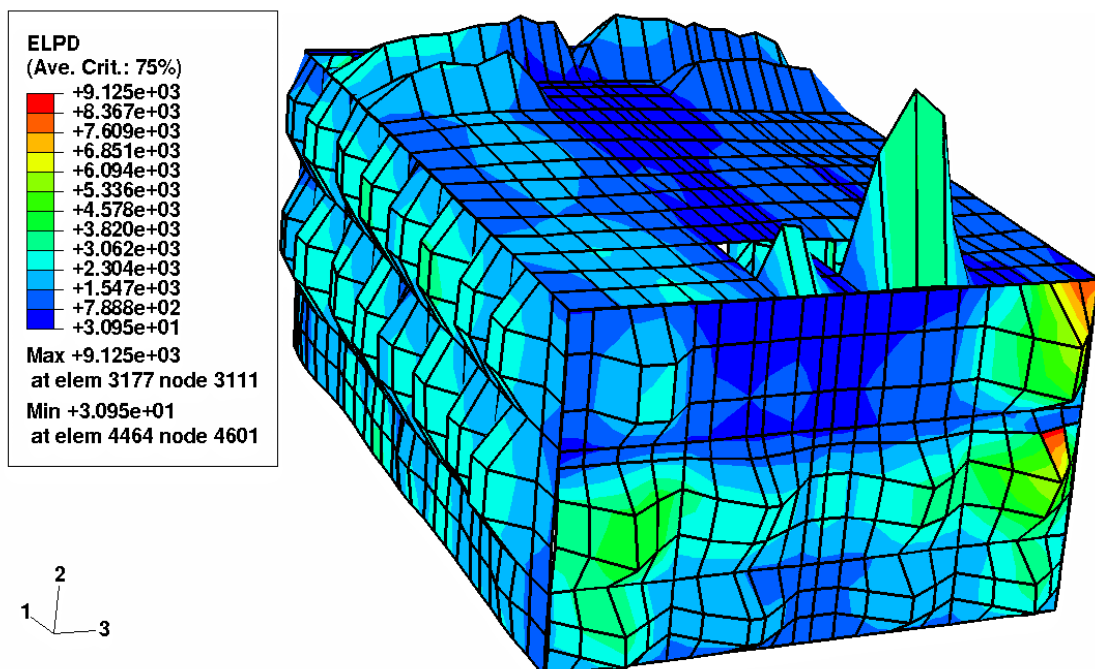


Fig. 14n: Maximum Plastic Energy (mJ) in Inner Corrugated Wall Group at Rear Wall for 16 gm Hydrogen Combustion Experiment (at 140 m Sec)

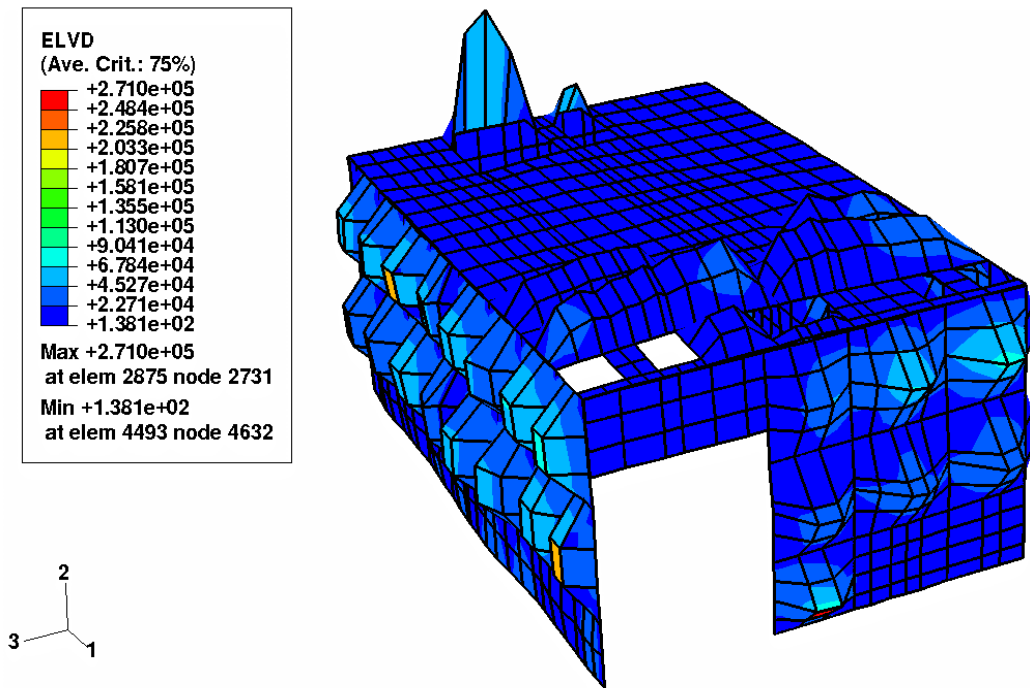


Fig. 14-o: Maximum Viscous Energy (mJ) in Inner Corrugated Wall Group at Front Wall for 16 gm Hydrogen Combustion Experiment (at 140 m Sec)

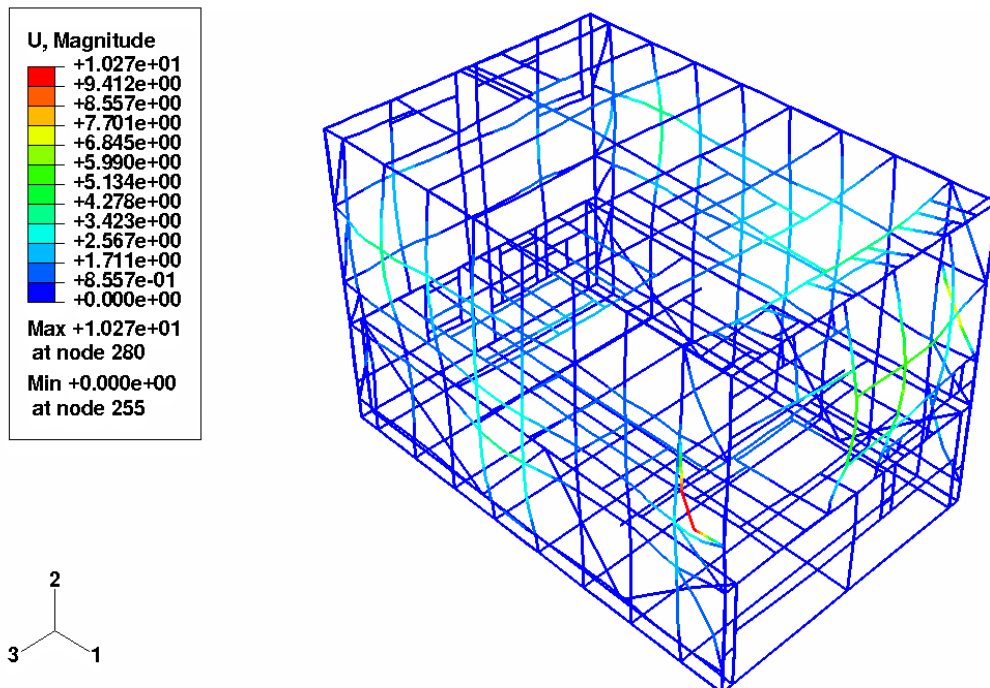


Fig. 14p: Maximum Displacement in Frame Group at Left Frame (Frame-A) for 16 gm Hydrogen Combustion Experiment (at 63.15 m Sec)

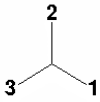
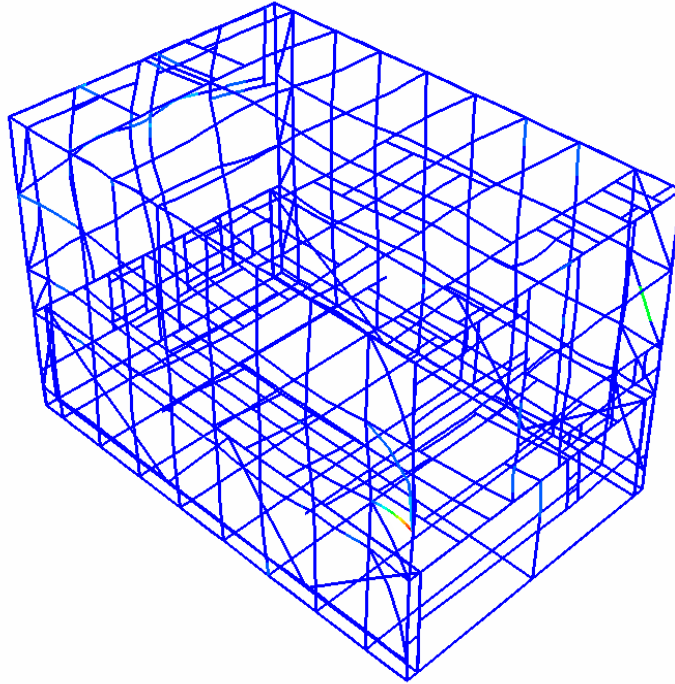
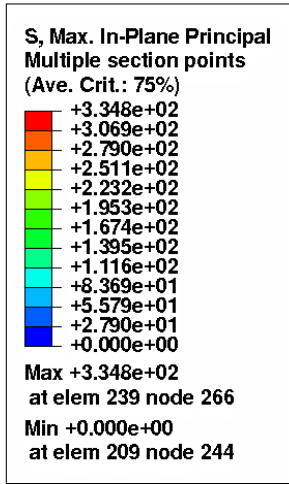


Fig. 14q: Maximum In-Plane Stress in Frame Group at Left Frame (Frame-A) for 16 gm Hydrogen Combustion Experiment (at 39.15 m Sec)

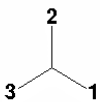
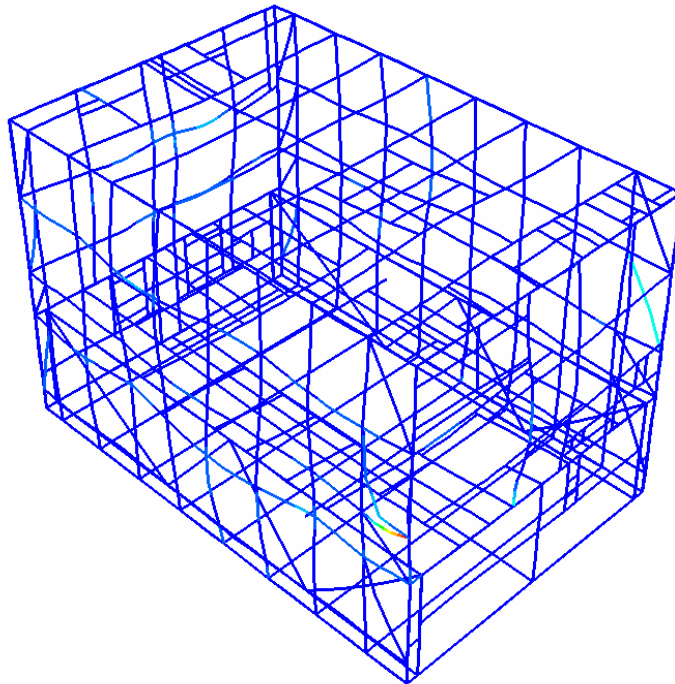
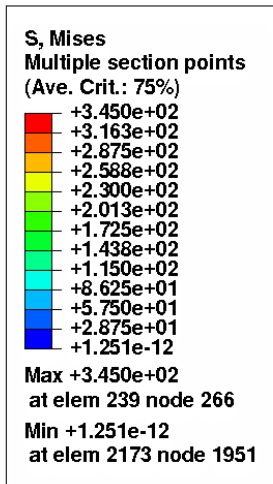


Fig. 14r: Maximum In-Plane von Mises Stress in Frame Group at Left Frame (Frame-A) for 16 gm Hydrogen Combustion Experiment (at 47.15 m Sec)

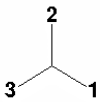
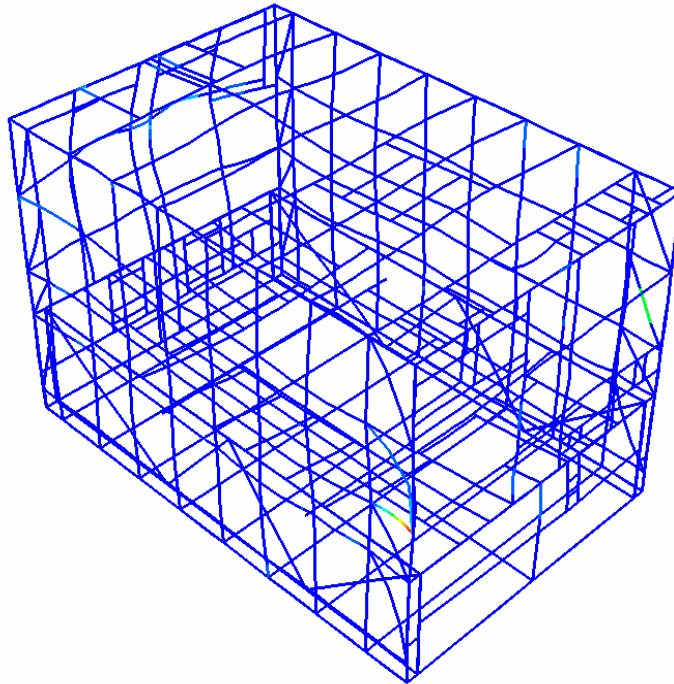
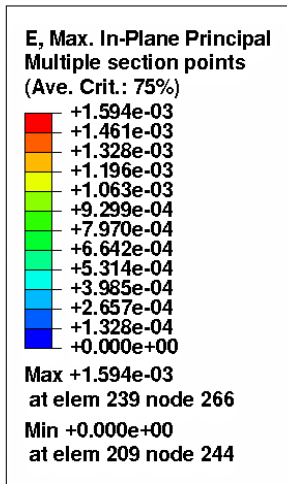


Fig. 14s: Maximum In-Plane Strain in Frame Group at Left Frame (Frame-A) for 16 gm Hydrogen Combustion Experiment (at 39.15 m Sec)

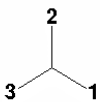
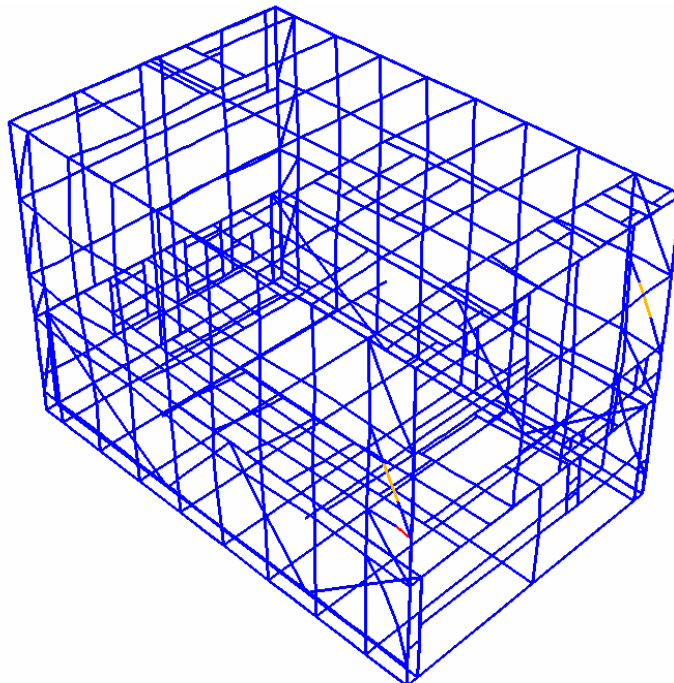
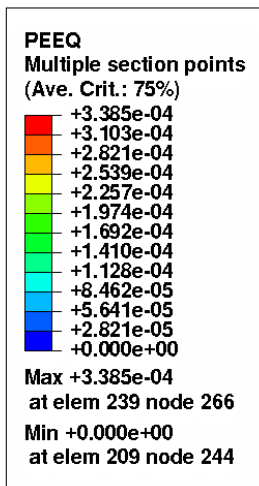


Fig. 14t: Maximum In-Plane Effective Plastic Strain in Frame Group at Left Frame (Frame-A) for 16 gm Hydrogen Combustion Experiment (at 140 m Sec)

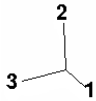
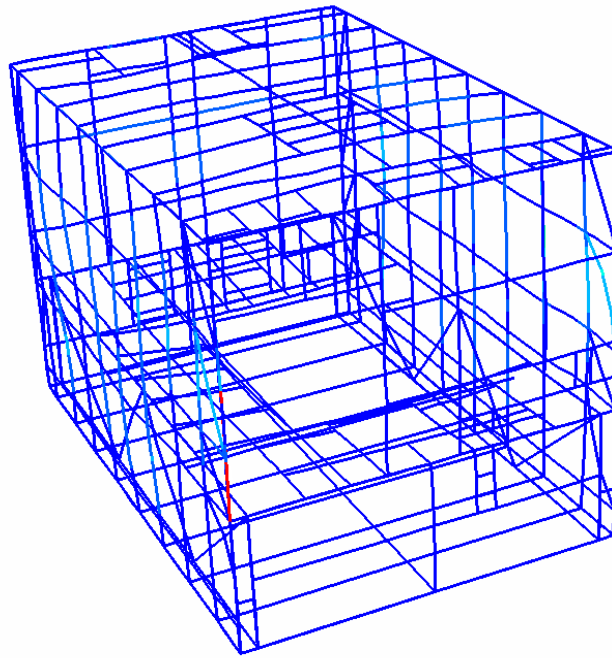
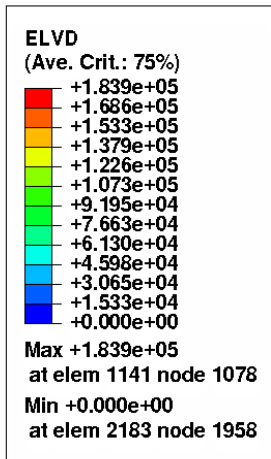


Fig. 14u: Maximum Viscous Energy (mJ) in Frame Group at Front Frame for 16 gm Hydrogen Combustion Experiment (at 140 m Sec)

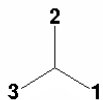
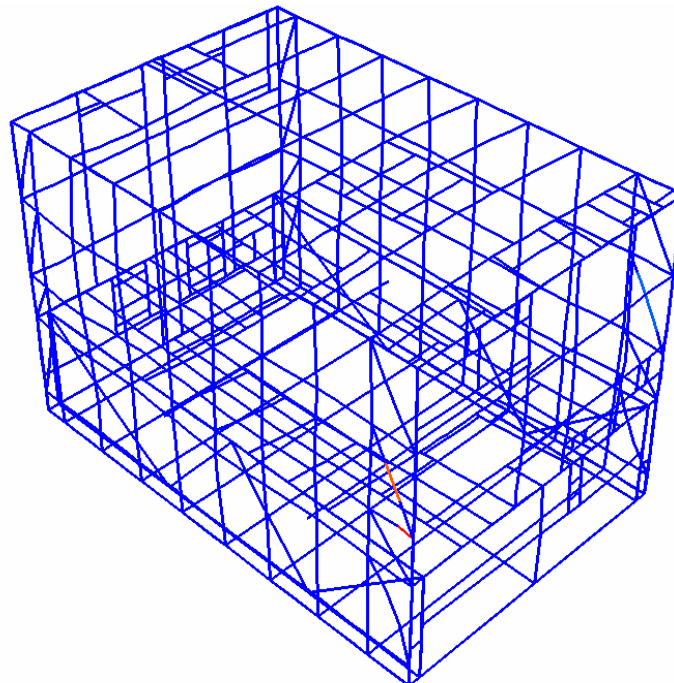
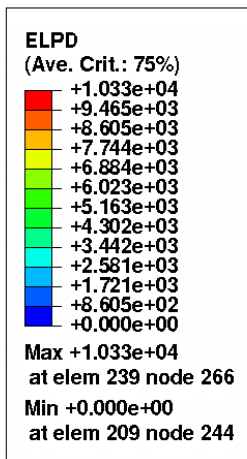


Fig. 14v: Maximum Plastic Energy (mJ) in Frame Group at Left Frame for 16 gm Hydrogen Combustion Experiment (at 140 m Sec)

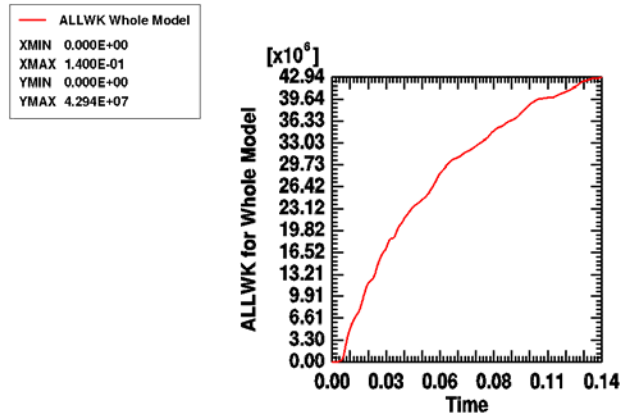


Fig. 15a: Total External Work (mJ) for 16 gm Hydrogen Combustion Experiment

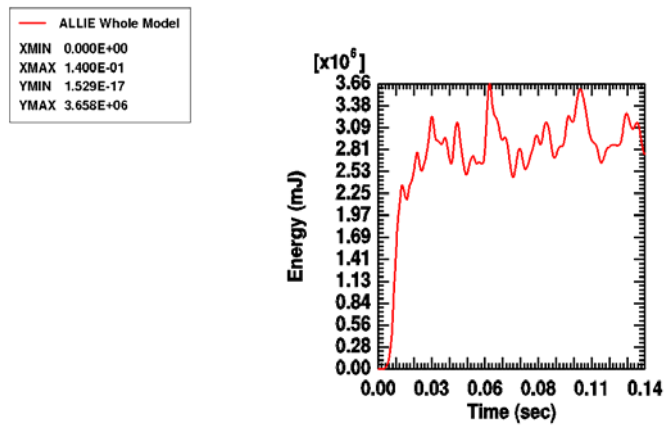


Fig. 15b: Total Internal Energy (mJ) for 16 gm Hydrogen Combustion Experiment

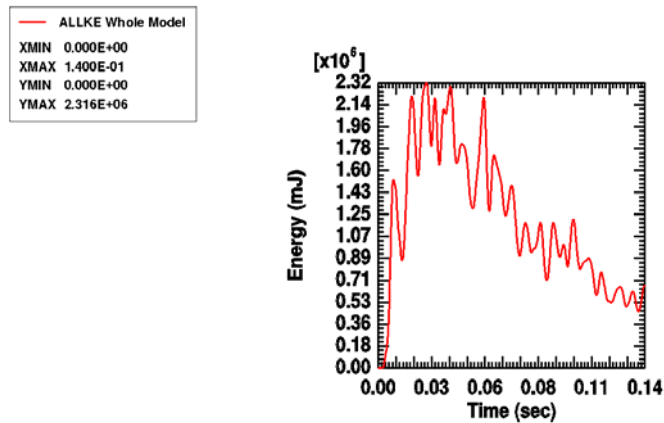


Fig. 15c: Total Kinetic Energy (mJ) for 16 gm Hydrogen Combustion Experiment

— ALLPD Whole Model
 XMIN 0.000E+00
 XMAX 1.400E-01
 YMIN 0.000E+00
 YMAX 2.134E+06

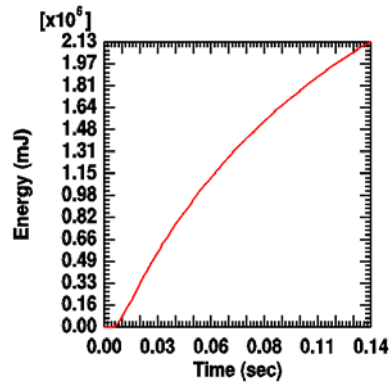


Fig. 15d: Total Plastic Energy (mJ) Dissipation for 16 gm Hydrogen Combustion Experiment

— ALLSE Whole Model
 XMIN 0.000E+00
 XMAX 1.400E-01
 YMIN 1.529E-17
 YMAX 2.669E+06

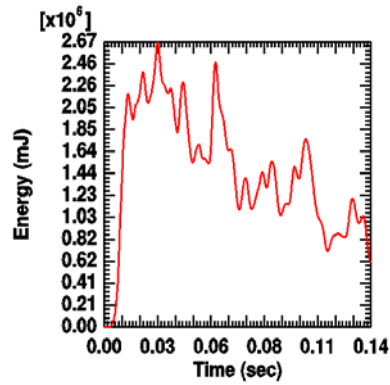


Fig. 15e: Total Strain Energy (mJ) for 16 gm Hydrogen Combustion Experiment

— ALLVD Whole Model
 XMIN 0.000E+00
 XMAX 1.400E-01
 YMIN 0.000E+00
 YMAX 3.951E+07

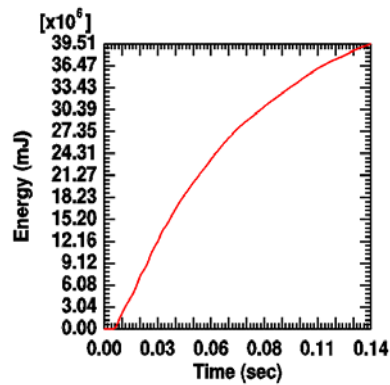


Fig. 15f: Total Viscous Energy (mJ) Dissipation for 16 gm Hydrogen Combustion Experiment

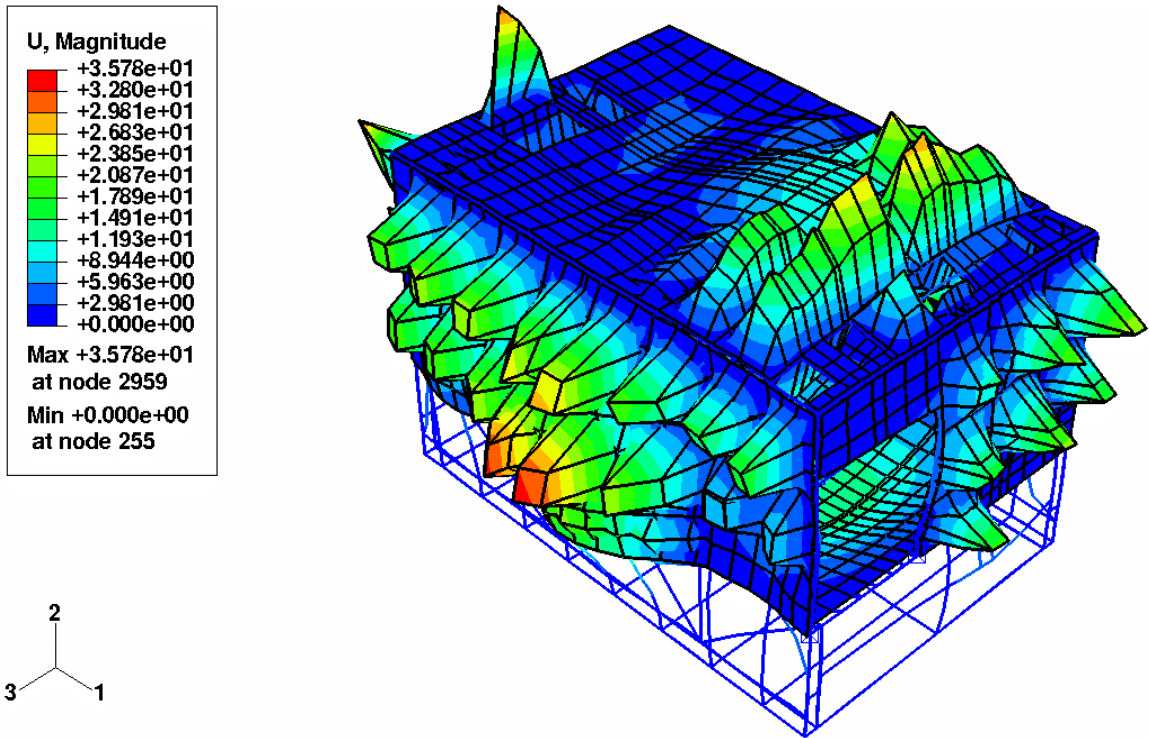


Fig. 16a: Deformed View of the Test Cell for 64 gm Combustion at 0.05 sec

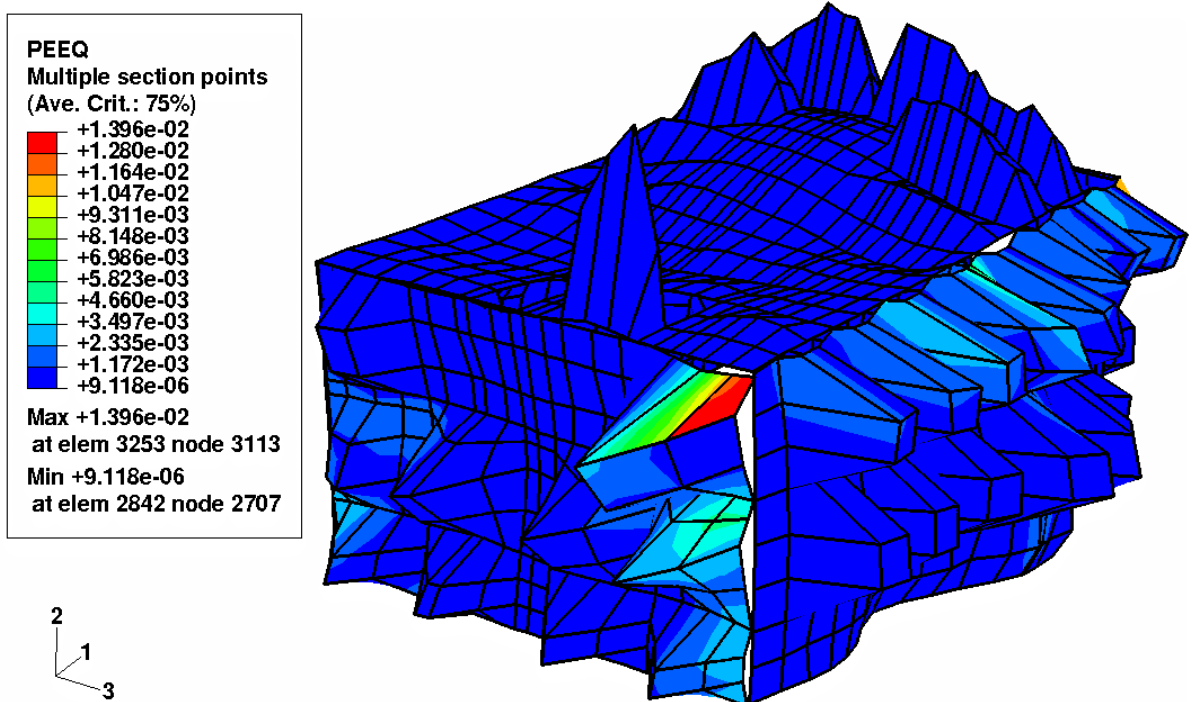


Fig. 16b: Maximum Effective Plastic Strain in the Corrugated Rear Wall of Test Cell for 64 gm Combustion at 0.05 sec

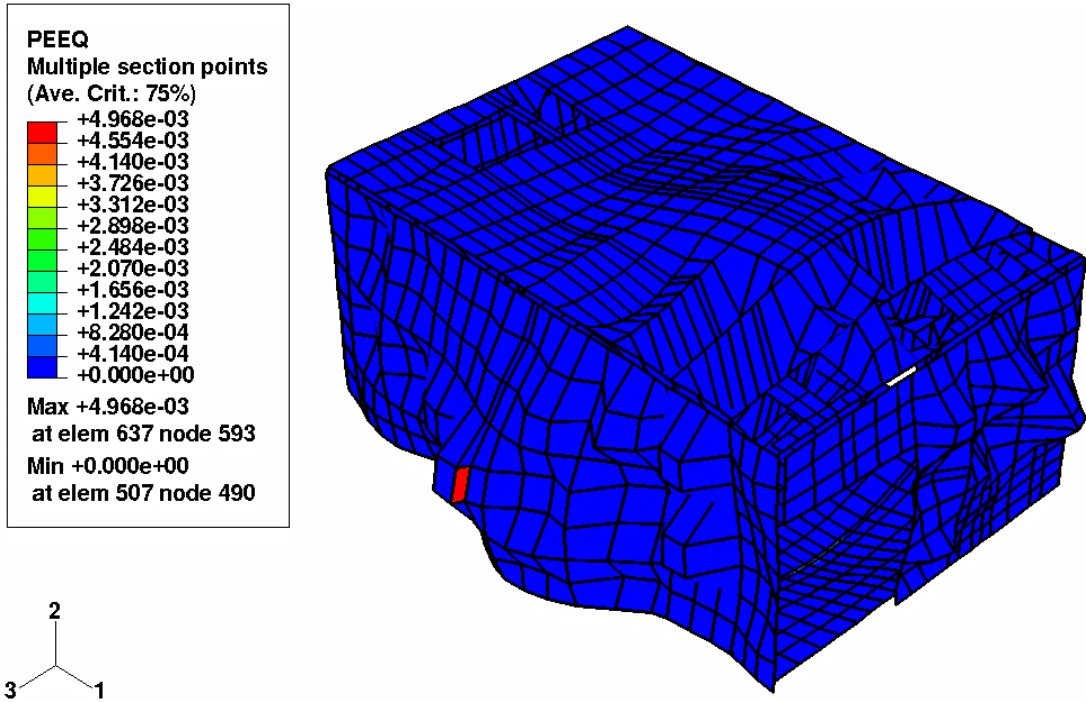


Fig. 16c: Maximum Effective Plastic Strain in the Outer Front Plate of the Test Cell for 64 gm Combustion at 0.05 sec

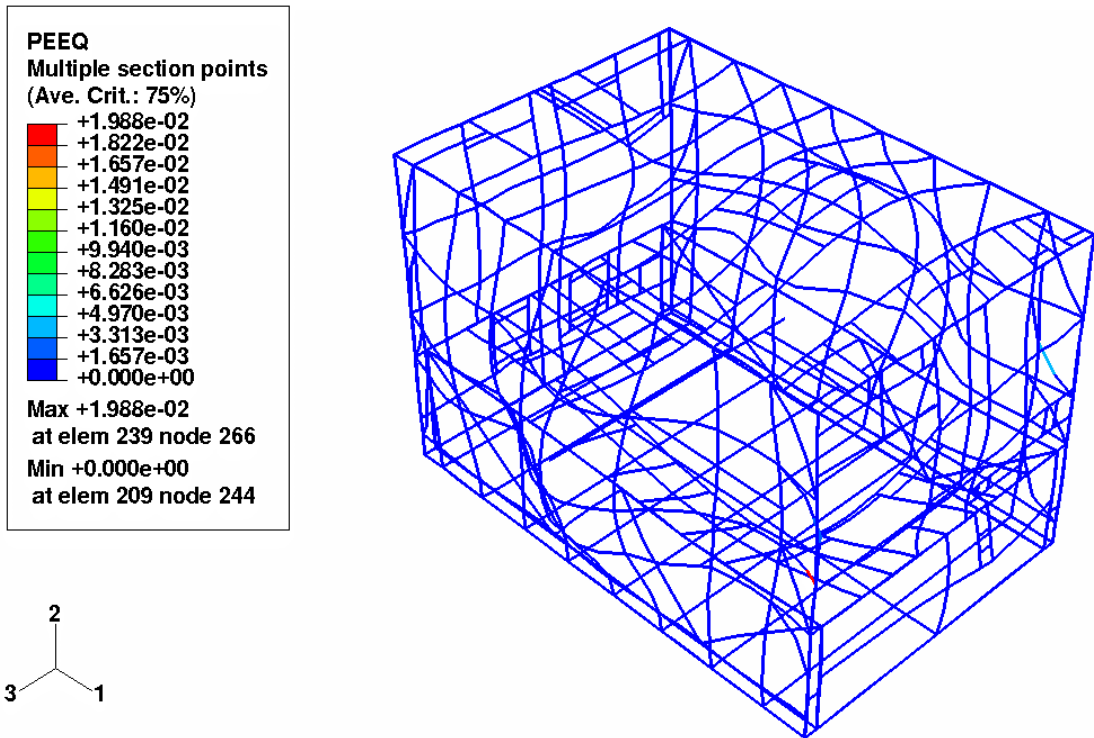


Fig. 16d: Maximum Effective Plastic Strain in the Left Frame of the Test Cell for 64 gm Combustion at 0.05 sec

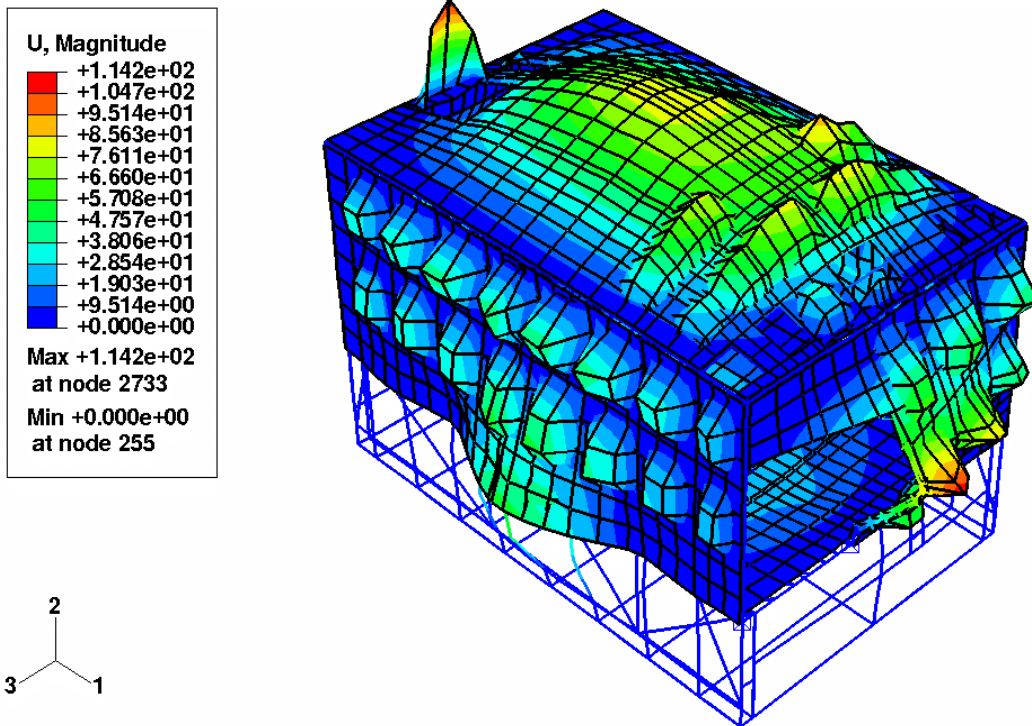


Fig. 17a: Deformed View of the Test Cell for Uniform Limiting Impulse of 0.012 MPa-s at 0.20 sec

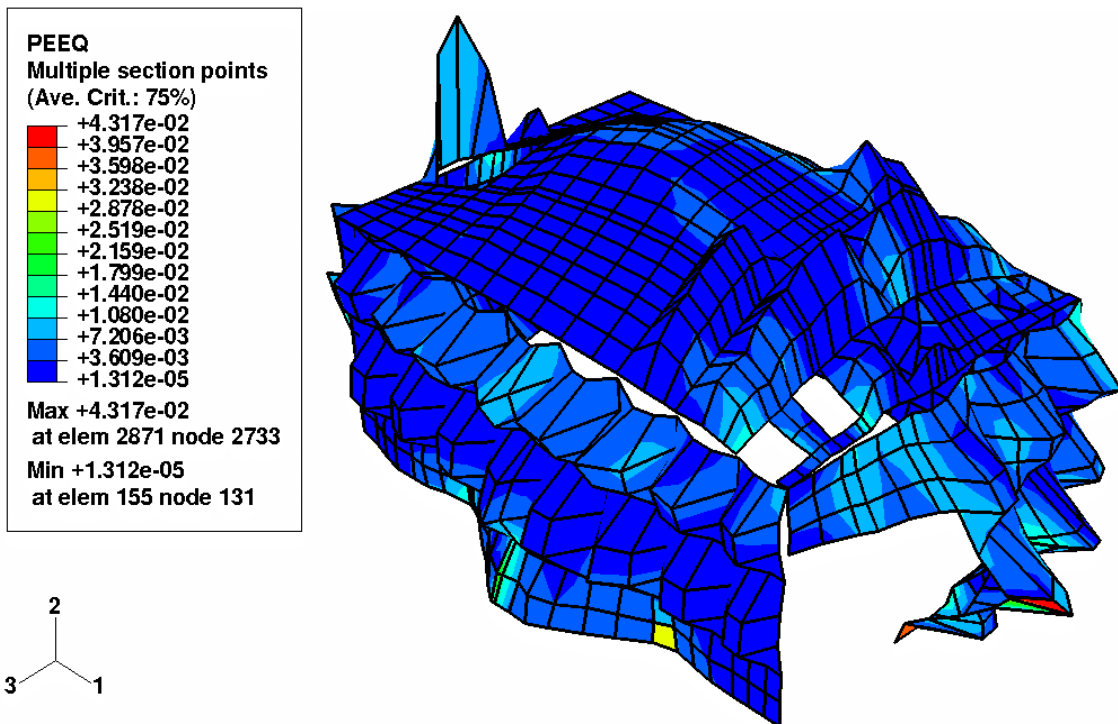


Fig. 17b: Maximum Effective Plastic Strain in the Corrugated Front Wall of the Test Cell for Uniform Limiting Long Duration Impulse of 0.012 MPa-s at 0.20 sec

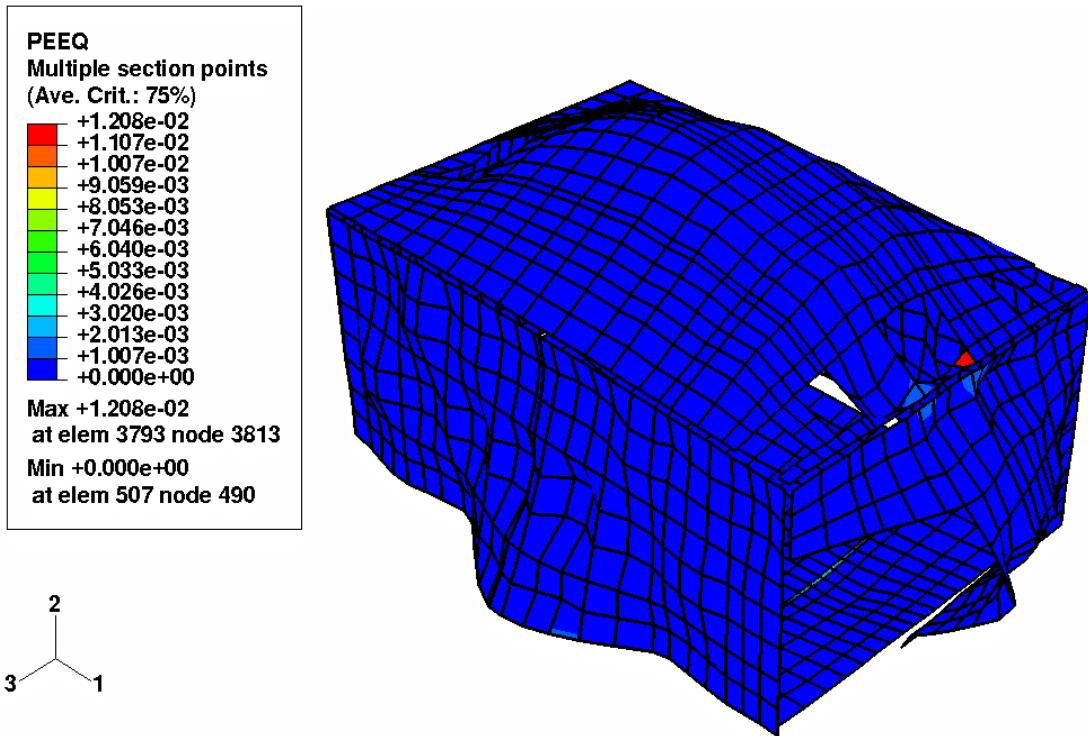


Fig. 17c: Maximum Effective Plastic Strain in the Outer Ceiling Plate of the Test Cell for Uniform Limiting Long Duration Impulse of 0.012 MPa-s at 0.20 sec

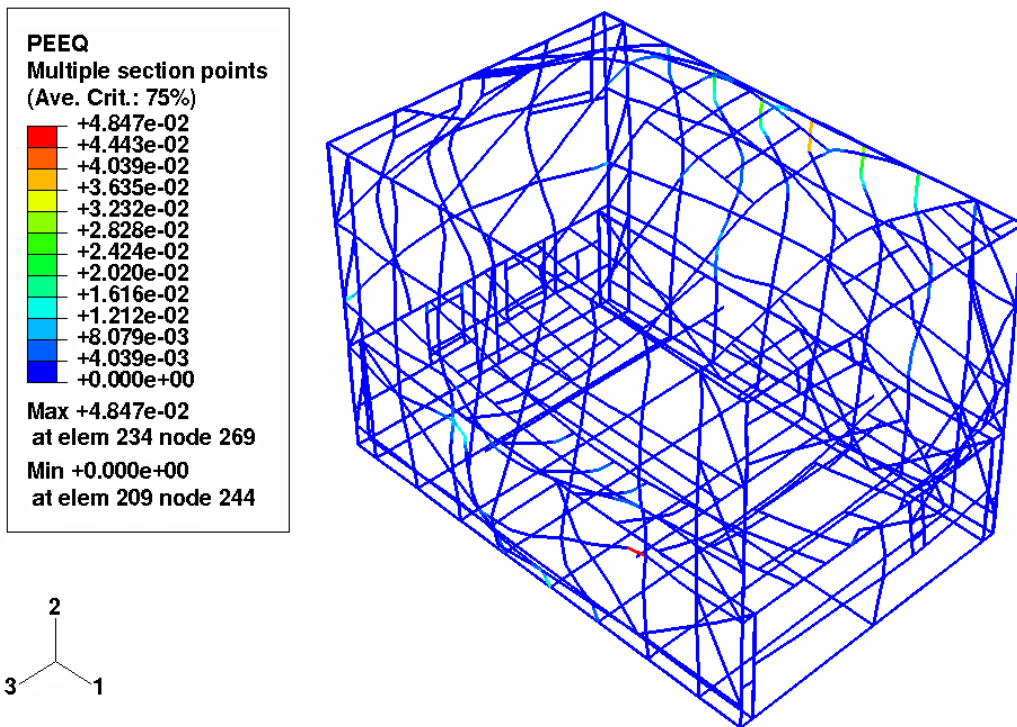


Fig. 17d: Maximum Effective Plastic Strain in the Left Frame of the Test Cell for Uniform Limiting Long Duration Impulse of 0.012 MPa-s at 0.20 sec

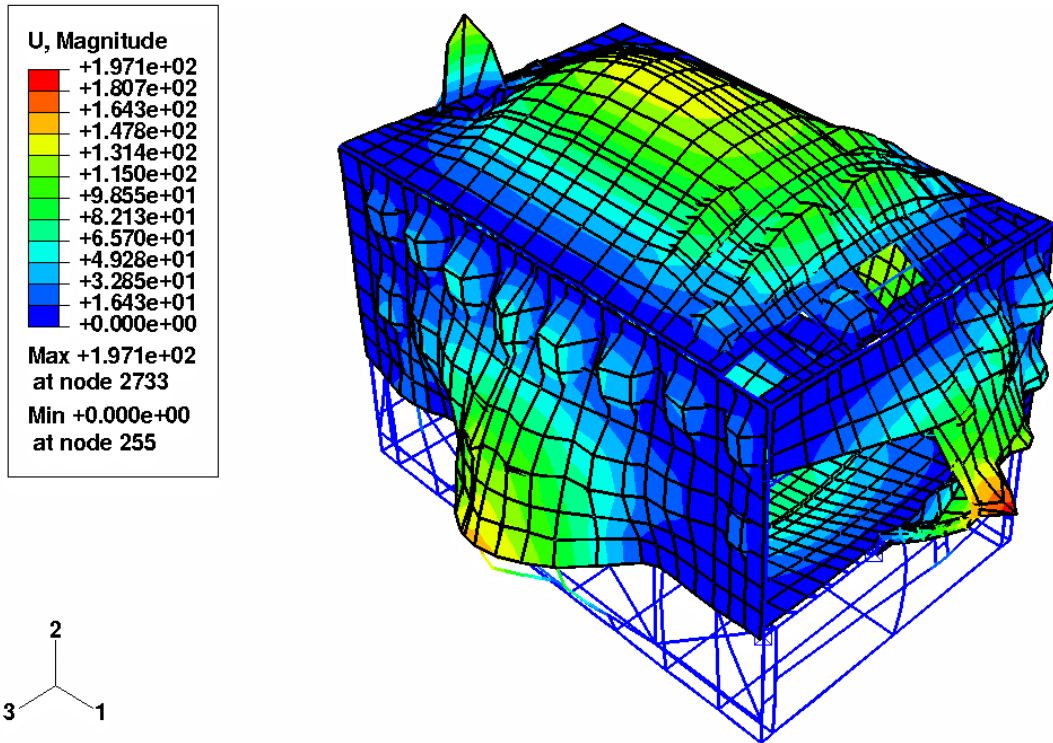


Fig. 18a: Deformed View of the Test Cell for Uniform Limiting Short Duration Impulse of 1.575E-3 MPa-s at 0.02 sec

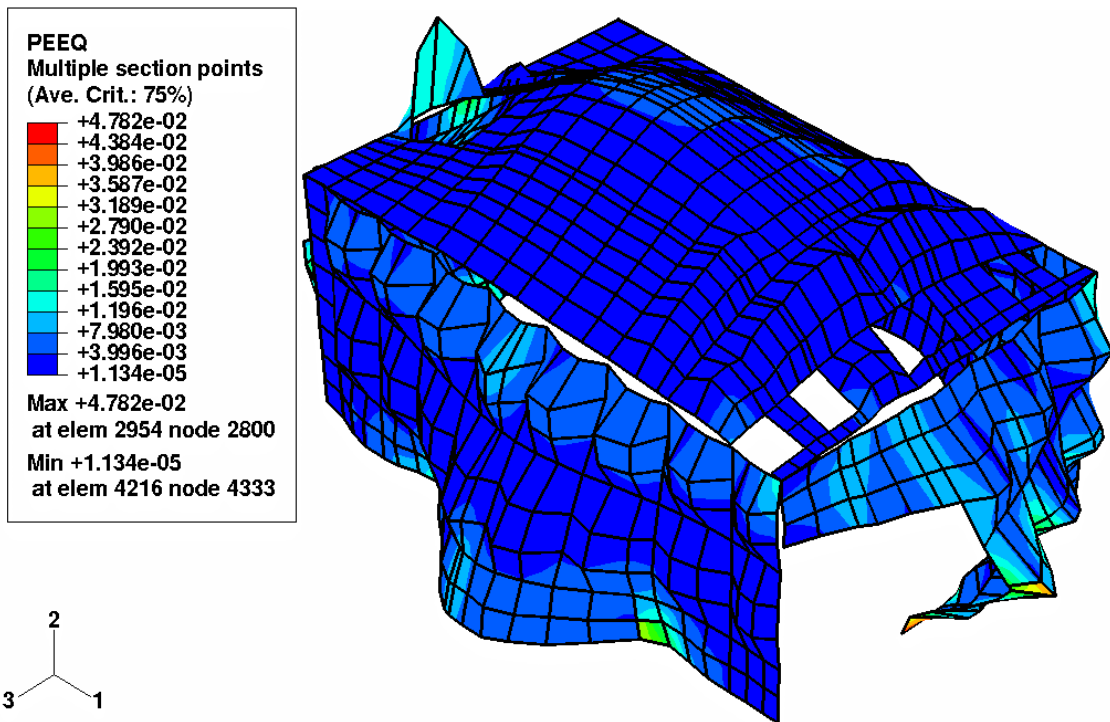


Fig. 18b: Maximum Effective Plastic Strain in the Corrugated Front Wall of the Test Cell for Limiting Short Duration Impulse of 1.575E-3 MPa-s at 0.02 sec

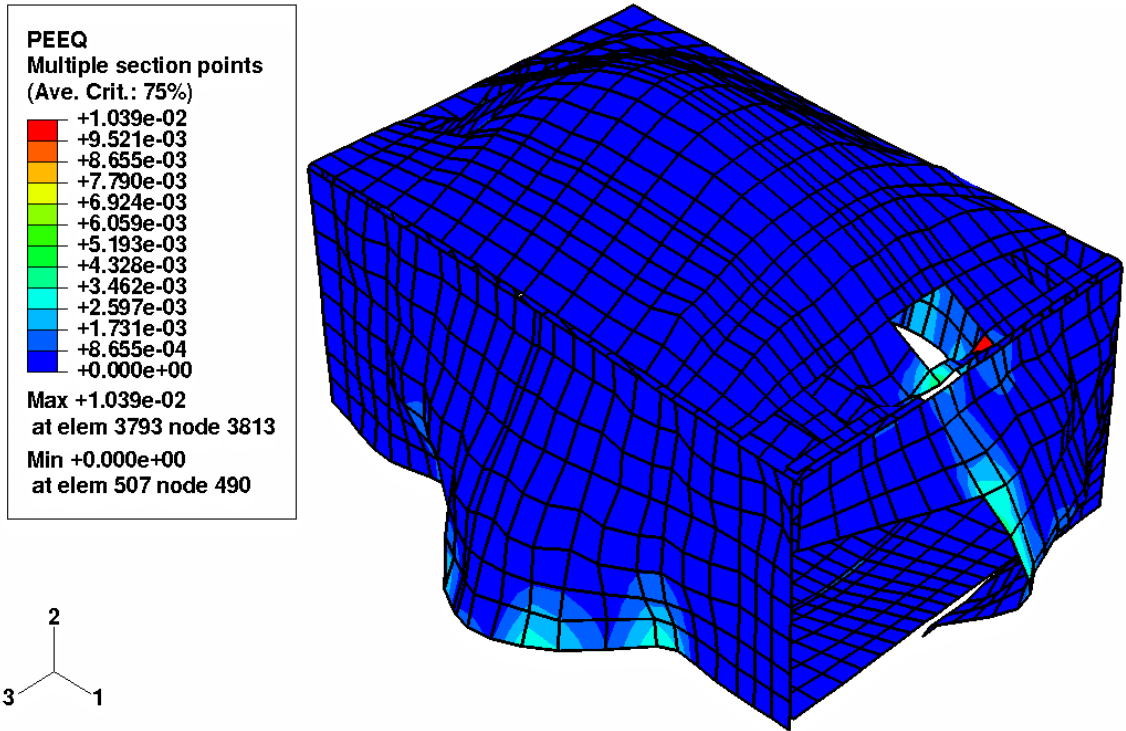


Fig. 18c: Maximum Effective Plastic Strain in the Outer Ceiling Plate of the Test Cell for Limiting Short Duration Impulse of 1.575E-3 MPa-s at 0.02 sec

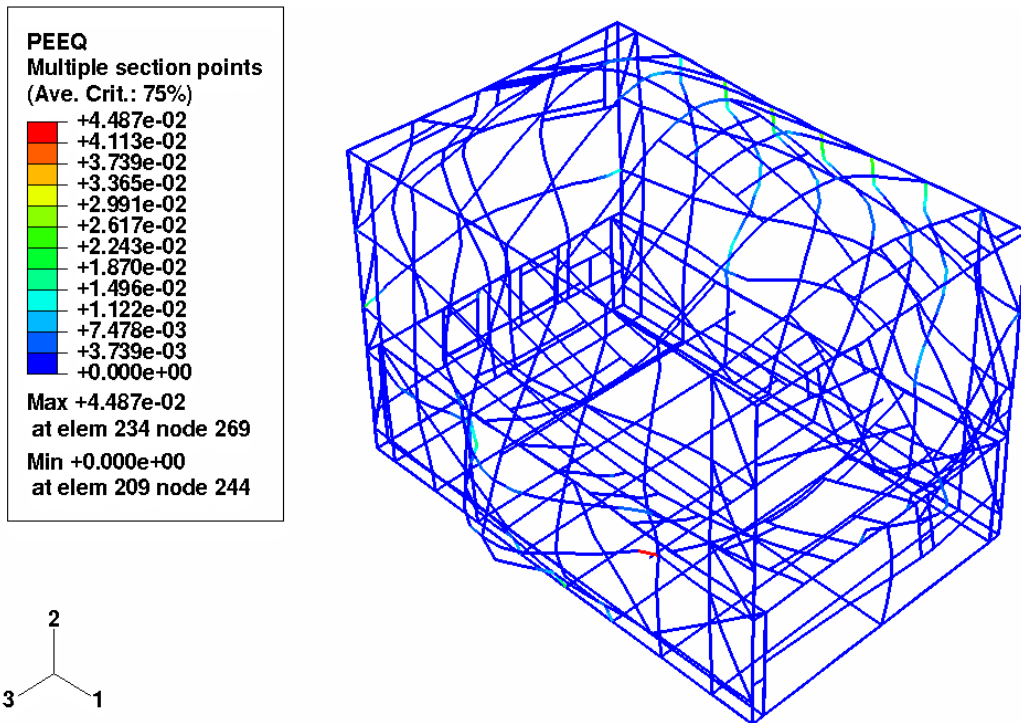


Fig. 18d: Maximum Effective Plastic Strain in the Left Frame of the Test Cell for Uniform Limiting Short Duration Impulse of 1.575E-3 MPa-s at 0.02 sec

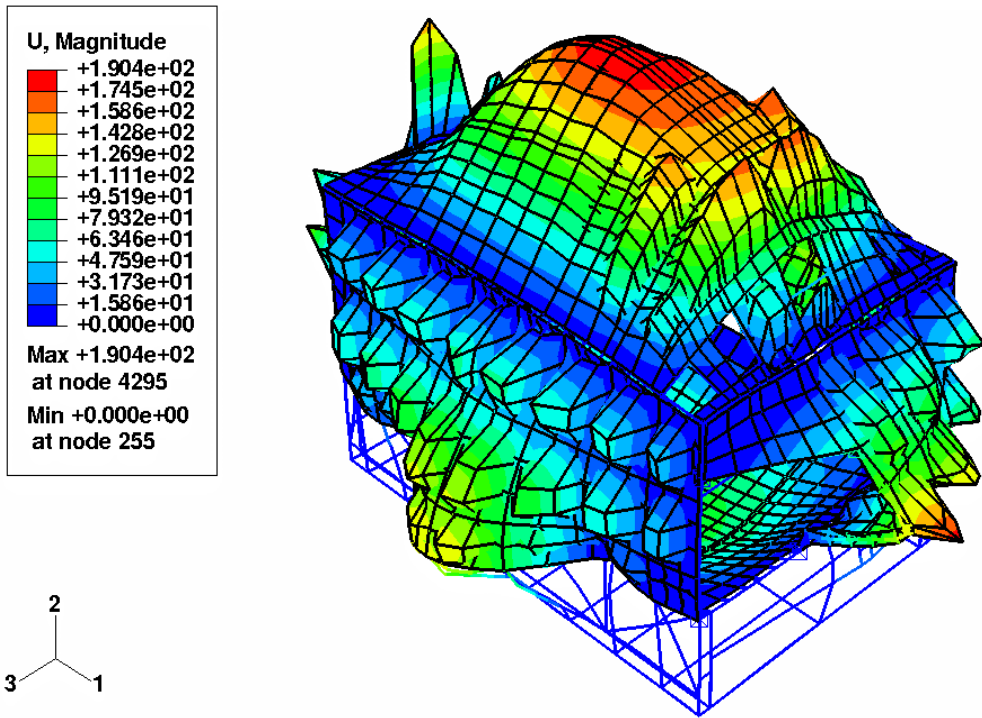


Fig. 19a: Deformed View of the Test Cell for Uniform Limiting Quasi-Static Pressure of 0.09 MPa at 0.5 sec

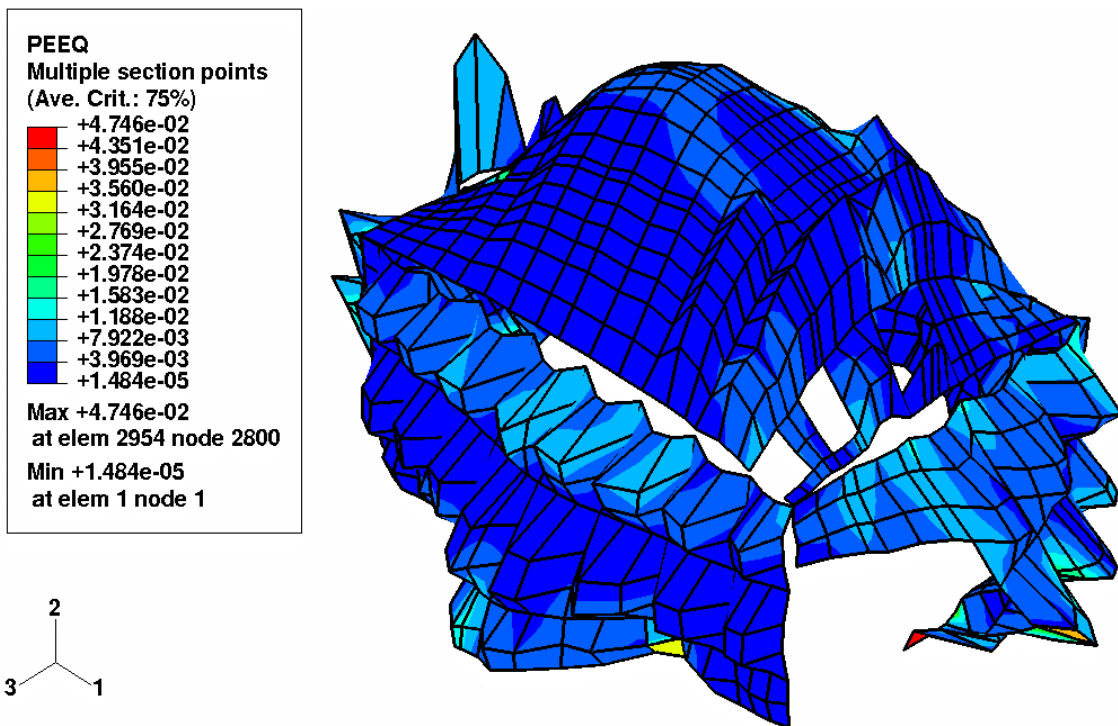


Fig. 19b: Maximum Effective Plastic Strain in the Corrugated Front Wall of the Test Cell for Uniform Limiting Quasi-Static Pressure of 0.09 MPa at 0.5 sec

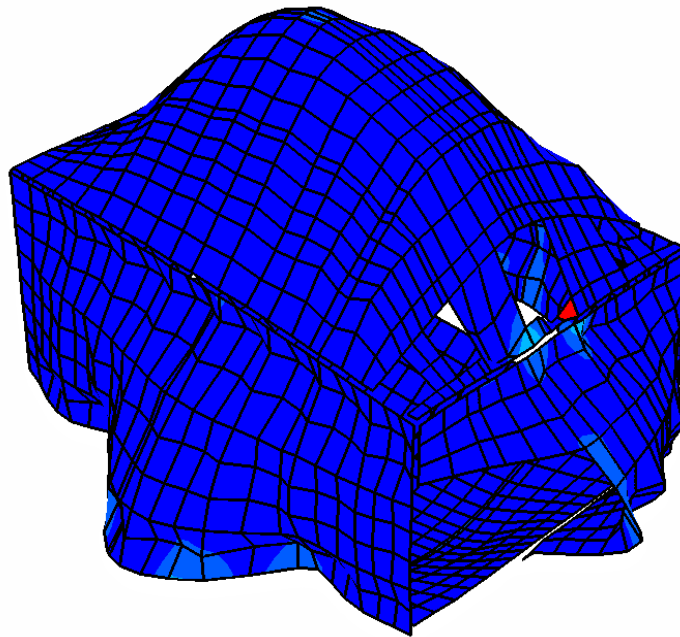
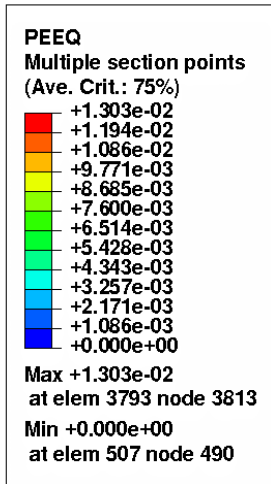


Fig. 19c: Maximum Effective Plastic Strain in the Outer Ceiling Plate of the Test Cell for Uniform Limiting Quasi-Static Pressure of 0.09 MPa at 0.5 sec

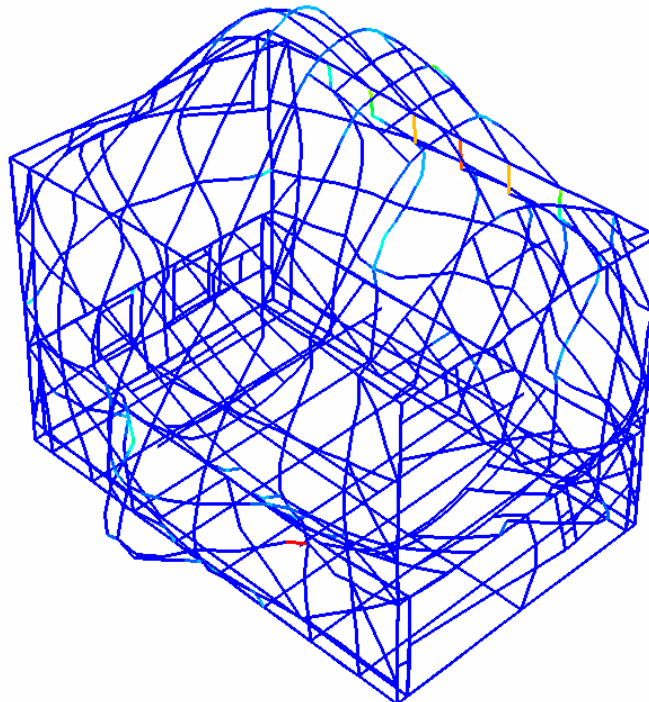
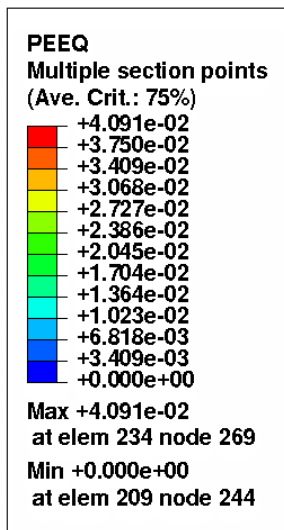


Fig. 19d: Maximum Effective Plastic Strain in the Left Frame of the Test Cell for Uniform Limiting Quasi-Static Pressure of 0.09 MPa at 0.5 sec

— U3 N: 702 NSET A3-L2-N2-PLATEA
 XMIN 1.000E+00
 XMAX 1.500E+00
 YMIN 1.772E-01
 YMAX 8.444E+01

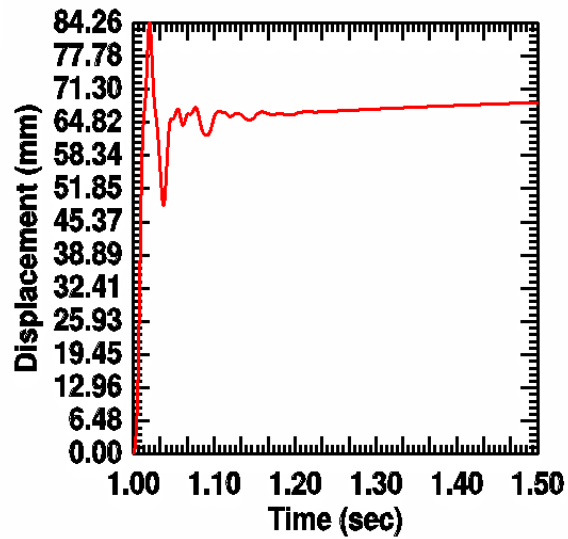


Fig. 20a: Displacement Time History on Left Plate at Transducer Laser L2/Needle N2 Positions for Quasi-Static Limiting Pressure of 0.09 MPa

— U3 N: 240 NSET A3-L2-N2-WALLA
 XMIN 1.000E+00
 XMAX 1.500E+00
 YMIN 1.905E-01
 YMAX 1.060E+02

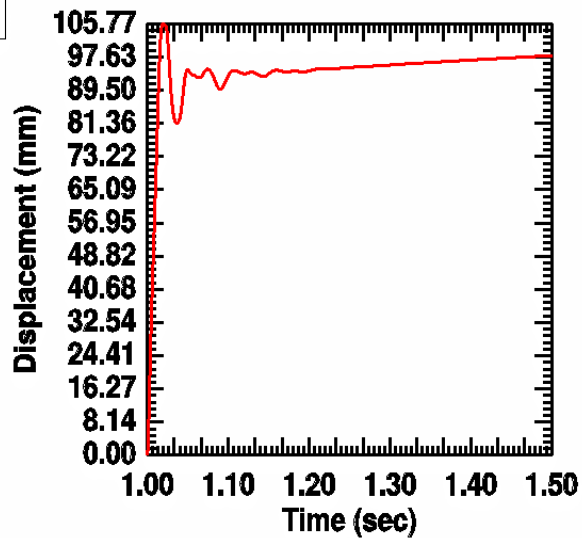


Fig. 20b: Displacement Time History on Left Wall at Transducer Laser L2/Needle N2 Positions for Quasi-Static Limiting Pressure of 0.09 MPa

— U3 N: 591 NSET N3-PLATEA
 XMIN 1.000E+00
 XMAX 1.500E+00
 YMIN 1.683E-01
 YMAX 8.461E+01

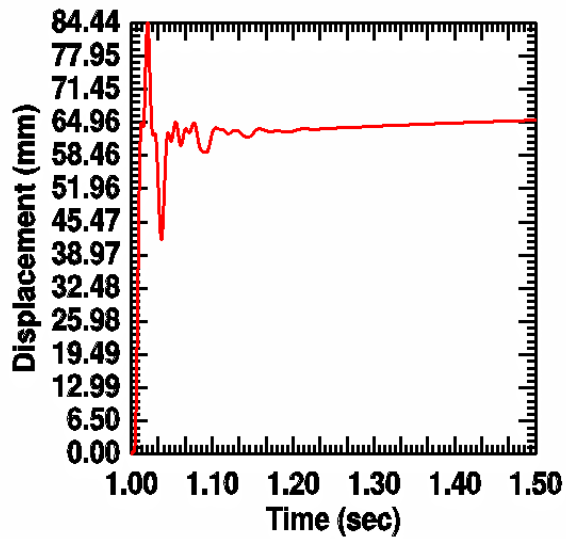


Fig. 20c: Displacement Time History on Left Plate at Transducer Needle N3 Position for Quasi-Static Limiting Pressure of 0.09 MPa

— U3 N: 239 NSET N3-WALLA
 XMIN 1.000E+00
 XMAX 1.500E+00
 YMIN 1.992E-01
 YMAX 1.168E+02

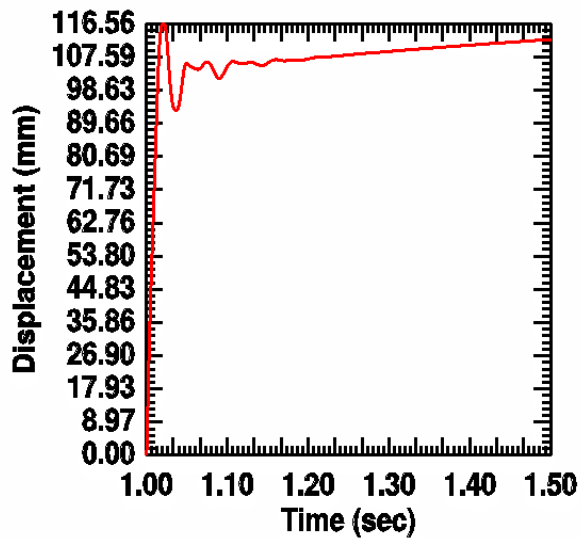


Fig. 20d: Displacement Time History on Left Wall at Transducer Needle N3 Position for Quasi-Static Limiting Pressure of 0.09 MPa

— U1 N: 3008 NSET A13-N4-N5-PLATE2
 XMIN 1.000E+00
 XMAX 1.500E+00
 YMIN -1.085E+02
 YMAX 2.181E-02

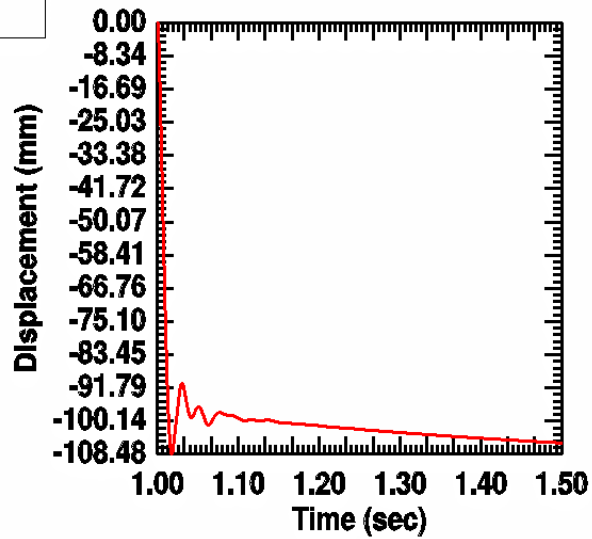


Fig. 20e: Displacement Time History on Rear Plate at Transducer Needle N4/Needle N5 Positions for Quasi-Static Limiting Pressure of 0.09 MPa

— U1 N: 3228 NSET A13-N4-N5-WALL2
 XMIN 1.000E+00
 XMAX 1.500E+00
 YMIN -1.082E+02
 YMAX 2.368E-02

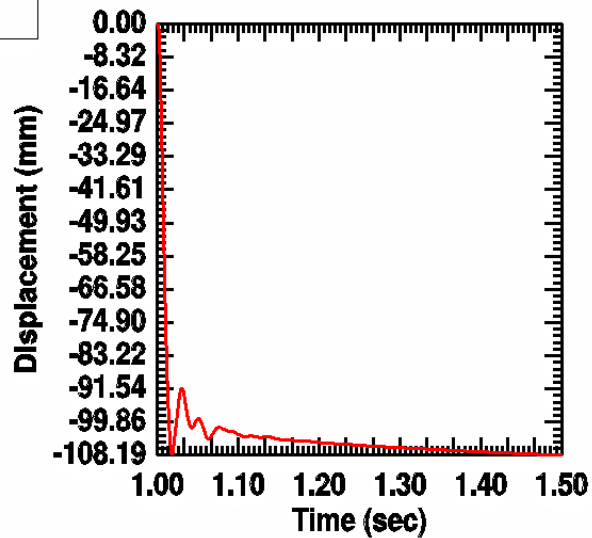


Fig. 20f: Displacement Time History on Rear Wall at Transducer Needle N4/Needle N5 Positions for Quasi-Static Limiting Pressure of 0.09 MPa

— U3 N: 2470 NSET N6-PLATEB
 XMIN 1.000E+00
 XMAX 1.500E+00
 YMIN -1.117E+02
 YMAX 5.208E-01

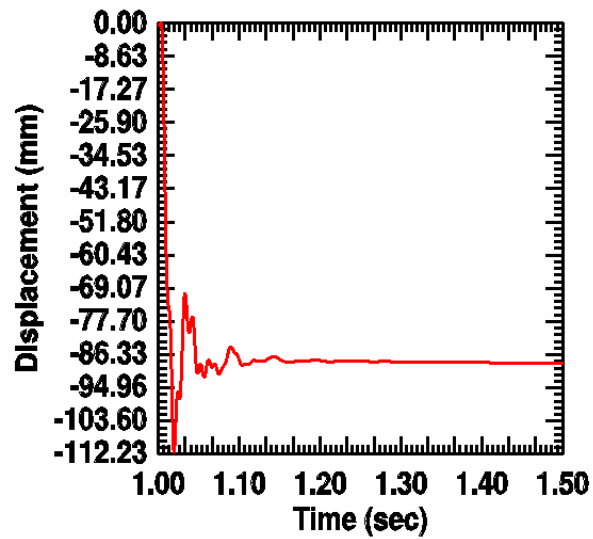


Fig. 20g: Displacement Time History on Right Plate at Transducer Needle N6 Position for Quasi-Static Limiting Pressure of 0.09 MPa

— U3 N: 2227 NSET N6-WALLB
 XMIN 1.000E+00
 XMAX 1.500E+00
 YMIN -1.238E+02
 YMAX -2.156E-01

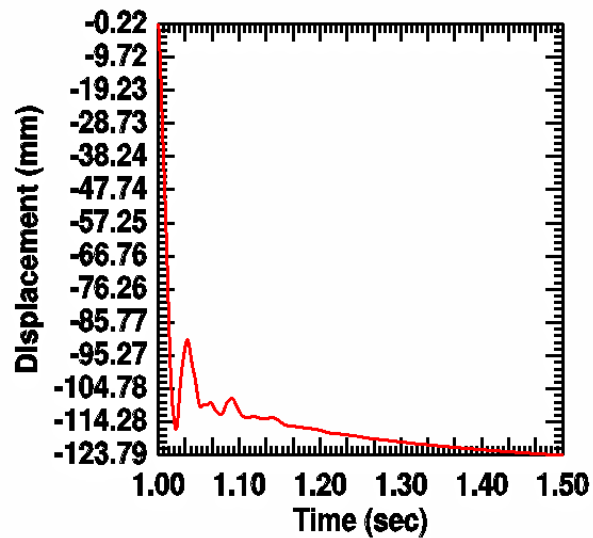
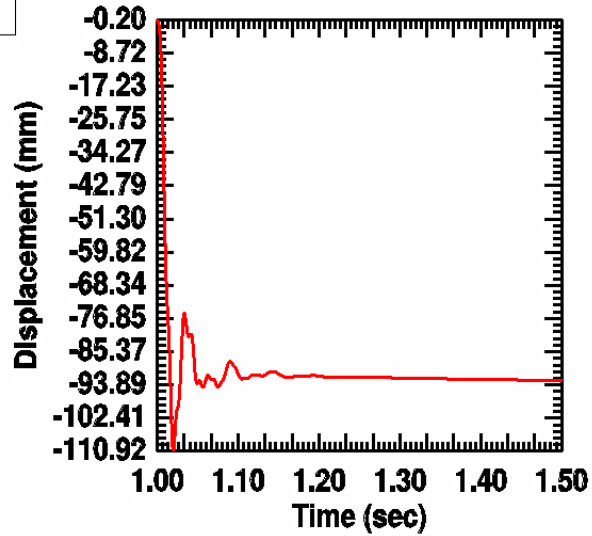


Fig. 20h: Displacement Time History on Right Wall at Transducer Needle N6 Position for Quasi-Static Limiting Pressure of 0.09 MPa

— U3 N: 2472 NSET A17-N7-PLATEB
 XMIN 1.000E+00
 XMAX 1.500E+00
 YMIN -1.109E+02
 YMAX -2.008E-01



**Fig. 20i: Displacement Time History on Right Plate at Transducer Needle N7
 Position for Quasi-Static Limiting Pressure of 0.09 MPa**

— U3 N: 2229 NSET A17-N7-WALLB
 XMIN 1.000E+00
 XMAX 1.500E+00
 YMIN -1.161E+02
 YMAX -2.141E-01

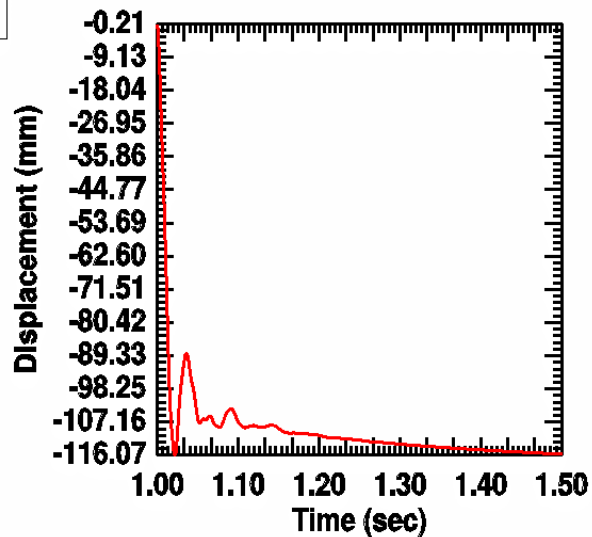


**Fig. 20j: Displacement Time History on Right Wall at Transducer Needle N7
 Position for Quasi-Static Limiting Pressure of 0.09 MPa**

— U1 N: 2571 NSET N8-N9-L10-PLATE1
 XMIN 1.000E+00
 XMAX 1.500E+00
 YMIN 2.610E-03
 YMAX 8.806E+01

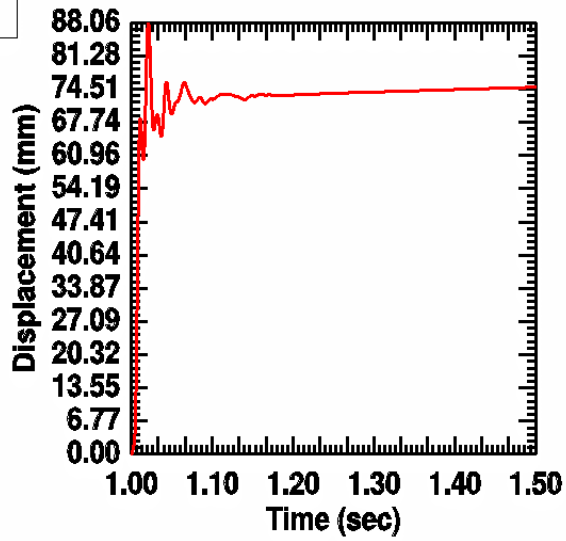


Fig. 20k: Displacement Time History on Front Plate at Transducer Needle N8/N9/Laser L1 Positions for Quasi-Static Limiting Pressure of 0.09 MPa

— U1 N: 2838 NSET N8-N9-L10-WALL1
 XMIN 1.000E+00
 XMAX 1.500E+00
 YMIN -3.429E-02
 YMAX 1.244E+02

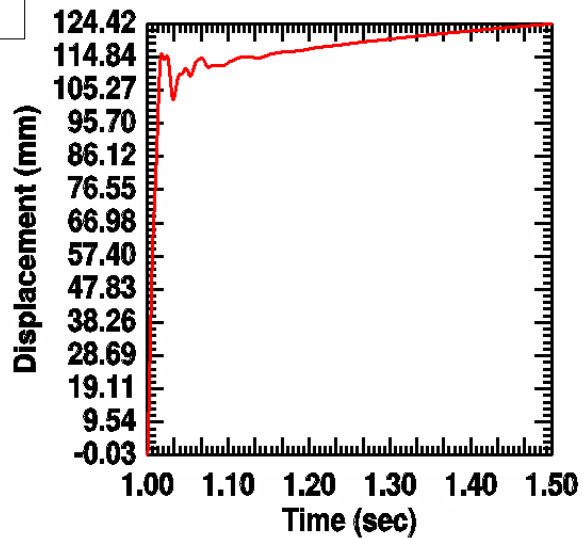


Fig. 20l: Displacement Time History on Front Wall at Transducer Needle N8/N9/Laser L1 Positions for Quasi-Static Limiting Pressure of 0.09 MPa

ANNEX II: Tables

Table 1: Mechanical Properties of Steels 1

Isotropic Properties of Steel grades for I Beams, Corrugated Sheet and Outer Steel Plate

Mechanical Properties 52-3	Steel St 37-2	Steel St
Young's Modulus of Elasticity (MPa)	2.1E05	2.1E05
Poisson's Ratio	0.3	0.3
Yield Stress (MPa)	235	355
Ultimate Stress (MPa)	340	510
% Elongation	26	22
Density (Kg/m ³)	7800	7800

Orthotropic Properties of Inner Corrugated Wall and Stiffened Plates

E_x (MPa)	E_y (MPa)	ν_{xy}	G_{xy} (MPa)	G_{xz} (MPa)	G_{yz} (MPa)
1.05483E10 1.15384E5 ^a	2.30769E5	0.3	2.30761E5	4.05703E9	
4.39243E7 8.54809E4 ^b	2.3066E5	0.3	2.28738E5	2.08406E5	
7.25047E5 8.54302E4 ^c	3.74448E5	0.3	2.05029E5	1.19791E5	

a- Inner Corrugated Wall Orthotropic Properties

b- Stiffened Floor Plate Orthotropic Properties

c- Floor Central Plate Orthotropic Properties

Uniform Damping Value ~ 7 % (as found during the hammer-test and the combustion experiments.) was used for all the transient implicit computations.

Notes

The following sign convention is used for defining corrugated wall / stiffened plate elastic orthotropic properties.

- E_x Young's modulus along the stiffener or corrugation direction (x)
- E_y Young's modulus perpendicular to stiffener or corrugation direction (y)
- ν_{xy} Poisson's ratio
- G_{xy} In-plane shear modulus of rigidity in xy plane
- G_{xz} Transverse shear modulus of rigidity along xz
- G_{yz} Transverse shear modulus of rigidity along yz

Table 2: Test Cell Maximum Displacement (mm) (Phase I Analysis)

Sensor Position	Experimental Results			Finite Element Model Results							
				LINK		FREE (Rotation free)		LINK-DAMPED (Damped Walls)		CONSTRAINED	
	PLATE	WALL		PLATE	WALL	PLATE	WALL	PLATE	WALL	PLATE	WALL
Laser L2/ Needle N2* (A-Left Wall)	16 gm	--	6.1/4.8*	+4.39	+10.0	+5.71	+10.4	+4.21	+9.12	+4.07	+4.31
	8 gm	--	4.1/3.3*	+2.19	+7.33	+3.03	+8.46	+2.09	+6.72	+2.92	+3.09
	4 gm	--	3.3/1.9*	+1.22	+5.62	+1.81	+6.02	+1.17	+4.95	+2.03	+2.15
	2 gm	--	1.5/0.9*	+1.12	+4.32	+1.62	+4.70	+1.12	+3.81	+1.37	+1.46
Needle N3 (A-Left Plate)	16 gm	6.6	--	+5.82	+14.6	+6.59	+15.6	+5.62	+13.1	+6.72	+7.10
	8 gm	4.0	--	+3.07	+11.0	+3.70	+12.8	+2.99	+10.0	+4.85	+5.13
	4 gm	2.4	--	+1.59	+8.40	+2.08	+9.01	+1.56	+7.34	+3.38	+3.58
	2 gm	1.0	--	+1.09	+6.73	+1.62	+7.20	+1.09	+5.98	+2.19	+2.31
Needle N4-N5 (2-Rear Plate -Wall*)	16 gm	5.6	7.3*	-6.57	-6.55	-12.4	-8.36	-6.47	-6.45	-0.454	-0.454
	8 gm	3.4	4.8*	-4.09	-4.08	-7.75	-5.25	-4.03	-4.02	-0.253	-0.253
	4 gm	2.0	3.4*	-2.40	-2.40	-5.10	-3.07	-2.40	-2.39	-0.142	-0.142
	2 gm	0.8	1.5*	-1.17	-1.17	-2.64	-1.88	-1.16	-1.16	-0.109	-0.109
Needle N6 (B-Right Plate)	16 gm	6.2	--	-8.84	-10.8	-8.75	-12.1	-8.62	-9.54	-0.752	-0.770
	8 gm	3.4	--	-4.71	-7.71	-4.21	-8.92	-4.63	-6.83	-0.477	-0.488
	4 gm	2.0	--	-2.30	-5.62	-2.45	-6.15	-2.23	-4.97	-0.302	-0.310
	2 gm	0.9	--	-1.57	-4.19	-2.40	-4.71	-1.57	-3.70	-0.170	-0.175
Needle N7 (B-Right Wall)	16 gm	--	5.7	-6.44	-7.92	-6.77	-8.95	-6.26	-7.05	-0.658	-0.670
	8 gm	--	3.3	-3.55	-5.67	-5.07	-6.29	-3.48	-5.23	-0.412	-0.419
	4 gm	--	2.0	-1.84	-4.11	-2.94	-4.46	-1.79	-3.70	-0.260	-0.262
	2 gm	--	0.9	-1.61	-2.82	-2.40	-3.14	-1.61	-2.51	-0.152	-0.155

Table 2 (Continued) Test Cell Maximum Displacement (mm) (Phase I Analysis)

Sensor Position	Experimental Results				Finite Element Model Results							
			LINK		FREE (Rotation free)		LINK-DAMPED (Damped Walls)		CONSTRAINED			
	PLATE	WALL	PLATE	WALL	PLATE	WALL	PLATE	WALL	PLATE	WALL		
Needle N8-N9	16 gm	7.6	5.0/5.4*	+3.83	+14.6	+5.15	+16.2	+3.80	+13.5	+8.03	+8.03	
(1-Front Plate	8 gm	4.6	3.2/3.8*	+2.38	+11.9	+3.36	+13.0	+2.38	+11.0	+6.15	+6.15	
-Wall) /	4 gm	3.1	2.4/2.8*	+1.14	+7.46	+1.69	+8.62	+1.16	+7.05	+5.76	+5.76	
Laser L1*	2 gm	1.6	1.2/1.7*	+0.563	+ 6.58	+1.51	+7.34	+0.569	+5.93	+2.98	+2.98	
(1-Front Wall)												

NOTES

For comparison the maximum out of plane displacement (in bulging mode) has been included in the experimental results along with the finite element predictions for the following four cases described below. The polarity sign (+/-) of finite element results is only indicative of the coordinate system adopted for the computational model and it always represents the bulging mode of deformation.

LINK Model - This finite element model simulates stiff link connections between the inner corrugated wall and the frame structure and between the outer plate and the frame structure. It provides constraints to displacement and rotation degrees of freedom with uniform damping of 7 percent for the test cell structure.

FREE Model - This finite element model simulates stiff link connections between the inner corrugated wall and the frame structure and between the outer plate and the frame structure. It provides constraints to only displacement degrees of freedom with uniform damping of 7 percent for the test cell structure.

LINK-DAMPED Model – This finite element model is same as LINK model with higher damping value of 10 percent for the inner corrugated walls and 7 percent damping for the other members of the test cell structure.

CONSTRAINED Model – This finite element model simulates ideal constraint between the inner corrugated wall and the outer plate structure with link connections to the frame structure. A uniform damping of 7 percent is used in this case.

Table 3: Test Cell Maximum Accelerations (10^6 mm/sec²) (Phase I Analysis)

Sensor Position	Experimental Results		Finite Element Model Results								
			LINK		FREE (Rotation free)		LINK-DAMPED (Damped Walls)		CONSTRAINED		
	PLATE	WALL	PLATE	WALL	PLATE	WALL	PLATE	WALL	PLATE	WALL	
7B (1-Front Wall)	16 gm	--	2.06	+0.445	+1.51	+0.633	+2.77	+0.494	+1.22	+0.405	+0.405
	8 gm	--	1.47	+0.295	+1.05	+0.273	+2.21	+0.300	+0.842	+0.285	+0.285
	4 gm	--	1.18	+0.164	+0.623	+0.140	+1.22	+0.160	+0.464	+0.174	+0.174
	2 gm	--	0.59	+0.117	+0.318	+0.0818	+0.601	+0.114	+0.301	+0.106	+0.106
15B ¹ (Ceiling Wall)	16 gm	--	10.1	+1.19	+4.87	+1.29	+5.11	+1.06	+4.01	+0.567	+0.599
	8 gm	--	5.0	+0.564	+3.18	+0.662	+3.27	+0.573	+2.60	+0.409	+0.431
	4 gm	--	2.35	+0.282	+1.97	+0.376	+2.08	+0.290	+1.59	+0.277	+0.291
	2 gm	--	2.24	+0.195	+1.07	+0.204	+1.14	+0.193	+0.861	+0.147	+0.154
3B (Ceiling Wall)	16 gm	--	1.67	+0.621	+0.621	+0.580	+0.595	+0.619	+0.619	+0.437	+0.436
	8 gm	--	1.01	+0.419	+0.420	+0.393	+0.404	+0.419	+0.419	+0.314	+0.313
	4 gm	--	0.56	+0.263	+0.264	+0.251	+0.258	+0.262	+0.263	+0.196	+0.196
	2 gm	--	0.44	+0.147	+0.147	+0.143	+0.146	+0.147	+0.147	+0.0920	+0.0920
1B (B-Right Wall)	16 gm	--	1.26	-0.540	-3.39	-1.14	-3.15	-0.531	-3.17	-0.764	-0.786
	8 gm	--	0.87	-0.341	-2.27	-0.771	-2.02	-0.330	-2.05	-0.465	-0.478
	4 gm	--	0.55	-0.180	-1.45	-0.520	-1.29	-0.177	-1.31	-0.297	-0.305
	2 gm	--	0.30	-0.0963	-0.782	-0.280	-0.714	-0.0911	-0.697	-0.178	-0.183
3A (A-Left Wall)	16 gm	--	1.34	+0.472	+6.08	+0.709	+6.52	+0.470	+5.77	+1.34	+1.41
	8 gm	--	0.79	+0.224	+4.06	+0.511	+4.26	+0.230	+3.84	+0.880	+0.929
	4 gm	--	0.53	+0.145	+2.59	+0.372	+2.72	+0.150	+2.43	+0.569	+0.602
	2 gm	--	0.34	+0.101	+1.43	+0.213	+1.50	+0.103	+1.35	+0.312	+0.330

¹ The experimental record of acceleration is associated with instrument problems and this transducer data may not be reliable.

Table 4: Test Cell Maximum Displacement (mm) with Improved Corrugated Wall and Bolt Model (Phase II Analysis)

Sensor Position	Experimental Results			Finite Element Model Results						BOLTED-WALL CONSTRAINED -PLATE MODEL	
				LINK		BOLTED- WALL		BOLTED-WALL-PLATE			
	PLATE	WALL		PLATE	WALL	PLATE	WALL	PLATE	WALL	PLATE	WALL
Laser L2/ Needle N2* (A-Left Wall)	16 gm	--	6.1/4.8*	+4.21	+7.22	+6.95	+8.84	+8.63	+9.95	+5.94	+6.13
	8 gm	--	4.1/3.3*	+2.05	+5.29	+3.67	+6.60	+4.50	+6.45	+4.21	+4.36
	4 gm	--	3.3/1.9*	+1.16	+3.79	+2.40	+4.66	+3.53	+4.43	+2.79	+2.89
	2 gm	--	1.5/0.9*	+1.07	+2.85	+2.40	+3.16	+3.53	+3.68	+1.80	+1.87
Needle N3 (A-Left Plate)	16 gm	6.6	--	+6.00	+10.2	+8.66	+12.2	+9.10	+13.2	+7.72	+8.04
	8 gm	4.0	--	+3.09	+7.73	+4.98	+9.12	+6.17	+8.78	+5.21	+5.41
	4 gm	2.4	--	+1.64	+5.51	+2.86	+6.52	+3.99	+6.35	+3.49	+3.64
	2 gm	1.0	--	+1.04	+4.28	+2.29	+4.93	+3.47	+5.06	+2.47	+2.58
Needle N4-N5 (2-Rear Plate -Wall*)	16 gm	5.6	7.3*	-6.67	-6.65	-8.50	-7.00	-17.4	-10.9	-5.96	-5.96
	8 gm	3.4	4.8*	-4.24	-4.22	-5.37	-4.05	-11.4	-6.35	-3.61	-3.61
	4 gm	2.0	3.4*	-2.51	-2.51	-3.16	-2.34	-6.79	-4.77	-2.28	-2.28
	2 gm	0.8	1.5*	-1.20	-1.19	-2.37	-2.34	-4.82	-4.77	-1.19	-1.19
Needle N6 (B-Right Plate)	16 gm	6.2	--	-9.21	-7.76	-8.22	-9.70	-10.4	-9.63	-4.99	-5.08
	8 gm	3.4	--	-4.87	-5.59	-5.11	-6.70	-6.46	-6.05	-3.05	-3.10
	4 gm	2.0	--	-2.20	-3.79	-3.03	-4.17	-4.18	-4.29	-1.88	-1.91
	2 gm	0.9	--	-1.45	-2.67	-2.48	-3.08	-3.79	-3.90	-1.83	-1.85
Needle N7 (B-Right Wall)	16 gm	--	5.7	-5.36	-6.46	-6.36	-7.94	-9.48	-8.07	-4.60	-4.66
	8 gm	--	3.3	-3.35	-4.59	-3.69	-5.31	-5.17	-5.03	-3.04	-3.09
	4 gm	--	2.0	-1.62	-2.93	-2.52	-3.20	-3.82	-3.93	-1.96	-1.99
	2 gm	--	0.9	-1.48	-1.87	-2.52	-2.55	-3.82	-3.93	-1.85	-1.87

Table 4 (Continued) Test Cell Maximum Displacement (mm) with Improved Corrugated Wall and Bolt Model (Phase II Analysis)

Sensor Position	Experimental Results		Finite Element Model Results						BOLTED-WALL CONSTRAINED -PLATE MODEL		
			LINK	BOLTED-WALL		BOLTED-WALL-PLATE		PLATE WALL	PLATE WALL		
	LATE WALL	PLATE WALL	PLATE WALL	PLATE WALL	PLATE WALL	PLATE WALL	PLATE WALL	PLATE WALL	PLATE WALL		
Needle N8-N9 (1-Front Plate -Wall) / Laser L1* (1-Front Wall)	16 gm 8 gm 4 gm 2 gm	7.6 4.6 3.1 1.6	5.0/5.4* 3.2/3.8* 2.4/2.8* 1.2/1.7*	+3.88 +2.68 +1.27 +0.589	+11.2 +8.77 +6.34 +4.47	+6.75 +3.59 +2.08 +1.73	+15.2 +11.4 +7.52 +5.51	+13.3 +5.99 +3.63 +3.63	+14.6 +11.2 +9.34 +5.47	+9.44 +6.85 +5.70 +3.09	+9.44 +6.85 +5.70 +3.09

NOTES

For comparison the maximum out of plane displacement (in bulging mode) has been included in the experimental results along with the finite element predictions for the following four cases described below. The polarity sign (+/-) of computational results is only indicative of the coordinate system adopted for the computational model and it always represents the bulging mode of deformation.

LINK Model - This finite element model simulates stiff link connections between the inner corrugated wall and frame structure and between the outer plate and the frame structure. It simulates the most rigid connection between the structural members.

BOLTED-WALL Model - This finite element model simulates the bolt stiffness between the inner corrugated plate and the frame structure and stiff link is simulated between the outer plate and the frame structure.

BOLTED-WALL-PLATE Model – This finite element model uses identical bolt stiffness values between the outer plate and the frame structure and between the inner corrugated wall and the frame structure. This model simulates most flexible connection.

BOLTED-WALL CONSTRAINED-PLATE Model– This finite element model simulates ideal constraint between the inner corrugated wall and the outer plate structure with bolt connections between the corrugated wall and the frame structure. Thus at the frame grid locations the inner corrugated wall and the outer plate are kinematically constrained to have identical displacements.

Table 5: Test Cell Maximum Accelerations (10^6 mm/sec²) with Improved Corrugated Wall and Bolt Model (Phase II Analysis)

Sensor Position		Experimental Results		Finite Element Model Results						BOLTED-WALL CONSTRAINED -PLATE MODEL	
				LINK		BOLTED- WALL		BOLTED-WALL-PLATE			
		PLATE	WALL	PLATE	WALL	PLATE	WALL	PLATE	WALL	PLATE	WALL
7B (1-Front Wall)	16 gm	--	2.06	+0.678	+0.879	+0.653	+1.79	+0.651	+1.75	+0.685	+0.685
	8 gm	--	1.47	+0.374	+0.629	+0.495	+1.45	+0.386	+1.22	+0.511	+0.511
	4 gm	--	1.18	+0.193	+0.373	+0.312	+0.942	+0.328	+0.747	+0.323	+0.323
	2 gm	--	0.59	+0.118	+0.213	+0.157	+0.474	+0.172	+0.416	+0.168	+0.168
15B ² (Ceiling Wall)	16 gm	--	10.1	+0.814	+2.35	+1.28	+3.37	+0.821	+3.31	+1.18	+1.19
	8 gm	--	5.0	+0.632	+1.54	+0.499	+2.20	+0.649	+2.16	+0.762	+0.768
	4 gm	--	2.35	+0.300	+0.940	+0.378	+1.32	+0.396	+1.30	+0.474	+0.497
	2 gm	--	2.24	+0.191	+0.507	+0.218	+0.739	+0.306	+0.734	+0.281	+0.294
3B (Ceiling Wall)	16 gm	--	1.67	+0.608	+0.608	+0.730	+2.85	+1.18	+2.82	+0.586	+0.582
	8 gm	--	1.01	+0.413	+0.413	+0.467	+1.59	+0.771	+1.61	+0.403	+0.400
	4 gm	--	0.56	+0.262	+0.263	+0.295	+0.857	+0.468	+0.868	+0.259	+0.257
	2 gm	--	0.44	+0.146	+0.146	+0.161	+0.398	+0.252	+0.407	+0.162	+0.163
1B (B-Right Wall)	16 gm	--	1.26	-0.535	-2.12	-1.39	-3.56	-1.01	-3.11	-1.17	-1.19
	8 gm	--	0.87	-0.294	-1.37	-0.788	-2.08	-0.663	-1.92	-0.768	-0.778
	4 gm	--	0.55	-0.161	-0.855	-0.490	-1.27	-0.445	-1.16	-0.491	-0.499
	2 gm	--	0.30	-0.103	-0.453	-0.260	-0.661	-0.219	-0.622	-0.274	-0.279
3A (A-Left Wall)	16 gm	--	1.34	+0.555	+4.52	+0.951	+5.46	+1.25	+5.52	+1.39	+1.43
	8 gm	--	0.79	+0.272	+2.93	+0.602	+3.39	+0.817	+3.51	+0.918	+0.941
	4 gm	--	0.53	+0.178	+1.88	+0.386	+2.10	+0.555	+2.20	+0.593	+0.608
	2 gm	--	0.34	+0.119	+1.02	+0.214	+1.13	+0.318	+1.20	+0.328	+0.336

² The experimental record of acceleration is associated with instrument problems and this transducer data may not be reliable.

Table 6: Maximum Energies (kJ) with Improved Corrugated Wall and Bolt Model (Phase II Analysis) for 16gm Combustion Experiment (Whole Model)

	LINK	BOLTED- WALL	BOLTED-WALL-PLATE	BOLTED-WALL CONSTRAINED -PLATE MODEL
Total Work	30.85	42.94	50.20	25.86
Internal Energy	2.865	3.658	4.489	2.498
Kinetic Energy	1.698	2.316	2.825	1.631
Strain Energy	1.965	2.669	3.279	1.828
Plastic Energy (% Dissipation)	1.526 (4.95)	2.134 (4.97)	2.850 (5.68)	1.485 (5.74)
Viscous Energy (% Dissipation)	28.06 (90.96)	39.51 (92.01)	45.06 (89.76)	23.39 (90.45)

Notes

1. The peak value of different energies over the entire impulse duration is included in this table for different models evolved for the present study.
2. The values within the bracket indicate the relative dissipation of energy with the total work (input energy) for the blast loaded test-cell.

Table 7: Maximum Energies (kJ) with Improved Corrugated Wall and Bolt Model (Phase II Analysis) (for Different Structural Members) - 16gm Combustion Experiment

	LINK			BOLTED- WALL			BOLTED-WALL-PLATE			BOLTED-WALL CONSTRAINED -PLATE MODEL		
Total Work (Whole Model)	30.85			42.94			50.20			25.86		
	WALL	PLATE	FRAME	WALL	PLATE	FRAME	WALL	PLATE	FRAME	WALL	PLATE	FRAME
Internal Energy	1.569	0.8355	0.7297	2.140	0.8518	1.228	2.208	1.215	1.568	1.413	0.3402	0.8065
Kinetic Energy	0.2236	0.6191	0.9354	0.4735	0.8694	1.203	0.5630	1.231	1.337	0.1620	0.7966	0.7663
Strain Energy	0.3805	0.7726	0.7297	0.2129	0.7897	1.228	0.2270	0.7973	1.568	0.0704	0.304	0.8065
Plastic Energy (% Dissipation)	1.402 (4.54)	0.1240 (0.40)	0.0000 (0.0)	2.023 (4.71)	0.0885 (0.21)	0.0222 (0.05)	2.087 (4.16)	0.7626 (1.51)	6.4E-4 (~0)	1.391 (5.38)	0.0941 (0.36)	0.0000 (0.0)
Viscous Energy (% Dissipation)	13.56 (44)	6.621 (21.5)	7.886 (25.6)	21.86 (50.9)	7.213 (16.8)	10.44 (24.3)	22.95 (45.7)	11.01 (21.9)	11.10 (22.1)	11.30 (43.7)	4.717 (18.2)	7.378 (28.5)

Notes

1. The peak value of energies for different structural members over the entire impulse duration is included in this table for different models evolved for the present study.
2. The values within the bracket indicate the relative dissipation of energy with the total work (input energy) for the blast loaded test-cell.

Table 8: Maximum Energies (kJ) with Improved Corrugated Wall and Bolt Model (Phase II Analysis) (for Different Structural Members) with LINK Model- 16gm Combustion Experiment with External Work of 30.85 kJ

Structural Members	Internal Energy	Kinetic Energy	Strain Energy	Plastic Energy	Viscous Energy
Whole Model	2.865	1.698	1.965	1.526	28.06
Wall-A	0.4541	0.1152	0.1479	0.4057	4.379
Plate-A	0.1980	0.1268	0.1979	0.000	1.127
Frame-A	0.1484	0.2679	0.1484	0.000	1.683
Wall-B	0.3616	0.09378	0.1145	0.2847	2.381
Plate-B	0.2403	0.2248	0.2402	0.000	1.440
Frame-B	0.1896	0.3526	0.1896	0.000	1.909
Wall-1	0.2336	0.04051	0.1161	0.1609	1.796
Plate-1	0.1016	0.07335	0.1016	0.000	0.3837
Frame-1	0.6212	0.1152	0.06212	0.000	0.5981
Wall-2	0.3781	0.1283	0.2530	0.2729	3.151
Plate-2	0.2641	0.2879	0.2640	0.000	1.039
Frame-2	0.1314	0.2753	0.1314	0.000	0.7035
Wall-Ceiling	0.3040	0.04057	0.04956	0.2774	1.849
Plate-Ceiling	0.2980	0.2376	0.2978	0.000	1.406
Frame- Ceiling	0.2278	0.2514	0.2278	0.000	1.711
Plate-Floor	0.2339	0.2206	0.1714	0.1240	1.226
Frame-Floor	0.2032	0.1587	0.2032	0.000	1.054
Frame-Support	0.07901	0.02397	0.07901	0.000	0.2270

Table 9: Maximum Energies (kJ) with Improved Corrugated Wall and Bolt Model (Phase II Analysis) for Different Combustion Experiments (Whole Model) with BOLTED-WALL Model

	2 gm Experiment	4 gm Experiment	8 gm Experiment	16 gm Experiment
Total Work	3.209	8.276	21.82	42.94
Internal Energy	0.547	1.147	1.985	3.658
Kinetic Energy	0.115	0.413	1.026	2.316
Strain Energy	0.140	0.452	1.149	2.669
Plastic Energy (% Dissipation)	0.466 (14.5)	0.698 (8.43)	1.416 (6.49)	2.134 (4.97)
Viscous Energy (% Dissipation)	2.635 (82.1)	7.009 (84.7)	19.69 (90.2)	39.51 (92.0)

Notes

1. The peak value of different energies over the entire impulse duration is included in this table for different combustion experiments.
2. The values within the bracket indicate the relative dissipation of energy with the total work (input energy) for the blast loaded test-cell.

Table 10: Maximum Energies (kJ) with Improved Corrugated Wall and Bolt Model (Phase II Analysis) for Different Combustion Experiments- Details of Energy Distribution in Different Structural Members with BOLTED-WALL Model

	2 gm Experiment			4 gm Experiment			8 gm Experiment			16 gm Experiment		
Total Work (Whole Model)	3.209			8.276			21.82			42.94		
	WALL	PLATE	FRAME	WALL	PLATE	FRAME	WALL	PLATE	FRAME	WALL	PLATE	FRAME
Internal Energy	0.482	0.0440	0.0654	0.759	0.1378	0.211	1.468	0.3492	0.5295	2.140	0.8518	1.228
Kinetic Energy	0.0194	0.0403	0.0600	0.0722	0.1462	0.215	0.1983	0.377	0.536	0.4735	0.8694	1.203
Strain Energy	0.0142	0.0439	0.0654	0.0571	0.1366	0.211	0.0917	0.3395	0.5295	0.2129	0.7897	1.228
Plastic Energy (Dissipation)	0.466 (14.5)	2.9E-5 (~0)	0.0000 (0.0)	0.697 (8.42)	9.6E-4 (0.01)	0.0000 (0.0)	1.402 (6.43)	0.0142 (0.07)	3.98E-4 (~0)	2.023 (4.71)	0.0885 (0.21)	0.0222 (0.05)
Viscous Energy (Dissipation)	1.460 (45.5)	0.454 (14.2)	0.7210 (22.5)	4.045 (48.9)	1.143 (13.8)	1.821 (22.0)	11.22 (51.4)	3.362 (15.4)	5.103 (23.4)	21.86 (50.9)	7.213 (16.8)	10.44 (24.3)

Notes

The peak value of energies for different structural members over the entire impulse duration is included in this table for different combustion experiments.

Table 11: Test Cell Maximum Displacement (mm) Prediction for 64 gm Combustion Case - Comparison with Limiting Impulsive and Quasi-Static Pressure Cases for BOLTED-WALL Model (Phase III Analysis)

Sensor	Case Studies	64 gm Case	Impulsive (0.015 sec)	Impulsive (0.15 sec)	Quasi-Static (0.09 MPa)
Laser L2/ Needle N2* (A-Left Wall)	PLATE	20.90	93.7	72.83	84.44
	WALL	26.88	114.5	94.00	106.00
Needle N3 (A-Left Plate)	PLATE	27.03	97.0	72.97	84.61
	WALL	32.36	123.3	103.4	116.8
Needle N4-N5 (2-Rear Plate -Wall*)	PLATE	25.41	132.2	89.17	108.5
	WALL	22.88	131.5	88.35	108.2
Needle N6 (B-Right Plate)	PLATE	27.22	130.8	93.90	111.7
	WALL	19.93	128.0	93.89	123.8
Needle N7 (B-Right Wall)	PLATE	21.87	127.7	92.13	110.9
	WALL	18.59	127.7	93.44	116.1
Needle N8-N9 (1-Front Plate -Wall) / Laser L1* (1-Front Wall)	PLATE	22.21	100.0	72.22	88.06
	WALL	26.79	134.6	98.31	124.4

For Impulsive (0.015 sec) Impulse value is 1.575E-3 MPa-sec, For Impulsive (0.15 sec) Impulse value is 1.2E-2 MPa-sec.

Table 12: Test Cell Maximum Energies (kJ) Prediction for 64gm Combustion Case- Comparison with Limiting Impulsive and Quasi-Static Pressure Cases for BOLTED-WALL Model (Phase III Analysis)

	64 gm Case			Impulsive Limit (0.015 sec)			Impulsive Limit (0.15 sec)			Quasi-Static Limit (0.09MPa)		
Total Work (Whole Model)	138.2			946.6			672.8			938.9		
	WALL	PLATE	FRAME	WALL	PLATE	FRAME	WALL	PLATE	FRAME	WALL	PLATE	FRAME
Internal Energy	10.36	6.982	10.47	114.1	127.5	322.7	91.32	83.63	281.6	128.3	117.8	383.5
Kinetic Energy	2.634	6.288	7.281	12.31	82.51	75.53	7.54	45.79	37.07	9.31	59.2	50.4
Strain Energy	1.495	6.515	9.905	9.19	97.33	116.8	8.00	71.66	102.3	8.65	90.1	119.2
Plastic Energy (% Dissipation)	8.898 (6.44)	0.912 (0.66)	2.430 (1.76)	97.04 (10.3)	39.62 (4.19)	233.7 (24.7)	83.98 (12.5)	17.91 (2.66)	215.9 (32.1)	106.4 (15.8)	34.5 (5.13)	275.4 (40.9)
Viscous Energy (% Dissipation)	55.34 (40.0)	23.66 (17.1)	26.83 (19.4)	102.2 (10.8)	84.49 (8.93)	105.2 (11.1)	90.87 (13.5)	111.2 (16.5)	111.0 (16.5)	110.7 (16.5)	79.4 (11.8)	92.3 (13.7)

Notes

For Impulsive (0.015 sec) Impulse value is 1.575E-3 MPa-sec, For Impulsive (0.15 sec) Impulse value is 1.2E-2 MPa-sec.

The peak value of energies for different structural members over the entire impulse duration is included in this table for 64 gm combustion case and two limiting impulsive loads and a quasi-static load of 0.09 MPa applied uniformly on the test cell walls.